Searching for a Pair-Produced Supersymmetric Top Partner Using Recursive Jigsaw Variables and Boosted Decision Trees with 139 fb^{-1} of Data From the ATLAS Detector

Jared David Little
The University of Texas at Arlington

August 2020

Abstract

The Standard Model of Particle Physics is the most comprehensive theory describing how fundamental particles and three of the four fundamental forces are related. However, the Standard Model is known to be an incomplete theory with several limitations. Supersymmetry is an extension of the Standard Model of Particle Physics, introducing supersymmetric partners to every fermion and boson in the Standard Model. Supersymmetry gives a diverse collection of theoretical models providing solutions to these phenomenological inconsistencies. It contains a mechanism for stabilizing the Higgs boson mass while predicting the existence of several new particles, including a suitable Dark Matter candidate.

The Large Hadron Collider (LHC) is the world's most powerful particle accelerator, located at the CERN laboratory near Geneva, Switzerland. In the Summer of 2012, the ATLAS and CMS experiments at CERN announced the discovery of a particle,which was later confirmed to be the Higgs boson. This was a massive accomplishment, the discovery of a particle hypothesized in 1964 that has remained elusive until now. However, this is not the end of the experimental effort. ATLAS and CMS are general purpose detectors performing a multitude of measurements, as well as carrying out many searches for Beyond the Standard Model (BSM) physics.

In this dissertation, two searches are conducted for a pair-produced stop squark, the supersymmetric partner to the top quark. The stop can decay to a variety of final states, depending upon the hierarchy of the mass eigenstates formed from the linear superposition of the SUSY partners of the Higgs boson and electroweak gauge bosons. In this stop search, the relevant supersymmetric mass eigenstate is the neutralino ($\tilde{\chi}^0$). The searches for the stop in the 3-body decay channel presented here consist of

a b-quark, W-boson, and a $\tilde{\chi}^0$, with both W-bosons decaying to a lepton and a neutrino. In order to discriminate the signal from background two techniques are employed, a cut-and-count technique using recursive jigsaw variables and a technique using Boosted Decision Trees. The recursive jigsaw variables are derived using the Recursive Jigsaw Reconstruction technique, a method for decomposing measured properties event-by-event by approximating the rest frame of each intermediate particle state. These variables are powerful discriminators on their own, as shown in the cut-and-count analysis. Machine learning techniques are also utilized by training boosted decision trees, using the recursive jigsaw variables in tandem with other kinematic variables, to study whether we can enhance our discovery potential. These analyses use 139 fb^{-1} of $\sqrt{s} = 13$ TeV data collected at the ATLAS experiment during Run-2 of the LHC from 2015 until 2018. No evidence of an excess beyond the SM background prediction is observed in the Recursive Jigsaw Reconstruction analysis, however, exclusion limits at 95% confidence levels are set far exceeding the previous limits. The potential for an improvement on these limits is demonstrated by training Boosted Decision Trees, a technique I hope is used in future BSM physics searches.

Dedicated to Kitty and Vera.

Acknowledgements

There are so many people I wish to thank, unfortunately doing so here is simply not possible. Nobody gets anywhere by themself and I am only where I am due to the support of so many people throughout my life.

First, I want to express my deepest gratitude to my advisor, Dr. Kaushik De, for his patience and guidance and for providing me with an amazing atmosphere for performing my research. While I was still working on my undergraduate degree from the University of Oregon, if you told me I would move to CERN to perform research for my Ph.D, there is no way I would have believed you. Thank you for your insight and encouragement, they were essential to my growth over the last seven years.

I am deeply indebted to Dr. Giulio Usai, who displayed a great deal of patience and was instrumental in almost all of my work since I relocated to CERN. Upon coming to CERN, I knew very little about computer programming, it was only thanks to the patience and guidance of Dr. Usai that I was able to overcome this deficiency and contribute to work on ATLAS in a number of ways. I am also grateful to many other people in the ATLAS SUSY group, especially Dr. Luigi Longo and Dr. Marco Rimoldi, whose valuable suggestions were crucial in the SUSY analyses presented in this dissertation.

I also wish to express my deepest appreciation to my committee members: Dr. Giulio Usai, Dr. Andrew White, Dr. Jonathan Asaadi, and Dr. Yue Deng. Thank you for your continued support and guidance through this process, and thank you to the Physics department and the High-Energy Physics group at UTA for providing support throughout my journey. Thank you to my academic professors from the graduate school: Dr. Amir Farbin, Dr. Haleh Hadavand, Dr. Chris Jackson, Dr. Ramon Lopez,

Dr Zdzislaw Musielak, Dr. David Nygren, and Dr. Qiming Zhang, for the immense work you put in, from teaching high-level coursework to advising and assistance with navigating the scientific community. I especially wish to say thank you to Dr. Chris Jackson for teaching me all about the quantum world, and for always being there for the harder times. I am also grateful for Dr. Louise Heelan and Dr. Mark Sosebee, who always provided a safe and friendly environment to ask questions, an element that is crucial to success in academia. Thank you for all of your patience, open ears, and clear and concise answers.

Many thanks to the administrative assistants, both in Texas and at CERN, who have helped me a great deal with numerous tasks, including international relocation: Jaclyn Johnston, Stacey Cody, and Alexia Leyval. Without your assistance this opportunity would not even present itself. You help countless dreams come to fruition, and a great number of people owe you their gratitude.

This journey would not have been possible without the support of my family and friends. To my parents and siblings, thank you for always encouraging me and teaching me to work for my dreams. To my friends, Anthony in Oregon, Bright and Lim in Texas, and the Behnke family in Thoiry, thank you for being my family away from home. You have provided much needed support and for that, I am deeply grateful.

Last but certainly not least, I would like to express my deepest appreciation for my wife, Kitty, and my daughter, Vera. You have provided me with constant support throughout my studies, and your grace and your strength are truly an inspiration.

Contents

List of Figures

List of Tables

Chapter 1

The Standard Model and Supersymmetry

1.1 The Standard Model

What has come to be known as the *Standard Model* of Particle Physics is nothing less than a remarkable success. It is the culmination of years of hard work by many brilliant minds, starting with Paul Dirac in 1928 when he managed to merge quantum theory with that of relativity in his relativistic quantum mechanical treatment of the electron [1]. This launched a decades-long search for a consistent quantum-mechanical and relativistic treatment of electrodynamics, which we refer to as *quantum electrodynamics* (QED). This search concluded in the 1940's with the work of Dyson, Feynman, Schwinger, and Tomanaga [2], introducing the covariant and gauge invariant formulation of QED, the first relativistic quantum field theory (QFT). QED was an incredible success, making predictions that were in agreement with observations at an unprecedented level of accuracy.

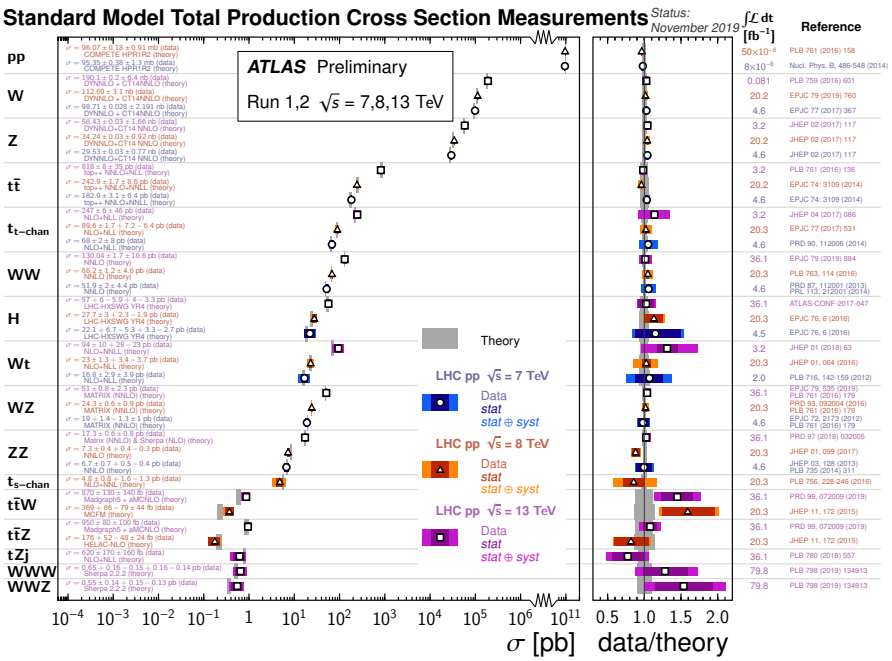

Figure 1.1: Ratio of several Standard Model total production cross section measurements compared to the corresponding theoretical expectations.

The Standard Model is a collection of quantum field theories that describes all of our current understanding of basic particles and their interactions. Several Standard Model cross section measurements are compared with their theoretical predictions in Figure 1.1. Two distinct classes of particles, quarks and leptons, are the building blocks of all visible matter in the universe. Gauge bosons, a third class of elementary particles, are the mediators in the fundamental interactions between particles referred to as force carriers. Particles are grouped according to their quantum attributes and interactions through the different forces.

The theory is composed of the Glashow-Weinberg-Salam theory of electroweak interactions, describing the electromagnetic and weak nuclear force, and Quantum Chromodynamics (QCD), describing the strong nuclear force. Quarks

Particle Type	Generation	Name (symbol)	Charge (e)	Mass
Quarks	I	Up (u)	$+2/3$	$2.2^{+0.5}_{-0.4}$ MeV
		Down (d)	$-1/3$	$4.7^{+0.5}_{-0.3}$ MeV
	II	Charm (c)	$+2/3$	$1.275^{+0.025}_{-0.035}$ GeV
		Strange (s)	$-1/3$	95^{+9}_{-3} MeV
	III	Top (t)	$+2/3$	173.0 ± 0.4 GeV
		Bottom (b)	$-1/3$	$4.18^{+0.04}_{-0.03}$ GeV
Leptons	I	electron (e)	-1	$0.511 \pm 3.1 \times 10^{-9}$ MeV
		Electron-neutrino (ν_e)	0	< 2 eV
	II	Muon (μ)	-1	$105.658 \pm 2.4 \times 10^{-6}$ MeV
		Muon-neutrino (ν_μ)	0	$< .19$ MeV
	III	Tau (τ)	-1	1776.86 ± 0.12 MeV
		Tau-neutrino (b)	0	< 18.2 MeV

Table 1.1: The Standard Model fermions, which are spin-1/2 particles, and their charge and mass. Interactions between these particles are mediated by the gauge bosons listed in table 1.2 [3].

and leptons are known as fermions, listed in table 1.1, with spin-$\frac{1}{2}$ and obeying Fermi-Dirac statistics. The force carriers, listed in table 1.2, have integer spin and obey Bose-Einstein statistics. All of the fermions and bosons have anti-particles, particles that carry the same mass and quantum numbers but opposite charge. The photon (γ) mediates the electromagnetic force, the vector bosons ($W^{\pm}/Z$) mediate the weak force, and gluons mediate the strong force. Interactions with the Higgs field (H) gives all massive particles their mass.

Force	Name (symbol)	Charge (e)	Mass
Electromagnetic	Photon (γ)	0	$< 10^{-18}$ eV
Weak	W boson ($W^{\pm}$)	± 1	80.379 ± 0.012 GeV
	Z boson (Z)	0	91.1876 ± 0.0021 GeV
Strong	Gluon (g)	0	0

Table 1.2: The Standard Model bosons, which are spin-1 particles, listed with their charge and mass. These particles mediate the interactions of the fermions listed in table 1.1 [3].

The road to the Standard Model began in the 1970s with Sheldon Glashow[4], Steven Weinberg[5], and Abdus Salam sharing the Nobel Prize in 1979 “for their

contributions to the theory of the unified weak and electromagnetic interaction between elementary particles, including, inter alia, the prediction of the weak neutral current [6]." The Higgs mechanism is essential within the Standard Model, it describes how all elementary particles acquire their masses by their interactions with the Higgs boson. This mechanism was first proposed by Phillip Warren Anderson in 1962[7], where he made early contributions to the idea of gauge symmetry breaking while working on the subject of superconductivity. The unified electroweak theory describes the electroweak force, including the force-carrying particles $\gamma, W^{\pm}, Z$. However, gauge invariance prohibits writing a dirac mass into the lagrangian, leading to these particles emerging massless. Experimentally, this is known to not be the case. In 1964 a theory capable of explaining this mass generation without breaking the gauge theory was published almost simultaneously by three independent groups: Robert Brout and François Englert[8]; Peter Higgs[9]; and Gerald Guralnik, C.R. Hagen, and Tom Kibble[10]. The Higgs mechanism mixes the $W_{0,1,2}$ and B into two charged, massive particles ($W^{\pm}$) as well as the Z boson. There is also the emergence of another spin-0 boson, the so-called Higgs boson.

On the 4th of July, 2012, the ATLAS and CMS experiments at CERN announced the observation of a particle consistent with this spin-0 boson, marking an absolutely monumental triumph of the Standard Model and the Higgs mechanism proposed 48 years prior [12–14]. Figure 1.2 is a summary of the different Higgs cross-sections as measured by ATLAS and normalized to their respective Standard Model Prediction.

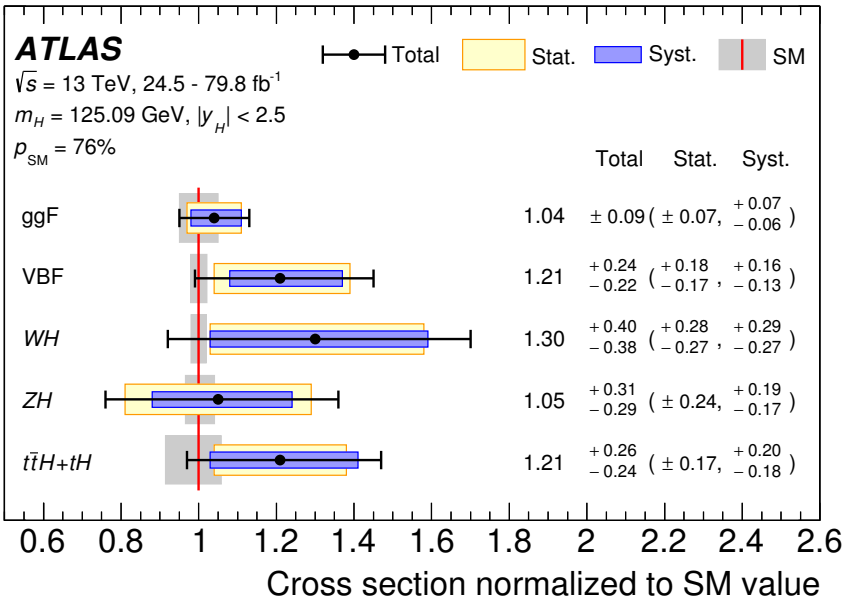

Figure 1.2: Cross-sections for ggF, VBF, WH, ZH and tt̄H+tH normalized to their SM predictions, measured with the assumption of SM branching fractions. The black error bars, blue boxes and yellow boxes show the total, systematic, and statistical uncertainties in the measurements, respectively. The grey bands indicate the theory uncertainties in the cross-section predictions [11].

Mathematical Formulation

The Standard Model is the most comprehensive quantum field theory of particle physics, encompassing a single concise model made up of two theories: the theory of Quantum Electrodynamics (QED) describing the electromagnetic and weak nuclear forces and QCD describing the strong nuclear force. These form the symmetry group of the Standard Model:

$$SU(3)_C \otimes SU(2)_L \otimes U(1)_Y \tag{1.1}$$

where $SU(3)_C$ is the gauge group of strong interactions (QCD), mediated by the eight gluons between color charged particles, and $SU(2)_L \otimes U(1)_Y$ is the

gauge group of electroweak theory. The subscript L here indicates coupling only to left-handed fermions and Y is the hypercharge, related to electric charge via $Q = I_3 + \frac{Y}{2}$, where I_3 is the weak isospin [15].

The gauge group of electroweak theory is spontaneously broken to the $U(1)_{EM}$ subgroup of electromagnetism,

$$SU(2)_L \otimes U(1)_Y \rightarrow U(1)_{EM} \tag{1.2}$$

The Standard Model is a quantum field theory with quantum fields as fundamental objects. These quantum fields include:

- Left-handed fermion doublets for quarks, $Q_L^f = \begin{pmatrix} u_L^f \\ d_L^f \end{pmatrix}$, and leptons, $L_L^f = \begin{pmatrix} \nu_L^f \\ e_L^f \end{pmatrix}$;
- Right-handed fermion singlets for quarks, u_R^f and d_R^f, and leptons, ν_R^f, e_R^f;
- electroweak boson fields, W_μ^A, B_μ;
- the gluon field, G_μ^A;
- and the Higgs field, a complex scalar doublet, $\phi = \begin{pmatrix} \phi^+ \\ \phi^0 \end{pmatrix}$;

with $f = 1, 2, 3$ denoting the generation of the fermion. Right-handed neutrinos do not exist in the Standard Model. Only the quarks (Q_L, u_R, and d_R) interact with the strong force mediated by the gluon gauge field G_μ^A, and thus transform under the $SU(3)_C$ gauge group. The left-handed fermion fields, along with the Higgs field, transform under the $SU(2)_L$ group. All fermion fields, excluding

only ν_R^f, are charged under $U(1)_Y$ hypercharge. A general covariant derivative for the Standard Model may be written as:

$$D_\mu = (\partial_\mu - ig_s G_\mu^A T^A - igW_\mu^a \tau^a - ig' Y B_\mu), \tag{1.3}$$

where $T^A = \frac{1}{2}\lambda^A$ and $\tau^a = \frac{1}{2}\sigma^a$ are the generators of $SU(3)$ and $SU(2)$, respectively, and $A = 1, 2, ..., 8$. λ^A are the Gell-Mann matrices and σ^a are the Pauli matrices [15].

The Standard Model Lagrangian

The Standard Model Lagrangian can be written as:

$$\begin{aligned}\mathcal{L} = &-\frac{1}{4}F_{\mu\nu}F^{\mu\nu}(\text{the gauge field kinetic energies and self-interaction terms})\\ &+ i\bar{\Psi}\not{D}\Psi(\text{fermion kinetic energies and interactions with } W^\pm, Z, \text{ and } \gamma)\\ &+ \Psi_i y_{ij}\Psi_j\phi + h.c.(\text{Yukawa interactions})\\ &+ |D_\mu\phi|^2 - V(\phi)(W^\pm, Z, \gamma, \text{ and Higgs masses and couplings}).\end{aligned} \tag{1.4}$$

The different terms will be discussed after we describe spontaneous symmetry breaking.

Spontaneous Symmetry Breaking

Spontaneous Symmetry Breaking is the process where a physical system in a symmetric state "breaks" into an asymmetric state. This process can be illustrated with a very simple example. Suppose you have some theory, $XY = 12$. This theory is symmetric, an interchange of X and Y gives you the same theory. However, we have many solutions, $X = 1, Y = 12; X = 2, Y = 6; X = 3, Y = 4$. None of these solutions are symmetric. In our case, we have equations of

motion, or the Lagragian, that obeys symmetries, but the lowest-energy vacuum solutions do not exhibit this symmetry. When the system goes into one of these solutions we say that it "breaks" the symmetry, even though the Lagragian retains the original symmetry.

Consider the ϕ^4-theory Lagrangian[16]:

$$\mathcal{L} = \frac{1}{2}(\partial_\mu \phi)^2 + \frac{1}{2}\mu^2\phi^2 - \frac{\lambda}{4!}\phi^4 \tag{1.5}$$

There is a discrete symmetry in this Lagrangian, it is invariant under the operation $\phi \to -\phi$. The minimum-energy classical configuration is a uniform field $\phi(x) = \phi_0$ with ϕ_0 chosen to minimize the potential

$$V(\phi) = -\frac{1}{2}\mu^2\phi^2 + \frac{\lambda}{4!}\phi^4 \tag{1.6}$$

with the minima defined by

$$\phi_0 = \pm v = \pm\sqrt{\frac{6}{\lambda}}\mu. \tag{1.7}$$

Here, the constant v is called the *vacuum expectation value* of ϕ.

Now suppose this system is near one of the minima and write $\phi(x)$ as

$$\phi(x) = v + \sigma(x). \tag{1.8}$$

Rewrite $\mathcal{L}$ in terms of $\sigma(x)$ by plugging 1.8 into 1.5 (and ignoring the constant terms):

$$\mathcal{L} = \frac{1}{2}(\partial_\mu \sigma)^2 - \frac{1}{2}(2\mu^2)\sigma^2 - \sqrt{\frac{\lambda}{6}}\mu\sigma^3 - \frac{\lambda}{4!}\sigma^4. \tag{1.9}$$

This Lagrangian describes a scalar field with mass $\sqrt{2}\mu$ with σ^3 and σ^4 inter-

actions, but the symmetry $\phi \to -\phi$ is no longer apparent. This is a simple example of a spontaneously broken symmetry. The Lagrangian has some global symmetry that appears to be lost when a ground state is realized for the field.

Gauge Fields

The gauge field kinetic energy and self-interactions are given by:

$$\mathcal{L} = -\frac{1}{4}F_{\mu\nu}F^{\mu\nu} = -\frac{1}{4}G^A_{\mu\nu}G^{\mu\nu A} - \frac{1}{4}W^a_{\mu\nu}W^{\mu\nu a} - \frac{1}{4}B_{\mu\nu}B^{\mu\nu}, \tag{1.10}$$

where

$$G^A_{\mu\nu} = \partial_\mu G^A_\nu - \partial_\nu G^A_\mu - g_s f_{ABC} G^B_\mu G^C_\nu \tag{1.11}$$

is the gauge field strength tensor for the gluon fields $G^{A=1,2,...,8}_\mu$, and the structure constants $f_{ABC}(A, B, C = 1, 2, ..., 8)$ are defined by the commutation relation:

$$[\lambda^A, \lambda^B] = 2if_{ABC}\lambda^C, \tag{1.12}$$

where $\lambda^{1,2,...,8}$ are the Gell-Mann matrices. Notice, W and B are the massless gauge bosons.

The Higgs Field

Now looking at the scalar part of the Lagrangian in 1.4:

$$\mathcal{L}_\phi = |D_\mu|^2 - V(\phi) = (D^\mu\phi)^\dagger(D_\mu\phi) - V(\phi) \tag{1.13}$$

where $\phi = \begin{pmatrix} \phi^+ \\ \phi^0 \end{pmatrix}$ is a complex Higgs scalar that transforms under the fundamental representation of $SU(2)$ with a $U(1)$ hypercharge $Y_\phi = +\frac{1}{2}$. V is the most general renormalizable potential invariant under $SU(2) \otimes U(1)$ and given

by:

$$V(\phi) = +\mu^2\phi^\dagger\phi + \lambda(\phi^\dagger\phi)^2. \tag{1.14}$$

With this potential we not only preserve renormalizability, but we can also generate masses for the charged fermions. The first term denotes the kinematic part of the field, which contains the interaction between the field ϕ and gauge bosons of the group $SU(2)_L \otimes U(1)_Y$. The second term in 1.14 is the potential of the field and is invariant under the gauge transformation $SU(2)_L$. λ is taken to be positive, insuring that V is bounded from below. μ^2 is the only parameter with units of mass in the classical Lagrangian. The Higgs couples to all fermions, the $W^\pm$, and Z vector bosons, as well as to itself via the cubic and quadratic self-interactions.

Now, let us explore how the gauge group of the electroweak theory gets broken. It is known from experimental observations that the fermions and gauge bosons of the weak interaction have mass, even though gauge invariance and renormalizability does not allow for bare mass terms in the Lagrangian for gauge boson and chiral fermions. Spontaneous symmetry breaking of the gauge invariance is introduced, preserving renormalizability and inducing masses for the lowest energy vacuum states, which are not gauge invariant. To find the vacuum states we should minimize the scalar Higgs potential of 1.14, restricted due to $SU(2) \otimes U(1)$ gauge invariance and renormalizability. Lorentz invariance of the vacuum requires us to set the fermion fields to zero and the $SU(2) \otimes U(1)$ gauge fields give a positive definite contribution to the Hamiltonian, so they also vanish in the vacuum. The covariant derivative of the Higgs field must also vanish in the vacuum. So, in the electroweak vacuum, the electroweak potentials are gauge equivalent to zero and the Higgs field is gauge equivalent to a constant [17].

What remains is the Higgs potential density, $V(\phi) = -\mu^2\phi^\dagger\phi + \lambda(\phi^\dagger\phi)^2$. To find the vacuum states we should minimize this potential, and the minimum of the Hamiltonian density occurs at the minimum of the potential:

$$\frac{dV}{d\phi} = -\mu^2\phi^\dagger + 2\lambda\phi^\dagger\phi\phi^\dagger = 0 \tag{1.15}$$

which has solutions,

$$\phi_{vac} = 0 \text{ and} \tag{1.16}$$

$$\phi^\dagger_{vac}\phi_{vac} = \frac{\mu^2}{2\lambda} \equiv \frac{v^2}{2}. \tag{1.17}$$

Clearly, $\phi_{vac} = 0$ is a local maximum, but the second solution corresponds to a closed continuous surface of minima:

$$\phi_{vac} = e^{i\theta_0}\mathbf{U}\begin{pmatrix} 0 \\ \frac{v}{\sqrt{2}} \end{pmatrix}, \tag{1.18}$$

where $\mathbf{U}$ is an element of the weak SU(2) which can be written as $\mathbf{U} = e^{i\frac{\tau_1}{2}\eta_1}e^{i\frac{\tau_2}{2}\eta_2}e^{i\frac{\tau_3}{2}\eta_3}$.

Putting this together we can get the general:

$$\phi_{vac} = \frac{v}{\sqrt{2}}\begin{pmatrix} e^{i(\theta'+\eta_1)}\sin\eta_2 \\ e^{i(\theta'-\eta_1)}\cos\eta_2 \end{pmatrix}, \tag{1.19}$$

where $\theta' = \theta_0 - \eta_3$. This is a continuous surface of minima on which one moves by $SU(2)\otimes U(1)$ gauge transformations, so that all points on the surface are gauge-equivalent. In order to consider our fluctuations about this minimum, we

can use any of these configurations, so we may as well choose the simplest:

$$\phi = \phi_0 + \phi' = \frac{1}{\sqrt{2}} \begin{pmatrix} 0 \\ v + H \end{pmatrix} \tag{1.20}$$

where ϕ' are quantum fields with a zero *vacuum expectation value*, and H is a Hermitian field. If we take the covariant derivative as in equation 1.3 the scalar kinetic energy is,

$$\begin{aligned}(D_\mu \phi)^\dagger D^\mu \phi &= \frac{1}{2}(0, v)(g W_\mu^a \tau^a + \frac{1}{2} g' B_\mu)(g W^{\mu b} \tau^b + \frac{1}{2} g' B^\mu) \begin{pmatrix} 0 \\ v \end{pmatrix} + \text{H terms} \\ &= \frac{v^2}{8}(g^2(W_\mu^1 + i W_\mu^2)(W^{1\mu} - i W^{2\mu}) + (-g W_\mu^3 + g' B_\mu)^2) + \text{H terms} \\ &\to M_W^2 W^{\mu +} W_\mu^- + \frac{M_Z^2}{2} Z^{0\mu} Z_\mu^0 + \text{H terms}\end{aligned} \tag{1.21}$$

where we have left out the kinetic term for the Higgs field as well as the gauge interaction terms. Three of the $SU(2) \times U(1)$ generators are broken, giving way to the observed massive gauge bosons.

$$\begin{aligned} W_\mu^\pm &= \frac{1}{\sqrt{2}}(W_\mu^1 \mp W_\mu^2) \\ Z_\mu^0 &= \cos\theta_W W_\mu^3 - \sin\theta_W B_\mu \end{aligned} \tag{1.22}$$

The fourth vector field,

$$A_\mu = \cos\theta_W B_\mu + \sin\theta_W W_\mu^3, \tag{1.23}$$

does not appear quadratically in the Lagrangian, and therefore, does not have

a mass term, though it does have the standard kinetic term. It is the vector potential associated with the massless photon. The masses of the gauge bosons are as listed in table 1.2:

$$\begin{aligned} M_W &= \frac{g_\nu}{2} = 80.385 \pm 0.015 \text{ GeV} \\ M_Z &= \sqrt{g^2 + g'^2}\frac{v}{2} = \frac{M_W}{\cos\theta_W} = 91.1876 \pm 0.0021 \text{ GeV} \end{aligned} \tag{1.24}$$

where

$$\tan\theta_W \equiv \frac{g'}{g} \rightarrow \sin^2\theta_W = 1 - \frac{M_W^2}{M_Z^2} = 0.23122 \tag{1.25}$$

is the weak (Weinberg) mixing angle.

Now, re-stating equation 1.21 with the H terms, the Higgs Lagrangian becomes:

$$\begin{aligned} \mathcal{L}_\phi =& (D_\mu\phi)^\dagger D^\mu\phi - V(\phi) \\ =& M_W^2 W^\mu + W_\mu^-(1+\frac{H}{v})^2 + \frac{M_Z^2}{2} Z^0\mu Z_\mu^0(1+\frac{H}{v})^2 \\ &+ \frac{1}{2}(\partial_\mu H)^2 - V(\phi) \end{aligned} \tag{1.26}$$

This equation has the $W_\pm$ and Z mass terms along with ZZH^2, $W^+W^-H^2$, ZZH, and W^+W^-H interactions. The last line is the canonical Higgs kinetic energy and the potential, which after symmetry breaking becomes

$$V(\phi) = -\frac{\mu^4}{4\lambda} - \mu^2 H^2 + \lambda v H^3 + \frac{\lambda}{4} H^4. \tag{1.27}$$

The first term in equation 1.27 is a constant, but the second term is the tree-level Higgs mass, $m_H = \sqrt{-2\mu^2} = \sqrt{2\lambda}v$. However, the quadratic coupling λ is unknown and m_H can't be predicted. The last two terms are the induced cubic

and quadratic interactions of the Higgs scalar.

Yukawa Interactions

The Yukawa terms are responsible for giving mass to all of the fermions, by coupling them to the Higgs boson.

$$\begin{aligned}\mathcal{L}_{\text{Yukawa}} = \Psi_i y_{ij} \Psi_j \phi + h.c. = &- y^{(d)}_{ij} (\bar{Q}^i_L)^a \phi_a d^j_R \\ &- y^{(u)}_{ij} \epsilon_{ab} (\bar{Q}^i_L)^a \phi^{\dagger b} u^j_R \\ &- y^{(e)}_{ij} (\bar{L}^i_L)^a \phi_a e^j_R \\ &- (y^{(\nu)}_{ij} \epsilon_{ab} (\bar{L}^i_L)^a \phi^{\dagger b} \nu^j_R) + \text{h.c.}\end{aligned} \tag{1.28}$$

After spontaneous symmetry breaking in the unitary gauge these Yukawa terms become:

$$\begin{aligned}\mathcal{L}_{\text{Yukawa}} \rightarrow &- y^{(d)}_{ij} \bar{d}^i_L (\frac{v+H}{\sqrt{2}}) d^j_R - y^u_{ij} \bar{u}^i_L (\frac{v+H}{\sqrt{2}}) u^j_R \\ &- y^{(e)}_{ij} \bar{e}^i_L (\frac{v+H}{\sqrt{2}}) e^j_R - y^\nu_{ij} \bar{\nu}^i_L (\frac{v+H}{\sqrt{2}}) \nu^j_R + h.c. \\ &= \bar{d}_L (M^{(d)} + h^{(d)} H) d_R + \bar{u}_L (M^{(u)} + h^{(u)} H) u_R \\ &+ \bar{e}_L (M^{(e)} + h^{(e)} H) e_R + \bar{\nu}_L (M^{(\nu)} + h^{(\nu)} H) \nu_R + h.c.\end{aligned} \quad , \tag{1.29}$$

where $\bar{u}_L = (\bar{u}_{1L}, \bar{u}_{2L}, \bar{u}_{3L})$. Likewise for u_R, d, e, and ν's. $M^{(x)} = y^{(x)}_{ij} v/\sqrt{2}$ is the fermion mass matrix and $h^{(x)} = M^{(x)}/v$ is the Yukawa coupling matrix. $M^{(x)}$ needs to be diagonalized in order to identify the physical fields. For each flavor, find a unitary matrix $U^{(u)}_{ij}$ and rotate $u^i_L \rightarrow U^{(u)\dagger}_{ij} u^j_L$, $u^i_R \rightarrow W^{(u)\dagger}_{ij} u^j_R$.

For the u-type quark masses, for example, we get:

$$U^{(u)}M^{(u)}W^{(u)\dagger} = M_D^{(u)} = \begin{pmatrix} m_u & 0 & 0 \\ 0 & m_c & 0 \\ 0 & 0 & m_t \end{pmatrix}, \tag{1.30}$$

a diagonal matrix with the eigenvalues equal to the physical masses. It can be written more generally when rotating to the mass eigenstates, $\psi_L'^i = U_{ij}^{(\psi)}\psi_L^j, \psi_R'^i = W_{ij}^{(\psi)}\psi_J^j$, where $\psi' = u'$,d',e', and ν' represent the mass eigenstates of the fermion fields. The Yukawa terms become:

$$\begin{aligned} \mathcal{L}_{\text{Yukawa}} = &- \sum_{i=1}^{3} m_{\psi'}^i \bar{\psi}'^i_L \psi_R'^i (1 + \frac{H}{v}) + h.c. \\ &- \sum_{i=1}^{3} m_{\psi'}^i \bar{\psi}'^i_L \psi_R'^i (1 + \frac{g}{2M_W} H) + h.c., \end{aligned} \tag{1.31}$$

where the sums are taken over all of the left- and right-handed fermion pairs. In conclusion, the Higgs field couples in a universal way to all the fermions, quarks, and leptons, with a strength proportional to their masses ($gm_i/2M_W$). Notice that this coupling is small, except in the case of the top quark. In the case of the gauge bosons, the coupling strength is proportional to the square of their mass. The Higgs boson does not couple directly to massless particles.

1.2 Physics Beyond the Standard Model

We have a theory that seems to explain everything: the electromagnetic and weak nuclear forces are described by QED while the strong nuclear force is described by QCD. We also have a mechanism (the Brout-Englert-Higgs mechanism) for giving mass to the force carriers, $W^{\pm}$ and Z, a fact that we knew to be true from experimental observations. On the 4th of July, 2012, the ATLAS and

CMS experiments at CERN announced the observation of a particle consistent with the Higgs boson in the mass region around 125 GeV [12–14], an essential component of the Brout-Englert-Higgs mechanism that gives rise to the mass of all particles. The more a particle interacts with the Higgs field, the more mass it obtains. Particles with no mass, like the photon, do not interact with the Higgs field.

We should not, however, hang up our hats and call it a day. The last 50 years have seen tremendous success in particle physics, and we owe a great debt to the previous generation of theories that have culminated in the Standard Model, but many fundamental questions remain unanswered as well as some insufficient explanations of experimentally observed phenomena.

Problems in the Standard Model

The first and most obvious example of the existence of physics beyond the Standard Model is the presence of a significant amount of gravitationally interacting non-luminous matter, commonly known as Dark Matter (DM). The presence of DM has been inferred from gravitational effects in cosmological observations such as galactic rotation curve, gravitational lensing, and measurements of the cosmic microwave background radiation. All of these observations lead us to conclude there must be a source of mass which makes up about 85% of the mass in the universe that we have not otherwise observed. Although the Standard Model does not incorporate gravity, it also does not postulate a viable candidate for DM. A viable candidate could not interact via the electromagnetic force, otherwise this would involve the release of light and we could observe it. It is also believed that DM would not interact strongly, otherwise we expect to observe it due to interactions with protons and electrons, leaving only its gravitational interactions as well as interacting via the weak nuclear force.

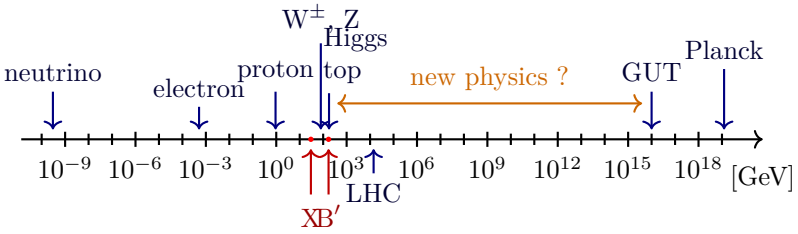

Figure 1.3: There are almost 10^{16} orders of magnitude between the low-TeV scale within reach of the LHC and the Plank-scale. Will we find new physics somewhere in between? Diagram created with TikZ [18] using [19].

The Standard Model also does not provide a sufficient explanation for the asymmetry between matter and anti-matter in the universe. The Big Bang should have created equal amounts of each, but everything we see is made up almost entirely of matter. There is, comparatively, hardly any anti-matter to be found.

In addition, there are still other physical phenomena that the Standard Model does not adequately explain. Many phenomena, such as electroweak mixing and CP violation, are determined by free parameters that must be set by experiment. It is also unclear why there are three generations of fermions or why there are orders of magnitude of difference in the masses of the quarks. Another example is the hierarchy problem, or the theoretical inconsistency between the relative strengths of the gravitational and electroweak forces. Of course, gravity is also not incorporated into the Standard Model.

An Argument for Naturalness

As described in section 1.1, the Higgs field is responsible for generating masses for the $W^{\pm}$, Z, and the fermions, but these interactions go both ways. The Higgs boson couples to all massive bosons via the gauge interaction as well as fermions via the Yukawa interactions, so quantum loops in the feynman

diagrams (shown in figure 1.4) are created to correct the Higgs mass. The largest of these corrections, Δm_H^2, from the higher order interactions with the top quark[20], is given by:

$$\begin{aligned} m_H^2 &= (m_H^2)_{bare} + \Delta m_H^2 \\ \text{with } \Delta m_H^2 &= -\frac{|y_T|^2}{16\pi^2}[-2\Lambda_{UV}^2 + 6m_f^2 ln(\frac{\Lambda_{UV}}{m_f}) + \dots], \end{aligned} \tag{1.32}$$

where y_T is the Yukawa coupling for the top quark and Λ_{UV} is the high-energy cutoff of the theory. The largest corrections involve higher-order interactions with the top quark. It can be seen from equation 1.32 that the correction is quadratically divergent with the cutoff scale. This means that if the Standard Model is the only theory up to the Planck scale where the SM and general relativity can no longer be kept separate since quantum gravity is expected to dominate, then $\Lambda_{UV}^2 \sim M_{Planck} = 1.22 \times 10^{19} GeV$. Given the observation of the Higgs boson mass around 125 GeV [12–14] we could reconcile this by setting the bare Higgs mass value in a way that perfectly settles the discrepancy between $(m_H^2)_{bare}$ and Δm_H^2 to give us this observed value. This means in the absence of extra terms to cancel out contributions in Δm_H^2 that the bare mass would have to be defined to a precision of about one part in 10^{19}. This is considered to be an unlikely proposition by physicists, since it is highly improbable and considered to be an incredibly lucky cancellation. This motivates us to search for a more *natural* solution, one where the dimensionless ratios between free parameters are of order one and not so finely tuned.

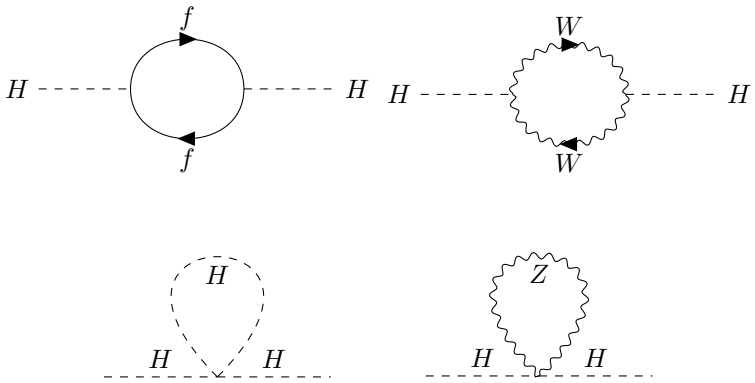

Figure 1.4: Examples of higher-order loop correction diagrams to the Higgs mass. The largest correction comes from the top quark.

There are several theories providing extensions to the Standard Model aiming to solve these issues, including Large Extra Dimension and Kaluza-Klein models. However, we will focus on supersymmetric models, a model we are searching for traces of at the Large Hadron Collider. Supersymmetry proposes an elegant and potentially *natural* solution.

Supersymmetry

Supersymmetry (SUSY) is a very popular theoretical framework for many reasons. It is a natural extension of the Standard Model. SUSY is also helpful when trying to understand how some of the biggest open questions in physics may be addressed while providing a set of very useful benchmarks for experimentalists searching for new physics beyond the Standard Model. If the supersymmetric particles are found to be somewhere in the weak scale, between around 100 GeV and a few TeV, it is expected that they will manifest in collisions at the Large Hadron Collider.

SUSY is a generalization of space-time symmetries that predicts new bosonic partners for the well-known fermions and new fermionic partners for the well-

known bosons of the Standard Model. These particles are similarly named, using the prefix *s-* for the superpartners to the Standard Model fermions (sfermions) while appending *-ino* for the superpartners to the Standard Model bosons (bosinos). So, for example, the supersymmetric partner to the top quark would be the *stop squark*.

If R-parity were to be conserved, a topic we will discuss more later, the lightest supersymmetric particle (LSP) would be stable. This provides us with a good candidate for **Dark Matter**, given the LSP is weakly interacting. The conservation of R-parity would also cause SUSY particles to be produced in pairs. SUSY offers a very elegant solution to the hierarchy problem since the new superpartners couple to the same Higgs sector as their Standard Model counterparts. Due to the symmetry with their Standard Model counterparts it turns out that the superpartners couple to the Higgs with the same Yukawa couplings only with the opposite sign, leading to a cancellation of all higher order corrections to the Higgs mass. This can reduce unnatural tuning in the Higgs sector by orders of magnitude if the superpartners to the top quark have masses not too far above the weak scale. The large top Yukawa coupling results in large $\tilde{t}_L - \tilde{t}_R$ mixing so that the mass eigenstate $\tilde{t}_1$ is typically the lightest of the squarks[21].

If SUSY were an unbroken symmetry, these sparticles would have the same mass as their Standard Model partner and we would have a supersymmetric transformation operator, Q, that turns a bosonic state into a fermionic state and a fermioninc state into a bosonic state:

$$Q_{susy}|\text{Boson}>\rightarrow|\text{Fermion}>, \quad Q_{susy}|\text{Fermion}>\rightarrow|\text{Boson}>. \tag{1.33}$$

Of course we have not observed any superpartners at these masses; therefore

SUSY must be a broken symmetry. If it exists, the mass spectrum of the supersymmetric particles is yet to be determined, which complicates our search by spanning a wide parameter space. As was discussed earlier, the ATLAS and CMS collaborations observation of a particle consistent with the SM Higgs at a mass of 125 GeV [12] has renewed our interest in electroweak symmetry breaking and the hierarchy problem. The Higgs boson is very sensitive to quantum corrections from physics at very high energy scales and demands a high level of fine-tuning to match our observation. As we discussed in section 1.2, the largest correction to the Higgs comes from the top quark[20], particularly the higher-order loop diagrams as shown in figure 1.5.

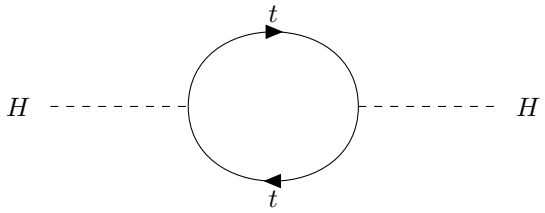

Figure 1.5: Loop correction to the Higgs mass from the top quark.

The possibility of unifying the four fundamental forces in the Standard Model into a Grand Unified Theory (GUT) is also a motivation for SUSY. For *the Minimal Supersymmetric Standard Model*, described below, the running gauge constants intersect at about an energy of 10^{16} GeV, as shown in figure 1.6. If these intersect, there is the possibility that there was a grand unified epoch in the early universe where these interactions were not yet distinct. Similar to how the electromagnetic and weak interactions unify into a single electroweak interaction, the strong interaction and electroweak interaction could unify into a single *electronuclear* interaction.

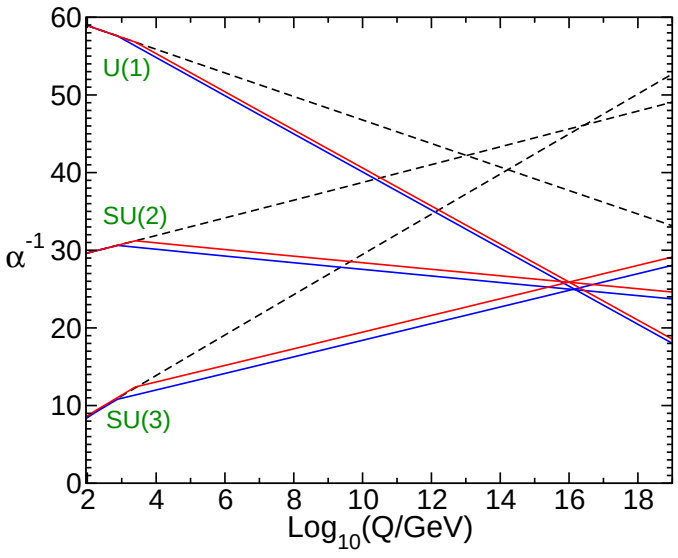

Figure 1.6: The evolution of the inverse gauge couplings α_a^{-1} in the Standard Model (dashed lines) and the MSSM (solid lines). In the case of the MSSM the gauge couplings meet at an energy scale of around $Q \approx 10^{16}$ GeV[20].

The Minimal Supersymmetric Standard Model

The *Minimal Supersymmetric Standard Model* (MSSM) is the minimum set of fields and interactions necessary for a consistent SUSY theory that can reproduce the Standard Model phenomenology. Before the supersymmetry breaking, the SUSY particles are written in *supermultiplets*, which are combinations of fermions and bosons. The supermultiplets of the MSSM are shown in table 1.3 organized according to their transformation properties under the usual Standard Model gauge group, $SU(3)_C \otimes SU(2)_L \otimes U(1)_Y$, and spin. This table includes all of the Standard Model fermions and bosons along with their superpartners, which differ in spin by 1/2. Two Higgs superfields are also required (H_u and H_d) to give mass to all of the particles and construct a minimal extension to the Standard Model. If there were only one Higgs chiral supermultiplet, the

electroweak gauge symmetry would suffer a gauge anomaly. The Standard Model Higgs, h^0, would then be a linear combination of H_u^0 and H_d^0. If SUSY were unbroken we would have superpartners of the leptons and quarks at the same mass as well as a massless photino and gluino. Therefore, any phenomenological model must contain a mechanism for spontaneous symmetry breaking if we want it to comport to reality.

Name		Spin-0	Spin-1/2	Spin-1
Chiral Supermultiplets				
Squarks / Quarks	Q=	$\begin{pmatrix}\tilde{u}_L \\ \tilde{d}_L\end{pmatrix}$	$\begin{pmatrix}u_L \\ d_L\end{pmatrix}$	–
3 Generations	$\bar{u}$	$\tilde{u}_R^*$	$u_R^\dagger$	–
	$\bar{d}$	$\tilde{d}_R^*$	$d_R^\dagger$	–
Sleptons / Leptons	L=	$\begin{pmatrix}\tilde{\nu} \\ \tilde{e}_L\end{pmatrix}$	$\begin{pmatrix}\nu_L \\ e_L\end{pmatrix}$	–
3 Generations	$\bar{e}$	$\tilde{e}_R^*$	$e_R^\dagger$	–
Higgs / Higgsinos	$H_u =$	$\begin{pmatrix}H_u^+ \\ H_u^0\end{pmatrix}$	$\begin{pmatrix}\tilde{H}_u^+ \\ \tilde{H}_u^0\end{pmatrix}$	–
	$H_d =$	$\begin{pmatrix}H_d^0 \\ H_d^-\end{pmatrix}$	$\begin{pmatrix}\tilde{H}_d^0 \\ \tilde{H}_d^-\end{pmatrix}$	–
Gauge Supermultiplets				
Gluino, Gluon		–	$\tilde{g}$	g
Winos, W		–	$\tilde{W}^\pm, \tilde{W}^0$	$W^\pm, W^0$
Binos, B		–	$\tilde{B}^0$	B^0

Table 1.3: The chiral- and gauge- supermultiplets in the MSSM using a Weyl spinor basis. The gauge group in the MSSM is the same as the Standard Model, $SU(3)_C \otimes SU(2)_L \otimes U(1)_Y$

The Lagrangian of the MSSM supermultiplets must be invariant under SUSY transformations even though the broken vacuum state is not. This Lagrangian, with all gauge and Yukawa interactions, can be written as:

$$\mathcal{L}_{SUSY} = \mathcal{L}_{\text{kinetic}} + \mathcal{L}_W \tag{1.34}$$

where we have the standard kinetic term and the Lagrangian of the SUSY *superpotential*, which includes the supermultiplets of table 1.3. All of the terms in the MSSM superpotential are renormalizable and invariant under supersymmetry and conserve **R-parity**. The superpotential for the MSSM is given by:

$$W_{MSSM} = \bar{u} y_u Q H_u - \bar{d} y_d Q H_d - \bar{e} y_e L H_d + \mu H_u H_d. \tag{1.35}$$

H_u, H_d, Q, L, $\bar{u}$, $\bar{d}$, $\bar{e}$ here are chiral superfields corresponding to the chiral supermultiplets in table 1.3. y_u, y_d, and y_e are 3×3 matrices representing dimensionless Yukawa couplings. After symmetry breaking, we can write the Lagrangian with all of the supersymmetry violating terms included in $\mathcal{L}_{\text{soft}}$, $\mathcal{L} = \mathcal{L}_{\text{SUSY}} + \mathcal{L}_{\text{soft}}$. In order for SUSY to resolve the hierarchy problem and naturally maintain a hierarchy between the electroweak scale and the Planck mass scale, the supersymmetry-breaking couplings should be soft, or contain only positive dimensions of mass. Particularly, there should be no dimensionless supersymmetry-breaking couplings.

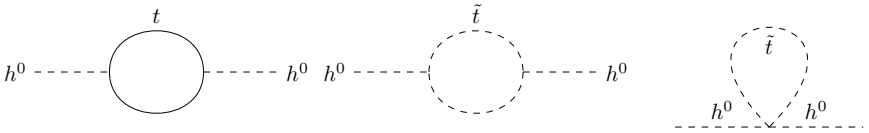

Figure 1.7: Contributions to the MSSM lightest Higgs squared mass from top- and stop-quark one-loop diagrams.

The tree-level formula for the squared mass of the Higgs is subject to substantial quantum corrections. The largest such corrections typically come from top and stop loops, shown in figure 1.7. The top and stop quarks contributions to the Higgs squared mass, shown in figure 1.7, have opposite sign and cancel to a

value proportional to the mass of the top and stop squarks:

$$\Delta m_{h^0}^2 = \frac{3}{4\pi} \cos^2 \alpha y_t^2 m_t^2 ln(m_{\tilde{t}_1} m_{\tilde{t}_2}), \tag{1.36}$$

where α is the SUSY Higgs sector mixing angle and y_t is the top Yukawa coupling. In order to get reasonable predictions for the Higgs scalar masses for a given set of model parameters we have to include all of the one-loop corrections as well as some of the more dominant two- and three-loop corrections. Even after this there are large theoretical uncertainties on the Higgs mass, but including such corrections it was estimated that

$$m_{h^0} \leq 135 \text{ GeV} \tag{1.37}$$

in the MSSM[20]. This estimation was made long before the discovery of the 125 GeV Higgs boson. Equation 1.37 assumes that all sparticles contributing to the Higgs mass in loops have masses under 1 TeV.

R-parity is a discrete symmetry defined as

$$R_p = (-1)^{3B+L+2s}, \tag{1.38}$$

where s is spin, B is baryon number, and L is lepton number. All Standard Model particles have R-parity of +1 and supersymmetric particles have R-parity of −1. This means that if R-parity is conserved we can only produce superpartners in pairs and the LSP is stable, since it would not be able to decay to Standard Model particles, providing a possible DM candidate.

In the Standard Model, there are no interactions that violate baryon or lepton number, but in the MSSM, it is possible to write down the renormalizable terms

that are usually excluded,

$$W_{\Delta L=1} = \frac{1}{2}\lambda^{ijk} L_i L_j \bar{e}_k + \lambda'^{ijk} L_i Q_j \bar{d}_k + \mu'^i L_i H_u, W_{\Delta B=1} = \frac{1}{2}\lambda''^{ijk} \bar{u}_i \bar{d}_j \bar{d}_k, \tag{1.39}$$

because they violate either baryon(B) or lepton(L) number. The existence of these terms would be rather surprising since they allow for observations that are not consistent with current experimental observations, most notably proton decay. If λ and λ' are not suppressed, the lifetime of the proton would be incredibly short. It could just be postulated that baryon- and lepton-number are conserved, but in the Standard Model this is not the case. It merely just stems from the fact that there are no possible renormalizable Lagrangian terms that violate these quantum numbers. Introducing *R-parity* into the MSSM eliminates the possibility of B and L violating terms in the renormalizable superpotential.

SUSY Electroweak Symmetry Breaking and Mass Eigenstates

Electroweak symmetry breaking in SUSY occurs in the same way as described in Section 1.1 for the Standard Model, however a bit more complicated due to the two complex Higgs doublets, H_u and H_d, rather than just one. It is not possible to diagonalize both the gauge and mass eigenstates due to the Yukawa couplings in the Higgs sector. Here we describe the mass eigenstates for the neutralinos, charginos, and stop quarks. However, the gluino is a color octet (and superpartner of the gluon) and it can not mix with the other particles in the MSSM.

Neutralino and Chargino Mass Eigenstates

The neutral higgsinos ($\tilde{H}_u^0, \tilde{H}_d^0$) and gauginos ($\tilde{B}, \tilde{W}^0$) combine to form four neutral mass eigenstates called *neutralinos* ($\tilde{\chi}^0$). Conventionally, we label the

neutralinos according to their mass, $m_{\tilde{\chi}_1^0} < m_{\tilde{\chi}_2^0} < m_{\tilde{\chi}_3^0} < m_{\tilde{\chi}_4^0}$. The lightest neutralino is typically assumed to be the lightest supersymmetric particle, or LSP, unless R-parity is violated. The charged higgsinos and winos ($\tilde{W}^{\pm}$) mix to form two mass eigenstates of charge ± 1 called *charginos*, similarly ordered as $m_{\tilde{\chi}_1^{\pm}} < m_{\tilde{\chi}_2^{\pm}}$. Consider as an example the case of the neutralino masses, we can write the Lagrangian in the gauge-eigenstate basis as:

$$\mathcal{L}_{neutralino} = \frac{1}{2}(\psi^0)^T \mathbf{M}_{\tilde{\chi}^0} \psi^0 + h.c. \tag{1.40}$$

where $\psi^0 = (\tilde{B}, \tilde{W}^0, \tilde{H}_d^0, \tilde{H}_u^0)$ and,

$$\mathbf{M}_{\tilde{\chi}^0} = \begin{pmatrix} M_1 & 0 & -c_\beta s_W m_Z & -s_\beta s_W m_Z \\ 0 & M_2 & c_\beta c_W m_Z & -s_\beta c_W m_Z \\ -c_\beta s_W m_Z & c_\beta c_W m_Z & 0 & -\mu \\ s_\beta s_W m_Z & -s_\beta c_W m_Z & -\mu & 0 \end{pmatrix}, \tag{1.41}$$

Here the two mixing angles have been abbreviated as: $s_k \equiv \sin\theta_k$ and $c_k \equiv \cos\theta_k$. The entries M_1 and M_2 comes from $\mathcal{L}_{soft}$. This matrix needs to be diagonalized in order to obtain the neutralino mass eigenstates. The same procedure can be repeated to obtain the chargino mass eigenstates.

Stop Mass Eigenstates

In this model, there is also mixing for squarks and sleptons. For example, the mass eigenstate for the stops are obtained as follows:

$$\begin{pmatrix} \tilde{t}_1 \\ \tilde{t}_2 \end{pmatrix} = \begin{pmatrix} c_{\tilde{t}} & -s_{\tilde{t}}^* \\ s_{\tilde{t}} & c_{\tilde{t}}^* \end{pmatrix} \begin{pmatrix} \tilde{t}_L \\ \tilde{t}_R \end{pmatrix}, \tag{1.42}$$

where $c_{\tilde{t}}$ and $s_{\tilde{t}}$ are mixing angles that incorporate Yukawa couplings and soft breaking terms which mix left/right-handed stops. [20]

1.3 Conclusion

Supersymmetry is an extension to the Standard Model, adding to its incredible success while trying to address its shortcomings. The observation of a 125 GeV Standard Model like Higgs boson hints that supersymmetry might be accesible at the TeV-scale, resolving the hierarchy problem while preventing excessive fine-tuning. The lightest supersymmetric particle could also provide us with a promising dark matter candidate. All of these arguments give us good reason to continue the search for supersymmetry. No evidence has been found as of yet, but there is good reason to be hopeful that supersymmetry may show up at the LHC, given we still have quite a bit of phase-space to explore. In Chapter 4 we will discuss more of the assumptions that go into the SUSY models we search for at the LHC, including simplified SUSY models with minimal assumptions. We can extrapolate more specific information from these models onto more specifical SUSY models while probing our data for SUSY in a more general way.

Chapter 2

The ATLAS Experiment

The ATLAS Experiment is located at the European Center for Nuclear Research (CERN). It is one of seven experiments located at beam crossings along the Large Hadron Collider. ATLAS, along with CMS, make up the two general-purpose detectors at CERN that investigate the largest range of physics possible. Having two independently designed detectors allows for the verification of any new discoveries made.

2.1 The Large Hadron Collider at CERN

The Large Hadron Collider (LHC) [22] first started up in 2008 and provides particle collisions for ATLAS. It is a 27 km super-conducting particle accelerator located approximately 100 m underground. The main purpose of the LHC is to provide proton-proton collisions at four interaction points along the ring, with a particle detector housing each of these collision points: ATLAS [23], CMS [24], ALICE, and LHCb.

The proton beams are guided around the accelerator ring by using 1232 super-conducting dipole magnets, each of them 15 m long. These magnets provide a

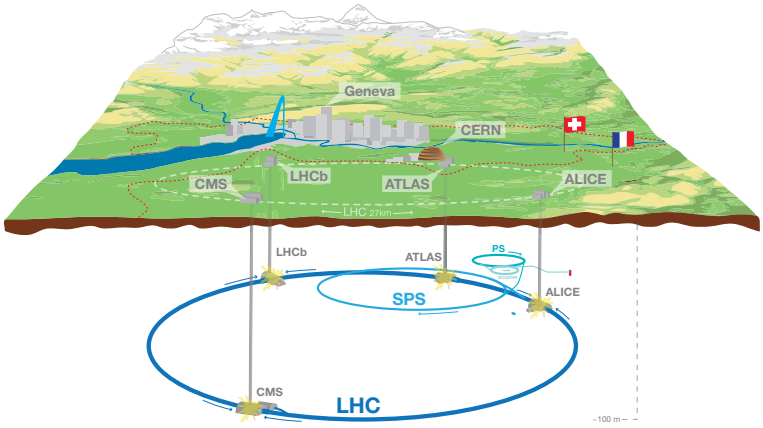

Figure 2.1: [25] Schematic layout of the LHC accelerator complex at CERN which sits on the border of France and Switzerland. The four main experiments are shown here: ALICE, ATLAS, CMS, and LHCb. All four experiments are located approximately 100m underground.

strong 8.3 T magnetic field for bending the trajectory of the protons. There are 392 main quadrupole magnets that help focus the proton bunches into a tight beam with four magnets placed symmetrically around the beam pipe to squeeze the beam either horizontally or vertically. The LHC produces collisions with a center-of-mass of up to $\sqrt{s} = 13$ TeV. When these beams are collided new particles are created which may lead to the production of new physics beyond the Standard Model.

The LHC is the final step in the accelerator train at CERN, shown in Figure 2.2. Protons are passed from low energies up to their final energy of 6.5 TeV per beam for a center-of-mass energy of $\sqrt{s} = 13$ TeV. The protons begin at LINAC2, a linear accelerator that takes the proton energies up to 50 MeV.

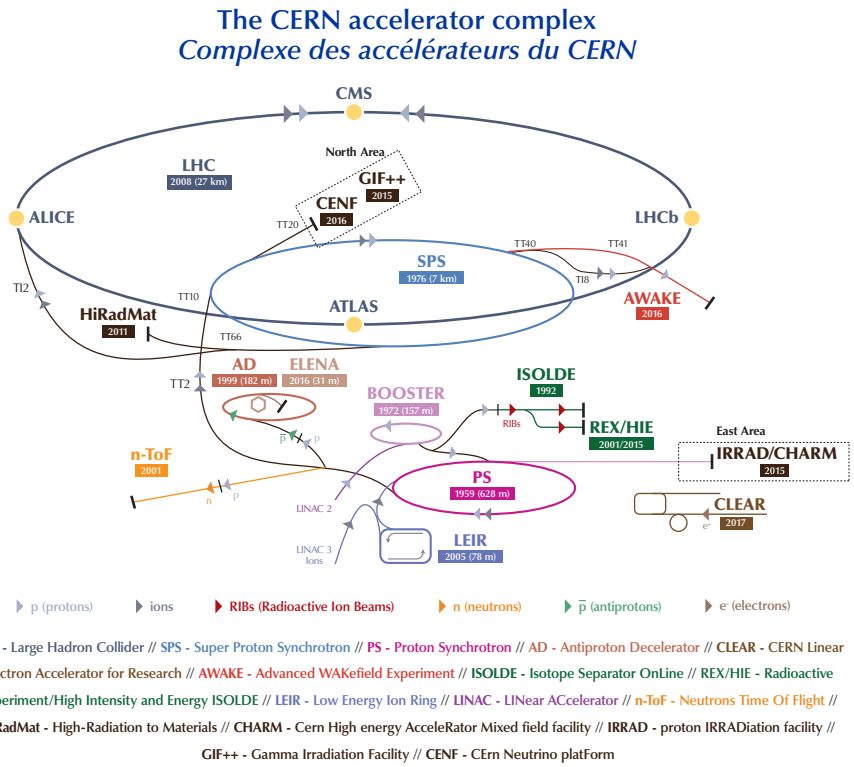

Figure 2.2: Schematic layout of the LHC accelerator complex at CERN [22] including the older accelerators used for ramping up the energy of the particles. The four collision points along the main collider are indicated with a yellow dot.

These protons are injected into the Proton Synchrotron Booster and accelerated up to 1.4 GeV. From the Proton Synchrotron Booster they are passed into the Proton Synchrotron where they are accelerated up to 25 GeV then sent to the Super Proton Synchrotron and accelerated to 450 GeV. After the Super Proton Synchrotron the protons are finally sent to the LHC which can run for many hours at a time, with each proton beam consisting of up to 2808 bunches and around 10^{11} protons per bunch.

Operation of the LHC during Run 2

In this dissertation I present a search for supersymmetry using the full Run 2 dataset, which consists of data taken from 2015-2018. During this period the center-of-mass energy was $\sqrt{s} = 13$ TeV with a total integrated luminosity of 140.4 fb^{-1} and a bunch spacing of 25 ns. The analysis uses 3.21 fb^{-1} of data collected from 2015, 32.86 fb^{-1} of data collected in 2016, 44.3 fb^{-1} of data collected in 2017, and 59.9 fb^{-1} of data collected in 2018.

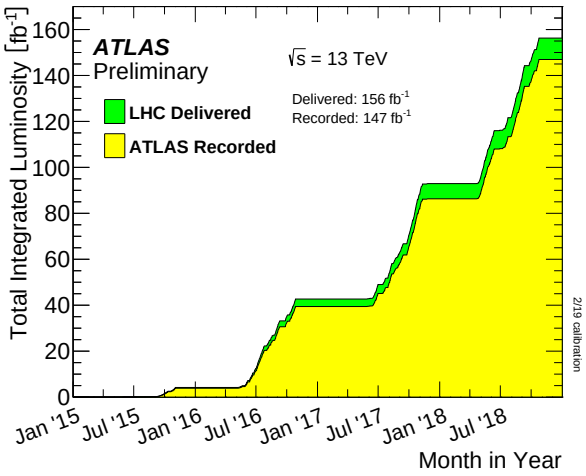

Figure 2.3: [26] Cumulative luminosity versus time delivered to (green) and recorded by (yellow) ATLAS during stable beams for proton-proton collisions at 13 TeV center-of-mass energy in LHC Run 2. There is a small difference between delivered and recorded luminosity, reflecting the small inefficiency of ATLAS Data AcQuisition (DAQ). The luminosity is derived from a method similar to that outlined in [27], from a calibration of the luminosity scale using x-y beam separation scans performed in 2015, 2016 (twice), and 2017.

Luminosity is a unit of measure proportional to the number of collisions. We often discuss both *instantaneous* ($L_{inst.}$) and *integrated* (L_{int}) luminosity. Instantaneous luminosity as shown in Figure 2.4 is proportional to the bunch crossing rate and represents the number of potential collisions per second while the integrated luminosity as shown in Figure 2.3 is the integral of the

instantaneous luminosity taken over the data taking period.

$$L_{int} = \int L \, dt = 140.4 fb^{-1}$$

The machine luminosity is described in [22] and depends only on the beam parameters. This can be written for a gaussian beam distribution as:

$$L = \frac{N_b^2 n_b f_{rev} \gamma_r}{4\pi \varepsilon_n \beta^*} F$$

where N_b is the number of particles per bunch, n_b the number of bunches per beam, f_{rev} the revolution frequency, γ_r the relativistic gamma factor, ε_n the normalized transverse beam emittance, β^* the beta function at the collision point, and F the geometric luminosity reduction factor due to the crossing angle at the interaction point:

$$F = \left(1 + \left(\frac{\theta_c \sigma_z}{2\sigma^*}\right)^2\right)^{-1/2}$$

θ_c is the full crossing angle at the interaction point, σ_z the RMS

bunch length, and σ^* the transverse RMS beam size at the interaction point.

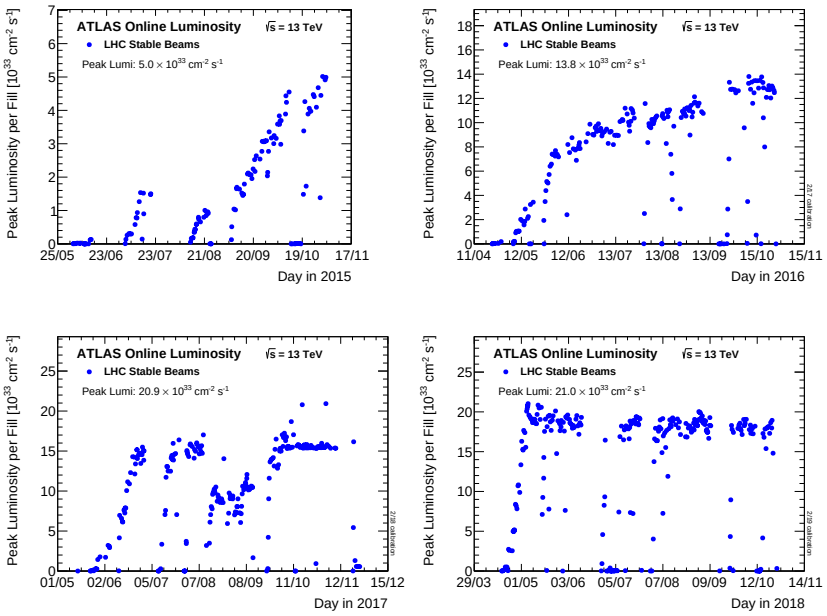

Figure 2.4: The peak instantaneous luminosity delivered to ATLAS during stable beams for proton-proton collisions at 13 TeV center-of-mass energy is shown for each LHC fill as a function of time in 2015 (top-left), 2016 (top-right), 2017 (bottom-left), and 2018 (bottom-right). The luminosity is determined using counting rates measured by the luminosity detectors.

Pileup Conditions at the LHC

In reality, due to the high luminosities at which the LHC operates, there are multiple proton-proton collisions in each bunch crossing. This effect is known as *pileup* and there are two main types; *in-time pileup* and *out-of-time pileup*. **In-time pileup** occurs when there are multiple proton-proton interactions in the same bunch crossing. These collisions contribute to a significant background

for all physics objects. In-time pileup events are generated using Pythia8 [28] and are passed through the standard ATLAS detector simulation [29]. **Out-of-time pileup** occurs when there are additional proton-proton interactions just before or after the collision of interest. The effects of out-of-time pileup depends on the detector technology, different time windows are used to include the appropriate level of background in each detector.

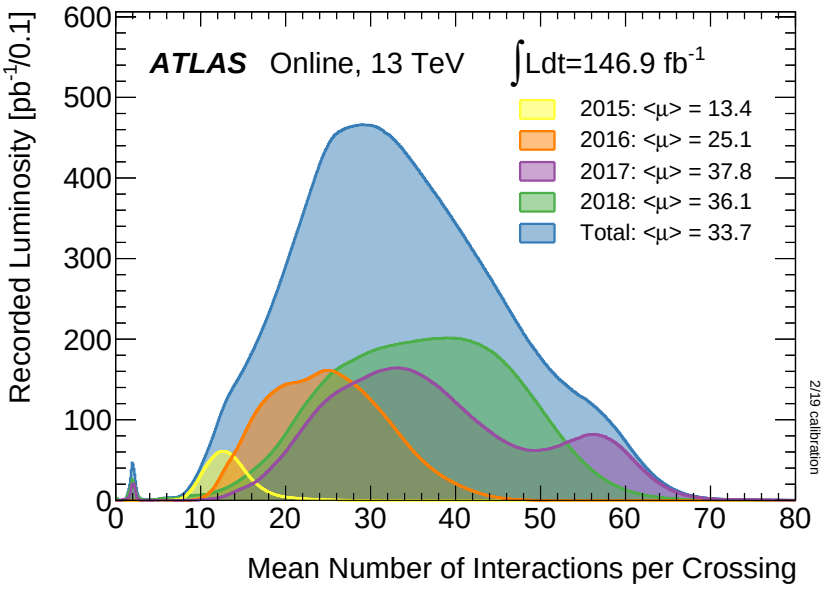

Figure 2.5: The distribution of the mean number of interactions per bunch crossing for each year of Run 2 data-taking. Also shown is the over distribution for all of Run 2 in blue. The mean is taken as the mean of the poisson distribution of the number of interactions per crossing, calculated for each bunch.

2.2 The ATLAS Experiment

The ATLAS detector 2.6 is one of the four main experiments, located at the Point 1 collision point of the LHC. ATLAS is the largest volume particle detector ever constructed. There are over 100 million electronic channels and over 3000 km of cables, making it one of the most complex particle detectors in existence. Particle collisions at the center of the detector create particles that travel in all directions, so ATLAS was cylindrically designed to encompass all of them.

There are four major components of the ATLAS detector: the inner detector, the calorimeter, the muon spectrometer, and the magnet system. The inner detector measures the direction, momentum, and charge of charged particles produced in each collision. The calorimeter measures the energy a particle loses as it passes through it. Most calorimeters are designed to stop or absorb most of the particles coming from the collisions, with exceptions being muons and neutrinos, allowing us to measure all (or most) of their energy within the detector. Muons leave minimal amounts of energy in the calorimeter and neutrinos pass through it without leaving a trace.

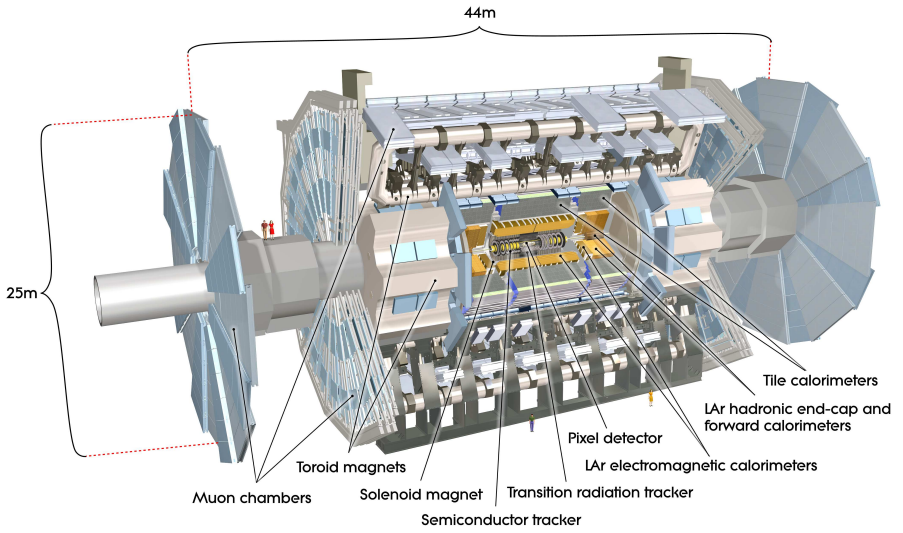

Figure 2.6: A diagram of the ATLAS detector [23] which weights about 7000 tonnes and is about 25 m high and 44 m in length. Two people are shown for scale between the muon chambers to the left.

The Inner Detector

The inner detector [30], shown in Figure 2.7, is built right around the beam pipe and is therefore the first detector to see the outgoing particles after the collision. It has a cylindrical geometry and is encapsulated within the 2 T solenoid magnet. The inner detector is designed to be very compact and to reconstruct charged particle tracks above $p_t > 500\ MeV$ for $|\eta| < 2.5$ with excellent momentum resolution. There are three different components that make up the inner detector and they are shown in Figure 2.7.

The pixel detector is the closest to the beam pipe and provides the best possible primary vertex and secondary vertex resolution.

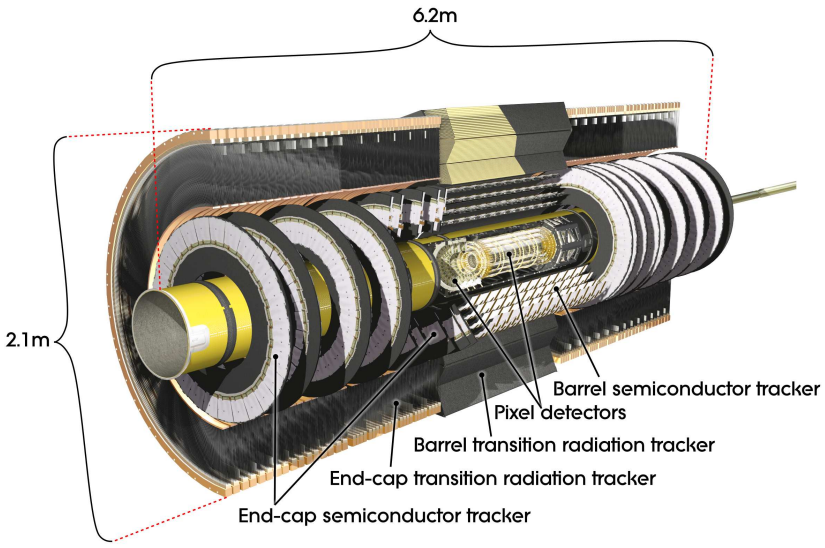

Figure 2.7: An overview of the inner detector[23], showing the three main pieces listed from smaller distances to larger distances from the beam pipe: the pixel detector, the semiconductor tracker, and the transition radiation tracker. [23]

The ability to detect short lived particles in ATLAS is determined by our ability to separate the primary and secondary vertices, as well as identifying b-jets due to their long lifetime. The pixel detector is made up of three barrel layers and three endcap disks at each end. The first barrel layer sits only 50.5 mm from the beam line, so the radiation at this point is incredibly intense. The layers and disks are equipped with pixels, silicon sensors that are segmented into small rectangles. The pixel detector consists of 80 million pixels, or readout channels. Each pixel has an area of $50x400$ μm^2 with a resolution of 14 μm in the ϕ-direction and 115 μm in the z-direction. The three barrel layers have 1456 modules each with

46,080 pixels. The three pixel disks in each endcap have 144 modules with 6.6 million readout channels.

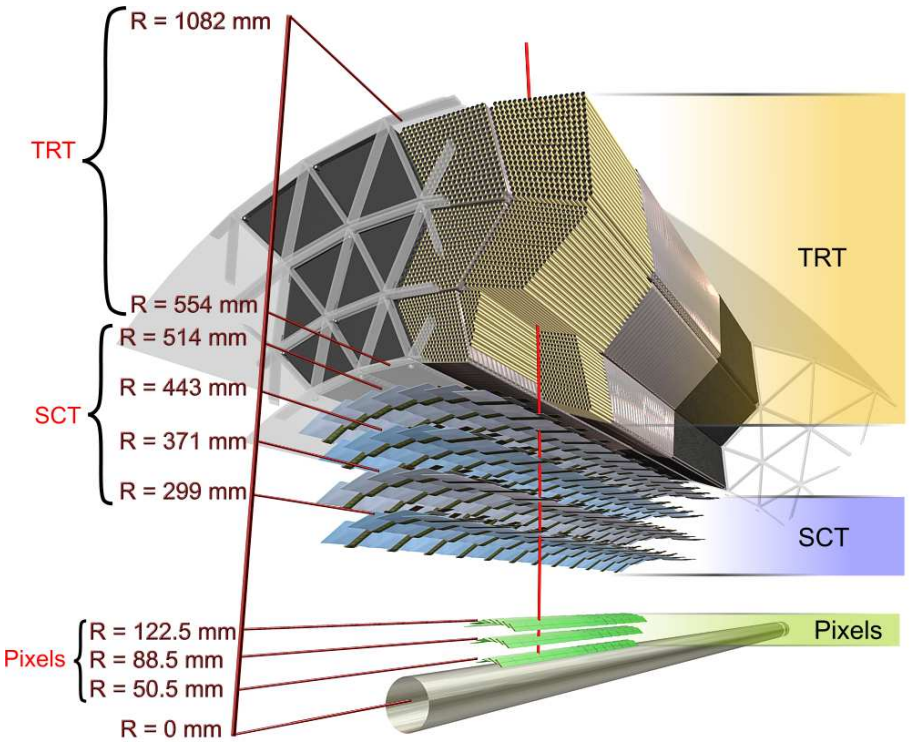

Figure 2.8: A cross-sectional view of the inner detector. [23]

The semiconductor tracker (SCT) sits just outside of the pixel detector. The particle density is lower further away from the beam line, so SCT uses longer and narrower silicon strips instead of pixels. This geometry allows us to cover a large area in a more economical way. Each readout channel will cover a larger area. Silicon microstrip sensors form the detecting medium for charged particles in the SCT barrel and endcap regions. There are 4088 two-sided modules and over 6 million strips covering 63 m^2 for $|\eta| < 2.5$.

The barrel consists of 8,448 identical rectangular single-sided p-in-n sensors while the endcap has 6,944 single-sided p-in-n sensors. The SCT provides a position resolution of 17 μm in the transverse plane and 580 μm in the z-axis. The SCT is designed to provide between 4 and 9 precision measurements in the intermediate radial range for each track. The pixel and SCT detectors contribute to the measurement of momentum, impact parameter, and vertex identification of a charged particle track.

The third and final component of the inner detector is the **transition radiation tracker (TRT)**. The TRT is made up of 300,000 drift tubes, or 350,000 readout channels. They cover 12 m^3 of space for $|\eta| < 2.0$. These drift tubes are 4 mm in diameter and 144 cm (37 cm) long in the barrel (endcap) region with a 0.03 mm diameter gold-plated tungsten wire. There are 250,000 tubes in both of the endcaps, and 50,000 in the barrel region. However, the barrel region is read out on each end separately. The TRT provides a position resolution of 130 μm in ϕ. Every charged particle track with $|\eta| < 2.0$ will traverse through at least 36 tubes providing transition radiation tracking for charged particle identification. If two different mass charged particles traverse the TRT with the same transverse momentum, the lighter-mass particle will emit more transition radiation photons than the heavier-mass par-

ticle. The TRT is therefore very helpful in distinguishing between electrons and charged hadrons such as pions.

The Calorimeters

The ATLAS calorimeter system is shown in Figure 2.8. There are two types of calorimeters used in ATLAS: electromagnetic and hadronic. An electromagnetic calorimeter is designed to measure the energy of particles that interact via the electromagnetic interaction while a hadronic calorimeter is designed to measure the energy of particles interacting via the strong force. Both of these calorimeters are sampling calorimeters, a type of calorimeter that uses an "active" material that provides the detectable signal and a different dense "absorber" material that reduces the particle energy. The dense material is chosen to absorb a lot of the particle energy, therefore only a fraction of the energy deposited in the calorimeter is sampled. This requires the calorimeter's energy response to be calibrated by studying the calorimeter response.

The ATLAS calorimeters cover the range $|\eta| < 4.9$ and are fully symmetric in ϕ. In the $|\eta|$ region matching the inner detector the electromagnetic calorimeter is just outside, allowing for precision measurements of electrons and photons. The hadronic calorimeter lies just beyond and is suitable for jet reconstruction and E_T^{miss} measurements.

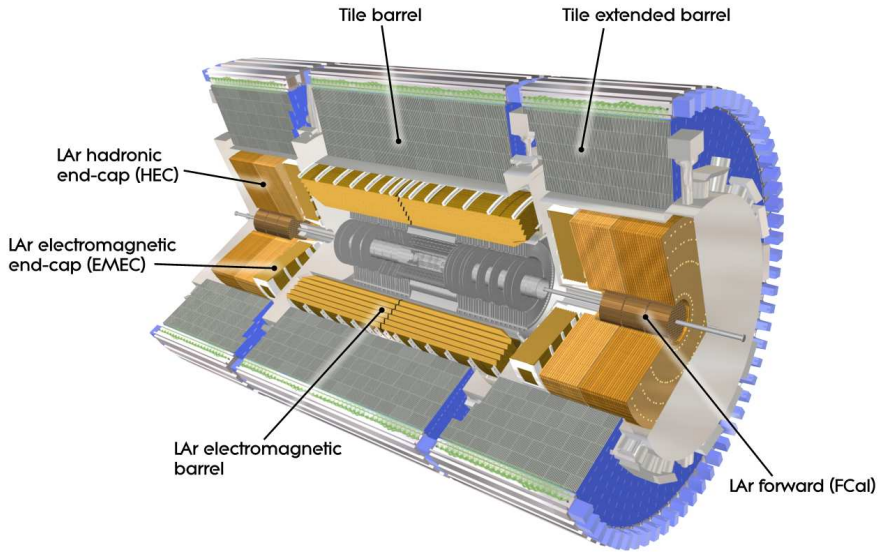

Figure 2.9: An overview of the ATLAS calorimeter system. [23]

The calorimeters must provide containment and excellent coverage for electromagnetic and hadronic showers and limiting energy leaks outside of the calorimeter and into the muon spectrometers. This containment is also important for measuring E_T^{miss}, which is crucial for many physics programs, particularly supersymmetry searches such as mine.

The Liquid Argon (LAr) Electromagnetic Calorimeter[31], consisting of the Electromagnetic Barrel (EMB) and Electromagnetic End Caps (EMEC), are Lead/Liquid Argon detectors with an accordion-like structure shown in Figure 2.10. This structure allows for a gapless measurement in the ϕ-direction while also allowing for

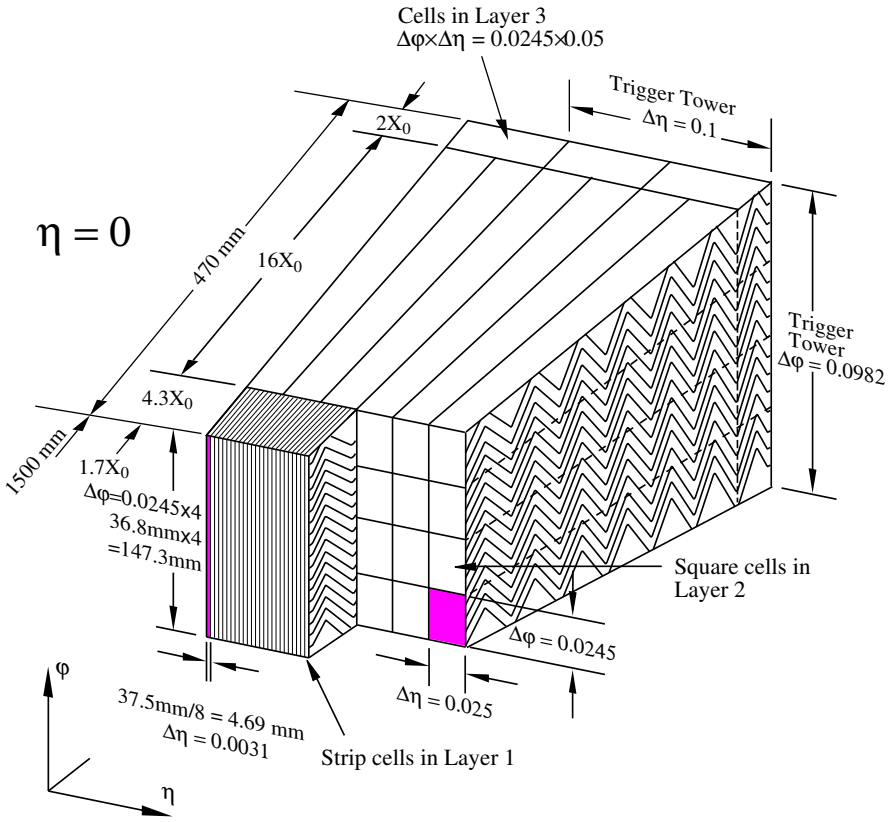

Figure 2.10: Here is a sketch of a barrel module [23] where the different layers are clearly visible with the ganging of electrodes in phi. You can see the accordion structure here clearly. The granularity in eta and phi of the cells of each of the three layers and of the trigger towers ($\eta \times \phi = 0.1 \times 0.1$) is shown.

a low latency read-out of the data. Two half-barrels extend up to $|\eta| < 1.475$ while the two end caps cover $1.375 < |\eta| < 3.2$. The LAr module has three layers, which you can also see in Figure 2.10. The first layer has eight "strips" finely segmented in $\Delta\eta = 0.0031$ in front of each cell. The very fine strips allow us to discriminate between electromagnetic showers from electrons or photons and electromagnetic showers from energetic pions. The second layer

collects the majority of the energy in the electromagnetic shower and is also finely segmented with $\Delta\eta = 0.0031$ and $\Delta\phi = 0.0245$. The third layer, which is much coarser with $\Delta\eta = 0.05$, collects the tail end of the electromagnetic shower. For measuring the energy of hadrons, Tile, the LAr hadronic end cap, and the forward calorimeter (FCal) cover $0 < |\eta| < 4.9$. The hadronic end cap (HEC) is a copper/liquid argon sampling calorimeter covering $1.5 < |\eta| < 3.2$. Each end cap consists of two wheels on each side, with each wheel being made up of 32 wedge-shaped modules.

The Tile Calorimeter (TileCal) [32] is a sampling calorimeter with steel as the absorption layer and scintillator as the active medium covering the region $|\eta| < 1.7$. Remember the LAr Hadronic end cap extends up to $|\eta| < 3.2$. The tile calorimeter is located behind the LAr EMB and EMEC, as seen in 2.9. It consists of two sections, the main barrel covering $|\eta| < 1.0$ and the two extended barrels covering $0.8 < |\eta| < 1.7$. There is a gap of about 600 mm between these sections, which is needed for the cables and electronics from the inner detector and LAr. The Intermediate Tile Calorimeter (ITC) is an extension from the extended barrel, intended to maximize the volume of active material in this region while still allowing room for the cables and services. Each barrel has 64 modules, shown in Figure 2.11, with each module covering

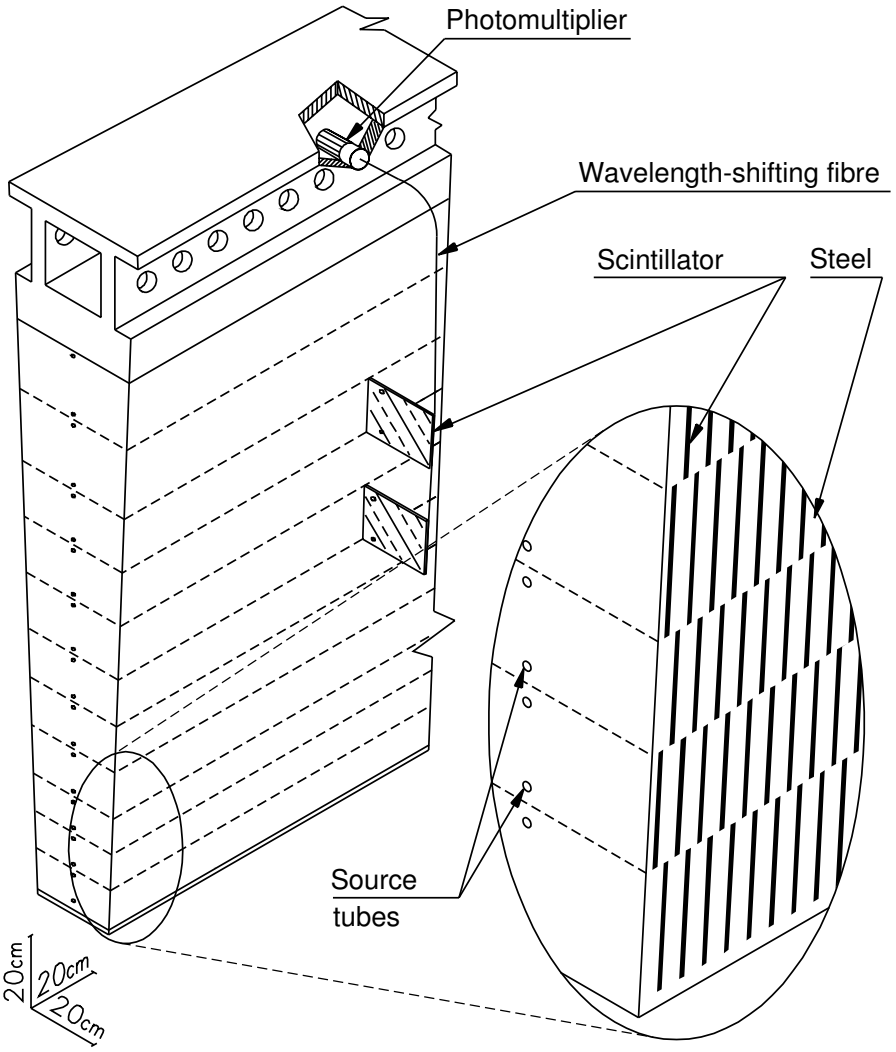

Figure 2.11: Sketch of a Tile module [23] showing how the mechanical assembly and the optical readout are integrated together. The various components of the optical readout are shown.

$\Delta\phi = 2\pi/64 = 0.1$. The scintillating tiles lie in the $r - \phi$ plane and span the width of the module. Wavelength-shifting fibers the running in the radial direction collect the light from the tiles and are grouped into readout cells that are read out by photomultiplier

tubes. These readout cells are then a three-dimensional segmentation of $\delta\eta \times \delta\phi = 0.1 \times 0.1$ (0.2×0.1 in the outer layer). The main function of TileCal is to contribute to the energy reconstruction of the jets produced in the proton-proton interactions and to contribute to a good E_T^{miss} measurement.

FCal further extends the sampling range, covering $3.1 < |\eta| < 4.9$, albeit with coarser granularity. This is the extreme forward region of the detector where particle flux is the highest, so FCal must be suitable to deal with high radiation densities. FCal is composed of three modules on each side of the detector, one electromagnetic Copper/LAr module and two hadronic Tungsten/LAr modules.

The Muon Spectrometer

The conceptual design of the muon spectrometer is shown in Figure 2.12. It is the outermost layer of the ATLAS detector and is designed to make high-precision measurements of the momentum of muons. Muon momenta down to about 3 GeV, but not lower due to energy loss in the calorimeters, can be measured by the muon spectrometer independently of the other subdetectors. The entire muon system is based on the magnetic deflection of muon tracks in the superconducting toroid magnets. The large barrel toroid bends muons in the region $|\eta| < 1.4$, while the two smaller end-cap magnets bend the muon tracks in the region $1.6 < |\eta| < 2.7$. In the

transition region, $1.4 < |\eta| < 1.6$, both the endcap and barrel play a role in bending the muon tracks.

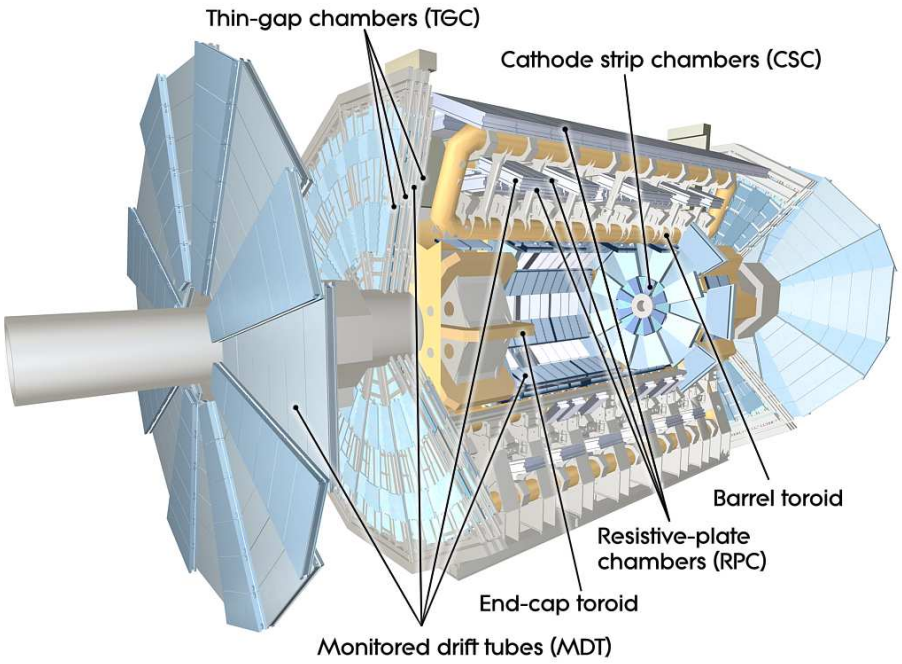

Figure 2.12: Cut-away view of the ATLAS muon system[23].

The muon system contains four primary subsystems: two precision muon trackers (monitored drift tubes (MDT) and Cathode Strip Chambers (CSC)) as well as two triggering subsystems (resistive plate chambers (RPC) and thin gap chambers (TGC)). For most the η-range the measurement of the track coordinates is provided by Monitored Drift Tubes while for larger η the Cathode Strip Chambers provide this measurement. The Cathode Strip Chambers are multiwire proportional chambers with cathodes segmented into strips and have higher granularity and can withstand the de-

manding rate and background conditions at large η.

The muon spectrometer also triggers on muons in the region $|\eta| < 2.4$. The trigger chambers provide bunch-crossing identification, well-defined p_T thresholds, and measure the coordinate in the direction orthogonal to the one determind by the precision-tracking chambers.

The Magnet System

Precise measure of charged particle momenta requires a strong magnetic field. Momenta of charged particles can be measured from their bending in a magnetic field, according to the Lorenz force law:

$$\frac{d\vec{p}}{dt} = q(\vec{E} + \vec{v} \times \vec{B}), \tag{2.1}$$

where $\vec{p}$ is the particle 4-momentum, q is the charge, $\vec{v}$ is the velocity, $\vec{E}$ is the electric field, and $\vec{B}$ is the magnetic field.

ATLAS houses a unique magnet system consisting of four large superconducting magnets that are 22 m in diameter and 26 m in length for assisting in making precise measurements of charged particle momenta. There is a central solenoid that lies just outside the inner detector and is very thin. The toroid system lies around the calorimeter, including a barrel region and two endcap regions, each consisting of eight coils radially assembled around the beam

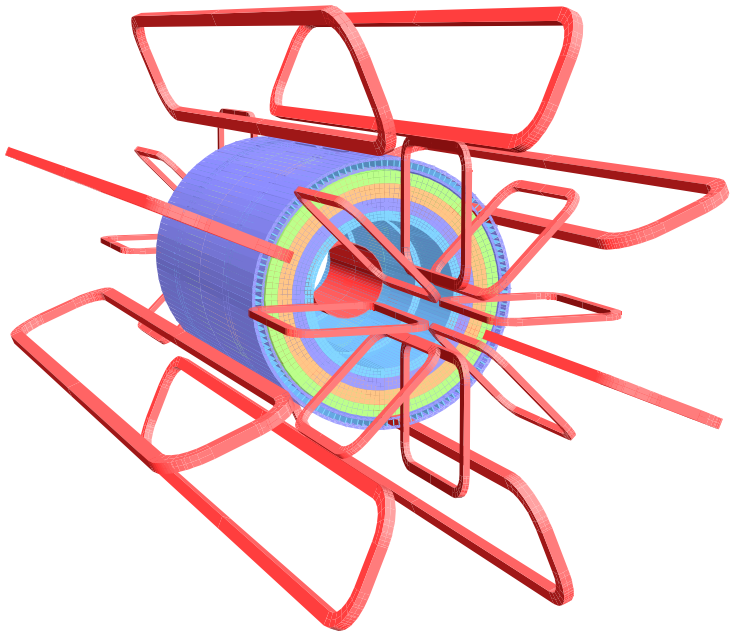

Figure 2.13: The eight barrel toroid coils and endcap coils are visible. The solenoid winding lies inside the of calorimeter. The tile calorimeter is modelled by four layers with different magnetic properties[23].

axis. The magnets are configured in such a way as to produce a field mostly in the azimuthal direction and orthogonal to the muon trajectories in order to provide maximum bending power.

The central solenoid is designed to provide a 2 T axial field at the nominal operating current (7.730 kA). As noted before, the central solenoid is carefully designed to keep the thickness in front of the calorimeters as minimal as possible, so it is merely 0.66 radiation lengths at normal incidence. The LAr calorimeter shares a common vacuum vessel with the solenoid windings, eliminating the need for two vacuum walls.

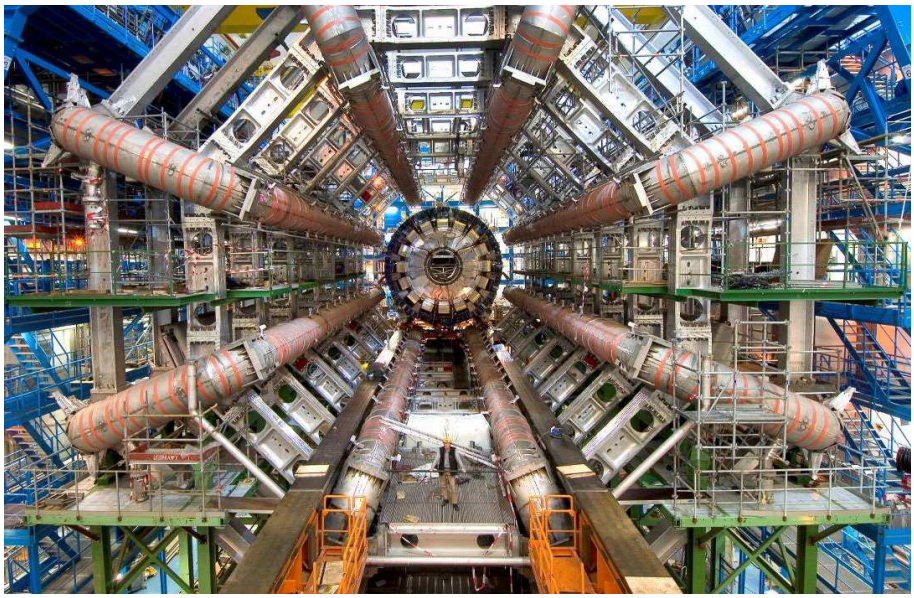

Figure 2.14: Barrel toroid as installed in the underground cavern. The scale is indicated by the person standing in between the two bottom coils. Also visible are the stainless-steel rails carrying the barrel calorimeter with its embedded solenoid, which await translation towards their final position in the centre of the detector.

The barrel toroid consists of eight coils, each encased in stainless steel vacuum vessels which can be seen in Figure 2.14. The toroid system measures 25.3 m in length with an inner diameter of 9.4 m and an outer diameter of 20.1 m. The barrel region produces a toroidal magnetic field of about 0.5 T while the endcap toroids produce a magnetic field of around 1 T.

Forward Detectors

There are, as well, several smaller detectors in the forward region to provide additional information for luminosity measurements and

for the ATLAS trigger system. Luminosity measurements are performed by several detectors and are essential for physics searches and understanding detector conditions.

LUCID (LUminosity Cherenkov Integrating Detector) is dedicated to online luminosity monitoring. It is the forward detector closest to the collision point. LUCID is a Cerenkov detector located just ± 17 m from the interaction point, so it is the closest detector to the collisions.

Further away is ZDC (Zero-Degree Calorimeter). It is located ± 140 m from the interaction point, which is where the LHC beam-pipe is divided into two separate pipes. ZDC plays an important role in heavy ion physics.

The most remote detector, ALFA (Absolute Luminosity For ATLAS), is located about ± 240 m from the interaction point. ALFA consists of scintillating-fiber trackers inside of Roman pots and it measures the elastic pp cross section at very small angles, which is use to determine the total pp cross section and luminosity in LHC.

Trigger and Data Acquisition During Run-2

The collision rate at the LHC is 40 MHz, corresponding to bunch-crossing interactions every 25 ns, at design luminosity. During run-2 there was an average of 34 pp collisions per bunch crossing, cor-

responding to around 10^9 interactions per second. At this rate, recording every collision is simply not possible. The majority of these events arise from uninteresting, soft collision processes that are unlikely to contain anything of interest. ATLAS has a complex system of custom build hardware and dedicated software, called the ATLAS Trigger and Data Acquisition (TDAQ), in order to reduce this rate to much more manageable levels while keeping the most interesting events for further processing.

The Run-II trigger system consists of two levels, the hardware-based low-level trigger referred to as the level-1 (L1) trigger and the software-based high-level trigger referred to as the high-level trigger (HLT). The L1 trigger uses measurements from the calorimeters and the muon spectrometer and performs the first selection, reducing the initial 40 MHz rate of events down to a maximum 100 kHz. It triggers on electrons and photons based upon energy deposits in the electromagnetic calorimeter. The hadronic calorimeter provides jet candidates to the L1 trigger system via calorimeter *towers* found using a sliding-window algorithm. This algorithm identifies local transverse energy maxima in the η-ϕ plane [33].

The L1 trigger identifies interesting candidates and forwards them to the HLT. The HLT consists of a L2 trigger and event filter. The L2 trigger is similar to the L1 trigger, but with more refined mea-

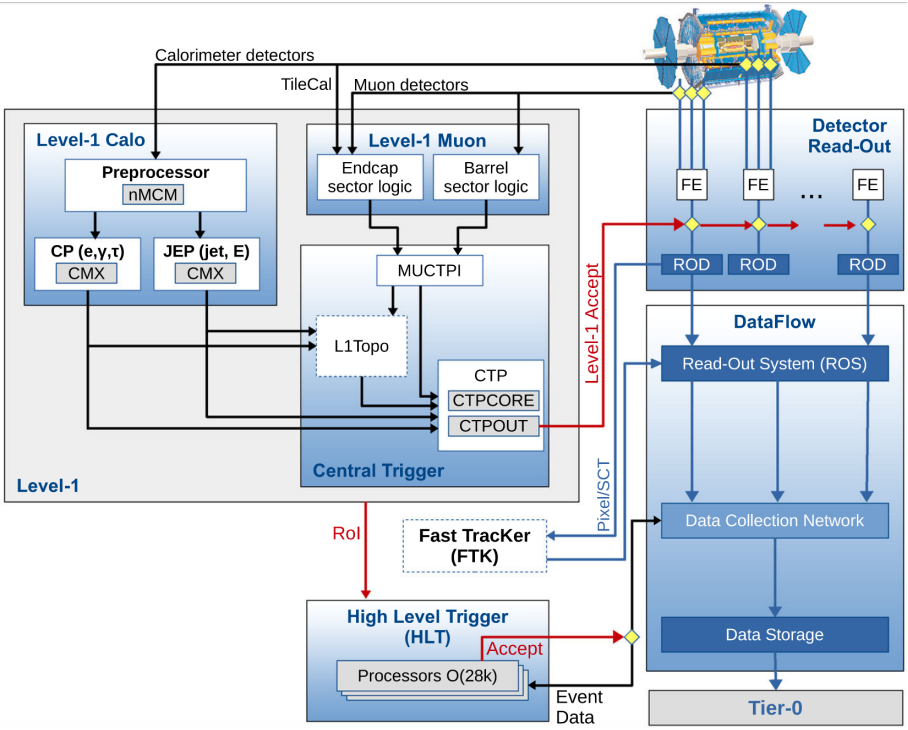

Figure 2.15: The ATLAS Trigger and Data Acquisition system during Run-II.

surements on the objects that resulted in the L1 trigger decision. The event filter is software-based and uses the ATLAS reconstruction framework to perform high level object reconstruction, using algorithms similar to those used in the offline environment. The HLT accept rate is kept at around 1 kHz, where the accepted events are sent to permanent storage and made ready for offline analysis. A diagram of the ATLAS Run-II TDAQ system is shown in 2.15.

2.3 Event Simulation and Object Reconstruction

The goal of the ATLAS experiment, in the end, is to measure the outgoing particles from the hard-scattering collisions in order to reconstruct the intermediate states such as Higgs bosons, top quarks, or possibly supersymmetric particles. Intermediate states are typically short-lived and may only be calculated based upon their final decay products.

In this chapter the reconstruction of the objects emerging from our *pp* collisions is discussed, as well as introduce the ATLAS Monte Carlo (MC) event simulation. Event reconstruction is performed for data as well as the MC simulation.

Simulation of Physics Events in the ATLAS Experiment

In Chapters 5 and 6 I will be presenting a search for new physics, meaning I need to have a theoretical model which predicts new phenomena beyond the Standard Model. In order to perform an analysis such as this, particle physicists typically simulate [34] the predicted *signal* as well as the Standard Model backgrounds and compare these with observed data. We can think of these simulated models as being created in three steps:

1. Simulate high-energy QCD processes using MC generators at the parton level [35].

2. Simulate the *soft physics* processes, or how partons shower and decay and form bound states.

3. The whole ATLAS detector must be simulated [36]. The propagation of particles through matter are simulated with GEANT4 [37].

The Simulation of Pileup

As mentioned previously, the simulation of pileup is handled by Pythia [28]. Pileup is modelled by separately generating a large sample of minimum-bias events, inelastic events selected with a loose trigger with as little bias as possible, and for each hard-scattering event of interest these events are overlaid prior to digitization and reconstruction. The number of overlaid events is dependent upon a sampling of the pileup distribution for the corresponding data, as illustrated in Figure 2.5. By overlaying the simulated events prior to digitization, we get a more precise simulation of the effects of pileup on the detector response is achieved.

Object Reconstruction

In order to convert the assembly of electrical signals read out by the ATLAS subdetectors into well-defined and meaningful representations of the underlying physics processes, several steps of reconstruction and identification must take place. The signature we

are searching for involves the use of leptons, jets, and the missing transverse momentum, $\mathbf{p}_T^{miss}$. The reconstruction of $\mathbf{p}_T^{miss}$ requires the accurate reconstruction of leptons and jets. It should be made clear, the methods used for reconstructing jets and leptons are not absolutely accurate, detector information arising from an electron may leave a signature similar to that of a jet.

Electrons and Muons

Reconstructing electron candidates requires the close matching of information from the inner detector and the EM calorimeter. Charged particle tracks in the inner detector are required to match closely in (η, ϕ) with localised clusters of energy in the EM calorimeter [38]. Generally it is possible to match multiple tracks to the same electromagnetic cluster, but all originating from the same primary electron. Electrons lose significant amounts of energy due to bremsstrahlung, where the electron may emit a photon when interacting with the medium. The photon emitted may convert into an electron-positron pair which can then interact again with the material and produce another photon. These electrons, positrons, and photons are usually emitted in a very collimated fashion and thus deposit most of their energy in a very localized section of the calorimeter.

A further requirement is imposed upon electrons to improve the selection of *true* electrons originating from the hard-scattering event,

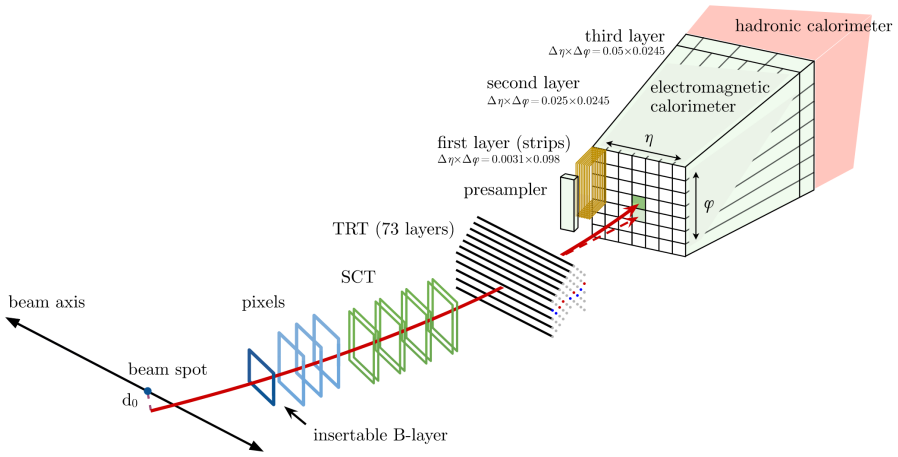

Figure 2.16: An illustration of the path of an electron through the detector. The red trajectory shows the expected path of an electron, which first travels through the tracking system before entering the calorimeter. The dashed red trajectory indicates the path of a photon produced by the interaction of the electron with the inner detector [39].

called *prompt leptons*, over the selection of *non-prompt leptons* such as those originating from photon conversions or misidentified charged pions. This identification is done by building a multivariate likelihood classification, referred to as the *electron likelihood identification*. The inputs to the classifier include measurements from the calorimeter, the inner detector, as well as quantities that that combine information from both [38].

The reconstruction of muon candidates is done by combining the tracking information from the inner detector with the muon spectrometer (MS) [40]. Muon reconstruction starts with the reconstruction of charged particle tracks in the inner detector and the muon spectrometer. These independently reconstructed tracks are

combined to form a complete track, representing the traversal of a muon through the whole detector.

Jets

Particles such as leptons and photons can be directly measured through their interactions in the inner detector, calorimeter, and muon systems. However, the same can not be said for quarks. Due to the confining nature of QCD, color-charged quarks or gluons produced in the hard-scattering processes due not exist as free states for any observable or meaningful timescale and thus do not leave clear signatures in the detector. Quarks and gluons originating from from the *pp* collisions at the LHC will shower, leaving a parton jet, or hadronize, leaving a particle jet and form colorless objects which deposit their energy in the calorimeter. This process is illustrated in Figure 2.17.

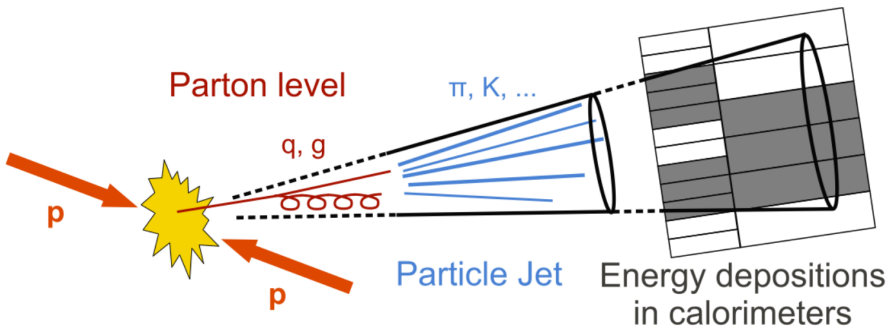

Figure 2.17: The formation of jets is illustrated, beginning with the *pp* collision and the initiating quark or gluon. These partons hadronize to form particle jets before depositing their energy in the calorimeter.

Jets are reconustructed using a clustering algorithm that determines the properties of the jet with the goal of reconstructing jets that accurately represent the properties of the underlying partons. Over the past decades, cone-algorithms have emerged as the most popular option among experimentalists [41]. Within ATLAS, the standard jet clustering algorithm is anti-k_t with a radius parameter of R=0.4 [42]. Jets are reconstructed from three-dimensional topological energy clusters in the calorimeter. These clusters have better noise suppresion and energy resolution than cells after being calibrated [43].

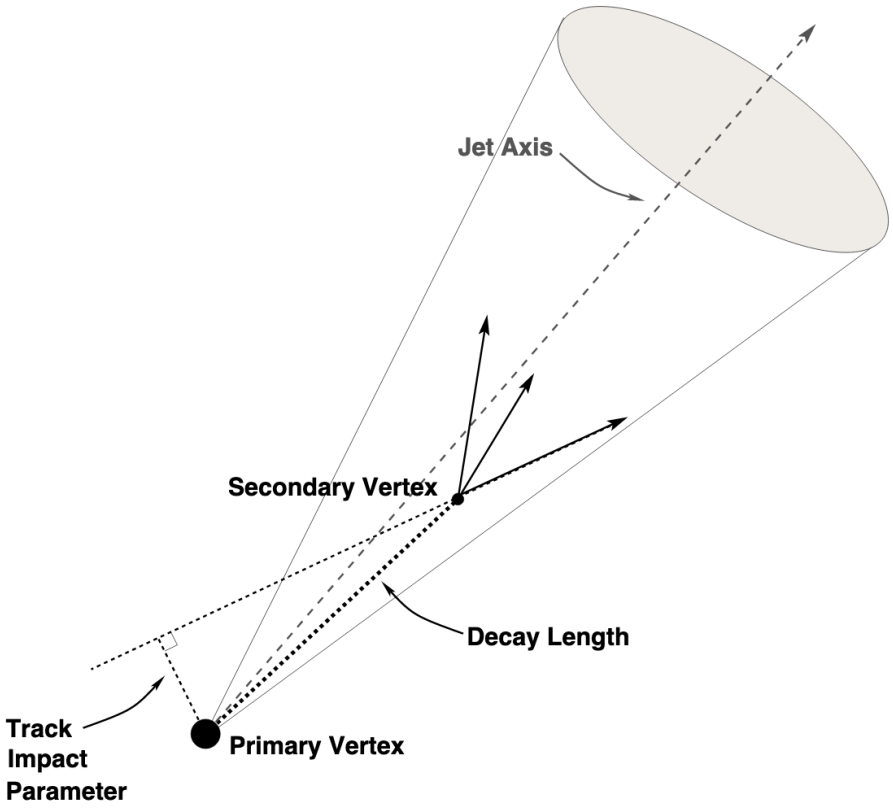

Figure 2.18: Long-lived particles are primarily identified by a secondary vertex, significantly displaced from the primary vertex.

b-Jets

The typical lifetime of a b-hadron is around $1-1.5$ pS, significantly longer than the lifetime of most other hadrons. This is long enough for b-hadrons to travel a few mm in the detector before decaying. This results in a *secondary vertex*, displaced from the primary hard-scattering vertex, such as that shown in Figure 2.18. In order to identify b-jets a multivariate algorithm is used, taking as its input information about the impact parameters of charged particle tracks,

parameters of reconstructed secondary vertices, and the topology of b- and c-hadron decays [44].

2.4 Conclusion

The ATLAS detector is a general purpose detector composed of many subdetectors that work together to reconstruct the entire collisions events, as much as is possible. It is an incredibly complex machine consisting of over 100 million readout channels from its subdetector systems. The Inner Detector is located at the center of the machine and measures the momentum of the charged particles. The Calorimeter system is responsible for measuring the energy of leptons, photons, and hadrons. It is also important that the calorimeter provides as much stopping of the particles as possible, in order to contain and measure all of their energy. This way we can get some idea of the total missing energy from the event, a crucial measurement in our searches for new physics. There is also a muon spectrometer for help in identifying muons, particles that pass through the entire detector. ATLAS is truly an impressive machine, built by a collaboration of thousands of scientists and engineers for the sole purpose of probing the fundamental laws of nature.

Chapter 3

High-Luminosity Upgrade to the ATLAS Tile Calorimeter

3.1 Introduction

As described in Section 2.2, the Tile Calorimeter (TileCal) [32] is the central section of the hadronic calorimeter of the ATLAS experiment at the Large Hadron Collider (LHC). It captures approximately 30% of jet energy and plays a crucial role in the measurement of jet-energy, missing-energy, jet substructure, electron isolation, and triggering.

The LHC is planning a series of upgrades, culminating with the High-Luminosity LHC (HL-LHC), which is expected to deliver 5-7 times the current instantaneous luminosity. TileCal will undergo an upgrade to accommodate the new HL-LHC parameters. The

read-out electronics will be redesigned, introducing a new strategy [45]. The full set of data generated in the detector will be digitized and sent off-detector using the PreProcessors (PPr) for every bunch crossing before any selection is applied, as illustrated in Figure 3.1. The TileCal PPr will represent the main interface between the data acquisition, trigger, and control systems and the on-detector electronics. It will implement pipeline memories to cope with the latencies and rates specified in the new trigger and provide preprocessed digital trigger information to the ATLAS Level 0 trigger.

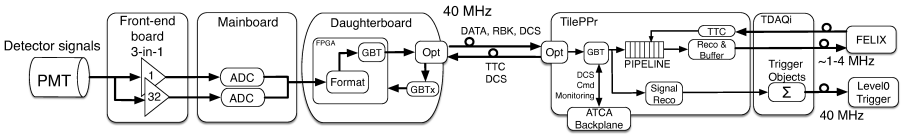

Figure 3.1: Phase-II TileCal front-end schematic [45].

3.2 The Tile Calorimeter Demonstrator

The Demonstrator Prototypes were built to evaluate the new read-out electronics while maintaining backwards compatibility with the current setup. The demonstrator has been tested in various test-beam campaigns. Demonstrator results shown in the following sections are heavily based upon my poster presentation at LHCP 2018 [46] in Bologna.

The *3-in-1* Front-End Board (FEB) acquires the PMT signals. These

are connected to a Mainboard that provides voltage and controls, digitizes the signal and sends it to the Daughterboard. The Daughterboard is the interface between the on- and off-detector electronics.

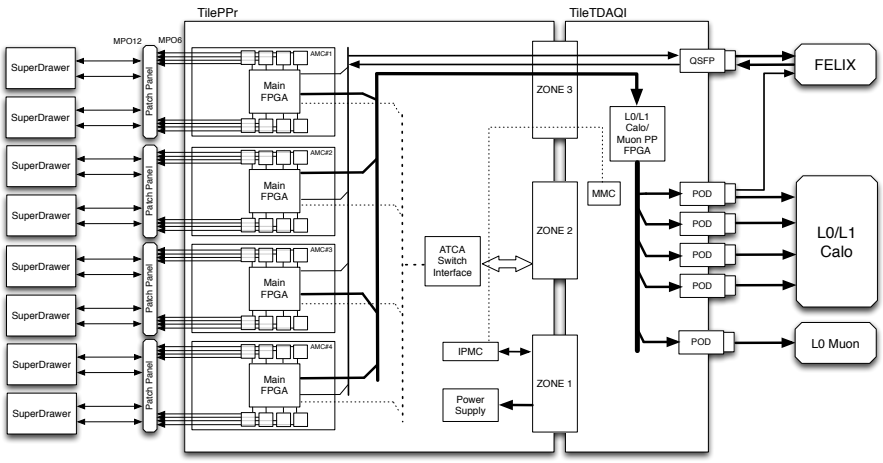

Figure 3.2: Block diagram of the final PPr design [45].

The PreProcessor is the core element of the back-end system [Figure 3.2], providing communication with the front-end to transmit commands and to receive the digitized PMT data. Once a trigger signal is received, the data is formatted and transmitted to the legacy Read-Out Driver to maintain compatibility. During the HL-LHC the Trigger and DAQ interface (TDAQi) will provide preprocessed information to the new trigger and Front-End Link eXchange (FELIX) systems, the core of the new ATLAS Trigger/DAQ architecture.

Test Beam

Extensive beam tests have been performed with the final electronics design planned for the TileCal upgrade for HL-LHC. Three TileCal modules were exposed to different particles with different energies and incident angles. The beams were produced by extracting $E_{beam} = 400$ GeV protons from the Super Proton Synchrotron machine and producing secondary and tertiary beams by placing beryllium and polyethylene in the path. These beams are expected to be composed mostly of pions and protons, but electrons, muons, and kaons are also present. Results obtained using experimental data are compared to simulation obtained using the GEANT4 toolkit [37].

The demonstrator was inserted into a long barrel module and equipped with *3-in-1* cards. The data selected by the trigger system is stored in raw data files through the legacy Read-Out System (ROS) and the new FELIX system in parallel. The ROS sends the data packets and saves the detector and beam data in a local disk. The PPr prototype [Figure 3.3] is the primary component of the off-detector electronics. It reads out the demonstrator and transmits the selected data to the legacy ROD and FELIX systems.

The ATLAS software framework (Athena) is used to reconstruct the raw data stored in the Event Builder and FELIX to energy and

time per cell. This operation is performed online for some events for monitoring.

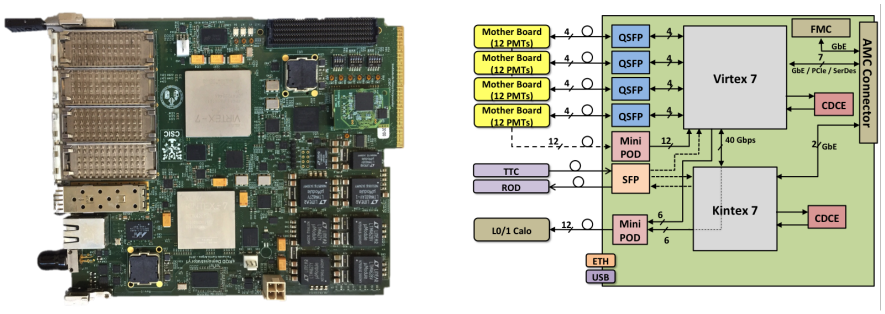

Figure 3.3: Picture (left) and block diagram (right) of the PPr Demonstrator module [45].

Test Beam Results

The interaction of muons with matter is well understood. The dominant energy loss process is ionisation and the amount of energy loss is essentially proportional to the muon track length.

Data was taken with $E_{beam} = 165$ GeV muon beams incident at 90 degrees. The response was studied as the ratio between the energy deposited in a cell (dE) over the track length (dl). In Figure 3.4 (left), the experimental and simulated distributions of dE/dl in cell A8 are shown. In Figure 3.4 (right), the Data/MC value for all of the A-cells are displayed. A uniformity of 1% and a maximum offset of 4% are observed.

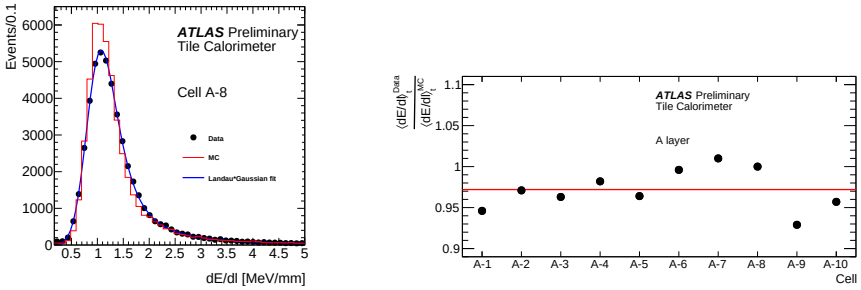

Figure 3.4: Deposited energy per unit length for cell A-8 shown for data and simulation (left) and comparison for Data/MC for A-layer (right) [45].

The responses of 20, 50, and 100 GeV electron beams incident on the center of cell A-4 at 20 degrees were measured. It is expected that electrons deposit all of their energy in the calorimeter, and since the layers were already calibrated at the EM scale is is expected that the energy read-out divided by the beam energy would be one. Results are presented in Figure 3.5.

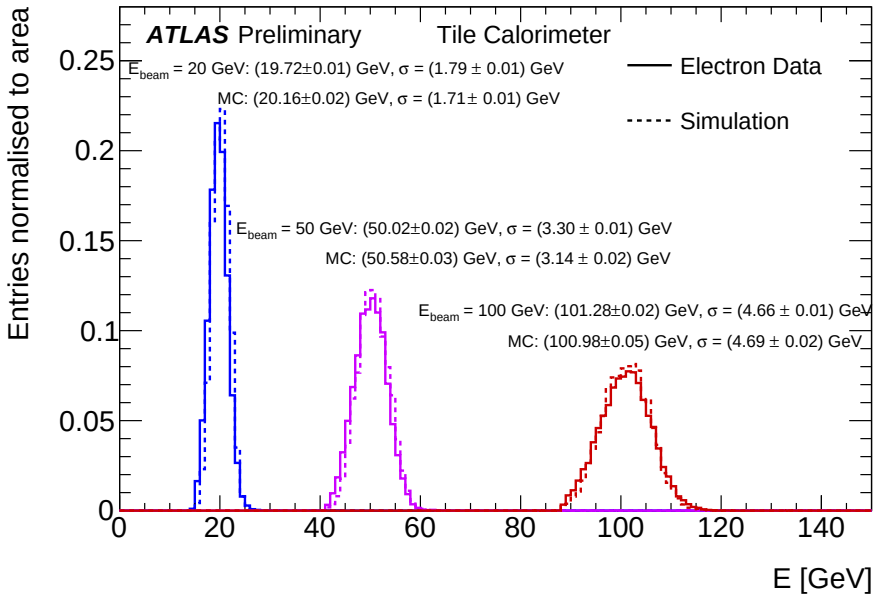

Figure 3.5: Electron data compared to simulation, for $E_{beam} = 20, 50$, and 100 GeV [45].

Since the primary role of the hadronic calorimeter in ATLAS is to measure the energy of jets, here are a few results showing the response for pions, kaons, and protons for different beam energies. The largest fraction of the shower energy is deposited in the cells of the demonstrator module. Particles are identified using the calorimeter response and three beam line Cherenkov counters. Electron contamination is reduced by a thin lead absorber along the beam line.

Response is calculated using the mean of a Gaussian fit performed within $\pm 2\sigma$ of the peak as shown in Figure 3.6 (left). In Figure 3.6 (right) the results for kaons, protons, and pions compared with

simulation are shown. The mean value of the fitted Gaussian is the reported value.

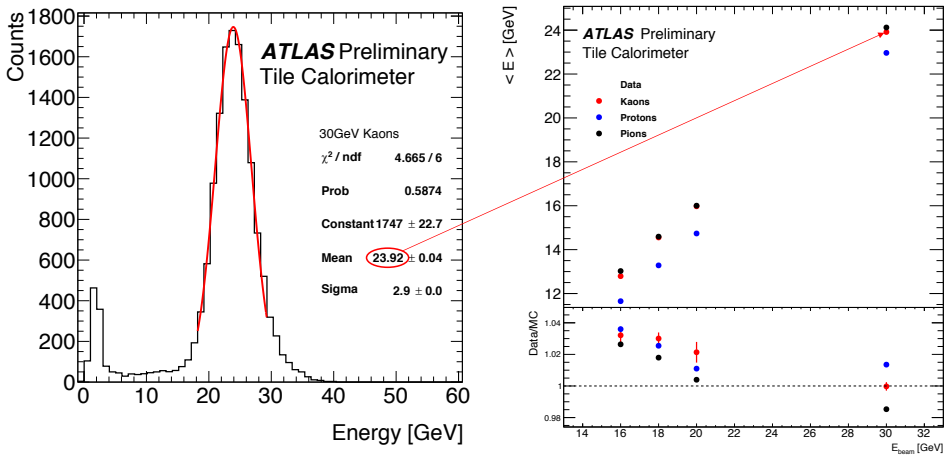

Figure 3.6: Kaon/Proton/Pion energy extracted and filled for multiple beam energies [45].

3.3 Prometeo: A Portable ReadOut ModulE for Tile ElectrOnics

Prometeo is a portable and completely stand-alone test-bench designed for the certification of the ATLAS Tile Phase-II upgrade to the front-end electronics. The design is based upon the currently used MobiDICK test bench [47]. The core functionality of the hardware is provided by a commercial Xilinx VC707 board which emulates the Tile PPr, described in Section 3.2, and a small Linux PC that hosts a Java-based web application running on a small

server. Currently, Prometeo is designed to provide all of the functionality to assess the certification of one mini-drawer. Once the PPr prototype is added, this will be expanded to servicing an entire super-drawer, or four mini-drawers. The VC707 board has two double QSFP FMC cards providing four QSFP connections to communicate with the front-end electronics. The VC707 and the PPr prototype use the same Virtex7 FPGA model, therefore the major part of the firmware is consistent in both modules.

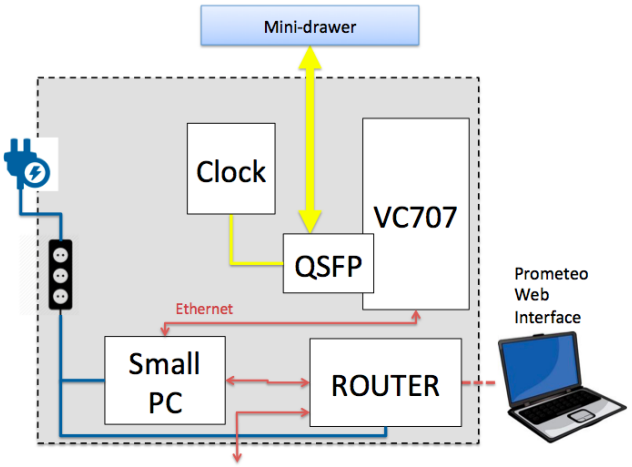

Figure 3.7: Block diagram of the Prometeo system.

The communication between the VC707 and the server is done through an Ethernet connection using the IPbus protocol. The computer is a fully capable PC with an Intel i5 processor and 8 GB of RAM. Its link to a router provides direct Ethernet connection on the front panel as well as wireless access.

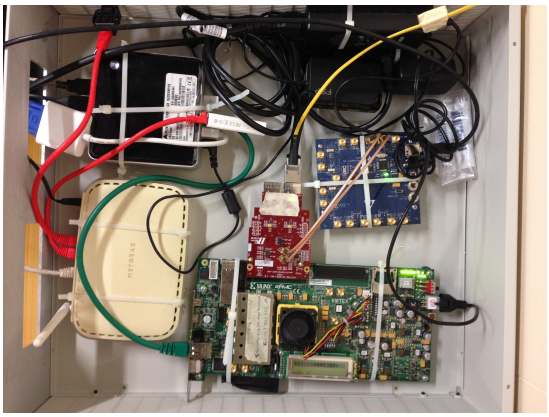

Figure 3.8: Picture of the Prometeo box under development.

A temporary test bench for testing and development of Prometeo diagnostic tests was set up, as shown in 3.9. Here we have the front-end electronics, a Main Board (MB) and a Daughter Board (DB) from one mini-drawer, two 3-in-1 cards for testing two channels, as well as a temporary power supply. We can communicate with the DB using the VC707 through the QSFP, connected with the fiber cable shown.

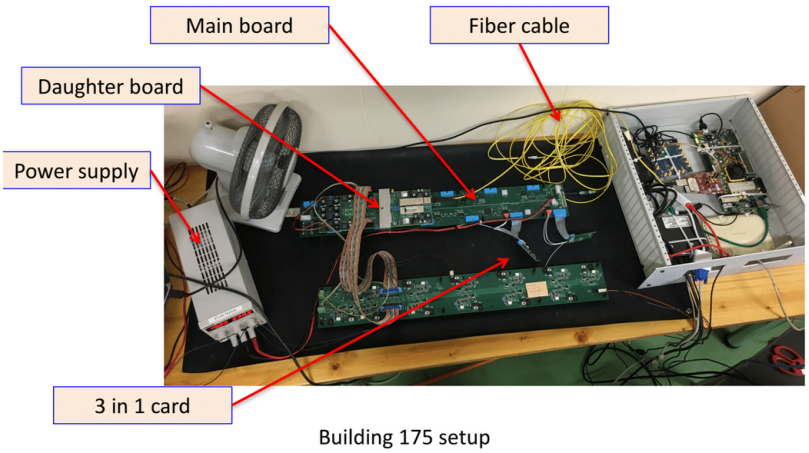

Figure 3.9: Our test-bench set up for the development of diagnostic tests and the Prometeo Web Interface.

Software

The Prometeo Web Interface is the software used to run the tests needed for certification and to view the results. It is platform independent and accessible using any web browser including on mobile devices. The application runs in the light-weight web server Tomcat 8. The full source and compiler is available in SVN[48]. The communication between the PPr and the PC uses a customised, lightweight version of the IPbus library [49]. This implementation is available for Java, C++ and Python and makes the application code easier and lighter than the official IPbus with similar performance. The client is a modular framework with plug-ins for each test. The system performs several tests aimed at diagnosing faulty components. These tests provide cross-checks with reference val-

ues for identifying faulty components like PMTs, DACs, ADCs, or failure in inter-connections and power supplies.

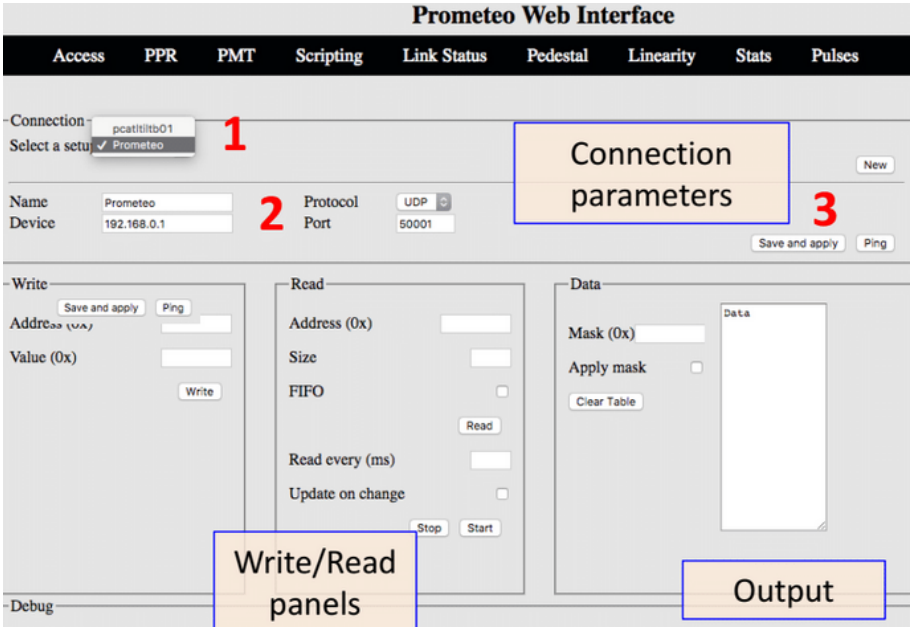

Figure 3.10: Prometeo Web Interface home page. Here you can connect to the test-bench and send commands, read and write from different registers, run different diagnostic tests, set the gain, or check and reset the links.

We had limited capabilities at this stage and couldn't access all of the features to implement every test. For example, we did not have access to the PMTs to test the outputs, such as the pulse shape. However, with our setup there were still some tests that could be developed.

Diagnostic Test: Setting and Reading Pedestal Values

The Pedestal Stability test, shown in Figure 3.11, measures the amount of noise for constant settings of the pedestal. You can pass

the pedestal value you wish to set and select the number of events you would like to sample. When running this test from the web interface, it will establish a connection and set the DACs according to the value you pass. For each gain (high or low) a histogram is filled with the ADC readout of each event. A gaussian is fit to each histogram and the results are summarized in another histogram by displaying, for each channel and gain, the mean and RMS results of our gaussian fit. As a baseline these results can be used to analyze the quality of our read-out.

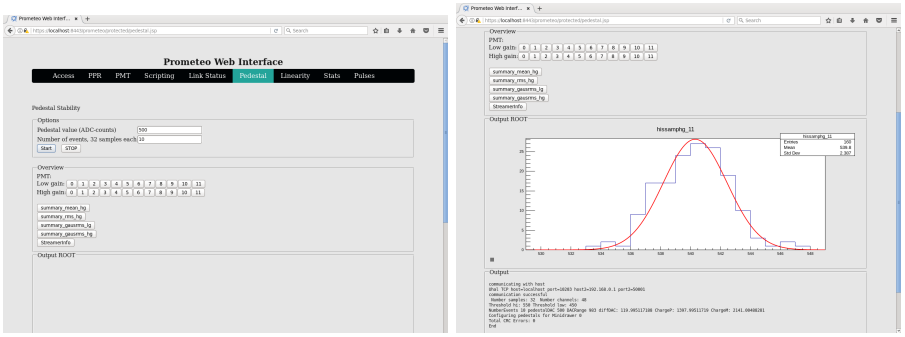

Figure 3.11: Pedestal Stability test on the Prometeo Web Interface. The plots are interactive: you can choose which to display and adjust zoom levels or set log scale, among other options.

A Pedestal Linearity test was also implemented, shown in Figure 3.12. It is similar to the stability test, except this time a handful of events is taken and the DAC is increased. The DAC is slowly increased, recording the ADC for a handul of events for each DAC setting, until the DAC (10-bits) is saturated. The ADC readout is 12-bits. The ADC readout is expected to respond linearly with the

DAC setting. The results of this test are summarized by fitting a line in each channel, with the goodness of the fit giving us an idea of the performance of each channel.

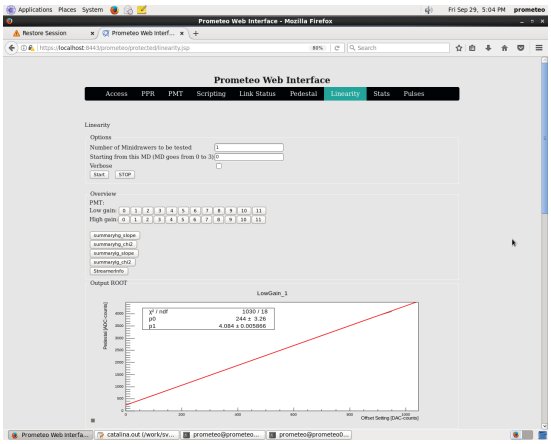

Figure 3.12: Pedestal Linearity test on the Prometeo Web Interface.

3.4 Conclusion

Research and development is ongoing for the TileCal Phase-II upgrades. Demonstrator prototypes have been produced and tested with beam while maintaining backwards compatibility, with the goal of insertion into ATLAS for more thorough testing. I was involved in different activities related to the development and testing of the demonstrator prototypes. There were multiple test-beam campaigns where tile modules were exposed to muons, electrons, pions, kaons, and protons with different energies and incident angles. The demonstrator prototype was inserted into one of these modules for extensive testing. All of the prototypes performed well

during the tests with beam, measuring the response to electrons, muons, and hadrons well.

A prototype test-bench was developed for certifying and diagnosing the upgraded front-end electronics. Although Prometeo isn't complete, a workable prototype was developed as shown, capable of running tests with control from any device that can access it remotely using a web browser. Work on Prometeo is still ongoing at CERN.

Chapter 4

Third Generation SUSY Searches at 13 TeV

As described in Chapter 1, the lighter mass eigenstate of the top quark superpartner, the stop ($\tilde{t}_1$), plays an important role in solving the hierarchy problem. Most SUSY scenarios prefer a $\tilde{t}_1$ mass around 1 TeV or lighter. If the $\tilde{t}$ exists and is indeed in this mass range, it may be easily produced in the 13 TeV pp collisions at the LHC. Therefore, stop searches play a prominent role in the search for SUSY at ATLAS.

Two different techniques were deployed in our search for the $\tilde{t}_1$. In both cases, a simplified *R-parity* conserving model is assumed, which requires top squarks to be produced in pairs. R-parity also requires the LSP to be stable, which is assumed to be the lightest

neutralino, $\tilde{\chi}_1^0$.

Section 4.1 is an overview that will introduce both $\tilde{t}$ searches presented in this paper. Then, the samples used in both analyses are presented in Section 4.2, including data and monte carlo samples. In Section 4.3 the triggers are discussed as well as reconstruction criteria used for cleaning the samples. Finally, in Section 4.4 a list of all of the systematic uncertainties are presented.

Everything in this chapter is common to both analyses, the recursive jigsaw analysis in Chapter 5 and the multivariate analysis in Chapter 6.

4.1 Analysis Strategy

This section introduces the general strategy used in Chapters 5 and 6 in order to perform a search for the stop quark.

Isolating New Physics in our Mountain of Data

In order to perform a search for physics beyond the Standard Model, it is important to first understand the signatures these new physics processes are expected to leave in the detector. This requires a strict definition of the final state in the physics model under investigation. For example, one signature may contain exactly one lepton, which gives a well-defined criteria to search for in the detector. Once a

signal model is chosen, its production and decay is simulated using MC methods in the same manner as the Standard Model processes.

The simulation of the signal model allows for a close look at the expected kinematics of the signal in greater detail. In this way, some phase space can be isolated where the signal is prevalent but the background is considerably reduced. The main background processes that are likely to dominate in the final phase-space selected in order to isolate the signal may also be identified. For a final state of two leptons with opposite charge, it is likely that Z-boson production will be relevant, this is one of the main final states defining Z-boson decay. Knowledge of this allows us to look for kinematic differences in this to reduce the background as much as possible, such as requiring a veto of events when the invariant mass of the two leptons is close to the Z-boson. In this case the Z-boson standard model background is a reducible background.

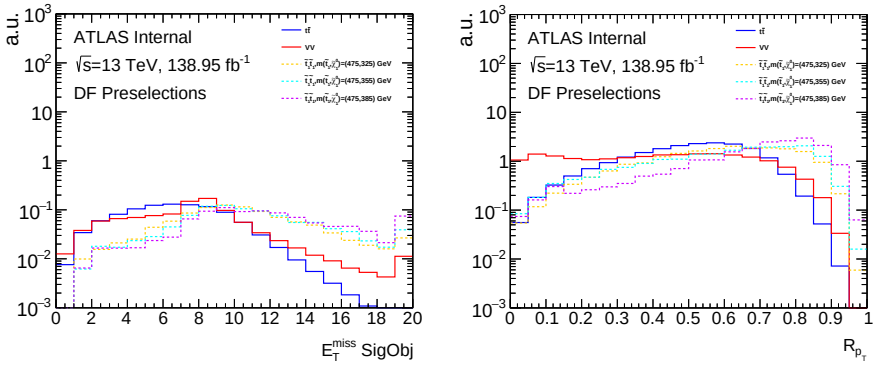

Figure 4.1: An example of two kinematic variables used in our Jigsaw Analysis to define our signal regions. Using a handful of kinematic variables, the aim is to isolate a region that is as pure as possible in signal events. In these plots the signal and backgrounds are normalized, in order to get an idea of their shapes.

There are also backgrounds that will be irreducible, particularly when the kinematics are too similar to the signal model. With the knowledge of the dominant background processes as well as the signal models, some idea of how the phenomenology and kinematics of the signal differs from the background can be obtained. A set of kinematic variables needs to be defined that will allow for the discrimination between the signal and background, defining phase spaces where there is a larger signal-to-background ratio. These phase spaces with increased signal purity are known as signal regions. An example of two variables used in the signal region definitions of the Jigsaw analysis is shown in Figure 4.1, described in Chapter 5. In this case a selection on events where the signal model peaks and the background tails off would be for high values of $E_{\mathrm{T}}^{\mathrm{miss}}$

significance and $R_{p_{\mathrm{T}}}$.

Trigger Strategy

The necessity of triggers was discussed in Section 2.2. Once the final state kinematics are identified, it is important to define a data acquisition strategy for gathering pp collision data that is consistent with this final state. This requires a selection of triggers to be used for recording collision events in ATLAS. Our analyses search for signal events with final states containing two leptons, electrons or muons. As a result, the triggers used are based on signatures of high-p_T leptons, configured to record an event if it contains a lepton above a given p_T threshold. If a lepton is identified in the online trigger system above the p_T threshold, the trigger 'fires' and the event is recorded. You can see an overview of the triggers used in both analyses in Table 4.1.

The W-bosons in the three-body decay are on-shell and thus lead to non-kinematically suppressed leptons. Each lepton is expected to have similar kinematics with transverse momenta, on average, above $m_W/2 \approx 40$ GeV. Therefore, reliance on the lepton triggers having online p_T thresholds above $10 - 18$ GeV is reasonable.

A trigger's efficiency is defined as its ability to make a decision to record an event when its requirements are truly satisfied. For

	Di-electron	Di-muon	Electron-Muon
2015	HLT_2e12_lhloose_L12EM10VH HLT_2e17_lhvloose_nod0_L12EM15VH8I	HLT_2mu14 HLT_mu20_mu8noL1 HLT_mu22_mu8noL1	HLT_e17_lhloose_mu14 HLT_e17_lhloose_nod0_mu14
2016	HLT_2e15_lhvloose_nod0_L12EM13VH HLT_2e17_lhvloose_nod0 HLT_2e17_lhvloose_nod0_L12EM15VHI	HLT_2mu14 HLT_mu20_mu8noL1 HLT_mu22_mu8noL1	HLT_e17_lhloose_nod0_mu14
2017	HLT_2e17_lhvloose_nod0_L12EM15VHI	HLT_2mu14 HLT_mu22_mu8noL1	HLT_e17_lhloose_nod0_mu14
2018	HLT_2e17_lhvloose_nod0_L12EM15VHI	HLT_2mu14 HLT_mu22_mu8noL1	HLT_e17_lhloose_nod0_mu14

Table 4.1: The triggers used in the analyses in Chapter 5 and 6. There were some differences in the conditions from year-to-year and therefore the thresholds of the triggers are slightly different.

example, if a trigger requires a 10 GeV lepton and it records every event that contains a 10 GeV lepton, this trigger would be 100% efficient. Of course, a trigger is never truly 100% efficient. You can see two efficiency plots in Figure 4.2 as a function of offline p_T selection. A trigger was selected where the offline lepton p_T selection put us well into the "plateau."

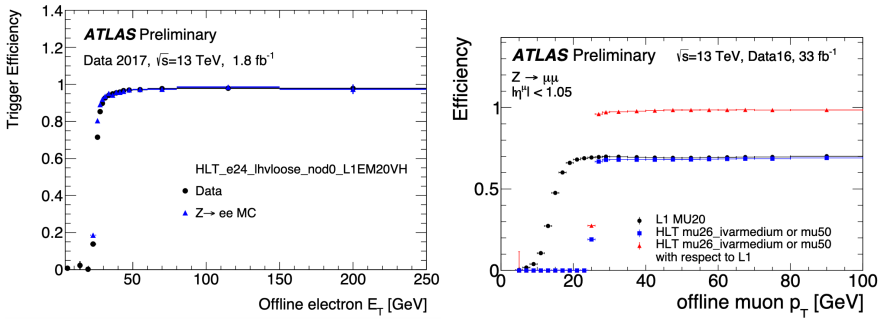

Figure 4.2: Examples of trigger efficiency plots, one for an electron trigger [50] and another for a muon trigger [51], as a function of offline section. As the offline p_T selection increases, as expected, the trigger efficiency increases.

Estimating the Main Backgrounds using the Control Region Method

Not only are *signal regions* defined to isolate the signal events from the background events, but *control regions* are also defined to constrain the predicted background to data. The goal is to understand, as much as possible, the behavior of the main backgrounds in the signal regions. The signal regions are regions with low background rates, meaning they are typically in phase spaces where the theoretical inputs into the MC are not as well understood as compared to the majority of the phase space. Therefore, the MC predictions alone may not be capable of adequately describing these processes. For the backgrounds that are less significant, reliance solely upon the MC simulation of the process is sufficient. However, for the dominant backgrounds remaining in the signal regions, it is better to define a control region for each one in order to increase the confidence in the background estimates. For each of these backgrounds, a control region is defined that is as pure as possible with the corresponding background. Care is taken, as well, to be sure the signal models are not prevalent in these regions. Each control region should also be orthogonal to the signal region, ensuring that any event satisfying the requirements of the control region does not populate the signal region as well. Each control region is then used to derive a *scale factor*, which is used to correct the predicted rates

in the specified background process.

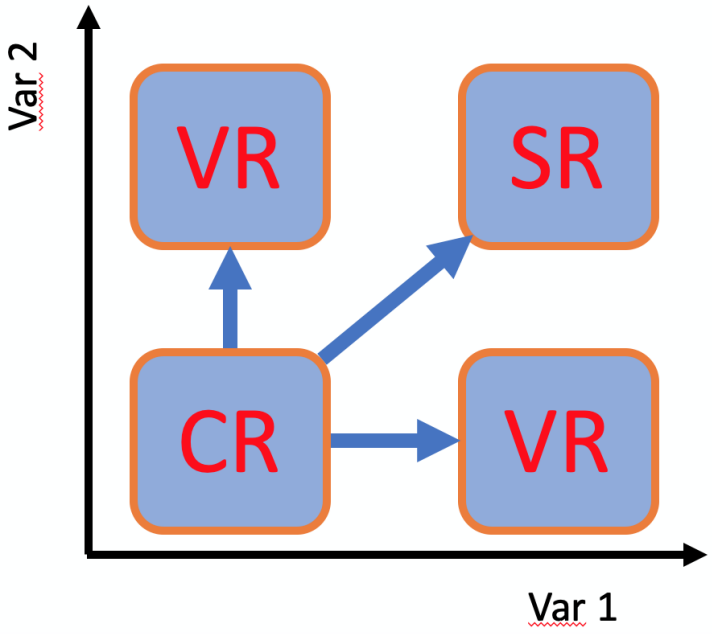

Figure 4.3: An illustration of control, validation, and signal regions. Each of the regions should be orthogonal since there will be a fit to data. This way the events are surely independent for the fit and subsequent extrapolation.

In addition to the *control regions*, *validation regions* are also defined in order to validate the results of the fit with the *scale factors*. Typically the validation regions are kinematically closer to the signal regions while maintaining orthogonality with both the signal regions and the control regions. The validation is done by comparing the data and MC in the validation regions, using the corrected MC predictions from the fitting process done in the control regions. An illustration of this extrapolation process is shown in Figure 4.3. The overall normalization and the general shape of the relevant

kinematic variables should be in good agreement.

Simplified SUSY Model

A full SUSY spectrum is naturally very complicated and depends on the mass of all of the sparticles. There are many sparticles with many different possible decays with different branching ratios, as shown in Figure 4.4 (left). Experimentalists like to work in simplified models, as shown in Figure 4.4 (right), which help present and interpret results. A small number of sparticles with 100% branching ratios is considered, in our case the stop decaying in the appropriate channel to a neutralino. These results can be extrapolated to more general new physics models which lead to the same event topology with similar mass hierarchies.

In this simplified SUSY scenario, R-parity conservation is assumed. As discussed in section 1.2, this means that the stop quark would only be produced in pairs and the Lightest Supersymmetric Particle (LSP) is stable. The left- and right-handed third generation squarks can mix in the MSSM to form two mass eigenstates, typically listed in order of mass, $\tilde{t}_1$ and $\tilde{t}_2$.

In most R-parity[52–54] conserving SUSY models the superparters to the third generation quarks are typically lighter than the superpartners to the first and second generation quarks. Addition-

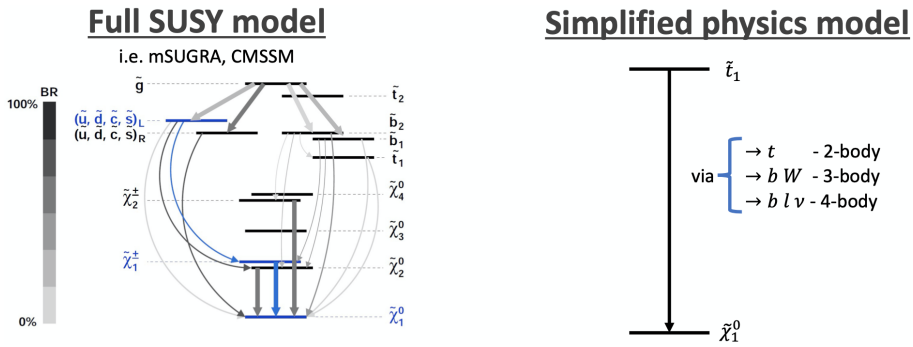

Figure 4.4: A typical SUSY spectrum is shown on the left with many sparticles and possible decay paths. On the right is the simplified model relevant to our analyses, considering only the stop decaying to the LSP.

ally, the lightest mass eigenstate, $\tilde{t}_1$, is expected to be significantly lighter than that of $\tilde{t}_2$. Naturalness arguments suggest top squarks can't be too heavy if it is to keep the Higgs boson mass close to the electroweak scale[55]. Therefore, $\tilde{t}$ pair-production can have a noticeable cross-section at the Large Hadron Collider. Previous ATLAS results [56], summarized in Figure 4.8, exclude stop quark masses up to $400-700$ GeV in the two-lepton final state. However, notice that in the 3- and 4-body regions only stop quark masses up to $350-400$ GeV are excluded, and this drops significantly when $\Delta m(\tilde{t}_1, \tilde{\chi}_1^0) \sim m_t$ or $\Delta m(\tilde{t}_1, \tilde{\chi}_1^0) \sim m_b + m_W$.

The neutralinos, along with the charginos ($\tilde{\chi}^{\pm}$), represent the mass eigenstates formed from the mixture of the higgsinos, winos, and binos, also known as the superpartners to the massless W and B gauge bosons and the Higgs bosons. The neutralinos and charginos

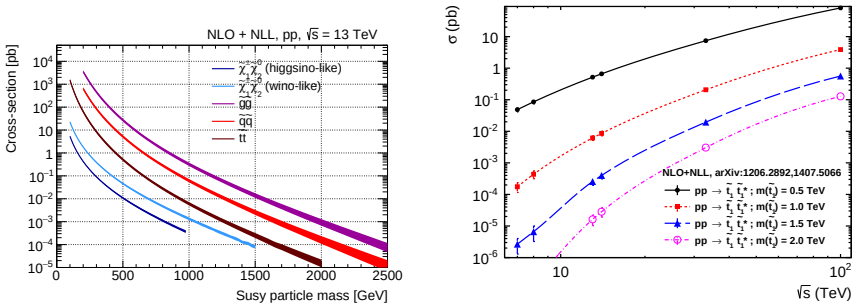

Figure 4.5: Sparticle production cross sections as a function of the sparticle mass (Left) and center-of-mass energy (Right). The plot on the left is for a center-of-mass of 13 TeV.

are designated in order of increasing mass, $\tilde{\chi}_i^{\pm}(i = 1, 2)$ for the charginos and $\tilde{\chi}_j^0(j = 1, 2, 3, 4)$ for the neutralinos. In a large variety of SUSY models, the LSP is the lightest neutralino, $\tilde{\chi}_1^0$.

You can see the production cross section for several SUSY processes at $\sqrt{s} = 13$ TeV in figure 4.5 (left), as well as the cross section for $\tilde{t}$ pair-production at different center-of-mass energies (right). Gluino pair-production has a higher cross-section than squark pair-production, however, this process is completely swamped by the Standard Model background processes. It is therefore more beneficial to search for squark pair-production. If the $\tilde{t}$ is in fact the lightest squark, it is expected to have the largest cross-section amongst the squarks. Therefore, $\tilde{t}$ searches become more important with increases in luminosity.

The $\tilde{t}$ can decay in a variety of ways depending upon the hierarchy

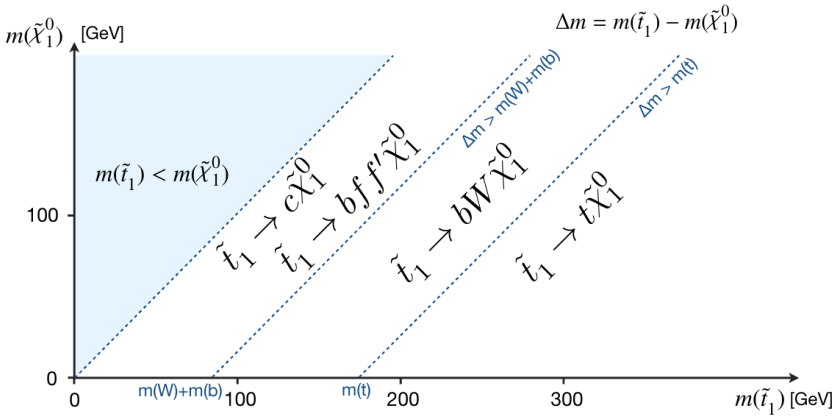

Figure 4.6: The different allowable decay regions of the $\tilde{t}_1$, depending on the mass of the $\tilde{t}_1$ and $\tilde{\chi}_1^0$. We are focused on the three-body region, when $\Delta m < m_t$ and $\Delta m > m_W + m_b$.

of the mass eigenstates involved in the decay chain, as can be seen in Figure 4.6. In our $\tilde{t}$ search, seen in figure 4.7, the relevant SUSY mass eigenstates are the $\tilde{t}_1$ and the $\tilde{\chi}_1^0$,

$$\tilde{t}_1\tilde{t}_1 \to bW^+\tilde{\chi}_1^0 bW^-\tilde{\chi}_1^0 \to bl^+\nu\tilde{\chi}_1^0 bl^-\nu\tilde{\chi}_1^0, \tag{4.1}$$

where the neutralino, $\tilde{\chi}_1^0$, is expected to be the Lightest Supersymmetric Particle (LSP).

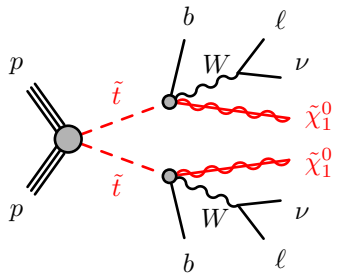

Figure 4.7: Feynman diagram representing the process considered in this analysis. $\tilde{t}_1$ pair-production decaying in the three body region to a b-quark, W boson, and a $\tilde{\chi}_1^0$. We target the final state where both W bosons decay to a lepton and a neutrino.

As mentioned before, in R-parity conserving models this LSP is expected to be stable since it can't decay to Standard Model particles and therefore is expected to show up as missing transverse energy, $E_{\mathrm{T}}^{\mathrm{miss}}$, in our detector. The three-body decay mode, described by Equation 4.1, can only happen when $\Delta m(\tilde{t}_1, \tilde{\chi}_1^0) > m_W + m_b$. Two-lepton final states are being targeted, with the $\tilde{t}_1$ decaying to a b-quark, W, and a $\tilde{\chi}_1^0$, with the W decaying leptonically. Since only this leptonic decay mode of the W is considered, events are characterized by the presence of two isolated leptons, electrons or muons, with opposite charge and two b-jets. Significant $E_{\mathrm{T}}^{\mathrm{miss}}$ is also expected from the neutrinos and neutralinos in the final state.

Figure 4.8 shows the previous exclusion limits on stop mass and neutralino mass as set by the ATLAS experiment. This plot overlays contours belonging to different stop decay channels, different

sparticle mass hierarchies, and simplified decay scenarios. The region pertinent to this analysis, the 3-body region decaying to a final state of 2 leptons, is shown in purple between the kinematic limits $\Delta m(\tilde{t}_1, \tilde{\chi}_1^0) < m_t$ and $\Delta m(\tilde{t}_1, \tilde{\chi}_1^0) > m_b + m_W$.

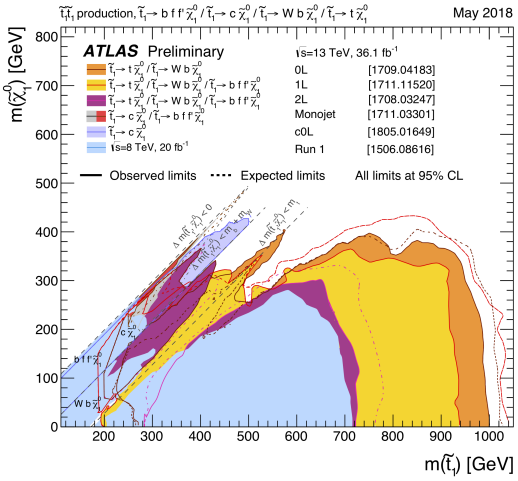

Figure 4.8: Summary of the previous dedicated ATLAS search results for top squark pair production based on 36.1 fb^{-1} of pp collision data taken at $\sqrt{s} = 13$ TeV. Exclusion limits at 95% confidence level are shown in the stop-neutralino mass plane. Four decay modes are considered separately with 100% BR: $\tilde{t}_1 \to t\tilde{\chi}_1^0$, $\tilde{t}_1 \to Wb\tilde{\chi}_1^0$, $\tilde{t}_1 \to c\tilde{\chi}_1^0$, and $\tilde{t}_1 \to bff'\tilde{\chi}_1^0$. The latter two decay modes are superimposed here. Also note that these plots overlay contours that belong to different stop decay channels, different sparticle mass hierarchies, and simplified decay scenarios[57].

4.2 Datasets

This section describes the details of all of the samples used, including a description of the data as well as the background and signal monte carlo samples.

Data Samples

Data used in this analysis was collected with the ATLAS detector during pp collisions from 2015 to 2018, or what is also called LHC Run-2. The protons had a center-of-mass energy of $\sqrt{s} = 13$ TeV and a peak instantaneous luminosity of L = $2.14{\cdot}10^{34}$ cm^{-2} s^{-1}, with a bunch spacing of 25 ns. The mean number of interactions per bunch crossing, or pileup (μ), ranges from 0.5 to 75. This changes significantly from 2015/2016 to 2017, and again in 2018. The data analyzed must satisfy the "Good Runs List" selection, which requires the data satisfies a few criteria. The LHC must have declared stable beams, the ATLAS detector was properly operating, and both the solenoid and toroid fields were at nominal conditions. After applying data-quality requirements, there was a total integrated luminosity of 138.95 fb^{-1} remaining. This total includes 3.21 fb^{-1} from 2015, 32.86 fb^{-1} from 2016, 44.3 fb^{-1} from 2017, and 58.45 fb^{-1} from 2018.

Background Samples

The SM background contributions are estimated by using centrally produced mc16a, mc16d and mc16e samples. Due to the different pileup profiles from 2015 to 2018, it was necessary to simulate the data with three different monte carlo campaigns. Data from 2015 and 2016 should be compared with mc16a, data from 2017 com-

pared with mc16d, and data from 2018 compared with mc16e. You can see more detailed information about all of the SM samples in Table A.1-A.4 of Appendix A.

For the production of $t\bar{t}$ and single top-quarks, the POWHEG-Box v2 generator is used, combined with PYTHIA8 for the showering with the A14 tune for the underlying events and the corresponding CTEQ6L1 PDFs [58]. The top quark mass is assumed to be 172.5 GeV. The Wt (single top) events are normalised to the NNLO + NNLL QCD [59] (NLO) cross sections.

Events containing Z/W bosons with associated jets, Z/γ^*+jets or W+jets, are produced using the SHERPA v2.2.1 generator with massive b/c-quarks to improve the treatment of the associated production of Z/W bosons with heavy flavour jets [60]. A global k-factor of 0.9751 (0.9702) is used to normalise the Z/γ^*+jets (W+jets) events to the NNLO QCD cross sections. These samples are generated in non overlapping slices filtered based on the vector boson p_{T} and on the presence of b- and c-jets.

SM diboson processes with up to four charged leptons are simulated using SHERPA v2.2.2 generator with the default tune, together with NNPDF30NNLO PDF set.

Triboson processes (WWW, WWZ, WZZ and ZZZ) with up to

six charged leptons are simulated using SHERPA v2.2.2 and described in Ref. [60].

Samples of $t\bar{t}V$ (with $V = W$ and Z, including non-resonant Z/γ^* contributions), $t\bar{t}WW$ and $t\bar{t}WZ$ production are generated at LO or NLO with MADGRAPH5_aMC@NLO v2.3.3 [61] with the PYTHIA 8.210 [62] parton shower model. MADGRAPH5_aMC@NLO is also used to simulate the tZ, $t\bar{t}t\bar{t}$ and $t\bar{t}t$ processes.

Signal Samples

A grid of signal points has been generated for different values of $m_{\tilde{t}}$, ranging from 350 to 600 GeV, and different values of $\Delta m = m_{\tilde{t}} - m_{\tilde{\chi}_1^0}$, simulating the appropriate 3-body $\tilde{t}$ decay:

$$\tilde{t}_1\tilde{t}_1 \rightarrow bW^+\tilde{\chi}_1^0\bar{b}W^-\tilde{\chi}_1^0.$$

$\tilde{t}$ pairs are generated with MADGRAPH 5 [61] with up to two additional partons and decayed with PYTHIA8.28.2+MADSPIN [62, 63]. To this purpose, SLHA input files are produced including the relevant mass hierarchy. In this framework the two basic parameters, governing the kinematics of the decay process, are the masses of the $\tilde{t}$ and the $\tilde{\chi}_1^0$. In order to maximize the available statistics, a filter is defined for the 3-body region, where two leptons with $p_T > 15$ GeV are required in the generation of the events.

The signal MC samples used in this analysis have been generated in the 2015 MC generation campaign. The samples were produced using ATLAS detector simulation [29] that utilizes a parameterization of the calorimeter response [64]. Geant4 [37] was used for the other parts of the detector. In all cases, production cross-sections are calculated at next-to-next-to-leading-order [1]. The details of the signal samples used for 3-body $\tilde{t}$ decay events are summarized in Table B.3 of Appendix B.

4.3 Event Reconstruction

Trigger and Cleaning Cuts

Events are selected using the dilepton triggers detailed in Table 4.1. In MC simulation, the same triggers used for the data are considered. The offline selection of $p_{\mathrm{T}} > 25,\ 20$ GeV for the leading and sub-leading leptons safely ensures being in the trigger efficiency plateau, as described in 4.1.

A number of cleaning cuts are applied following recommendations for cleaning out bad events due to data corruption, noise bursts and detector problems:

- LAr/Tile error (data only): events with noise bursts and data

[1] See https://twiki.cern.ch/twiki/bin/view/LHCPhysics/SUSYCrossSections13TeVstops-bottom

integrity errors in the LAr calorimeter are removed;

- Tile Trip (data only): events with Tile trips must be removed;
- SCT error (data only): events affected by the recovery procedure for single event upsets in the SCT are removed;
- Cosmic or bad muons (data and MC): fake muons are reconstructed, muons not corresponding to true objects coming from proton-proton collisions. They can sometimes be created from high hit multiplicities in the muon spectrometer in events where some particles from very energetic jets punch through the calorimeter into the muon system, or from badly measured inner detector tracks in jets wrongly matched to muon spectrometer segments. They can also be caused by the cavern background creating hits in the muon spectrometer. Cosmic muons are also a source of muons unrelated to the hard scatter. If an event contains at least one cosmic muon (defined as having $|z_0^{PV}| > 1$ mm or $d_0^{PV} > 0.2$ mm, with PV staying for primary vertex) or at least one bad baseline muon before overlap removal (satisfying $\sigma(q/p)/(q/p) > 0.4$) then the event is rejected.
- Bad jets (data and MC): non-collision background processes can lead to (fake or real) energy deposits in the calorimeters. These energy deposits are reconstructed as jets. Jet proper-

ties can be used to distinguish background jet candidates not originating from hard scattering events from jets produced in proton-proton collisions. Events with a LooseBad jet with $p_T > 20$ GeV after overlap removal, as recommended by the Jet/E_T^{Miss} group [65], are rejected.

- Primary Vertex (data and MC): events must have a primary vertex, selected as the one with the highest $\sum p_T^2$ of associated tracks, with at least two tracks.

Object Definitions

Electron and muons have two sets of definitions, baseline and signal. Objects defined as a baseline object pass looser selection criteria and are used in the overlap removal procedure to resolve ambiguity between the objects. Signal objects pass tighter selection criteria after initially passing the baseline definitions. From this stage forward the signal objects are used to define the signal, control, and validation regions.

The object definitions implemented correspond to those in the analysis release Base,21.2.92, and these criteria agree with the prescriptions provided by combined performance groups for the considered data periods[2].

[2]https://twiki.cern.ch/twiki/bin/view/AtlasProtected/SusyObjectDefinitionsr2113TeV

Electrons

The baseline and signal electrons selection criteria used in the analysis are defined as described here.

Baseline selection:

- $p_{\mathrm{T}} > 4.5$ GeV;
- $|\eta| < 2.47$;
- Identification: LooseAndBLayer requirement;
- Impact parameter: $|z_0 \cdot sin(\theta)| < 0.5$ (recommended by the Tracking Combined Performance group).

Signal selection:

- $p_{\mathrm{T}} > 4.5$ GeV;
- Identification: MediumLH requirement;
- Isolation: Gradient criteria based on track and calorimeter information;
- Impact parameter: $|d_0/\sigma(d_0)| < 5$ (recommended by the Tracking Combined Performance group).

In MC a multiplicative event weight is applied for each selected electron to the overall event weight in order to correct for differences in

reconstruction, identification and isolation efficiency between data and MC.

Muons

The baseline and signal muons selection criteria are defined accordingly:
Baseline selection:

- $p_{\mathrm{T}} > 4$ GeV;
- $|\eta| < 2.7$ for the 4-body selection, $|\eta| < 2.4$ for the 2/3-body selection;
- Identification: Medium muon quality requirement [66] (based on the number of hits in the different ID and muon spectrometer subsystems, and on the significance of the charge to momentum ratio q/p)
- Impact parameter: $|z_0 \cdot sin(\theta)| < 0.5$

Signal selection:

- $p_{\mathrm{T}} > 4$ GeV;
- Isolation: FCLoose criteria based on track and calorimeter information;
- Impact parameters: $|d_0/\sigma(d_0)| < 3$.

In order to correct for differences in efficiency between Data and MC a smearing procedure is applied to the muon p_{T} and multiplicative event weight is applied for each selected muon in MC.

Jets

Jets are reconstructed from three-dimensional energy clusters in the calorimeter and are calibrated with the JetCalibrationTool, following the release 21 recommendations[3].

Jets selection:

- $p_{\mathrm{T}} > 20$ GeV;
- $|\eta| < 2.8$;
- Collection : AntiKt4EMTopo jet clustering algorithm;
- Quality : jets are retained if $p_{\mathrm{T}} > 120$ GeV OR $|\eta| > 2.5$ OR (JVT > 0.59 if $|\eta| > 2.5$ OR JVT > 0.11 if $|\eta| \in [2.4, 2.5]$) (a significant fraction of the tracks associated with each jet must have an origin compatible with the primary vertex for separate hard scatter jets from pileup; SUSYTools implements the JVT recalculation since the discriminant must be updated to use the calibrated jet pt) [67]. The cut is applied after overlap removal procedure;

[3] https://twiki.cern.ch/twiki/bin/view/AtlasProtected/ApplyJetCalibrationR21

- Jet cleaning recommendation is applied using the JetCleaningTool with LooseBad criterion (IsBadJet), in order to remove events with fake $E_{\mathrm{T}}^{\mathrm{miss}}$ [65, 68].

Jets resulting from b-quarks (called b-jets) are identified using the MV2c10 b-tagging algorithm, which is based on quantities such as impact parameters of associated tracks and reconstructed secondary vertices [69, 70]. This algorithm is used at a working point that provides 77% b-tagging efficiency in simulated $t\bar{t}$ events. A multiplicative event weight is applied to MC to correct for differences in b-tagging efficiency between data and MC.

Missing Transverse Momentum

The missing transverse energy ($E_{\mathrm{T}}^{\mathrm{miss}}$) is rebuilt using the xAOD container "MET_RefFinal" as input and using the calibrated electron, muon and jet objects (and photons according to SUSYTools definitions). In this version of the analysis, the track soft term is used for building the $E_{\mathrm{T}}^{\mathrm{miss}}$ following the defaults in the SUSYTools tag included in the Analysis Release.

The object based $E_{\mathrm{T}}^{\mathrm{miss}}$ Signficance is a measure of how significant the $E_{\mathrm{T}}^{\mathrm{miss}}$ is based upon the p_T, p_T resolution, and ϕ resolution of

all objects in the event. It is defined as

$$E_{\mathrm{T}}^{\mathrm{miss}}\text{significance} = \sqrt{\frac{|\vec{E}_T^{miss}|^2}{\sigma_{\mathrm{L}}^2(1-\rho_{\mathrm{LT}}^2)}} \tag{4.2}$$

where $\vec{E}_T^{miss}$ is the vector of missing momentum in the transverse plane, σ_{L} is the total estimated longitudinal (parallel to the $\vec{E}_T^{miss}$) momentum resolution of all jets and leptons at a given p_{T} and $|\eta|$ and the quantity ρ_{LT} is a correlation factor between each object's longitudinal and transverse momentum resolution (again with respect to $\vec{E}_T^{miss}$). You can find more details on the definition and calculation of this variable in Ref.[71]. Studies of the sensitivity increase to SUSY searches by the use of $E_{\mathrm{T}}^{\mathrm{miss}}$ significance have been published on the Appendix B of Ref.[72]. These analyses make extensive use of this form of $E_{\mathrm{T}}^{\mathrm{miss}}$ significance.

Overlap Removal

Overlap removal (OR) is performed to resolve ambiguities between objects that are classified in more than one type of collection. Only baseline objects (electrons, muons and jets) are considered and it is applied using the standardized implementation in `SUSYTools` [73]. This configuration is described by the following steps:

- Any calo-tagged muons sharing an ID track with an electron are removed. Any electrons sharing an ID track with remain-

ing muons are removed.

- Any jet within a cone of size dR$<$ 0.2 around an electron is discarded if it is not b-tagged for a working point providing 85% b-tagging efficiency or if the electron has $p_{\mathrm{T}} > 100$ GeV;

- An electron is discarded in favour of a jet if

$$dR < min(0.4, 0.04 + 10/P_T^{e^{\pm}})$$

- Jet is discared in favour of a muon if NumTrack$<$ 3 and dR$<$ 0.2

- A muon is discarded in favour of a jet if

$$dR < min(0.4, 0.04 + 10/P_T^{\mu^{\pm}})$$

4.4 Systematic Uncertainties

Predictions of each Standard Model background is subject to various systematic uncertainties. These uncertainties can impact the expected event yields in the control and signal regions as well as the extrapolation from the control region to the signal region. It is crucial that this be taken into account when interpreting an analysis. There are two types of systematic uncertainties:

1. **Experimental Systematic Uncertainties** are detector-based

sources of uncertainty such as object calibration, pileup, or luminosity.

2. **Theoretical Systematic Uncertainties** include uncertainties such as cross-section or parton showering uncertainties, among others.

Most of the systematics are assessed by comparing the results of the analysis using the nominal samples with the same results using systematically varied samples.

Experimental Systematic Uncertainties

The following is a list of the sources of uncertainty and the corresponding names of the variations.

- **Electron energy scale uncertainty** (`EG_SCALE{up,down}`).
- **Electron resolution uncertainty** (`EG_RESOLUTION{up,down}`).
- **Electron efficiency uncertainties** (`EL_EFF_{ChargeIDSel,ID,Iso,Reco,TriggerEff,Trigger}{up,down}`) associated with the electron efficiency scale factors provided by the Egamma CP group.
- **Muon momentum scale uncertainty** (`MUON_SCALE{up,down}`).
- **Muon resolution uncertainty for the inner detectorn and muon spectrometer** (`MUON_ID{up,down}`, `MUON_MS{up,down}`).

- **Muon efficiency uncertainties**
  (`MUON_EFF_BADMUON_{STAT,SYST}{up,down}`,
  `MUON_EFF_ISO_{STAT,SYST}{up,down}`,
  `MUON_EFF_RECO_{STAT,SYST}{up,down}`,
  `MUON_EFF_RECO_{STAT,SYST}_LOWPT{up,down}`,
  `MUON_EFF_TTVA_{STAT,SYST}{up,down}`,
  `MUON_EFF_Trig{Stat,Syst}Uncertainty{up,down}`) corresponding to the statistical and systematic uncertainties in the muon efficiency scale factors provided by the Muon CP group.

- **Muon charge dependent momentum scale uncertainty**
  (`MUON_SAGITTA_{RESBIAS,RHO}{up,down}`) related to the charge dependent uncertainty in the scale of the momentum.

- **Jet energy scale uncertainty** (JES) coming from several primary sources based on Monte Carlo studies and in-situ measurements, from the eta-intercalibration and from samples flavour response. Sets of strongly reduced parameters are provided for analyses. One of the strongly reduced uncertainty sets provided by the Jet/$E_{\mathrm{T}}^{\mathrm{miss}}$ CP group,
  i.e. `R4_SR_Scenario1_SimpleJER.config`, is used. The following three nuisance parameters
  `JET_GroupedNP_{1,2,3}{up,down}` are consequently taken into account together with

JET_EtaIntercalibration_NonClosure_{highE,negEta,posEta} and JET_Flavor_Response. The reduced set also contains a fourth parameter (JET_RelativeNonClosure_AFII{up,down}) which is for AF2 MC closure.

- **Jet energy resolution uncertainty** (JER) derived using the reduce nuisance parameter set (JET_JER_DataVsMC{up,down}, JET_JER_EffectiveNP_{1,2,3,4,5,6,7restTerm}{up,down}).

- **JVT efficiency uncertainty** (JET_JvtEfficiency{up,down}) associated with JVT efficiency scale factors provided by the Jet/$E_{\mathrm{T}}^{\mathrm{miss}}$ CP group.

- **Flavour tagging uncertainties** (FT_EFF_{B,C,Ligh}_systematics{up,down}, FT_EFF_extrapolation{up,down}, FT_EFF_extrapolation_from_charm{up,down}) related to the $b-$tagging efficiency scale factors provided by the flavour tagging group.

- $E_{\mathbf{T}}^{\mathbf{miss}}$ **soft term uncertainties** (MET_SoftTrk_ResoPara, MET_SoftTrk_ResoParp, MET_SoftTrk_Scale{up,down}) associated to the TST uncertainties provided by the Jet/$E_{\mathrm{T}}^{\mathrm{miss}}$ CP group

- **Pileup reweighting uncertainty** (`PRW_DATASF{up,down}`) evaluated changing the nominal average correction factor of 1/1.03 to 1 and to 1/1.18 and re-evaluating the reweighting factors. These two values are based on studies of the number of vertices as well as the results from the measurement of inelastic cross-section.

- **Luminosity uncertainty** which has been evaluated for the full Run-2 data to be 1.7%.

In general, all experimental systematic uncertainties are treated as double sided uncertainties, except `MET_SoftTrk_ResoPara`, `MET_SoftTrk_ResoParp` and the JER uncertainties, which are treated as symmetrized uncertainties.

Theoretical Systematic Uncertainties

Systematic uncertainties in the theoretical modeling of the observed final states can be classified in the following categories:

1. uncertainties in the parton-level cross-section due to missing higher-order corrections in the perturbative QCD calculation,

2. uncertainties in the proton Parton Distribution Function and in the strong coupling constant that effects the description of the parton-level final states,

3. uncertainties arising from the parton showering and hadronization models that convert the partons into exclusively hadronic final states.

In this analysis, the estimates of theoretical uncertainties follow from the ATLAS PMG and SUSY working group recommendations [74] [75] [76]. Theoretical systematics for the main backgrounds were considered: $t\bar{t}$, $t\bar{t}$ Z, and diboson.

$t\bar{t}$ theoretical systematic uncertainties

For the $t\bar{t}$ background the following uncertainties were considered:

- **Hard-Scattering uncertainty**, comparing the nominal sample, PowhegPythia8, with aMC@NLO+Pythia8.
- **Parton Shower uncertainty**, comparing the nominal sample, PowhegPythia8, with PowhegHerwig7.
- **Initial State Radiation (ISR) uncertainty**: both up and down variations are estimated with internal weights. The up variation is obtained by dividing the renormalization and factorization scales by 2 and varying the showering with the internal weight *Var3cUp*. The down variation is estimated from the nominal sample, doubling the renormalization and factoriza-

tion scales and varying the showering with the internal weight *Var3cDown*.

- **Final State Radiation (FSR) uncertainty**: up and down variations are respectively estimated using the parton shower weights *isr:muRfac=10_fsr:muRfac=20* and *isr:muRfac=10_fsr:muRfac=05*.

$t\bar{t}Z$ theoretical systematic uncertainties

For the $t\bar{t}Z$ background, the following uncertainties were considered:

- **Renormalization/Factorization uncertainties** are estimated with the internal weights.
- **Parton Shower uncertainty** is assessed by comparing the nominal sample, aMC@NLO+Pythia8, with aMC@NLO+Herwig7.
- **Radiation uncertainty** is done using the Pythia8 tune variations.

Diboson theoretical systematic uncertainties

For the diboson background the following uncertainties were considered:

- **Scale uncertainties** were estimated with the internal weights with the exception of matching (CKKW) and resummation (QSF) scale variations. These were calculated from a comparison between the nominal sample and the variation samples.
- **Heavy Flavour (HF) Fragmentation** is assumed to be 30% on the number of events having at least 1 $b-$quark and 1 $b-$tagged jet and applied only for those selections where the diboson normalisation is driven by a 0 $b-$tagged jet region.

Chapter 5

Recursive Jigsaw Analysis

The *Recursive Jigsaw* analysis makes use of the high-level *Recursive Jigsaw Reconstruction* technique, as described in [77]. This is a generalization of the techniques used in [78] referred to as 'Super Razor.' The recursive jigsaw reconstruction (RJR) technique is a method for decomposing measured properties event-by-event to provide a foundation for defining kinematic variables. In order to accomplish this the rest frame of each intermediate particle state for each event is approximated. This view gives rise to a natural basis of kinematic observables, calculated by evaluating the momentum and energy of different objects in these reference frames. Background processes can be reduced by testing whether each event exhibits the properties of the imposed decay tree while applying minimal selection criteria on the visible object momenta as well as missing momenta. This process is recursive in that it steps through the decay chain

one link at a time. The algorithm for resolving the unknowns in a single decay step is called a *jigsaw*. One event is analyzed by *recursively* applying a series of jigsaws, moving through the decay tree from the lab frame to the rest frame of each intermediate particle appearing in the event. This means that conclusions drawn at the earlier decay steps about the kinematic properties of the particles present aren't lost or altered as the decay chain is traversed.

5.1 The Recursive Jigsaw Reconstruction Technique

In Figure 5.1 you can see a standard decay tree applied to pair-produced particles which decay directly to a visible state, $V_{(a,b)}$, and an invisible state, $I_{(a,b)}$. It will be the case that the signature will have the same topology as a background process and therefore you would have the same recursive jigsaw decay tree. However, the kinematics will be quite different between them and any variable derived from the four-vectors from this decay tree will potentially discriminate between the signal and background processes.

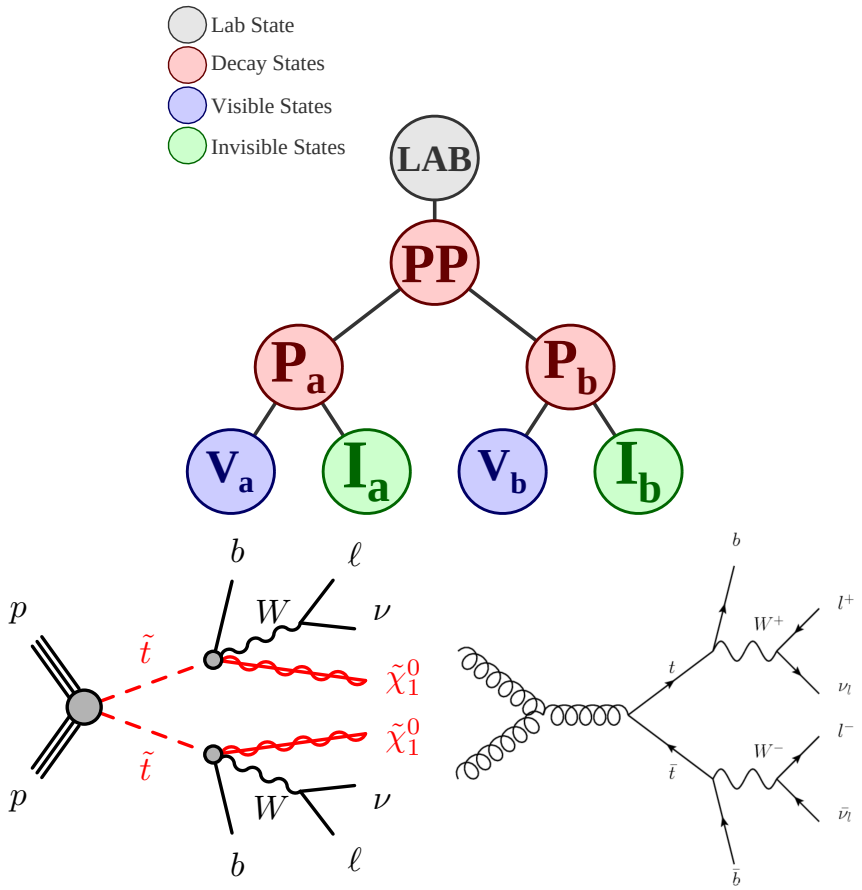

Figure 5.1: A generic decay tree (top) applied to pair-produced particles, or sparticles, P, decaying to visible states "V" and invisible states "I." The three body signature of interest (bottom left) and a typical $t\bar{t}$ signature (bottom right). You can see how we allocate these objects in the recursive jigsaw decay tree. We take as the visible objects only the leptons and as the invisible objects the neutrinos and neutralinos. Both the signal and background events will have the same decay tree, but the variables defined should be able to discriminate.

In our search for the 3-body decay of the $\tilde{t}_1$, we use the decay tree as shown in Figure 5.1. The visible system $(V_a + V_b)$ is provided only the two leptons while the invisible system $(I_a + I_b)$ is provided the missing transverse momentum. The most general decay tree

possible was chosen for targeting R-parity conserving SUSY models in order to make the least number of assumptions possible. You might think it best to choose a more specific decay tree, after all there are more objects in our signature. However, this would require the ability to separate the b-tagged jets and leptons into the visible states, requiring at least four visible objects to be reconstructed. However, what is really needed is a means to separate our pair-produced SUSY signal from the background while making as few assumptions as possible.

In a perfect world we would be able to determine the intermediate rest frames in our decay tree, if this were possible then we could easily construct variables that could perfectly distinguish between a signal and background event. Unfortunately, this is not the case. There are multiple weakly interacting particles in the final state, as well as the presence of b-jets that we can not distinguish with 100% efficiency. The RJR technique provide us with a means of resolving these unknowns on an event-by-event basis. The rest frame for each intermediate particle state is approximated, giving us a basis for defining kinematic observables.

In the RJR decay tree used illustrated in Figure 5.1 there are six under-constrained degrees-of-freedom,

- Two degrees of freedom due to the longitudinal momenta of the invisible states: $\mathbf{p}_{I_i,z}$,

- Two degrees of freedom due to the splitting of the missing transverse momentum between the invisible states: $\mathbf{p}_{I_a,T} + \mathbf{p}_{I_b,T} = E_{\mathrm{T}}^{\mathrm{miss}}$

- Two degrees of freedom due to the mass of the invisible system: m_{I_a} and m_{I_b}.

The RJR technique aims to provide approximations for these unknowns through a series of assumptions that it makes about the boosts between the different rest frames. RJR is, as the name suggests, recursive. The algorithm moves from the first known reference frame, the lab frame, and traverses down the decay tree using only the information from the current reference frame to determine the boost into the next rest frame. Only information from the lab frame is used to move to the PP (center-of-mass) frame, and information from this PP frame is used to move into either of the decay frames, P_i.

The first step that RJR takes is approximating the mass of the invisible system, m_I, composed of I_a and I_b. This information is necessary to consistently perform boosts between the references frames while keeping each side of the decay balanced. In general,

the invisible system will have a non-trivial opening angle between the two invisible states balancing the visible system. In order to satisfy this requirement, the RJR technique takes for m_I [1] the smallest Lorentz-invariant mass consistent with the observed variables in the lab frame that accommodate the subsequent boosts while preventing the states from breaking the speed of light barrier. For the generic decay tree chosen, this is

$$m_I^2 = m_V^2 - 4m_{V_a}m_{V_b}, \tag{5.1}$$

where V is the total visible system.

The next step taken is to determine the boost from the lab frame to the PP frame. To do this, the longitudinal momentum of the invisible system, $p_{I,z}^{LAB}$, must be determined. This value is chosen such that the rapidity of the visible and invisible systems are equal. This results in the PP rest frame being longitudinally boost-invariant, as well as the total mass (m_{V+I}^{PP}) of the PP frame taking its minimum value.

With the longitudinal momentum and mass of the invisible system determined, we can build the expression for the boost from the lab

[1] From special relativistic mechanics, the mass of a system composed of two subsystems is $m_{12} = m_1^2 + m_2^2 + 2(E_1E_2 - |\mathbf{p}_1||\mathbf{p}_2|cos\theta_{12})$, where θ_{12} is the opening angle between $\mathbf{p}_1$ and $\mathbf{p}_2$.

frame to the PP frame,

$$\beta_{PP}^{LAB} = \frac{\mathbf{p}_{PP}^{LAB}}{E_{PP}^{LAB}} = \frac{\mathbf{p}_{V}^{LAB} + \mathbf{p}_{I}^{LAB}}{E_{V}^{LAB} + \sqrt{|\mathbf{p}_{I}^{LAB}|^2 + m_I^2}} \tag{5.2}$$

Using this boost we can define observables in the PP rest frame. This information is also used in order to construct the boost into the individual sparticle rest frames, P_I. This boost will provide us with the final basis for building our observables. The last assumption the RJR technique makes is that $m_{V_a} = m_{V_b}$, which is reasonable since these particles are either an electron or a muon and in the context of the processes we consider $m_{e^-} \approx m_{\mu^-}$. Since the current frame is the PP center-of-mass frame, this choice dictates that the boosts of each individual sparticle rest frame is equal in magnitude and anti-parallel to the other. The RJR technique takes the solution

$$\beta_{PP}^{LAB} = \frac{\mathbf{p}_{V_a}^{PP} - \mathbf{p}_{V_b}^{PP}}{E_{V_a}^{PP} + E_{V_b}^{PP}}. \tag{5.3}$$

Now that we have the boost into the sparticle rest frames, the splitting of invisible momentum can now be determined, requiring $\mathbf{p}_{V_i}^{P_i} + \mathbf{p}_{I_i}^{P_i} = 0$. This splitting of the invisible momentum was the final under-constrained degree-of-freedom of the RJR decay tree. With the application of this technique, all of the unknowns for determining the rest frames in the decay tree have been approximated and

a basis for defining discriminating variables has been formulated.

5.2 Discriminating Observables

The *recursive jigsaw reconstruction* technique provides an approximation of the center-of-mass frame of the $\tilde{t}$ system, as described above, as well as an approximation of the decay frames. From here, multiple variables for discriminating our signal from background can be computed. It is a natural start to compute the total energy of the available objects in our decay tree. This approximate center-of-mass energy, or invariant mass, is referred to as m_{PP}. It will also be useful to define the associated transverse momentum of the COM frame, $|p_T^{PP}|$. Then, using m_{PP} and $|p_T^{PP}|$, the ratio R_{p_T} can be defined,

$$R_{p_\mathrm{T}} = \frac{|p_T^{PP}|}{|p_T^{PP}| + m_{PP}/4}. \tag{5.4}$$

Distributions of R_{p_T} for different (same) flavor are shown on the left (right) in Figure 5.2. You can see that for pair-produced particles decaying to heavy final state objects more of their energy is distributed to the transverse plane, therefore R_{p_T} tends to one.

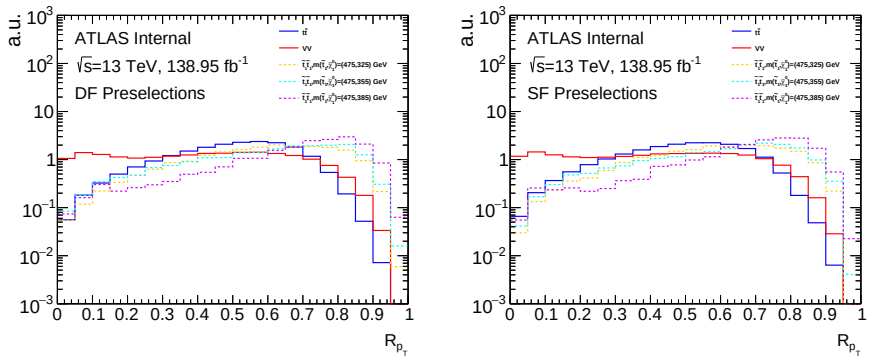

Figure 5.2: Normalized distributions of the R_{p_T} variable for the three benchmark signal points and the dominant background processes $t\bar{t}$ and diboson VV. The only selection applied is the requirement of two oppositely charged leptons with leading lepton p_{T} greater than 25 GeV, subleading lepton p_{T} greater than 20 GeV, and M_{Δ}^{R} greater than 75 GeV. Different (same) flavor events are shown on the left (right).

Another variable used for discriminating between the signal and background uses the relative velocity of the COM frame as seen in the LAB frame, as well as the total visible system, $V = V_a + V_b$, as seen in the COM frame. This variable, $\Delta\phi_{\beta}^{R}$, is the angle between the boost from the LAB frame to the COM frame and the visible system, V. In our case, the visible system is simply the dilepton system as seen in the COM frame. Distributions of $\Delta\phi_{\beta}^{R}$ are shown in Figure 5.3.

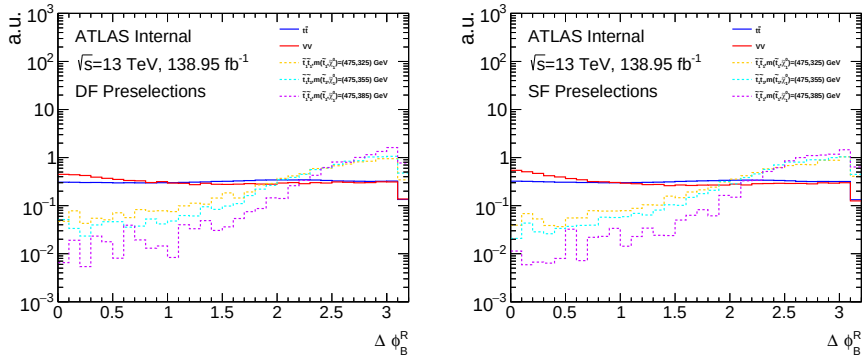

Figure 5.3: Normalized distributions of the $\Delta\phi_\beta^R$ variable for the three benchmark signal points and the dominant background processes $t\bar{t}$ and diboson VV. The only selection applied is the requirement of two oppositely charged leptons with leading lepton p_{T} greater than 25 GeV, subleading lepton p_{T} greater than 20 GeV, and M_Δ^R greater than 75 GeV. Different (same) flavor events are shown on the left (right).

You can see the $\tilde{t}_1$ signals clearly peak when $\Delta\phi_\beta^R$ approaches π and seem to be roughly independent of the mass splitting, $\Delta m(\tilde{t}_1, \tilde{\chi}_1^0)$. Instead, $\Delta\phi_\beta^R$ is more dependent on the assumptions made when constructing the underlying RJR decay tree from which $\Delta\phi_\beta^R$ is derived, namely that $m_I = m_V$. For the massive $\tilde{\chi}_1^0$ particles in the invisible final state of the $\tilde{t}_1$ signal decay, this assumption is clearly incorrect and the boost from the LAB frame to the PP frame is an over boost.

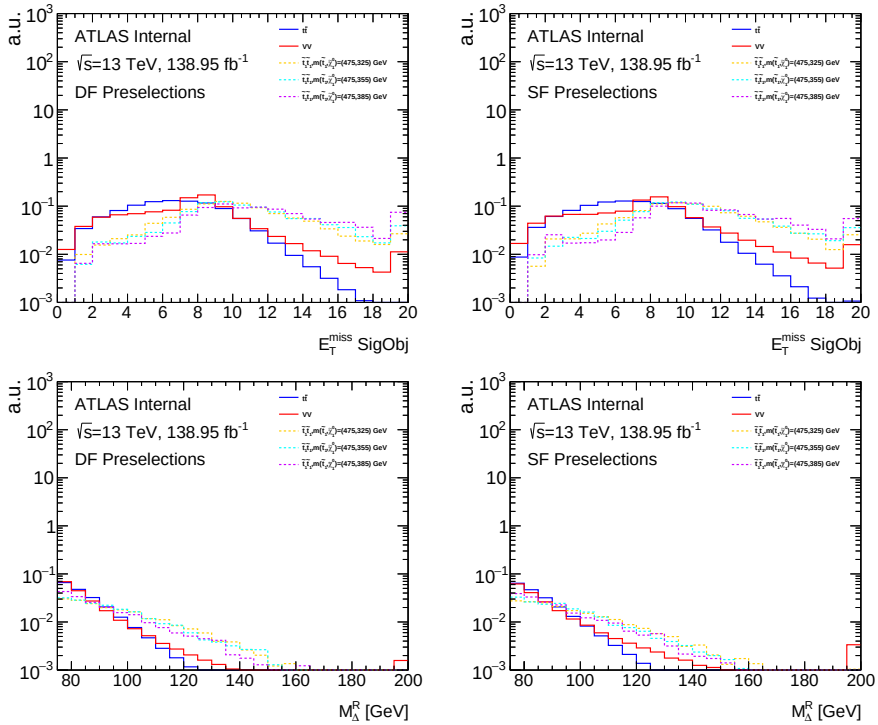

Figure 5.4: Normalized distributions of the $E_{\mathrm{T}}^{\mathrm{miss}}$ significance and M_{Δ}^{R} variables for the three benchmark signal points and the dominant background processes $t\bar{t}$ and diboson VV. The only selection applied is the requirement of two oppositely charged leptons with leading lepton p_{T} greater than 25 GeV, subleading lepton p_{T} greater than 20 GeV, and M_{Δ}^{R} greater than 75 GeV. Different (same) flavor events are shown on the left (right).

Yet another variable defined, M_{Δ}^{R}, is useful for discriminating the signal from background. This variable is sensitive to the mass differences between the pair-produced $\tilde{t}_1$ and $\tilde{\chi}_1^0$. It corresponds to the energy of one of the leptons, V_i, with respect to the sparticle, (P_i) frame of reference and has an endpoint proportional to

$$M_{\Delta}^{R} \propto \frac{m_{P_i}^2 - m_{I_i}^2}{m_{P_i}}. \tag{5.5}$$

Distributions of M_{Δ}^{R} are shown in Figure 5.4.

The next Jigsaw variable we define is the 'visible shape' of the COM frame. In the case where $m_{V_a} = m_{V_b} \approx 0$, which is true for this analysis, this variable corresponds to the inverse boost factor (γ) from the PP frame to the P_i frames. The visible shape is defined as

$$PP \text{ Visible Shape} \rightarrow 1/\gamma_{R+1} \equiv \frac{\sqrt{2(|\vec{p}_{V_a}^{PP}||\vec{p}_{V_b}^{PP}| + \vec{p}_{V_a}^{PP} \cdot \vec{p}_{V_b}^{PP})}}{|\vec{p}_{V_a}^{PP}| + |\vec{p}_{V_b}^{PP}|}. \tag{5.6}$$

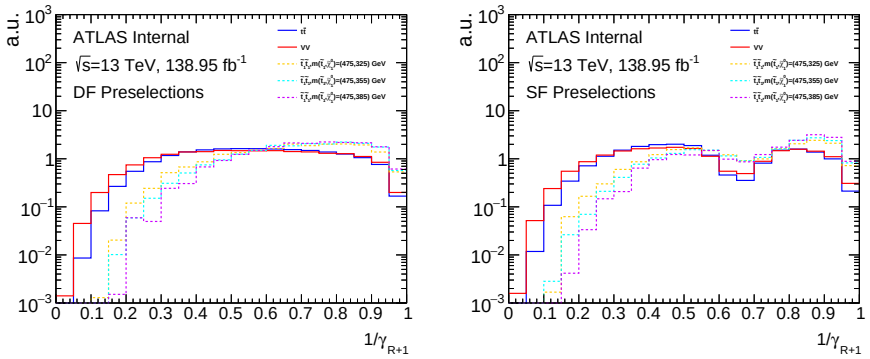

Figure 5.5: Normalized distributions of the $1/\gamma_{R+1}$ variable for the three benchmark signal points and the dominant background processes $t\bar{t}$ and diboson VV. The only selection applied is the requirement of two oppositely charged leptons with leading lepton p_{T} greater than 25 GeV, subleading lepton p_{T} greater than 20 GeV, and M_{Δ}^{R} greater than 75 GeV. Different (same) flavor events are shown on the left (right).

The quantity $1/\gamma_{R+1}$ is a measurement of how the two visible systems, V_a and V_b, are distributed, and hence the name "visible shape". It tends towards one when V_a and V_b, which are the two leptons here, are equal in momenta and collinear while tending toward zero

when they are back-to-back or have different momenta. In decays with massive particles contributing to the missing transverse momentum, the legs in the final state V_a and V_b will tend to not be back-to-back since they will not only be balancing each other, but they must also balance the invisible particles. This effect is exaggerated when the decays are highly active, as in $t\bar{t}$, and when the invisible system is composed of heavy particles. This exaggeration in highly active decays is particularly because we considered only final state leptons in V_a and V_b, $1/\gamma_{R+1}$ is blind to any jets in the event and the corresponding shape is in response to balacing these jets. When the invisible system contains heavy particles the legs recoil harder off of these heavier particles and thus tend to be collinear. You can see $1/\gamma_{R+1}$ distributions in Figure 5.5.

Finally, a selection on the $E_{\mathrm{T}}^{\mathrm{miss}}$ significance was applied, the quantity described in equation 4.2,

$$E_{\mathrm{T}}^{\mathrm{miss}}\text{significance} = \sqrt{\frac{|\vec{E}_T^{\,miss}|^2}{\sigma_{\mathrm{L}}^2(1-\rho_{\mathrm{LT}}^2)}}.$$

This variable helps to distinguish events where the $E_{\mathrm{T}}^{\mathrm{miss}}$ arises from mismeasured objects from events where the $E_{\mathrm{T}}^{\mathrm{miss}}$ comes from invisible particles.

All of these variables are dependent on their being massive particles contributing to the missing transverse momentum, they are used

to construct regions sensitive to detecting our SUSY models.

5.3 Signal Region Optimization

In order to optimize the selections defining the signal regions, a scan across our different discriminating variables to find optimum values for selecting signal and rejecting background processes was performed. These scans were done using the three benchmark signal models:

- $m(\tilde{t}_1, \tilde{\chi}_1^0) = (475, 325)$
- $m(\tilde{t}_1, \tilde{\chi}_1^0) = (475, 355)$
- $m(\tilde{t}_1, \tilde{\chi}_1^0) = (475, 385)$.

For each variable, a scan across different values of that variable counting the number of events above or below a given threshold is performed, counting both the number of background events as well as the number of signal events in each model. With the background and signal events, the significance is computed with

$$Z = \sqrt{2\left(n \ln\left(\frac{n(b+\sigma^2)}{b^2+n\sigma^2}\right) - \frac{b^2}{\sigma^2}\ln\left(1+\frac{\sigma^2(n-b)}{b(b+\sigma^2)}\right)\right)}, \quad (5.7)$$

for each value. These scans are summarized in Figure 5.11 for SR_W and Figure 5.12 for SR_t.

These signal regions are defined around two conditions:

1. The $\tilde{t}_1 \to bW\tilde{\chi}_1^0$ decay kinematics change when you go from the mass-splitting region $\Delta m(\tilde{t}_1, \tilde{\chi}_1^0) = m_{top}$ to $\Delta m(\tilde{t}_1, \tilde{\chi}_1^0) = m_W$.

2. The variable $\Delta\phi_\beta^R$ is roughly independent of the mass-splitting $\Delta m(\tilde{t}_1, \tilde{\chi}_1^0)$, as can be seen in Figure 5.3.

Due to the different decay kinematics, two signal regions will be defined, one targeting the m_W diagonal called "SR$_W$" and the other targetting the m_{top} diagonal called "SR$_t$." You can see in Figure 5.6 that for the $\tilde{t}_1 \to bW\tilde{\chi}_1^0$ decay with $\Delta m(\tilde{t}_1, \tilde{\chi}_1^0)$ nearer to the m_W diagonal the reconstructed b-jet multiplicity tends to 0, while when $\Delta m(\tilde{t}_1, \tilde{\chi}_1^0)$ is closer to m_{top} there tends to be the presence of reconstructed b-jets. This effect is also clear in the N-1 plots shown in 5.13 and 5.14. This delineates the main difference between SR$_W$ and SR$_t$.

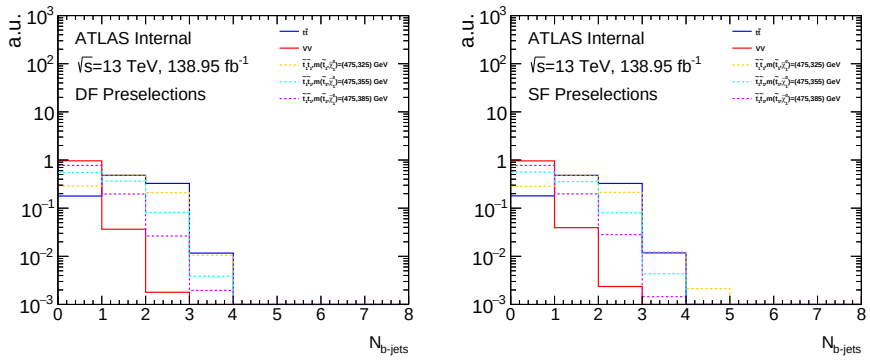

Figure 5.6: Normalized distributions of the number of b-tagged jets for the three benchmark signal points and the dominant background processes $t\bar{t}$ and diboson VV. The only selection applied is the requirement of two oppositely charged leptons with leading lepton p_{T} greater than 25 GeV, subleading lepton p_{T} greater than 20 GeV, and M_{Δ}^{R} greater than 75 GeV. Different (same) flavor events are shown on the left (right).

Since $\Delta\phi_{\beta}^{R}$ is roughly independent of the mass-splitting, $\Delta m(\tilde{t}_1, \tilde{\chi}_1^0)$, it is used to construct control regions that are orthogonal to both signal regions. You can see in Figure 5.3 the signal yield is much higher for high values of $\Delta\phi_{\beta}^{R}$ for all three benchmark samples.

From this point, an optimization scan was performed over the remaining jigsaw variables defined above, outlined in the following section, resulting in our final definitions of two control regions targeting different mass-splittings.

$\Delta m \sim m_W$ and $\Delta m \sim m_t$ Preselections

Targeting the $\Delta m \sim m_W$ (SR_W) and $\Delta m \sim m_t$ (SR_t) we require the following preselection cuts:

- 2 oppositely charged (OS) leptons passing signal quality and trigger requirements
- Leading lepton $p_{\mathrm{T}} > 25$ GeV, sub-leading lepton $p_{\mathrm{T}} > 20$ GeV
- $m_{\ell\ell} > 20$ GeV (to remove contribution of mis-modeling of low-mass resonances or Drell-Yan MC)
- $|m_{\ell\ell} - m_Z| > 20$ GeV if leptons are same-flavor
- $M_{\Delta}^{R} > 75$ GeV
- $b-$jet veto for SR_W or at least one b-tagged jet for SR_t

Depending on the b-jet multiplicity, this level of selection is called **preselection + b-veto** (SR_W) or **preselection + >0 b-jets** (SR_t).

A comparison of data and MC between the key kinematic variables at the b-veto preselection level is shown in Figure 5.7 for final states with different flavour leptons and in Figure 5.8 for final states with same flavour leptons.

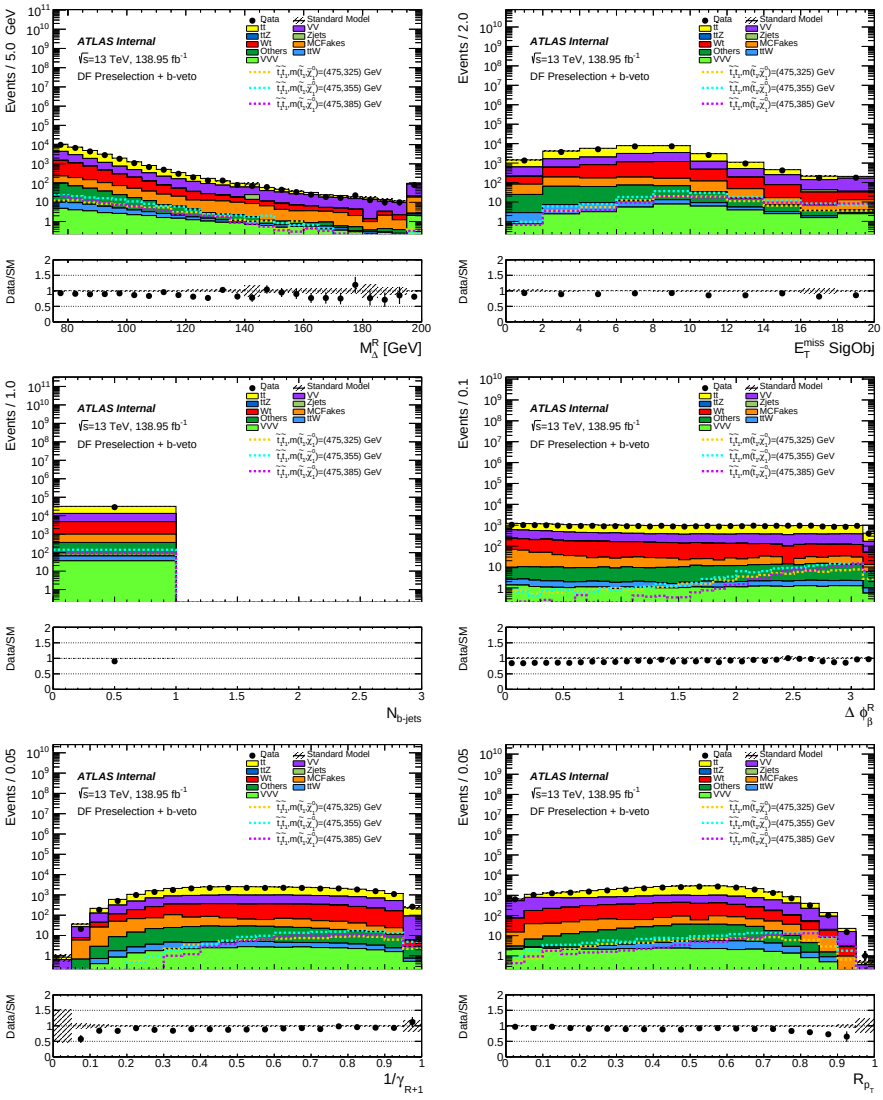

Figure 5.7: Distributions at preselection level for the $\Delta m \sim m_W$ selection in the DF channel with the $b-$jet veto applied. The error band on the MC represent statistical uncertainties only.

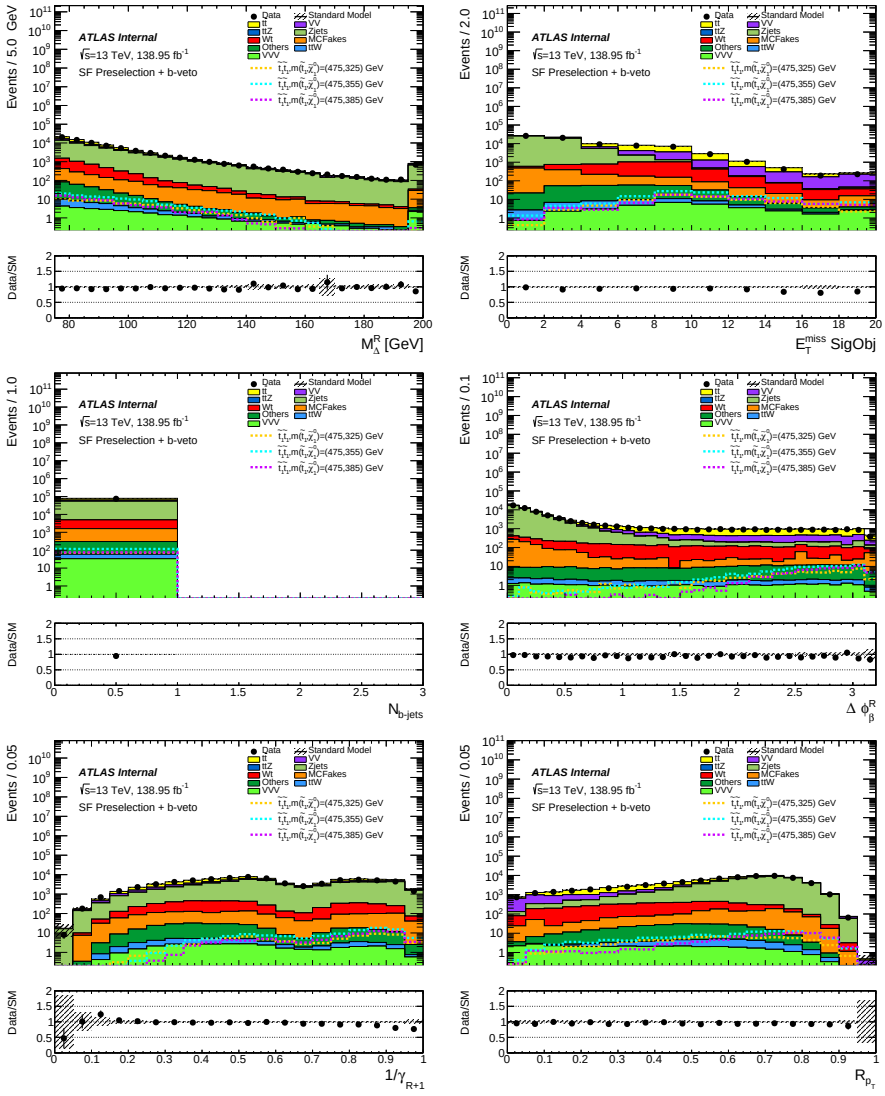

Figure 5.8: Distributions at preselection level for the $\Delta m \sim m_W$ selection in the SF channel with the $b-$jet veto applied. The error band on the MC represent statistical uncertainties only. MC estimates are absolute.

A comparison of data and MC between the key kinematic variables at the b-jets preselection level is shown in Figure 5.9 for different flavour leptons and in Figure 5.10 for same flavour leptons.

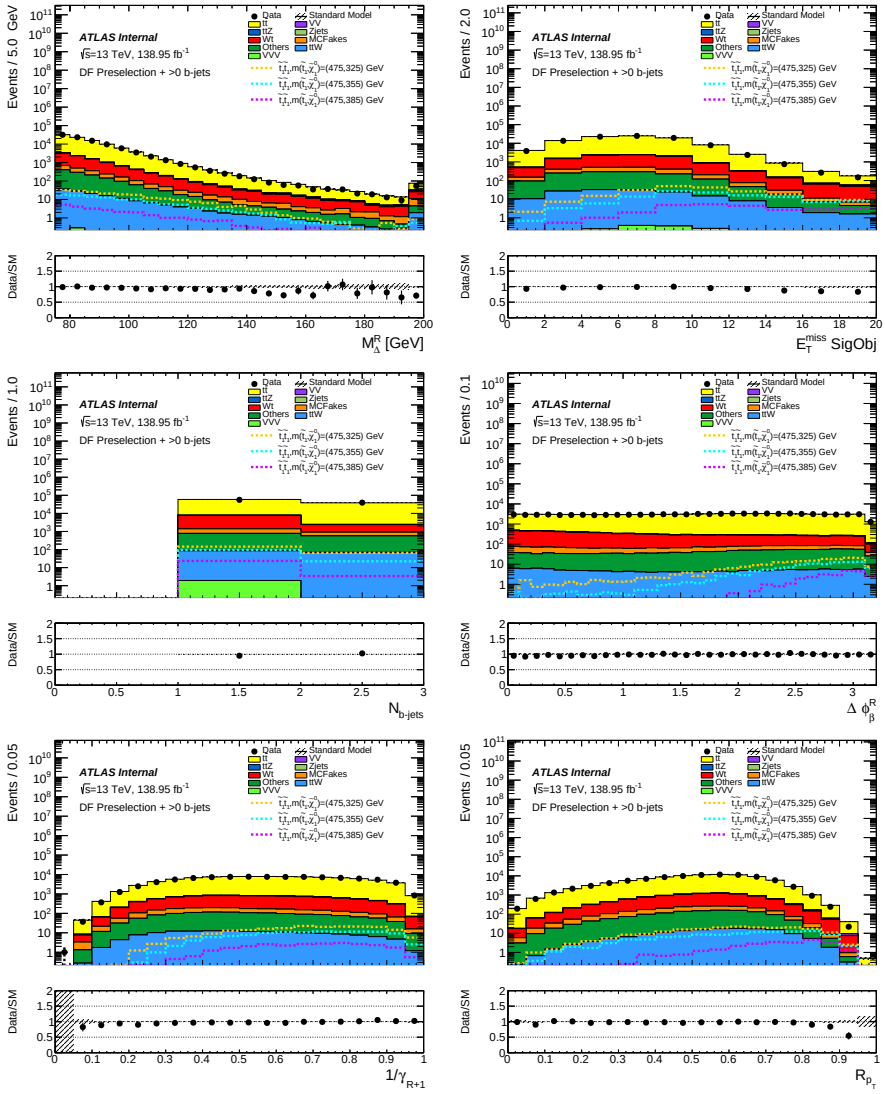

Figure 5.9: Distributions at preselection level for the $\Delta m \sim m_t$ selection in the DF channel requiring >0 $b-$jets. The error band on the MC are statistical uncertainties only. MC estimates are absolute.

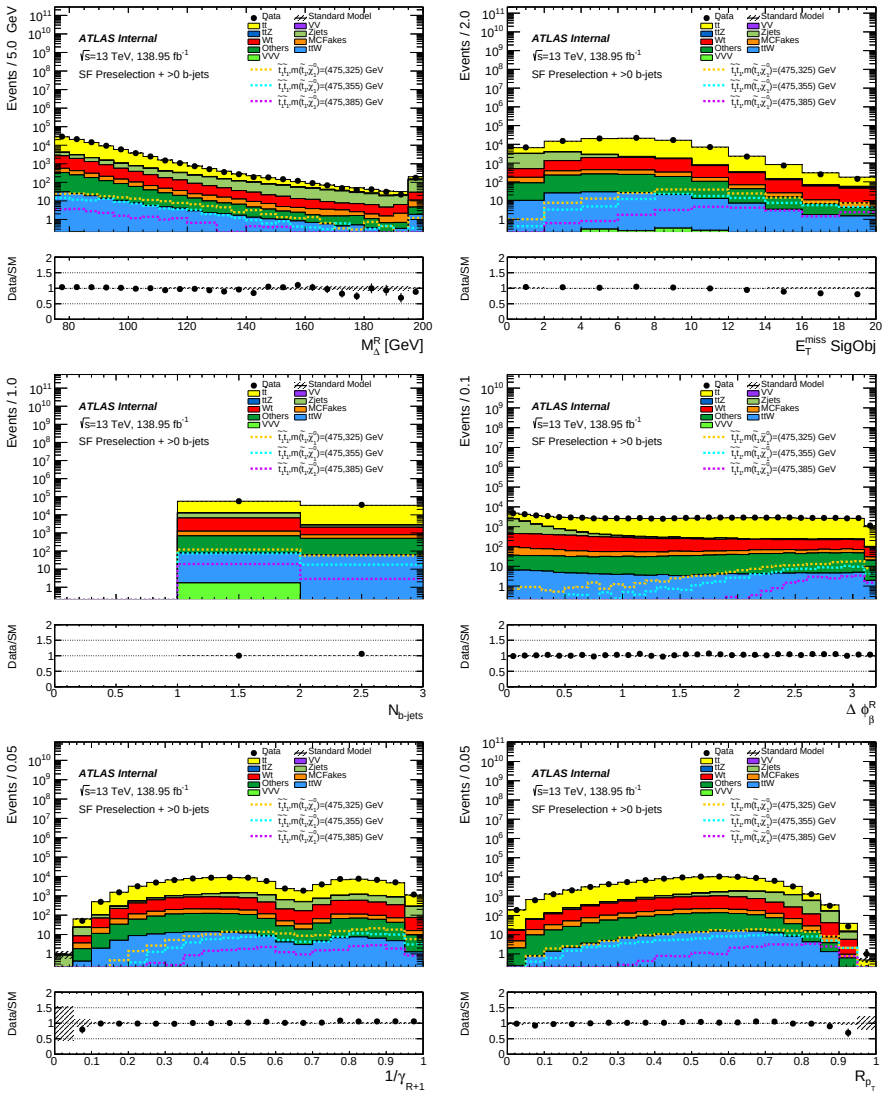

Figure 5.10: Distributions at preselection level for the $\Delta m \sim m_t$ selection in the SF channel requiring >0 $b-$jets. The error band on the MC are statistical uncertainties only. MC estimates are absolute.

Signal Region Definitions

As discussed before, the signal tends to higher values of $\Delta\phi_\beta^R$ independently of our signal model. For this reason, a strategy to de-

velop orthogonality between the control regions and signal regions was based upon a selection on this variable. The signal regions will have high $\Delta\phi_\beta^R$, while the control regions will have lower $\Delta\phi_\beta^R$. After an initial optimization scan across all variables, a selection at $\Delta\phi_\beta^R > 2.3$ was chosen in order to maximize Z, as defined in Equation 5.7.

Outlined in Figure 5.11 is the optimization procedure for SR_W. Starting with M_Δ^R in the top-left, shown is a comparison of the signal and total combined background. In the lower section of the plot is Z, if a selection at that value is chosen. For this procedure, Z is computed with 20% uncertainty. I have also placed an arrow to indiciate the cut defining the final selection. The next plot shown, $1/\gamma_{R+1}$, is made after applying the cut shown on M_Δ^R. In the end, you can see that by applying a selection on $E_{\mathrm{T}}^{\mathrm{miss}}$ significance at 12, we obtain a significance of around 3.

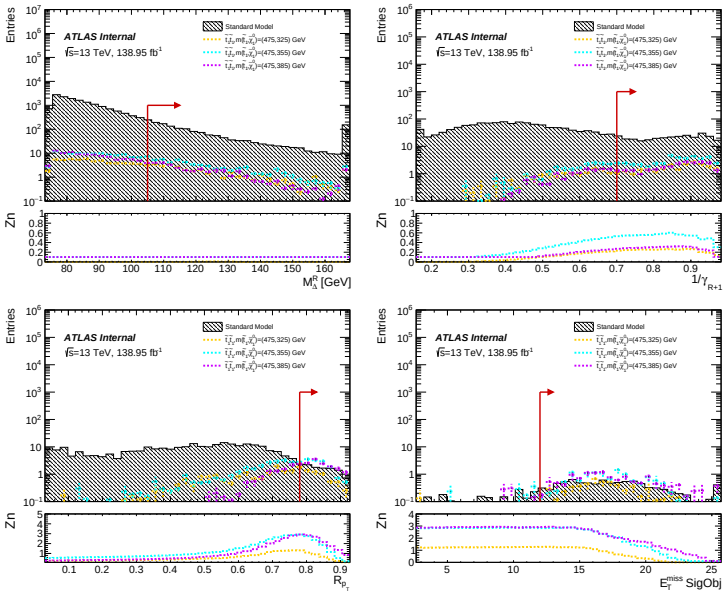

Figure 5.11: The last few steps of the optimization are shown for the $\Delta m \sim m_W$ selection. All of the selections are applied except for the variables shown. The Final cuts applied are shown with the red arrow and then applied for the following step.

Shown in Table 5.1 are the expected yields in SR_W if the selections shown above for both the different flavor and same flavor final states are chosen.

Table 5.1: MC expected yields for an integrated luminosity of 138.95 fb^{-1}in the different-flavor and same-flavor channels of the $\Delta m \sim m_W$ (SR_W) signal region for the main background processes contributing to the analysis. The last three rows include expected yields from the three benchmark signal samples with the stop and neutralino masses shown.

	SRW_{DF}^{3-body}	SRW_{SF}^{3-body}
MC exp. SM events	5.30 ± 0.78	3.95 ± 0.76
MC exp. ttbar events	1.31 ± 0.52	0.79 ± 0.35
MC exp. Wt events	0.30 ± 0.05	0.21 ± 0.03
MC exp. Zjets events	0.00 ± 0.00	0.04 ± 0.02
MC exp. VV events	2.69 ± 0.58	2.66 ± 0.59
MC exp. VVV events	0.18 ± 0.01	0.13 ± 0.01
MC exp. ttZ events	0.08 ± 0.03	0.07 ± 0.04
MC exp. ttW events	0.01 ± 0.00	0.02 ± 0.01
MC exp. other events	0.02 ± 0.01	0.02 ± 0.00
MC exp. DDFakes events	0.71 ± 0.00	0.00 ± 0.00
$\tilde{t}_1\tilde{t}_1, m(\tilde{t}_1, \tilde{\chi}_1^0) = (475, 385)$ GeV	7.90 ± 0.63	5.39 +/- 0.53
$\tilde{t}_1\tilde{t}_1, m(\tilde{t}_1, \tilde{\chi}_1^0) = (475, 355)$ GeV	7.08 ± 0.55	5.70 +/- 0.68
$\tilde{t}_1\tilde{t}_1, m(\tilde{t}_1, \tilde{\chi}_1^0) = (475, 325)$ GeV	2.99 ± 0.37	2.52 +/- 0.35

Likewise, the same procedure for SR_t is performed, as outlined in Figure 5.12. After the selections are applied the yields are presented in Table 5.2.

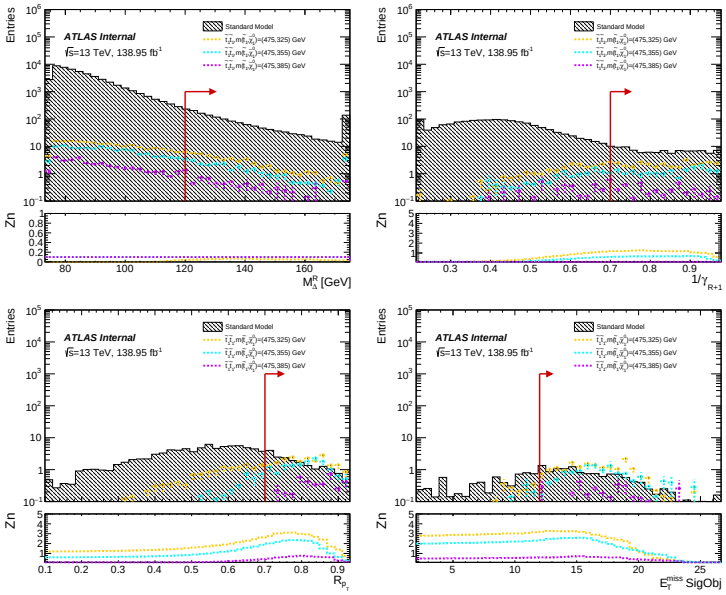

Figure 5.12: The last few steps of the optimization are shown for the $\Delta m \sim m_t$ selection. All of the selections are applied except for the variables shown. The cuts applied are shown with the red arrow and then applied for the following step.

	SRt^{3-body}_{DF}	SRt^{3-body}_{SF}
MC exp. SM events	7.27 ± 1.40	4.85 ± 1.11
MC exp. ttbar events	4.01 ± 1.13	1.83 ± 0.75
MC exp. Wt events	$0.44^{+0.54}_{-0.44}$	0.54 ± 0.19
MC exp. Zjets events	0.00 ± 0.00	$0.01^{+0.03}_{-0.01}$
MC exp. VV events	0.18 ± 0.07	0.36 ± 0.11
MC exp. VVV events	0.03 ± 0.01	0.02 ± 0.00
MC exp. ttZ events	2.17 ± 0.21	1.59 ± 0.26
MC exp. ttW events	0.31 ± 0.05	0.21 ± 0.03
MC exp. other events	0.14 ± 0.03	0.11 ± 0.02
MC exp. DDFakes events	0.00 ± 0.00	0.17 ± 0.00
$\tilde{t}_1\tilde{t}_1, m(\tilde{t}_1, \tilde{\chi}^0_1) = (475, 385)$ GeV	2.09 ± 0.29	1.38 +/- 0.30
$\tilde{t}_1\tilde{t}_1, m(\tilde{t}_1, \tilde{\chi}^0_1) = (475, 355)$ GeV	8.20 ± 0.80	4.71 +/- 0.54
$\tilde{t}_1\tilde{t}_1, m(\tilde{t}_1, \tilde{\chi}^0_1) = (475, 325)$ GeV	9.69 ± 0.65	8.61 +/- 0.76

Table 5.2: MC expected events yields in the signal region SR_t for an integrated luminosity of 138.95 fb^{-1}. The main background processes contributing to the analysis are shown together with the expected event yields from the benchmark signal samples.

Table 5.3 summarises the final signal region selections targeting the $\Delta m \sim m_W$ and the $\Delta m \sim m_t$ regions after performing our optimization scan. Some $N-1$ plots for SR_W are shown in Figure 5.13 and for SR_t in Figure 5.14.

Signal Region Selections		
	SR_W	SR_t
$b-$jet multiplicity	exactly 0	> 0
$\Delta\phi_\beta^R$	> 2.3	
$E_{\mathrm{T}}^{\mathrm{miss}}$ significance	> 12	
$1/\gamma_{R+1}$	> 0.7	
$R_{p_{\mathrm{T}}}$	> 0.78	> 0.70
M_Δ^R (GeV)	> 105	> 120

Table 5.3: Definition of the signal region selections, SR_W and SR_t targeting respectively the $\Delta m \sim m_W$ and $\Delta m \sim m_t$ regions.

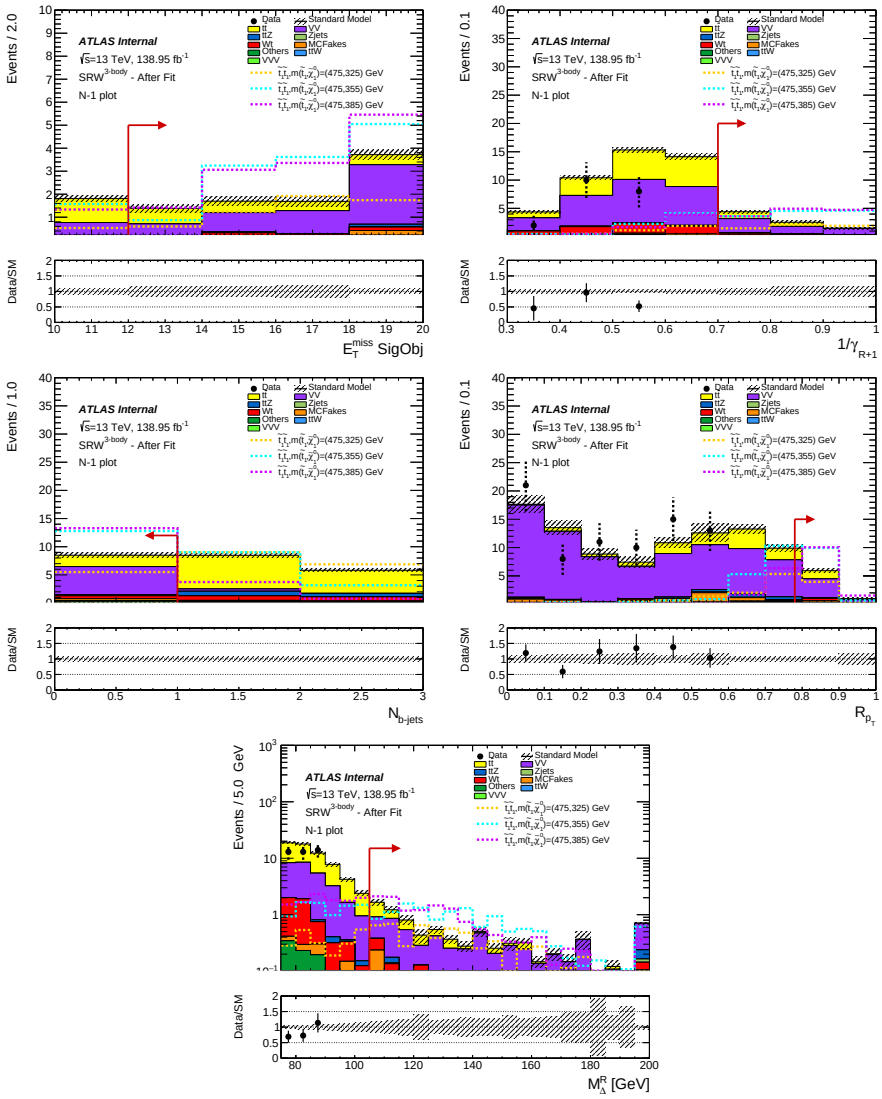

Figure 5.13: $N-1$ distributions in SR_W for $E_{\mathrm{T}}^{\mathrm{miss}}$ significance (upper-left), $1/\gamma_{R+1}$ (upper-right), number of b-tagged jets (lower-left), and $R_{p_{\mathrm{T}}}$ (lower-right). The data passing the criteria on the variable plotted shown is blinded.

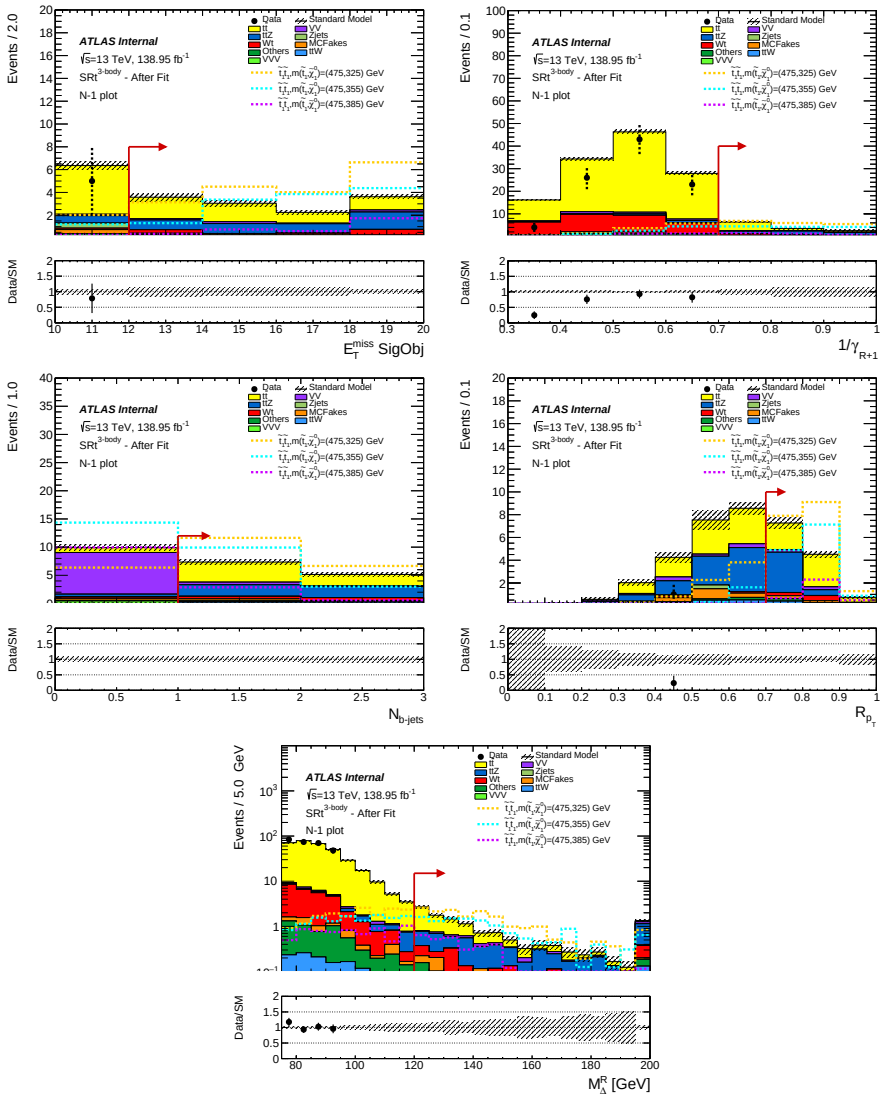

Figure 5.14: $N-1$ distributions in SR_t for $E_{\mathrm{T}}^{\mathrm{miss}}$ significance (upper-left), $1/\gamma_{R+1}$ (upper-right), number of b-tagged jets (lower-left), and $R_{p_{\mathrm{T}}}$ (lower-right). The data passing the criteria on the variable plotted shown is blinded.

Expected Sensitivity

In Figure 5.15 is the expected number of events for each signal point in the $(m_{\tilde{t}}, m_{\tilde{\chi}_1^0})$ grid in each signal region. In Figure 5.16 is the expected sensitivity across the $(m_{\tilde{t}}, m_{\tilde{\chi}_1^0})$ signal grid using 20% uncertainty on the full background computed for each signal region, SR_W and SR_t. Also shown is a combined exclusion, computed by adding the SR_W and SR_t exclusions in quadrature for each point.

Comparing Figure 5.16 with Figure 4.8 you can see we expect to push the contour up quite a bit as compared to the previous round, to a mass of around $550 - 600$ GeV near the $\Delta m \sim m_t$ as well as for the $\Delta m \sim m_W$ mass splitting.

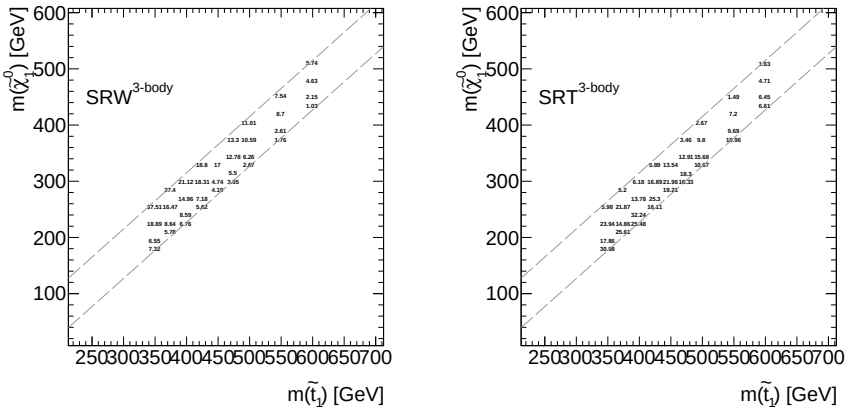

Figure 5.15: Signal yields in SR_W (top-left) and SR_t (top-right) for each point in the grid in the $(m_{\tilde{t}}, m_{\tilde{\chi}_1^0})$ plane.

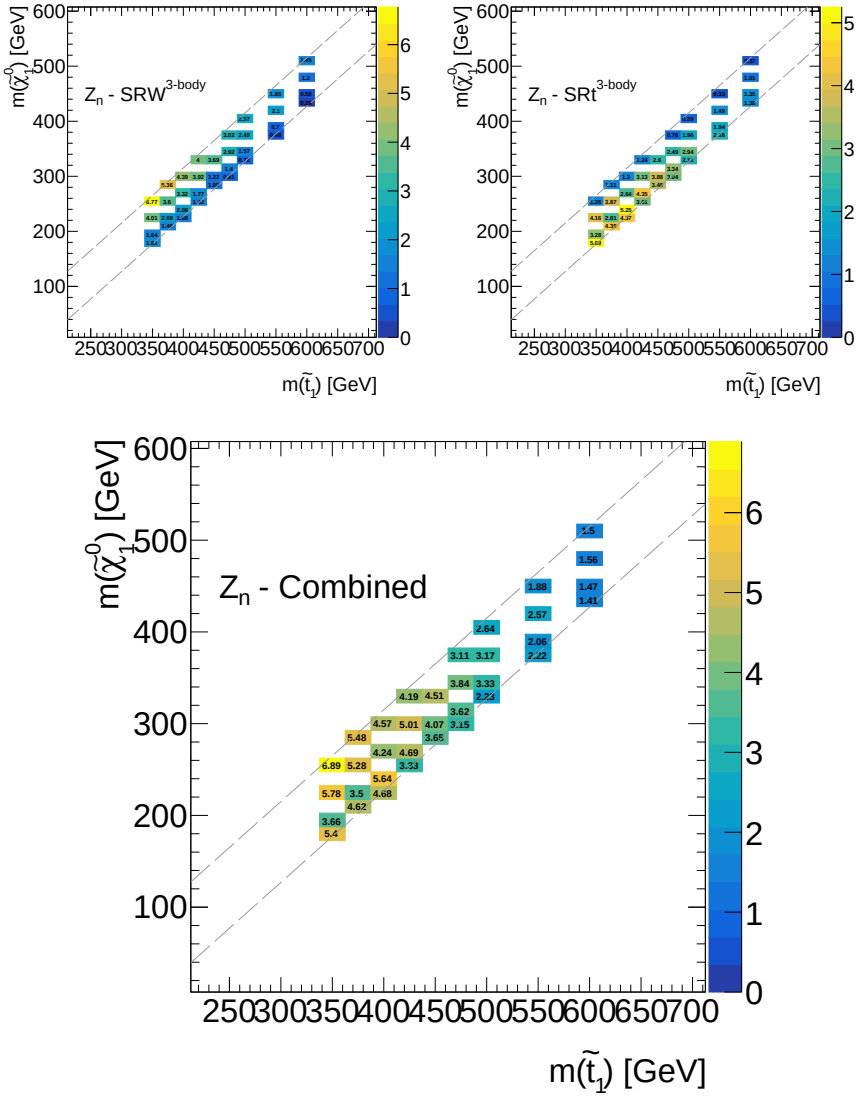

Figure 5.16: The Z_n values, estimated with a 20% of uncertainty on the full background, for SR_W (middle-left) and SR_t (middle-right) for each point in the grid in the $(m_{\tilde{t}}, m_{\tilde{\chi}_1^0})$ plane. The combined exclusion is shown on the bottom, computed by adding SRW and SRt exclusions in quadrature.

5.4 Background Estimation

The methods used for estimating the Standard Model background contamination in the signal regions will now be outlined in this section. Looking at Tables 5.1 and 5.2, the main backgrounds in the signal regions are $t\bar{t}$ and diboson processes. These are the overwhelmingly dominant processes in our signal regions and they will be estimated using control regions. Control and validation regions are defined for each of these processes to provide a normalization correction for their MC prediction in the signal regions. All other SM processes are estimated directly from MC simulation. However, as you can see in Tables 5.1 and 5.2, these processes are a very minor contribution in the signal regions.

The definitions for the control and validation regions are based around the signal region definition. The control regions are mainly defined by inverting the cut on $\Delta\phi_{\beta}^{R}$ while maintaining a similar selection as the signal regions. Then a scan over the variables was performed to ensure a good selection in the different control regions while maintaining enough statistics. The validation regions are in the same $\Delta\phi_{\beta}^{R}$ phase-space as the signal regions with orthogonality maintained with selections on other variables. Both $t\bar{t}$ validation regions are orthogonal through a combination of cuts on the number of b-tagged jets and M_{Δ}^{R}, while the VV validation region remains

orthogonal with a cut at $0.45 < 1/\gamma_{R+1} < 0.7$. A summary of all of the cuts, with the cuts ensuring orthogonality highlighted in red, is shown in Table 5.6.

Selection	$\mathrm{CR}_{t\bar{t}}{}^{3-body}$	$\mathrm{CR}_{VV}{}^{3-body}$	$\mathrm{VR1}_{t\bar{t}}{}^{3-body}$	$\mathrm{VR2}_{t\bar{t}}{}^{3-body}$	$\mathrm{VR}_{VV}{}^{3-body}$
Leptons	DFOS	–	DFOS	DFOS	–
$m_{\ell\ell}$	–	$\lvert m_{\ell\ell} - 91.2\rvert > 20$ for SF events	–	–	$\lvert m_{\ell\ell} - 91.2\rvert > 20$ for SF events
Lepton p_{T} (lead, sub-lead) [GeV]	$>(25, 20)$	$>(25, 20)$	$>(25, 20)$	$>(25, 20)$	$>(25, 20)$
$b-$tag multiplicity	≥ 2	$== 0$	$== 0$	≥ 1	$== 0$
Signal jet (non-b) multiplcity	–	–	–	–	–
M_{Δ}^{R} [GeV]	> 80	> 100	$[80, 105]$	$[80, 120]$	> 100
$R_{p_{\mathrm{T}}}$	$--$	> 0.3	> 0.7	> 0.7	> 0.7
$1/\gamma_{R+1}$	> 0.7	> 0.7	> 0.7	> 0.7	$[0.45, 0.7]$
$E_{\mathrm{T}}^{\mathrm{miss}}$ significance	> 10	> 10	> 12	> 12	> 12
$\Delta\phi_{\beta}^{R}$	< 2.3			> 2.3	

Table 5.4: Definitions of the control and validation regions for the $t\bar{t}$ and VV backgrounds. Included at the level of preselection (but not listed here) is the requirement that the dilepton mass, $m_{\ell\ell}$, be greater than 20 GeV for all regions.

The estimation of the contiribution of non-prompt or misidentified leptons to the various regions in this analysis is done using the data-driven matrix method. This estimation technique and its implementation is harmonized across all of the dilepton stop analyses and is fully described in [79].

There are a few $t\bar{t} + Z$ events in the SR_t region, as well. This contribution is not necessarily significant, but it is significant in the 2-body analysis. The analyses were harmonized and therefore the control and validation regions were able to be borrowed from the 2-body analysis. These regions require 3 and 4 lepton events, respectively. In the $t\bar{t} + Z \rightarrow 3\ell$ process, the Z-boson decays to two leptons. One top quark decays hadronically while the other decays to a lepton, at least one jet and neutrinos. These two regions use

a couple of variables not otherwise used in the 3-body analysis, $E_{\mathrm{T,corr}}^{\mathrm{miss}}$ and m_{T2}^{4lep}. $E_{\mathrm{T,corr}}^{\mathrm{miss}}$ is defined as the vectorial sum of the momentum of the same-flavor opposite sign lepton pair to the $\mathbf{p}_{\mathrm{T}}^{\mathrm{miss}}$ vector. For $\mathrm{VR}_{t\bar{t}+Z}{}^{3-body}$, events with four leptons is required with at least two of the four leptons being same-flavor and opposite sign as well as compatible with the Z-decay. The $E_{\mathrm{T,corr}}^{\mathrm{miss}}$ and the p_T of the other two leptons are used to calculate m_{T2}^{4lep}. A list of the selection criteria for these regions is outlined in Table 5.5.

Selection	$CR_{t\bar{t}+Z}$	$VR_{t\bar{t}+Z}$
$m_{\ell\ell}$ [GeV] (SF OS pair)	71.2 – 111.2	–
n_{lep}	== 3	== 4
Lepton p_T [GeV]	–	$> (25, 20, 20, 20)$
$E_{\mathrm{T,corr}}^{\mathrm{miss}}$ [GeV]	> 140	–
m_{T2}^{4lep} [GeV]	–	> 110
Jets	$n_{\text{b-jet}} > 1$ and $n_{\text{jet}} > 2$	$n_{\text{b-jet}} > 0$

Table 5.5: Definitions of the control and validation regions for the $t\bar{t} + Z$ background. Included at the level of preselection (but not listed here) is the requirement that the dilepton mass, $m_{\ell\ell}$, be greater than 20 GeV for all regions.

Top-Quark Pair Production

As already mentioned, the top control region is orthogonal to the signal region due to the cut on $\Delta\phi_\beta^R$. We also ask for two or more b-jets, M_Δ^R above 80 GeV, $1/\gamma_{R+1}$ above 0.7, and $E_{\mathrm{T}}^{\mathrm{miss}}$ signficance greater than 10.

Signal contamination in the $\mathrm{CR}_{t\bar{t}}{}^{3-body}$, $\mathrm{VR}_{t\bar{t}}{}^{3-body}$, and $\mathrm{VR}_{t\bar{t}}{}^{3-body}$ regions are shown in Figures 5.17 and 5.18.

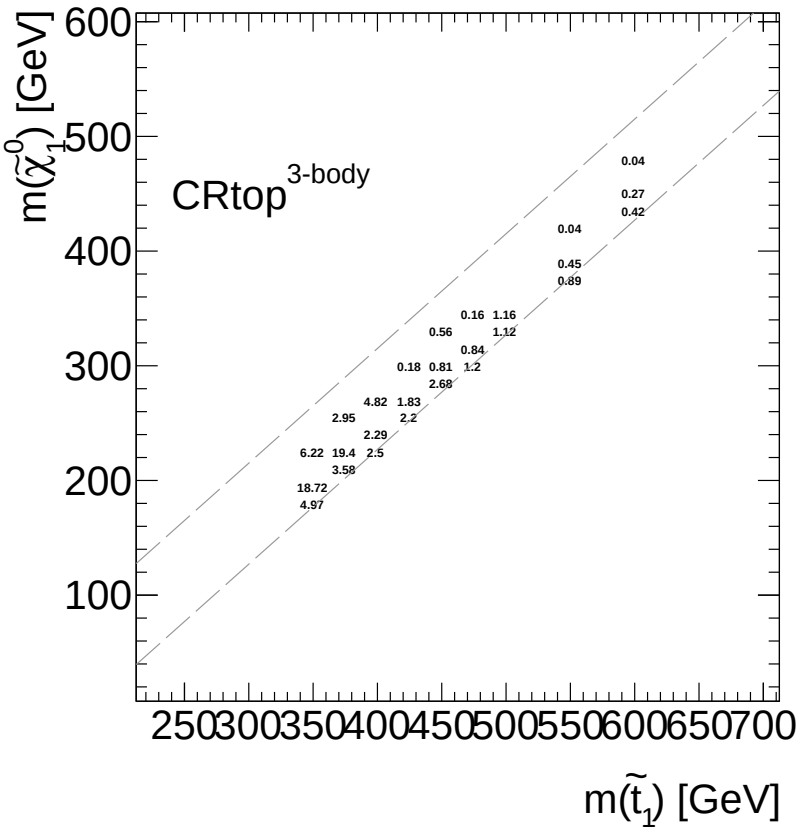

Figure 5.17: Percentage signals contamination in the $\mathrm{CR}_{t\bar{t}}{}^{3-body}$.

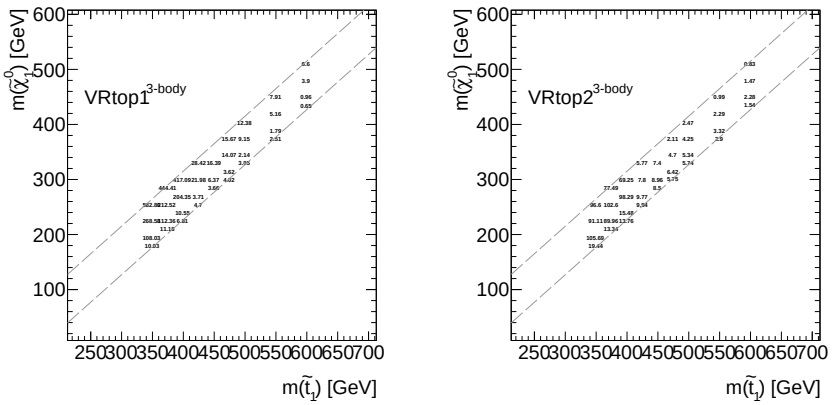

Figure 5.18: Percentage signals contamination in the $\mathrm{VR}_{t\bar{t}}{}^{3-body}$.

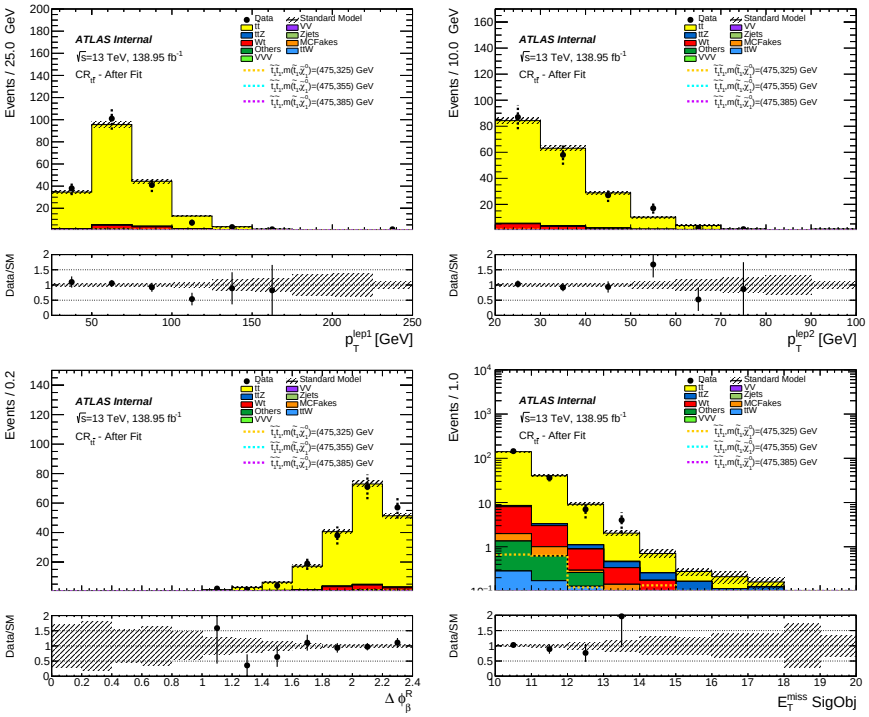

Figure 5.19: Distributions of the leading (upper left) and sub-leading (upper right) lepton p_{T}, $\Delta\phi_{\beta}^{R}$ (lower left), and $\cos\theta_b$ (lower right) in the $t\bar{t}$ control region. The error on the SM processeses are statistical uncertainties. Scale factors (Tab. 5.7) are applied to the corresponding processes.

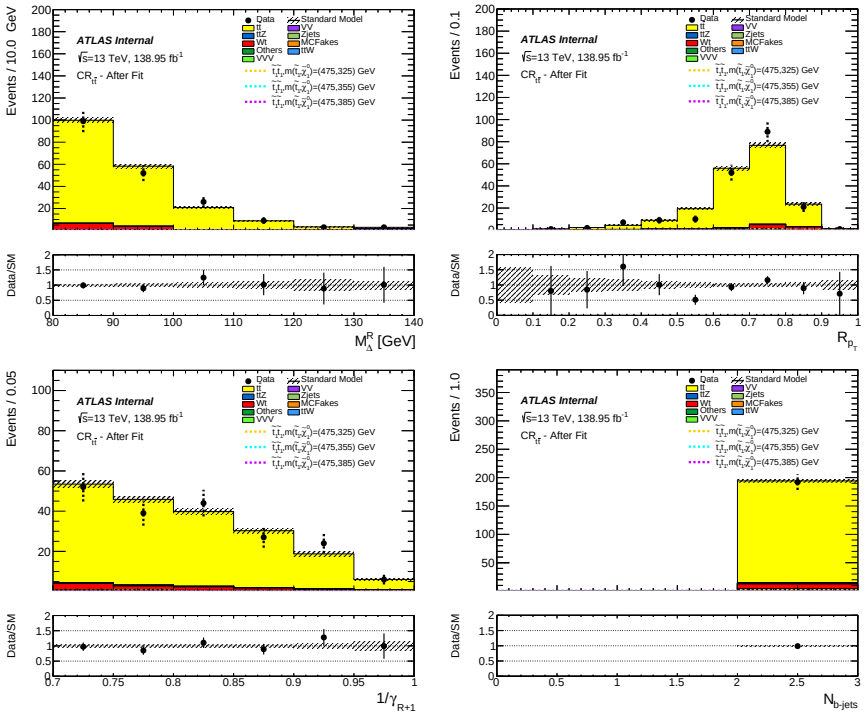

Figure 5.20: Distributions of M_{Δ}^{R} (upper left), $R_{p_{\mathrm{T}}}$ (upper right), $1/\gamma_{R+1}$ (lower left), and $b-$jet multiplicity (lower right) in the $t\bar{t}$ control region. The error on the SM processes are statistical uncertainties. Scale factors (Tab. 5.7) are applied to the corresponding processes.

Two top validation regions were defined, one with a b-veto and the other requiring at least one b-tagged jet. The top validation regions are closer to the signal region in that they are in the same phase space in $\Delta\phi_\beta^R$ while still being orthogonal with the cut on MDR. For $\mathrm{VR1}_{t\bar{t}}^{3-body}$, M_Δ^R must be in the range [80,105] while for $\mathrm{VR2}_{t\bar{t}}^{3-body}$ M_Δ^R is required to be within [80,120]. In both top validation regions, it is required that R_{p_T} and $1/\gamma_{R+1}$ be above 0.7 GeV as well as $E_\mathrm{T}^\mathrm{miss}$ significance greater than 12, putting us closer to the signal regions.

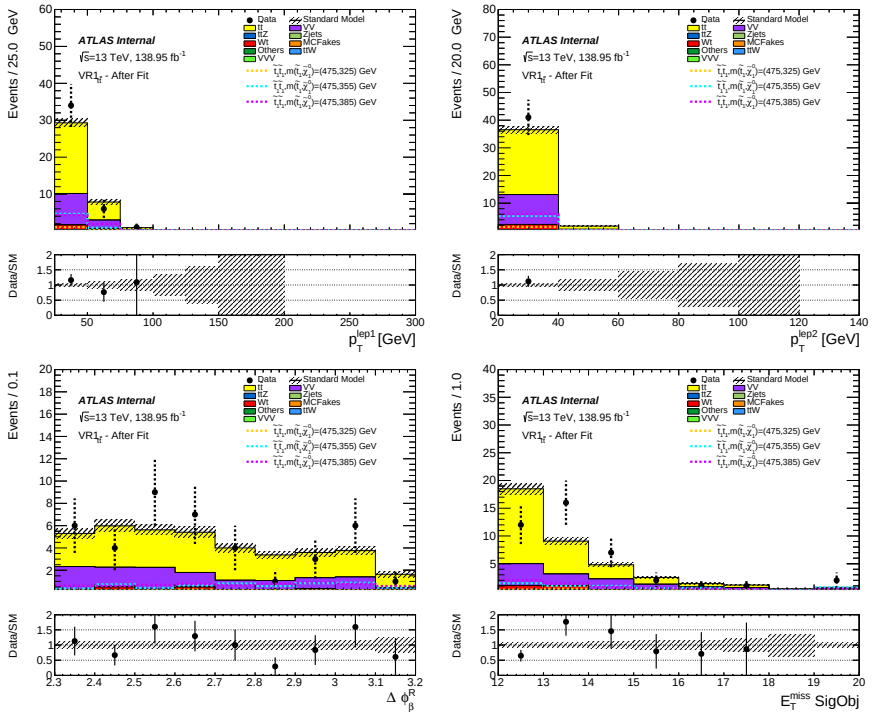

Figure 5.21: Distributions of the leading (upper left) and sub-leading (upper right) lepton p_T, $\Delta\phi_\beta^R$ (lower left), and $\cos\theta_b$ (lower right) in the first $t\bar{t}$ validation region. The error on the SM processeses are statistical uncertainties. Scale factors (Tab. 5.7) are applied to the corresponding processes.

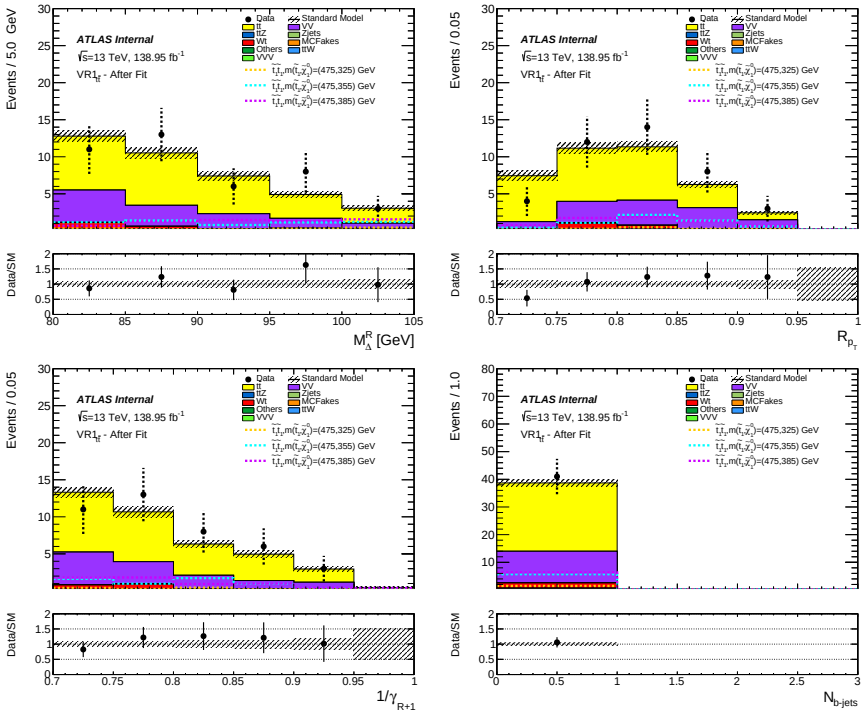

Figure 5.22: Distributions of M_{Δ}^{R} (upper left), $R_{p_{\mathrm{T}}}$ (upper right), $1/\gamma_{R+1}$ (lower left), and $b-$jet multiplicity (lower right) in the first $t\bar{t}$ validation region. The error on the SM processes are statistical uncertainties. Scale factors (Tab. 5.7) are applied to the corresponding processes.

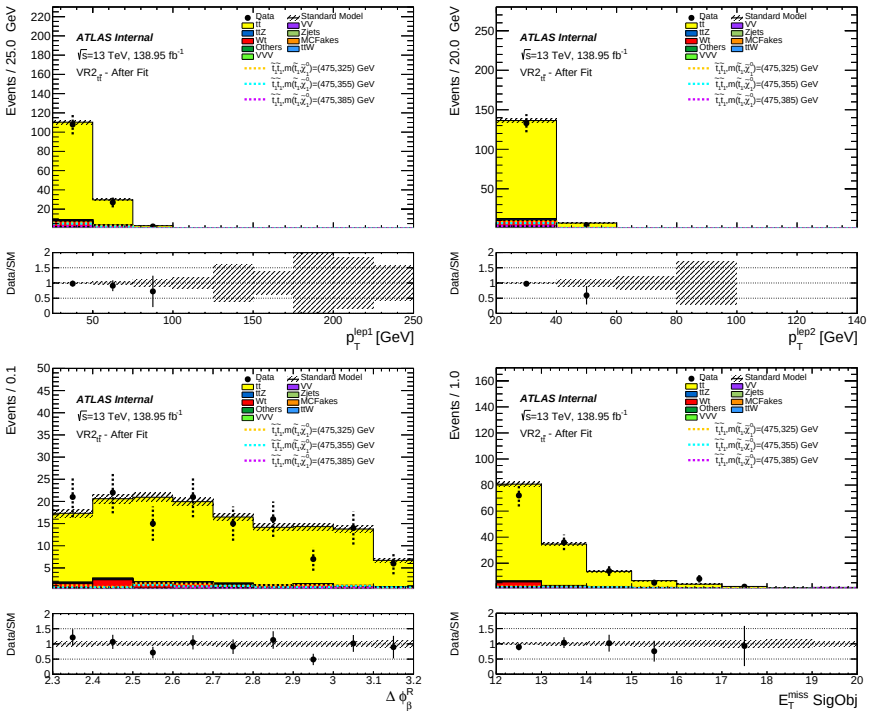

Figure 5.23: Distributions of the leading (upper left) and sub-leading (upper right) lepton p_{T} $\Delta\phi_{\beta}^{R}$ (lower left), and $\cos\theta_b$ (lower right) in the second $t\bar{t}$ validation region. The error on the SM processeses are statistical uncertainties. Scale factors (Tab. 5.7) are applied to the corresponding processes.

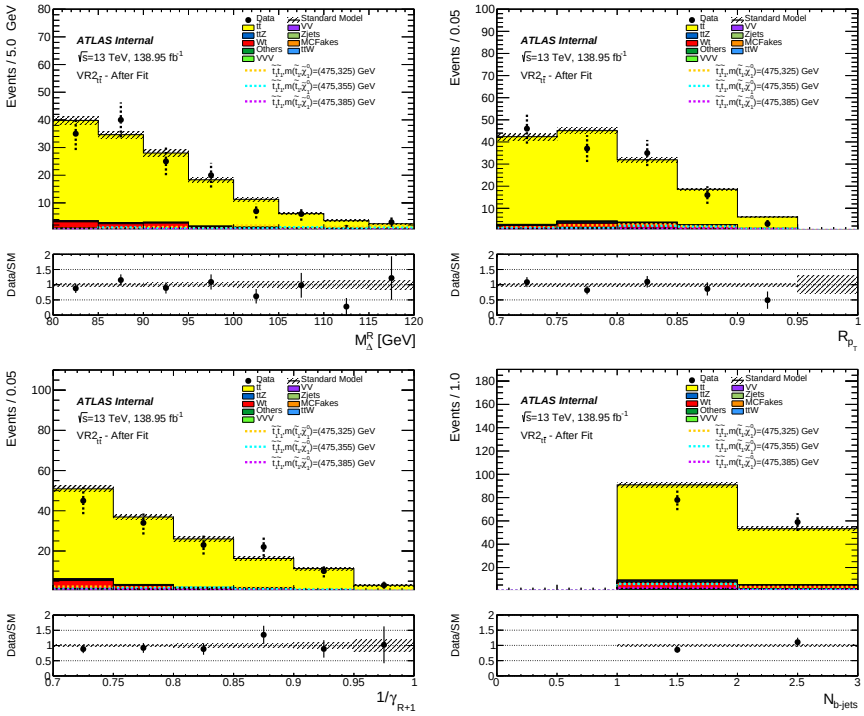

Figure 5.24: Distributions of M_{Δ}^{R} (upper left), $R_{p_{\mathrm{T}}}$ (upper right), $1/\gamma_{R+1}$ (lower left), and $b-$jet multiplicity (lower right) in the second $t\bar{t}$ validation region. The error on the SM processes are statistical uncertainties. Scale factors (Tab. 5.7) are applied to the corresponding processes.

Diboson Production

The diboson control region, like the other control region, maintains the same orthogonality with the signal region with a cut at $\Delta\phi_{\beta}^{R} < 2.3$. The diboson validation region is similar to the signal region with $\Delta\phi_{\beta}^{R} > 2.3$, but maintains orthogonality by selecting events with $1/\gamma_{R+1}$ between $[0.45, 0.7]$, while the diboson control region requires $1/\gamma_{R+1} > 0.7$ like the signal region. The diboson control region requires $R_{p_{\mathrm{T}}} > 0.3$ and $M_{\Delta}^{R} > 100$ while the validation region has $R_{p_{\mathrm{T}}} > 0.7$ and $M_{\Delta}^{R} > 100$. The diboson control region is orthogonal to the top control region with the requirement of no b-tagged jets. The diboson validation region requires zero reconstructed b-jets as well, but the orthogonality between the validation region and the first top validation region is maintained by their selection on $1/\gamma_{R+1}$. A selection of $E_{\mathrm{T}}^{\mathrm{miss}}$ significance above 10 is also required for the VV control region and above 12 for the VV validation region.

Signal contamination in the $\mathrm{CR}_{VV}{}^{3-body}$ and $\mathrm{VR}_{VV}{}^{3-body}$ regions are shown in Figure 5.25.

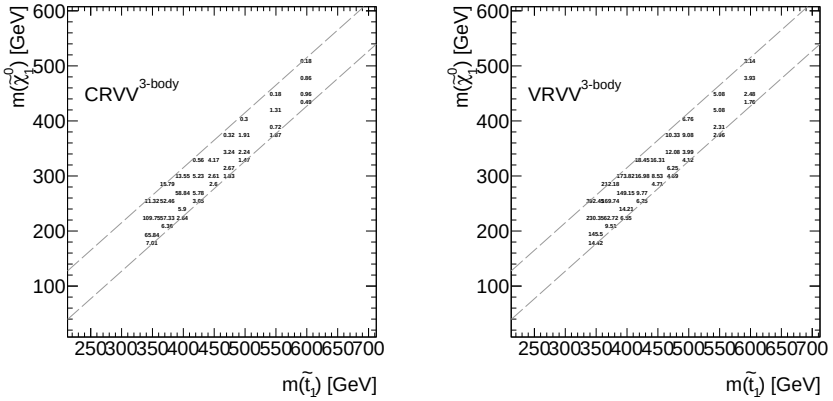

Figure 5.25: Percentage signals contamination in $\mathrm{CR}_{VV}{}^{3-body}$ and $\mathrm{VR}_{VV}{}^{3-body}$.

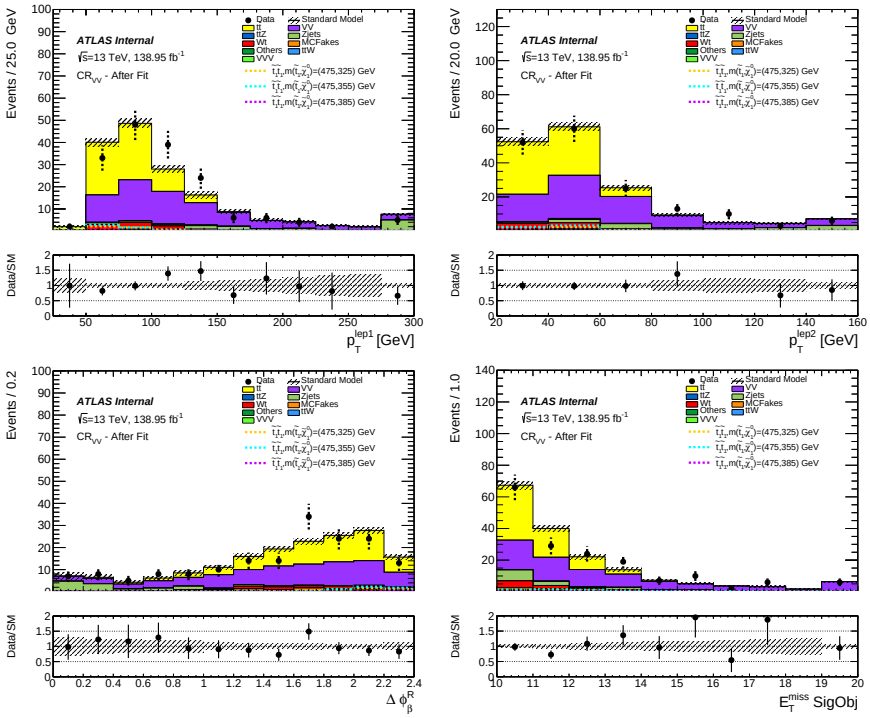

Figure 5.26: Distributions of the leading (upper left) and sub-leading (upper right) lepton p_{T} $\Delta\phi_{\beta}^{R}$ (lower left), and $\cos\theta_b$ (lower right) in the VV control region. The error on the SM processeses are statistical uncertainties. Scale factors (Tab. 5.7) are applied to the corresponding processes.

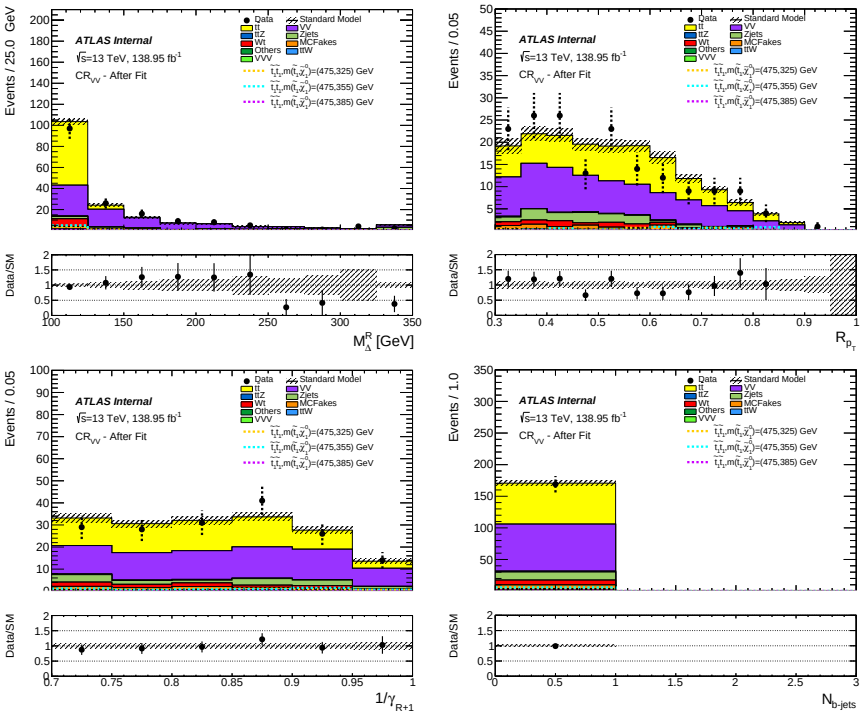

Figure 5.27: Distributions of M_{Δ}^{R} (upper left), $R_{p_{\mathrm{T}}}$ (upper right), $1/\gamma_{R+1}$ (lower left), and $b-$jet multiplicity (lower right) in the VV control region. The error on the SM processes are statistical uncertainties. Scale factors (Tab. 5.7) are applied to the corresponding processes.

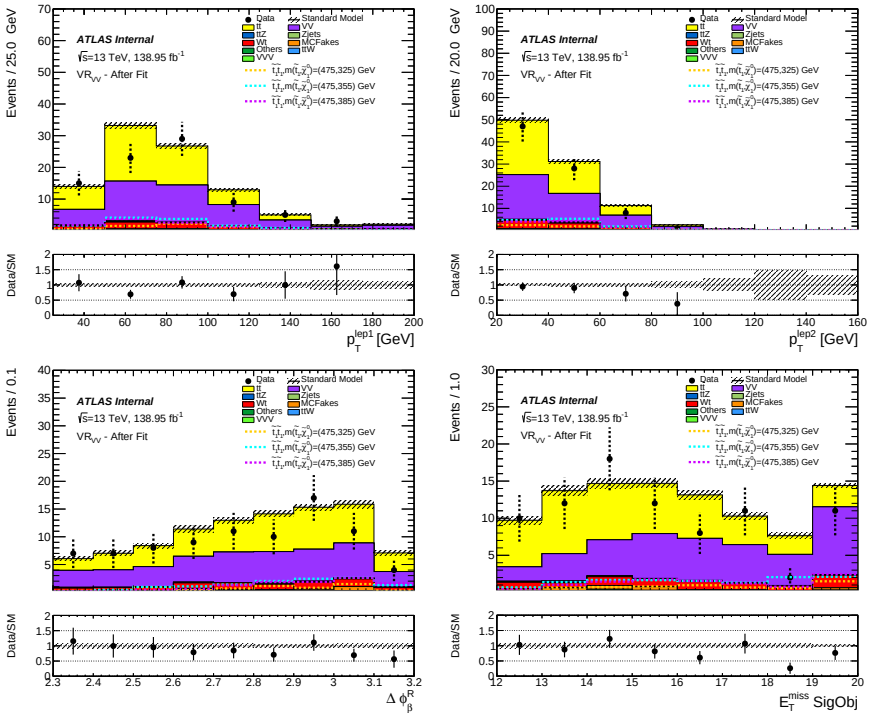

Figure 5.28: Distributions of the leading (upper left) and sub-leading (upper right) lepton p_{T} $\Delta\phi_{\beta}^{R}$ (lower left), and $\cos\theta_b$ (lower right) in the VV validation region. The error on the SM processeses are statistical uncertainties. Scale factors (Tab. 5.7) are applied to the corresponding processes.

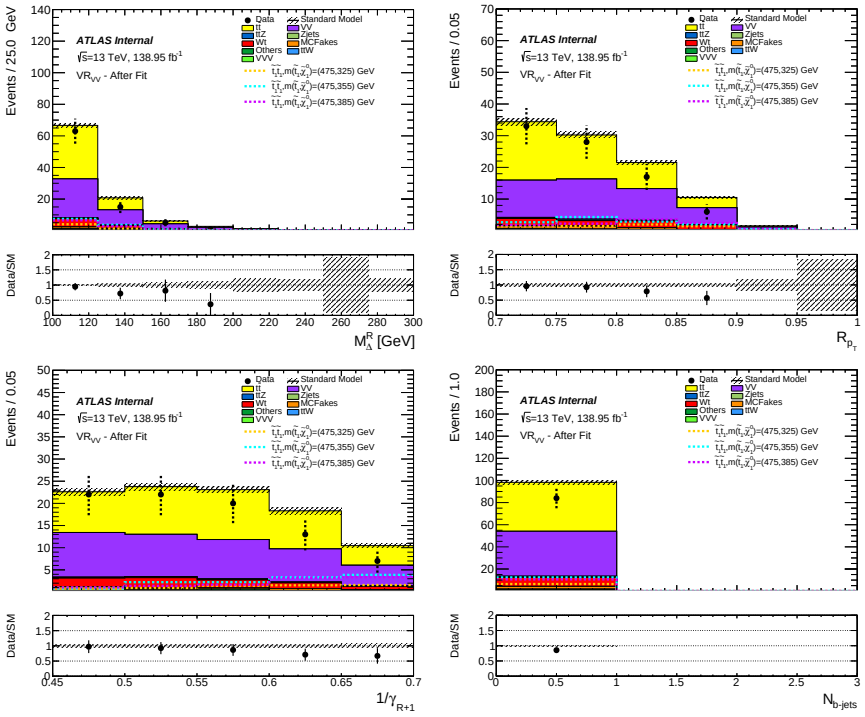

Figure 5.29: Distributions of M_{Δ}^{R} (upper left), $R_{p_{\mathrm{T}}}$ (upper right), $1/\gamma_{R+1}$ (lower left), and $b-$jet multiplicity (lower right) in the VV validation region. The error on the SM processes are statistical uncertainties. Scale factors (Tab. 5.7) are applied to the corresponding processes.

	SRW^{3-body}	SRt^{3-body}	$CR_{t\bar{t}}^{3-body}$	CR_{VV}^{3-body}	$VR1_{t\bar{t}}^{3-body}$	$VR2_{t\bar{t}}^{3-body}$	VR_{VV}^{3-body}
Lepton flavour	–	–	DF	–	DF	DF	–
$n_{b\text{-jets}}$	$== 0$	> 0	≥ 2	$== 0$	$== 0$	≥ 1	$== 0$
$E_{\mathrm{T}}^{\mathrm{miss}}$ significance	>12		>10			>12	
$R_{p_{\mathrm{T}}}$	> 0.78	> 0.7	–	> 0.3		> 0.7	
$\Delta\phi_{\beta}^{R}$	> 2.3		< 2.3			> 2.3	
M_{Δ}^{R} [GeV]	> 105	> 120	> 80	> 100	$[80, 105]$	$[80, 120]$	> 100
$1/\gamma_{R+1}$	> 0.7		> 0.7		> 0.7		$[0.45, 0.7]$

Table 5.6: Definitions of all regions with the cuts guaranteeing the orthogonality highlighted in red.

The expected event yields in the control and validation regions, as defined in Table 5.4, are presented in Table 5.8. The scale factors

for the $t\bar{t}$, $t\bar{t}+Z$, and VV processes are listed in Table 5.7.

Setup	Normalization Factor
$t\bar{t}$	0.96 ± 0.096
VV	0.93 ± 0.277
$t\bar{t}+Z$	1.08 ± 0.111

Table 5.7: Scale factors for $t\bar{t}$, $t\bar{t}+Z$, and VV background processes. Errors are statistical only.

	$CR_{t\bar{t}}^{3-body}$	CR_{VV}^{3-body}	$CR_{t\bar{t}+Z}$	$VR1_{t\bar{t}}^{3-body}$	$VR2_{t\bar{t}}^{3-body}$	VR_{VV}^{3-body}
Observed events	192	169	247	41	137	84
Fitted bkg events	191.84 ± 13.84	169.07 ± 12.96	246.91 ± 15.70	38.31 ± 5.93	141.89 ± 24.99	96.89 ± 14.93
Fitted ttbar events	179.99 ± 13.92	64.71 ± 14.52	0.00 ± 0.00	24.71 ± 4.55	130.22 ± 24.42	44.20 ± 11.40
Fitted Wt events	9.03 ± 1.42	7.61 ± 2.27	0.00 ± 0.00	1.88 ± 0.63	8.15 ± 2.05	8.13 ± 1.14
Fitted Zjets events	0.00 ± 0.00	12.79 ± 4.64	0.00 ± 0.00	0.00 ± 0.00	0.00 ± 0.00	$0.04^{+0.05}_{-0.04}$
Fitted VV events	0.06 ± 0.03	74.43 ± 21.28	15.54 ± 5.70	11.40 ± 4.03	0.93 ± 0.43	40.67 ± 13.75
Fitted VVV events	0.01 ± 0.00	2.44 ± 0.11	0.09 ± 0.01	0.16 ± 0.02	0.02 ± 0.01	0.59 ± 0.05
Fitted ttZ events	1.60 ± 0.31	1.38 ± 0.30	174.47 ± 17.53	$0.07^{+0.12}_{-0.07}$	1.63 ± 0.69	0.99 ± 0.41
Fitted ttW events	0.73 ± 0.08	0.49 ± 0.08	3.98 ± 0.34	0.05 ± 0.05	0.62 ± 0.10	0.32 ± 0.05
Fitted other events	0.42 ± 0.03	0.26 ± 0.04	36.39 ± 2.40	0.02 ± 0.01	0.32 ± 0.03	0.15 ± 0.02
Fitted DDFakes events	0.00 ± 0.00	4.97 ± 0.00	16.45 ± 0.00	0.00 ± 0.00	0.00 ± 0.00	1.80 ± 0.00
MC exp. SM events	198.57 ± 10.23	177.50 ± 16.67	235.17 ± 5.68	40.10 ± 5.74	146.62 ± 26.45	101.64 ± 13.44
MC exp. ttbar events	186.85 ± 9.76	67.34 ± 13.03	0.00 ± 0.00	25.65 ± 4.50	135.02 ± 25.70	45.90 ± 11.41
MC exp. Wt events	9.01 ± 1.43	7.62 ± 2.28	0.00 ± 0.00	1.87 ± 0.63	8.14 ± 2.06	8.12 ± 1.15
MC exp. Zjets events	0.00 ± 0.00	12.83 ± 4.68	0.00 ± 0.00	0.00 ± 0.00	0.00 ± 0.00	$0.04^{+0.05}_{-0.04}$
MC exp. VV events	0.07 ± 0.02	80.27 ± 3.46	16.70 ± 2.62	12.27 ± 1.90	0.99 ± 0.33	43.79 ± 5.42
MC exp. VVV events	0.01 ± 0.00	2.44 ± 0.11	0.09 ± 0.01	0.16 ± 0.02	0.02 ± 0.01	0.59 ± 0.05
MC exp. ttZ events	1.48 ± 0.24	1.28 ± 0.22	161.63 ± 2.95	$0.07^{+0.11}_{-0.07}$	1.52 ± 0.60	0.92 ± 0.36
MC exp. ttW events	0.73 ± 0.08	0.49 ± 0.08	3.97 ± 0.35	0.05 ± 0.05	0.62 ± 0.10	0.32 ± 0.05
MC exp. other events	0.42 ± 0.03	0.26 ± 0.04	36.33 ± 2.42	0.02 ± 0.01	0.32 ± 0.03	0.15 ± 0.02
MC exp. DDFakes events	0.00 ± 0.00	4.97 ± 0.00	16.45 ± 0.00	0.00 ± 0.00	0.00 ± 0.00	1.80 ± 0.00

Table 5.8: Yields for an integrated luminosity of $139\,\text{fb}^{-1}$ in the control and validation regions for the $t\bar{t}$, $t\bar{t}+Z$, and VV Standard Model processes, or the main background processes, contributing to the analysis. Presented in the lower portion are the before-fit expected yields determined solely from the MC estimates of these processes. The upper-portion of the table presents the after-fit yields where the $t\bar{t}$, $t\bar{t}+Z$, and VV processes' overall normalizations have been determined by the background-only fit in their respective control regions. The errors shown are statistical and systematics.

5.5 Results

The different sources of systematic uncertainty in the SM estimates in the signal regions are summarized in Table 5.9. These different sources were described in Section 4.4, while more detailed breakdowns are included in Appendix C, including the fit parameters in Figure C.1 and the reduced correlation matrix in Figure C.2.

Signal Region	SR_W^{DF}	SR_W^{SF}	SR_t^{DF}	SR_t^{SF}
Total background systematic	±0.94 [18.48%]	±0.96 [25.71%]	±1.36 [18.24%]	±1.09 [21.70%]
VV Theoretical Uncertainties	±0.41 [8.0%]	±0.39 [10.3%]	±0.05 [0.60%]	±0.07 [1.5%]
$t\bar{t}$ Theoretical Uncertainties	±0.41 [8.2%]	±0.25 [6.6%]	±1.02 [13.6%]	±0.43 [8.6%]
$t\bar{t}$ $+Z$ Theoretical Uncertainties	±0.01 [0.11%]	±0.01 [0.18%]	±0.09 [1.2%]	±0.10 [2.0%]
$t\bar{t}$-Wt interference	±0.02 [0.36%]	±0.02 [0.51%]	±0.01 [0.19%]	±0.05 [1.1%]
MC Statistical Statistical	±0.30 [5.8%]	±0.28 [7.4%]	±0.42 [5.6%]	±0.33 [6.7%]
VV Normalization	±0.76 [14.9%]	±0.75 [20.0%]	±0.05 [0.68%]	±0.10 [2.0%]
$t\bar{t}$ Normalization	±0.12 [2.3%]	±0.07 [1.9%]	±0.36 [4.9%]	±0.17 [3.3%]
$t\bar{t}$ $+Z$ Normalization	±0.01 [0.22%]	±0.01 [0.28%]	±0.31 [4.1%]	±0.23 [4.5%]
Jet Energy Scale	±0.28 [5.5%]	±0.14 [3.7%]	±0.28 [3.8%]	±0.21 [4.1%]
Jet Energy Resolution	±0.12 [2.3%]	±0.42 [11.2%]	±0.67 [9.0%]	±0.89 [17.8%]
MET Mismodelling	±0.06 [1.1%]	±0.08 [2.2%]	±0.22 [3.0%]	±0.09 [1.8%]
Flavor Tagging	±0.16 [3.1%]	±0.11 [2.9%]	±0.12 [1.6%]	±0.05 [0.93%]
Pileup Reweighting and JVT	±0.04 [0.84%]	±0.02 [0.55%]	±0.03 [0.37%]	±0.02 [0.32%]
Lepton Modelling	±0.07 [1.3%]	±0.07 [2.0%]	±0.07 [1.00%]	±0.12 [2.5%]
Fake and Non-Prompt Leptons	±0.09 [1.7%]	±0.00 [0.00%]	±0.00 [0.00%]	±0.23 [4.6%]

Table 5.9: A summary of the different sources of systematic uncertainty in the final SM background estimates.

The expected yields in the different signal regions are presented in Table 5.10. Here you can see the expected number of events in each of the different background processes in the lower half, as well as results after applying the scale factor in the upper half. The top line shows the number of events that were observed in the data. No significant excesses beyond the expected SM contributions were observed in the signal regions, however, our results can be

translated into upper limits on contributions from physics beyond the SM.

	SRW_{DF}^{3-body}	SRW_{SF}^{3-body}	SRt_{DF}^{3-body}	SRt_{SF}^{3-body}
Observed events	1	5	5	5
Fitted bkg events	5.07 ± 0.94	3.74 ± 0.96	7.29 ± 1.37	4.89 ± 1.07
Fitted ttbar events	1.26 ± 0.49	0.76 ± 0.32	3.86 ± 1.07	1.76 ± 0.71
Fitted Wt events	0.30 ± 0.05	0.21 ± 0.03	$0.44^{+0.54}_{-0.44}$	0.54 ± 0.19
Fitted Zjets events	0.00 ± 0.00	0.04 ± 0.02	0.00 ± 0.00	$0.01^{+0.03}_{-0.01}$
Fitted VV events	2.50 ± 0.97	2.47 ± 0.94	0.17 ± 0.09	0.34 ± 0.14
Fitted VVV events	0.18 ± 0.01	0.13 ± 0.01	0.03 ± 0.01	0.02 ± 0.00
Fitted ttZ events	0.09 ± 0.03	0.08 ± 0.05	2.34 ± 0.32	1.72 ± 0.32
Fitted ttW events	0.01 ± 0.00	0.02 ± 0.01	0.31 ± 0.05	0.21 ± 0.03
Fitted other events	0.02 ± 0.01	0.02 ± 0.00	0.14 ± 0.03	0.11 ± 0.02
Fitted DDFakes events	0.71 ± 0.00	0.00 ± 0.00	0.00 ± 0.00	0.17 ± 0.00
MC exp. SM events	5.30 ± 0.78	3.95 ± 0.76	7.27 ± 1.40	4.85 ± 1.11
MC exp. ttbar events	1.31 ± 0.52	0.79 ± 0.35	4.01 ± 1.13	1.83 ± 0.75
MC exp. Wt events	0.30 ± 0.05	0.21 ± 0.03	$0.44^{+0.54}_{-0.44}$	0.54 ± 0.19
MC exp. Zjets events	0.00 ± 0.00	0.04 ± 0.02	0.00 ± 0.00	$0.01^{+0.03}_{-0.01}$
MC exp. VV events	2.69 ± 0.58	2.66 ± 0.59	0.18 ± 0.07	0.36 ± 0.11
MC exp. VVV events	0.18 ± 0.01	0.13 ± 0.01	0.03 ± 0.01	0.02 ± 0.00
MC exp. ttZ events	0.08 ± 0.03	0.07 ± 0.04	2.17 ± 0.21	1.59 ± 0.26
MC exp. ttW events	0.01 ± 0.00	0.02 ± 0.01	0.31 ± 0.05	0.21 ± 0.03
MC exp. other events	0.02 ± 0.01	0.02 ± 0.00	0.14 ± 0.03	0.11 ± 0.02
MC exp. DDFakes events	0.71 ± 0.00	0.00 ± 0.00	0.00 ± 0.00	0.17 ± 0.00

Table 5.10: Yields for an integrated luminosity of $139\,\text{fb}^{-1}$ in the signal regions for the main background processes contributing to the analysis.

In Figure 5.30, N-1 plots are presented for M_{Δ}^{R} and $1/\gamma_{R+1}$ in the two signal regions.

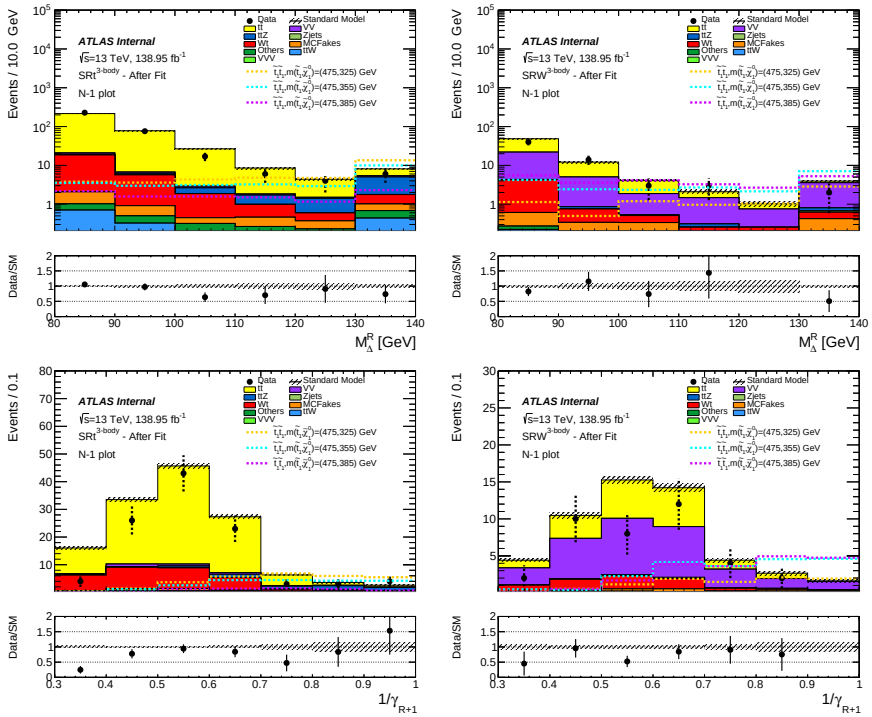

Figure 5.30: **Top:** Distributions of M_{Δ}^{R} in the SR_t signal region on the left and the SR_W signal region on the right. **Bottom:** Distributions of $1/\gamma_{R+1}$ in the SR_t signal region on the left and the SR_W signal region on the right. The requirement on the variable being plotted is removed.

Overall, good agreement is found between data and SM predictions for the four regions, with one under-fluctuation present in SRW_{DF}.

Chapter 6

Multivariate Analysis

The Multivariate Analysis relies on the training of Boosted Decision Trees (BDTs) in order to learn to discriminate between signal and background. Machine learning is an expansive subject with many different methods, used widely in the field of high-energy physics. Decision Trees are a predictive modeling technique used in machine learning. Training and boosting decision trees in order to learn how to discriminate between signal and background in collision events is a very powerful classification technique.

6.1 An Introduction to Machine Learning

Machine Learning is a field in computer science that gives computers the ability to learn and improve from experience without being explicitly programmed. It is used extensively in high-energy physics where we have massive amounts of data and a big need

for efficient and innovative analyses. Using machine learning, it is possible to build accurate models for discriminating signal from background without a priori knowledge of the properties of signal or background events. Instead of using knowledge of the kinematic differences the computer learns solely from the data and its correlations to develop its own conclusion with automated algorithms.

A Toolkit for Multivariate Analysis

The Toolkit for Multivariate Analysis (TMVA) [80] provides a ROOT-integrated environment for processing, evaluating, and applying multivariate classification and regression techniques. Classification techniques are utilized in order to classify events as either signal or background. TMVA provides a platform for many *supervised learning* techniques, including BDTs, which make use of training on events where we know the desired output. Training and testing is performed on MC simulated events listed in 4.2, in order to create a mapping function from an N-dimensional parameter space into a one-dimensional decision boundary.

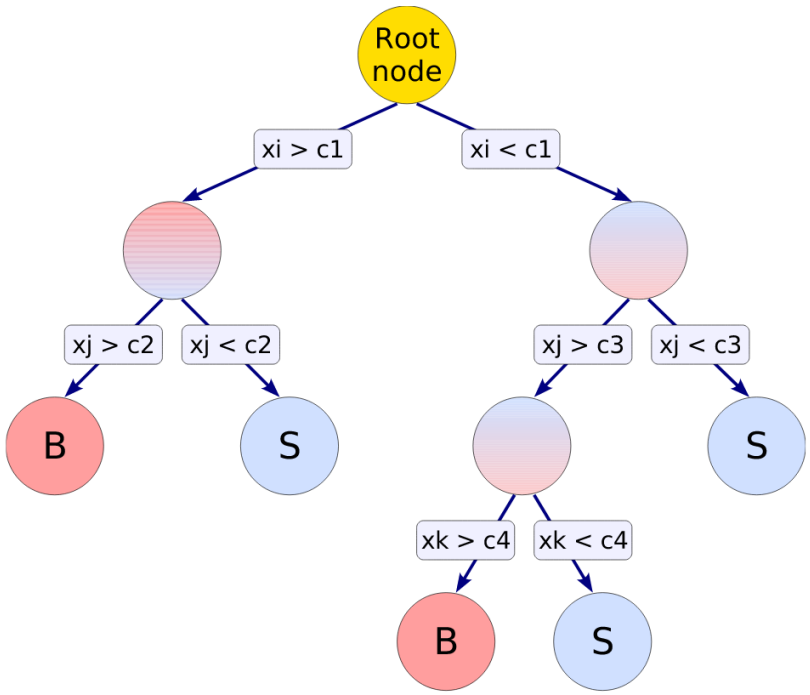

Figure 6.1: A typical Decision Tree. Starting from the root node, a series of binary splits using the discriminating variables x_i is applied to the data. Each split uses the variable that, at this node, gives the best separation between signal and background when being cut on. Therefore, each variable may be used at several notes with other variables not being used at all. The final nodes are labelled signal or background, depending on the classification of the majority of events in those nodes. [80]

6.2 Decision Trees

A decision tree is a series of binary choices culminating in a tree-like model of decisions and their possible consequences. Figure 6.1 shows a generic decision tree. The repeated left/right decisions on one variable at a time until some ”stop” criterion is fulfilled. The phase space is split up in this way into many regions that are

classified as signal or background, depending on the majority of training events that end up in the final node.

The trees are grown starting from the root node. The cut value and discriminating variable at each node are chosen such that it provides the best separation between signal and background. The training stops at a node as soon as the critical lower bound of events, chosen by the user, is reached at that node. The leafs, or the final nodes, are then classified as signal or background depending upon their purity,

$$p = \frac{S}{S+B}. \tag{6.1}$$

If $p > 0.5$ the event is considered to be signal, otherwise it is classified as a background event. The quality of this separation is defined using an "impurity function," which can take different forms such as:

- Gini Index: $p \cdot (1-p)$
- Cross Entropy: $-p \cdot \ln(p) - (1-p) \cdot \ln(1-p)$
- Misclassification Error: $1 - max(1, 1-p)$
- Statistical Significance: $\frac{S}{\sqrt{S+B}}$

TMVA then chooses the variable and corresponding cut value that maximizes the increase in the impurity function from the parent

node to the two daughter nodes, weighting by their relative fraction of events. The cut values are optimized by a scan over the variable with a granularity that is set by the user (with a default value of 20).

In principle, this training could continue until each leaf node contained only signal or background events, achieving perfect discrimination. However, such a decision tree would be highly overtrained. Such overtraining can be reduced by the pruning of our trees. Overtraining and Pruning will be discussed in Section 6.4.

6.3 Boosting a Decision Tree

Boosting is a way of enhancing an otherwise classification (or regression) method by sequentially applying the algorithm to a reweighted (or boosted) version of the training data, then taking a weighted majority vote of the sequence of MVA algorithms produced. In classification problems, a larger weight is given to events that are misclassified when training the following tree. This not only enhances our decision tree, but also makes it more robust against statistical fluctuations in the training sample. This method typically results in a dramatic performance increase. Simple decision trees are a perfect candidate for using boosting methods, turning them into a very powerful classifier. This section will introduce

two popular boosting algorithms, adaptive boosting and gradient boosting.

Adaptive Boosting

The most common method of boosting is Adaptive Boosting (AdaBoost). This method starts with the original event weights when training the first tree, then during the training of the subsequent tree the weights are modified by multiplying the previously misclassified event by a common *boost weight*, α. This weight is derived from the misclassification rate, err, of the previous tree,

$$\alpha = \frac{1 - err}{err}. \tag{6.2}$$

Of course, the weights of the entire event sample are renormalized so that the sum of weights remains constant.

The results of an individual classifier are defined as $h(\vec{x}) = +1$ for signal and $h(\vec{x}) = -1$ for background events. Here, $\vec{x}$ is the tuple of input variables. The standard boosting algorithm is given by

$$y_{boost}(x) = \frac{1}{N_{collection}} \cdot \sum_{i}^{N_{collection}} \ln(\alpha_i) \cdot h_i(x), \tag{6.3}$$

where the sum is taken over all of the classifiers in the collection. Small values of y_{boost} indicate a background-like event while large values indicate a signal-like event.

AdaBoost performs best on small decision trees with a depth of 2 or 3, meaning the trees would have very little discrimination power by themselves. The smaller trees are much less prone to overtraining compared to a larger decision tree, and smaller AdaBoosted trees outperform the larger trees, typically by a great deal.

Gradient Boosting

Using boosting we can estimate the form different functions take. Consider a function, $F(\vec{x})$, which is a weighted sum of some parametrized base functions $f(x; a_m)$. These base functions are our "weak learners", or simple decision trees,

$$F(\vec{x}; P) = \sum_{m=0}^{M} \beta_m f(x; a_m); P \in \{\beta_m; a_m\}_0^M. \tag{6.4}$$

The boosting procedure can now be used in order to estimate the parameters, P, such that the deviation between the model response $F(\vec{x})$ and the true value y obtained from the training sample is minimized. This deviation is measured using a *loss function* L(F,y), such as the *squared error loss function* $L(F, y) = (F(\vec{x}) - y)^2$. From the loss function, the boosting procedure can be fully modelled.

For example, *AdaBoost* is based on the exponential loss function, $L(F(x), y) = e^{-F(x)y}$, which leads to the reweighting algorithm described by equation 6.3. However, exponential loss does have its

shortcomings, namely that is lacks robustness in the presence of outliers or mislabelled data points. We expect the performance AdaBoost to degrade in noisy scenarios.

The *GradientBoost* algorithm attempts to improve upon this by allowing for other loss functions while trying to maintain the good performance of *AdaBoost*. The TMVA implementation of *GradientBoost* uses a binomial log-likelihood *loss function*,

$$L(F, y) = \ln(1 + e^{-2F(\vec{x})y}) \tag{6.5}$$

for classification. The boosting algorithm for this loss function can not be easily obtained, we must take a steepest-descent approach to do the minimization. TMVA does this by calculating the current gradient of the *loss function* and growing a regression tree whose leaf values are adjusted to match the mean of the gradient in each region as defined by the tree structure. Iterating this procedure gives us the set of decision trees minimizing our *loss function*. *GradientBoost*, like *AdaBoost*, performs best on weak classifiers.

6.4 Overtraining / Pruning

When training a classifier, you must be wary of overtraining. Overtraining occurs when a classifier becomes too adapted to a specific training sample, where similar samples can have a completely differ-

ent response to the training classifier. This is problematic since the real data would likely also be classified differently, leaving our classifier unable to confidently determine optimal cut values. In general, overtraining is prevalent because too many model parameters of an algorithm were adjusted to too few data points. Therefore, the sensitivity to overtraining depends on the classifier. Boosted Decision Trees are highly susceptible to overtraining, given their large number of nodes. An overtrained classifier would seem to have very good performance with the training sample, but a performance decrease when measured with an independent test sample. TMVA checks for overtraining by randomly splitting the sample during classification, training on one and leaving the second independent for testing. The performance results are then compared between these training and test samples.

In order to reduce overtraining, you could employ a technique called *pruning*. *Pruning* a decision tree is the process of cutting back a tree from the bottom up, after it has been built. The purpose is to remove any statistically insignificant nodes, thus reducing the overtraining of the tree. First growing the tree to its full size and then pruning has been shown to be far more effective than interrupting the splitting at an earlier stage, due to seemingly insignificant splits actually leading to more effective splits at a later stage. In the end,

however, it is typically more effective to limit the tree depth before training and allowing the boosting algorithm to dramatically improve our discriminating power without overtraining, rendering the pruning method obsolete.

6.5 Training our BDT

The best multivariate method to be used for any given problem can be very challenging to identify a priori, no general recommendation can be given. Work is constantly ongoing in high-energy physics to train on more sophisticated algorithms, but to date BDTs have been the most effective classifier for signal discrimination. TMVA gives us a pretty easy to use framework to evaluate a few benchmark quantities and assess the performance of different classifiers. A few of these quantities are

- The Signal efficiency: TMVA will calculate the **signal efficiency**, defined as 1-rejection, evaluated at a few different background efficiency points. TMVA also calculates the area of the background rejection verse signal efficiency curve, where the larger the area is the better the classification,
- The **separation**, $\langle S^2 \rangle$, of a classifier, y, defined by the integral

$$\langle S^2 \rangle = \frac{1}{2} \int \frac{(\hat{y}_S(y) - \hat{y}_B(y))^2}{\hat{y}_S(y) + \hat{y}_B(y)} dy \tag{6.6}$$

where $\hat{y}_S$ and $\hat{y}_B$ are the signal and background PDFs of y. The **separation** is 0 if the signal and background shapes are identical, and it is 1 for shapes with no overlap,

- The discrimination **significance** of a classifier, which is the difference between the means of the signal and background distributions divided by the quadratic sum of their root-mean-squares.

Overall this is a pretty powerful set of tools to assess the discriminating power of the different classifiers, and allows for a solid comparison. Of course, you should also be on the lookout for *overtraining* as well, as discussed in 6.4. For this, TMVA superimposes the classifier for both the training and test sample to check that the response is consistent. From these distributions the Kolmogorov-Smirnov test statistic is computed, an efficient way of determining if two samples are significantly different from each other. The details and evaluation of the Kolmogorov-Smirnov test are best found in a stastics journal [81]. This test statistic approaches 1 (0) the more (less) likely the two distributions are compatible.

Training Input

Three benchmark samples with increased statistics are used for training, described in Table B.3, corresponding to $\Delta m(\tilde{t}_1, \tilde{\chi}_1^0) =$

$(475, 325), (475, 355), (475, 385)$. In order to explore the discriminating power of the BDT, training was performed on the same variables used in the Recursive Jigsaw analysis of Chapter 5. This way, we can explore if we can cover more of the $\Delta m(\tilde{t}_1, \tilde{\chi}_1^0)$ phase space while also validating our choice of cuts in the jigsaw analysis. All of the variables used for training are,

- M_Δ^R [GeV], described in Equation 5.5,
- $\Delta\phi_\beta^R$, the azimuthal angle between the boost, from the LAB frame to the COM frame, and the visible dilepton system,
- R_{p_T}, described in Equation 5.4,
- $1/\gamma_{R+1}$, described in Equation 5.6,
- $E_\mathrm{T}^\mathrm{miss}$ significance, described in Equation 4.2,
- $n_{b\text{-jets}}$.

The same preselection cuts as the Recursive Jigsaw analysis were maintained for a more direct comparison,

- 2 oppositely charged (OS) leptons passing signal quality and trigger requirements,
- Leading lepton $p_\mathrm{T} > 25$ GeV, sub-leading lepton $p_\mathrm{T} > 20$ GeV,
- $m_{\ell\ell} > 20$ GeV,

- $|m_{\ell\ell} - m_Z| > 20$ GeV if leptons are same-flavor,
- $M_\Delta^R > 75$ GeV.

The distribution of our input variables, after our preselections, are shown in 6.2.

In that analysis we also asked for a requirement on the $n_{b\text{-jets}}$ depending on the kinematic region being targeted, but here we leave this requirement out and instead pass $n_{b\text{-jets}}$ variable for training. We expect some kinematic differences depending on the flavor of the two leptons in the final state, so we split the training on each signal model into DF and SF.

Training on $\Delta m(\tilde{t}_1, \tilde{\chi}_1^0) = (475, 325)$

As described in Section 6.5, TMVA provides us with some preliminary information, such as the *separation*, in order to assess our choice of variables. Ranking the *variable importance* after the training is also crucial to gain some idea of how often each variable is used to split decision tree nodes and their effectiveness. This is done by counting how often each variable is used and weighting each split occurrence by the separation gain-squared it has achieved and by the number of events in the node [82]. You can see the *separation* and *variable importance* summarized in Table 6.1.

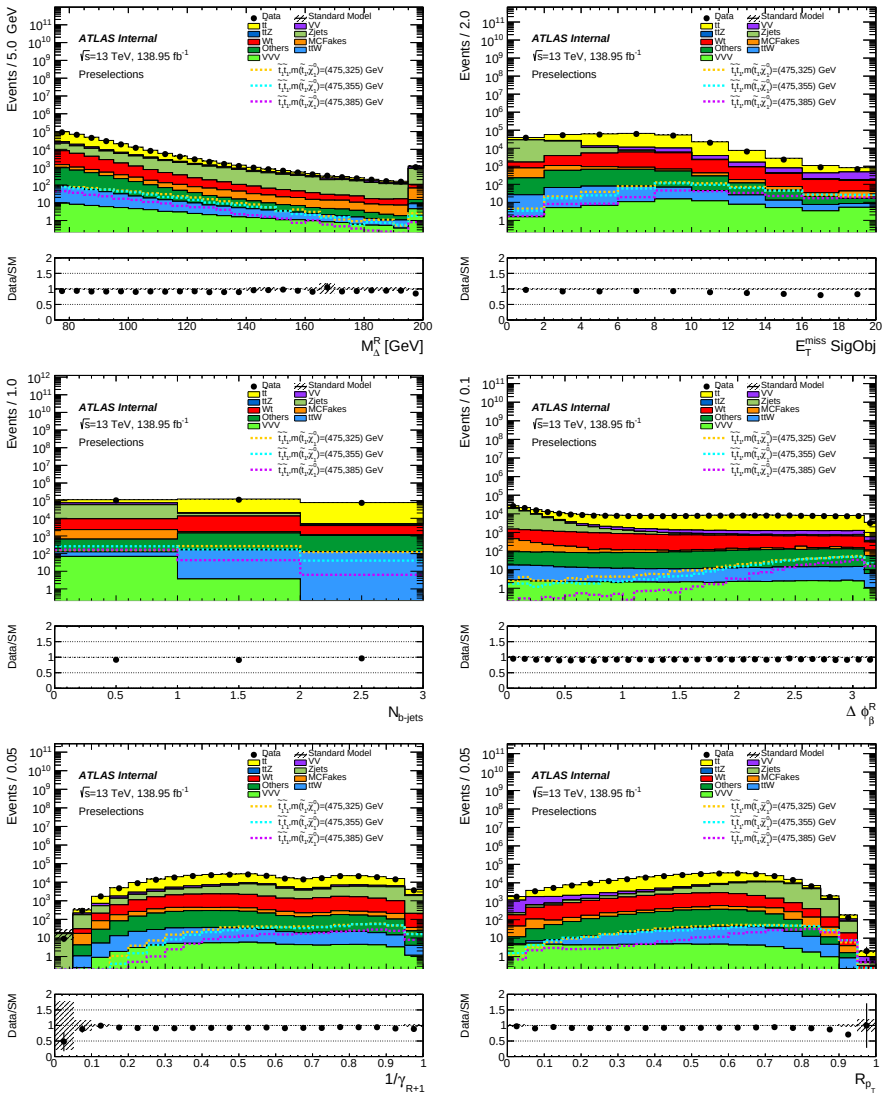

Figure 6.2: Distributions at preselection level. The error band on the MC represent statistical uncertainties only.

The correlations matrices describing how the different input variables are correlated are shown in Figure 6.3.

	Separation		Variable Importance	
Variable	Different Flavor	Same Flavor	Different Flavor	Same Flavor
$E_{\mathrm{T}}^{\mathrm{miss}}$ significance	0.23	0.36	0.16	0.16
$\Delta\phi_{\beta}^{R}$	0.21	0.39	0.22	0.27
M_{Δ}^{R} (GeV)	0.15	0.079	0.12	0.089
$R_{p_{\mathrm{T}}}$	0.10	0.065	0.20	0.20
$1/\gamma_{R+1}$	0.076	0.063	0.21	0.18
$n_{b\text{-jets}}$	0.0063	0.029	0.087	0.10

Table 6.1

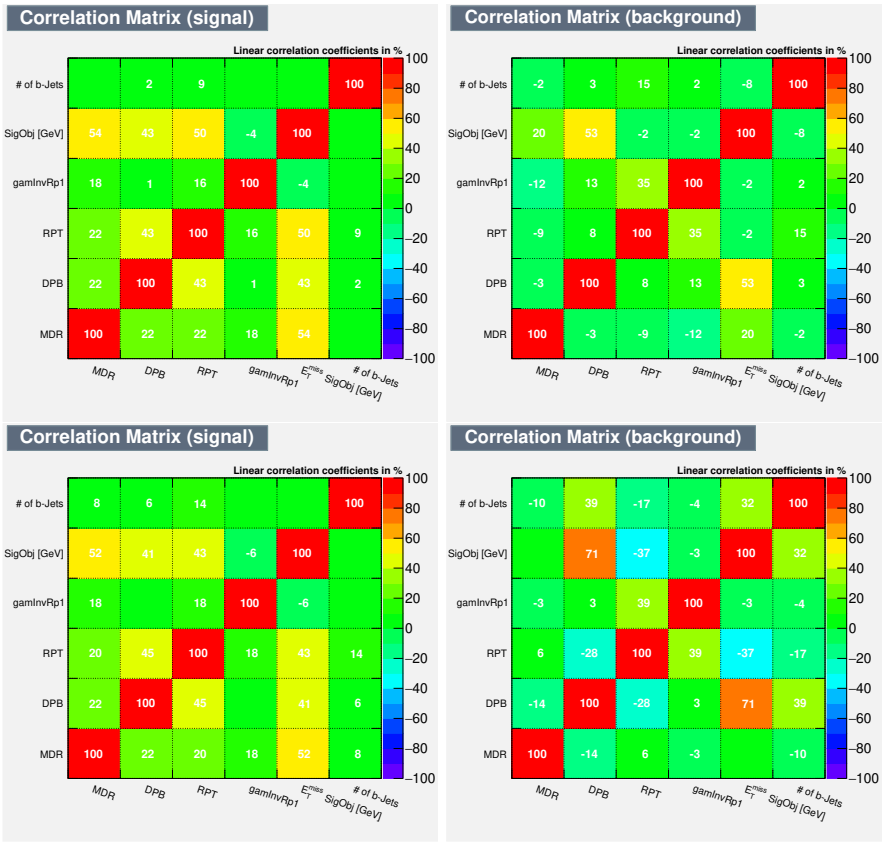

Figure 6.3: Input variable correlations matrices for signal (left) and background (right) samples. They are shown here for both different flavor (top) and same flavor (bottom) events.

In Figure 6.4, some evaluation of the training results are presented. In the top half are some efficiency plots, comparing the cut efficiencies for the signal and background as well as the $\frac{S}{\sqrt{S+B}}$ to quantify the discrimination. The signal and background here are the expected yields for 138.95 fb^{-1}.

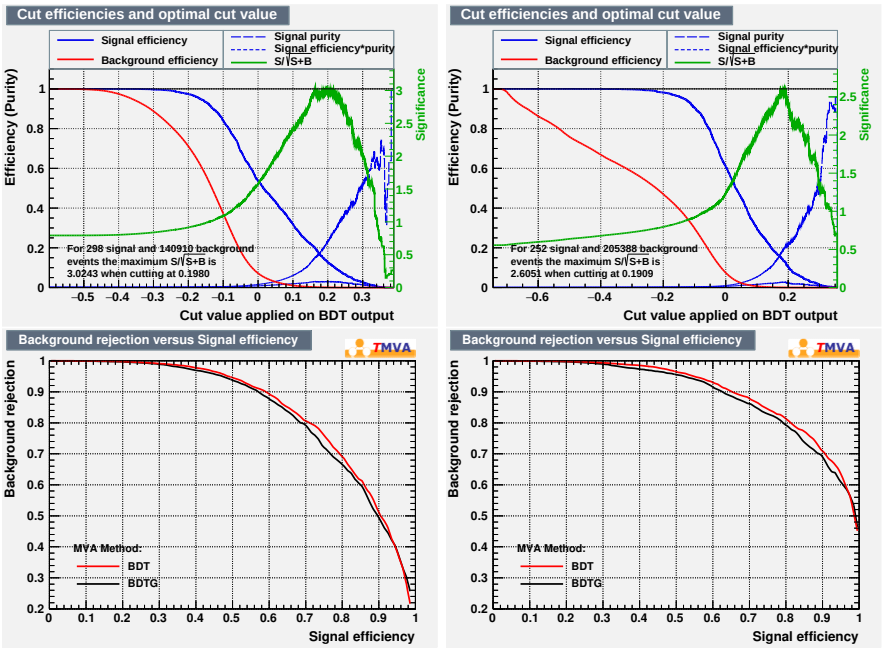

Figure 6.4: Here we show a couple more tests for evaluating the different classifiers. Cut efficiencies and optimal cut values are shown in the top half, while the ROC curves are presented in the bottom half. Different flavor training results are presented on the left, while same flavor results are shown on the right.

The bottom plots in Figure 6.4 are the ROC curves, or the area of the background rejections vs signal efficiency. The larger the area under the ROC curve the better the discriminator is at separating signal from background. Decision trees were trained using both

gradient boosting and adaptive boosting, but we found in each case the adaptive boosting to be the more powerful method.

Evaluating the $\Delta m(\tilde{t}_1, \tilde{\chi}_1^0) = (475, 325)$ BDT Classifier

For evaluating and optimizing the classifier, the MC events that were not used during training are used. Of course these events are rescaled to 138.95 fb^{-1}for our data/MC comparisons, which is shown in Figure 6.5.

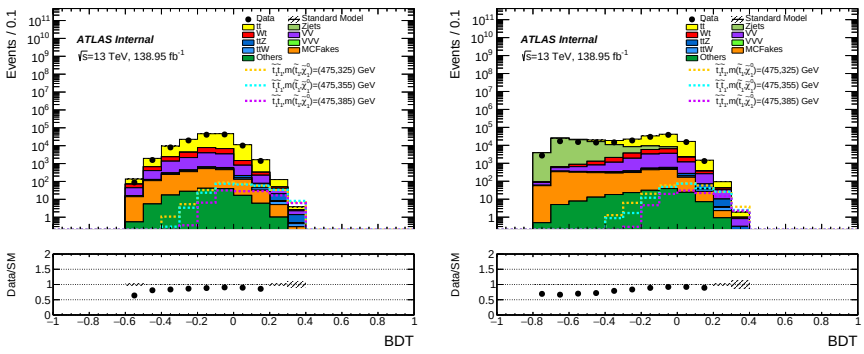

Figure 6.5: Data/MC comparisons of the BDT classifier trained on the $\Delta m(\tilde{t}_1, \tilde{\chi}_1^0) = (475, 325)$ sample, with the data blinded in the bins with larger signal contamination. The full dataset is used, but only the MC events that weren't used in the training and testing. Once again different flavor events are shown on the left while same flavor events are shown on the right.

In Figure 6.4 the $\frac{S}{\sqrt{S+B}}$ was used to measure the discriminating power, however, in the end, the significance used in the jigsaw anal-

ysis, equation 6.7, would give us a better comparison.

$$Z = \sqrt{2\left(n\ln\left(\frac{n(b+\sigma^2)}{b^2+n\sigma^2}\right) - \frac{b^2}{\sigma^2}\ln\left(1+\frac{\sigma^2(n-b)}{b(b+\sigma^2)}\right)\right)} \tag{6.7}$$

A scan was made across the BDT response, computing the significance, Z, in the bottom pad of the plots in 6.6.

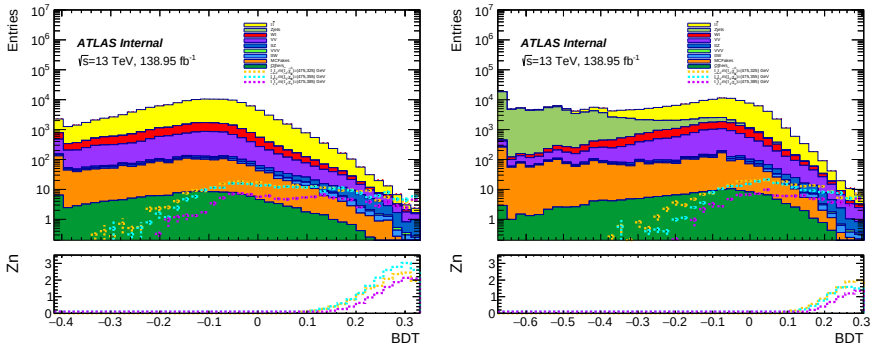

Figure 6.6: Optimization scan of our BDT classifier trained on the $\Delta m(\tilde{t}_1, \tilde{\chi}_1^0) = (475, 325)$ sample. Here only the MC events that weren't used in the training and testing are used for this scan. Different flavor is shown on the left while same flavor on the right.

This scan is used to maximize the significance and define our signal regions.

Evaluating the $\Delta m(\tilde{t}_1, \tilde{\chi}_1^0) = (475, 385)$ BDT Classifier

Here, the same evaluation for the $\Delta m(\tilde{t}_1, \tilde{\chi}_1^0) = (475, 385)$ BDT classifier is presented. Data/MC plots are shown in Figure 6.7.

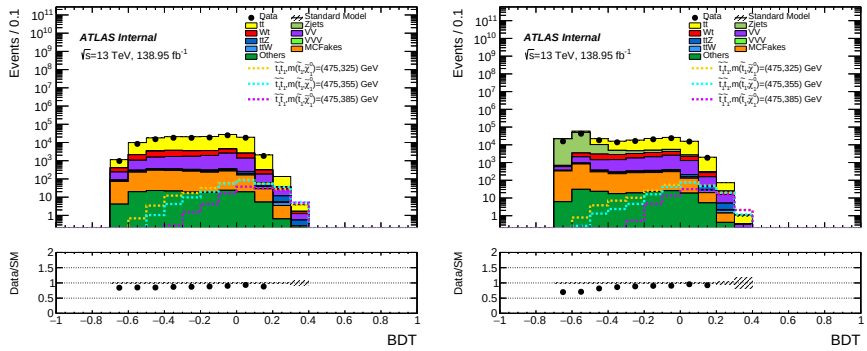

Figure 6.7: Data/MC comparison of our BDT classifier trained on the $\Delta m(\tilde{t}_1, \tilde{\chi}_1^0) = (475, 385)$ sample, with the data blinded in the bins with larger signal contamination. The full dataset is used, but only the MC events that weren't used in the training and testing. Once again different flavor events are shown on the left while same flavor events are shown on the right.

Figure 6.8 shows the optimization of the BDT classifier trained on $\Delta m(\tilde{t}_1, \tilde{\chi}_1^0) = (475, 385)$.

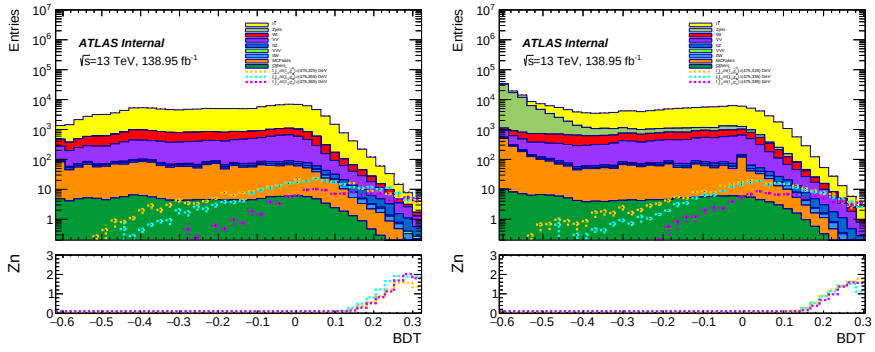

Figure 6.8: Optimization scan of our BDT classifier trained on the $\Delta m(\tilde{t}_1, \tilde{\chi}_1^0) = (475, 385)$ sample. Here only the MC events that weren't used in the training and testing are used for this scan. Different flavor is shown on the left while same flavor on the right.

Signal Regions

Using the optimization scans in Figure 6.6 and Figure 6.8, a signal region is defined for each scenario. The signal regions are outlined in Table 6.2. In addition to the signal region, we provide the expected SM and signal yields as well as the *significance*.

Signal Region Definition				
	SR_t^{DF}	SR_t^{SF}	SR_W^{DF}	SR_W^{SF}
BDT Cut	> 0.29	> 0.28	> 0.28	> 0.26
SM Background	6.42 ± 0.42	6.88 ± 0.40	9.73 ± 0.47	7.81 ± 0.45
$\tilde{t}_1\tilde{t}_1, m(\tilde{t}_1, \tilde{\chi}_1^0) = (475, 325)$ GeV	8.68 ± 0.77	7.28 ± 1.10	7.47 ± 0.90	6.74 ± 1.01
$\tilde{t}_1\tilde{t}_1, m(\tilde{t}_1, \tilde{\chi}_1^0) = (475, 355)$ GeV	11.18 ± 1.26	5.43 ± 0.68	8.99 ± 1.06	6.14 ± 0.82
$\tilde{t}_1\tilde{t}_1, m(\tilde{t}_1, \tilde{\chi}_1^0) = (475, 385)$ GeV	7.57 ± 0.85	4.96 ± 0.71	9.49 ± 1.02	6.22 ± 0.71
Z - $(475, 325)$ GeV	2.50	2.08	1.78	1.82
Z - $(475, 355)$ GeV	3.09	1.61	2.09	1.68
Z - $(475, 385)$ GeV	2.23	1.48	2.19	1.70

Table 6.2: Definition of the signal region selections. SR_t^{DF} and SR_t^{SF} use the BDT response trained on the $\Delta m(\tilde{t}_1, \tilde{\chi}_1^0) = (475, 325)$ sample while SR_W^{DF} and SR_W^{SF} use the BDT response trained on the $\Delta m(\tilde{t}_1, \tilde{\chi}_1^0) = (475, 385)$ sample. Accompanying this are the SM background expected yields, as well as the expected signal yields for the three benchmark samples. In the bottom portion are the values for the *significance*, Z.

6.6 Outlook

Training a shallow decision tree using adaptive boosting techniques looks like a very promising classifier. For a comparison, a BDT was trained using the variables in the jigsaw analysis, and right away get a similar outlook. It would be interesting to pursue this and explore whether the countour could be pushed even further. After all, maybe SUSY lies just outside of our previous boundaries.

Further sensitivity may be gained if we apply a similar cut on $n_{b\text{-jets}}$ as the jigsaw analysis, looking at Figure 5.6 you can see there is a clear distinction in the signal models depending on the number of b-tagged jets. Making this cut would likely improve our sensitivity, especially considering $n_{b\text{-jets}}$ seems to be the variable with the least separation and variable importance, while simultaneously giving us orthogonal signal regions.

It would also be interesting to play with adding other variables as well as varying the parameters. Our selection of variables isn't always as straightforward as a cut and count analysis, we could gain significantly by adding more. It would also be wise to tweak the training parameters, like the number of trees and the depth of each tree, and see how they may effect our classifier.

In Figure 6.9, the yields for each signal model in the 3-body signal grid are shown. The expected sensitivity is presented in Figure 6.10, which can be compared with the Jigsaw analysis, such as in Figure 5.16. It can be seen that we expect, even with minimal optimization, that we will get similar or better results using Boosted Decision Trees to discriminate between signal and background events.

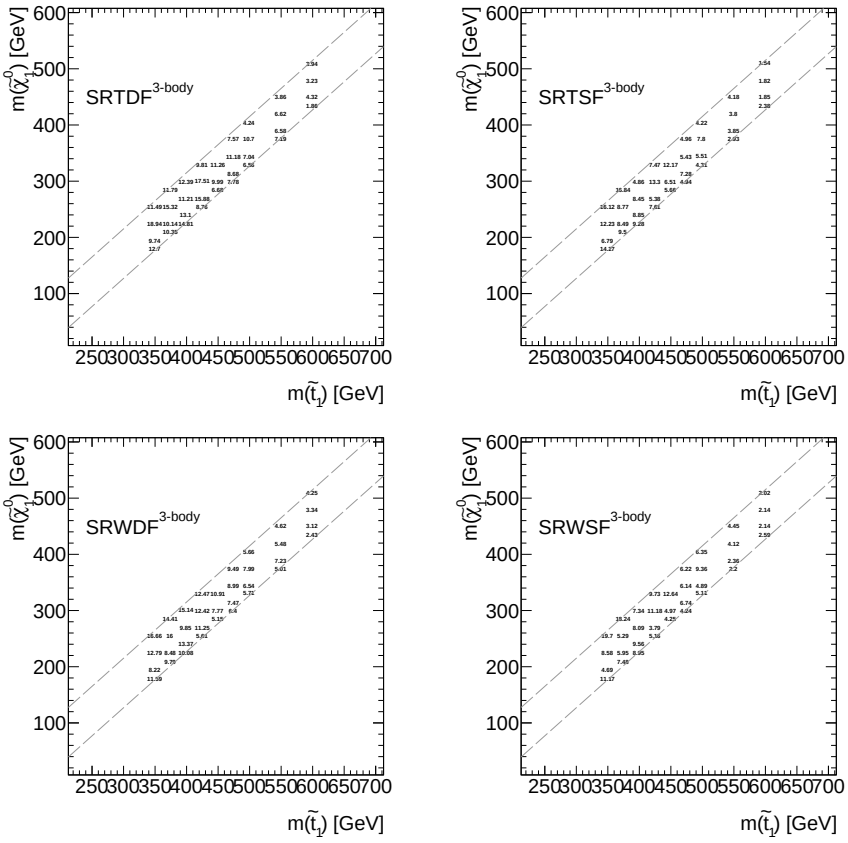

Figure 6.9: Signal yields in SR_W (top-left) and SR_t (top-right) for each point in the grid in the $(m_{\tilde{t}}, m_{\tilde{\chi}_1^0})$ plane.

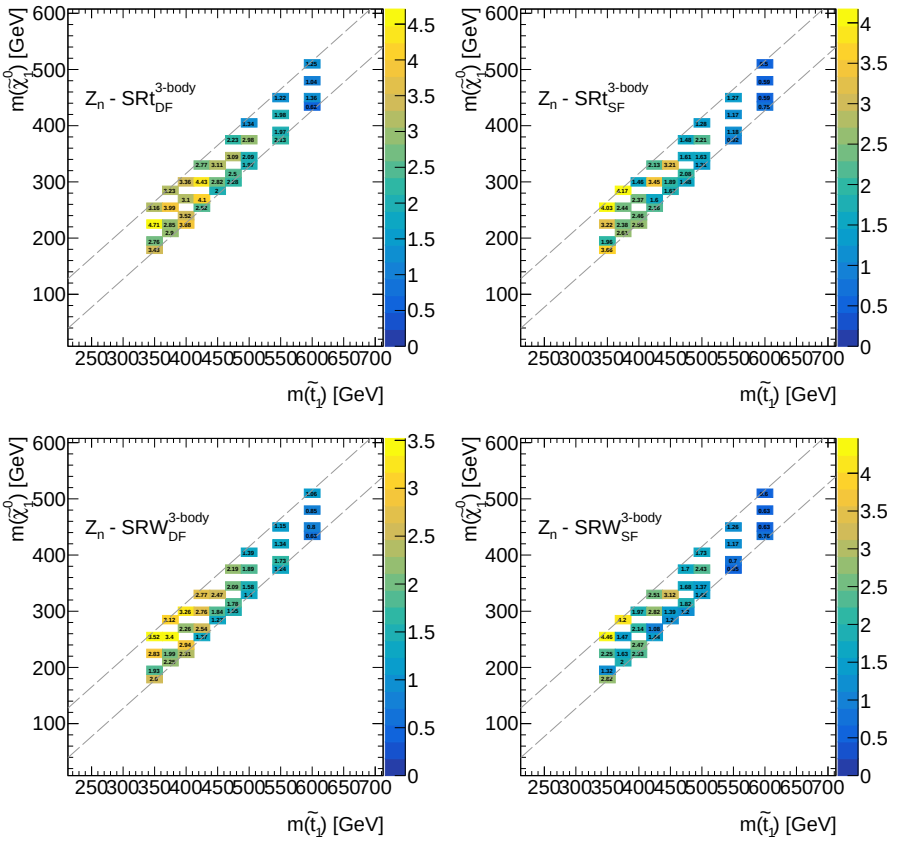

Figure 6.10: The Z_n values, estimated with a 20% of uncertainty on the full background, for SR_W (middle-left) and SR_t (middle-right) for each point in the grid in the $(m_{\tilde{t}}, m_{\tilde{\chi}_1^0})$ plane. The combined exclusion is shown on the bottom, computed by adding SRW and SRt exclusions in quadrature.

Chapter 7

Interpretation of Experimental Results

No significant excess was observed in Section 5.5. The results are interpretted by setting limits on the masses of the SUSY particles under observation, describing the masses of the SUSY particles that can be excluded based upon the data that was observed. This is done using inverted hypothesis tests.

7.1 Confidence Levels and Limit Setting

Hypothesis testing is performed based upon a frequentist significance test using a likelihood ratio as a test statistic [83]. In the end, a comparison is made of the probability, $P(data|H_b)$, of the observed data given a background only hypothesis (H_b) with the probability, $P(data|H_{s+b})$, of the observed data given a signal +

background hypothesis (H_{s+b}). To start off, the null hypothesis is taken as the background only hypothesis, $H_0 = H_b$, which is tested against the alternative hypothesis, $H_1 = H_{s+b}$. The background only hypothesis is not rejected, and therefore the results are interpreted as exclusion limits using more hypothesis testing. When setting the exclusion limits, the roles of $H_0 = H_{s+b}$ and $H_1 = H_b$ are reversed and the level of agreement in H is quantified as the *p-value*.

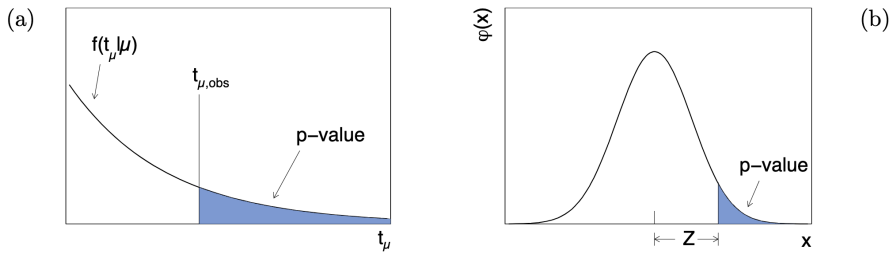

Figure 7.1: An illustration of the p-value obtained from an observed value of the test statistic, t_μ is shown in (a). In (b), the standard normal distribution $\phi(x) = (1/\sqrt{2\pi})exp(-x^2/2)$ relating the significance and the p-value.

The *p-value* is the probability of, under the assumption of H, finding data of equal or greater incompatibility with the agreement of H. In particle physics, the p-value is typically converted into an equivalent significance, $Z = \Phi^{-1}(1-p)$, defined such that a Gaussian distributed variable found Z standard deviations above its mean would have an upper tail probability equal to p. Φ^{-1} is the inverse of the cumulative distribution of the standard gaussian. Historically, the particle physics community regards a rejection of

the background hypothesis with a significance of at least $Z = 5$ as the appropriate level to constitute discovery, which corresponds to $p = 2.87 \times 10^{-7}$. For setting limits, a threshold of $p = 0.05$ is taken for a 95% confidence level, in order to exclude the signal hypothesis corresponding to $Z = 1.64$.

Likelihood Function

As described above, using hypothesis tests, an excess of signal over background is sought in mass windows, performing a counting experiment in each window. A likelihood function is constructed from a parametric model of the observed data, the signal (s), and the background (b) predictions, parametrized by the systematic uncertainty. Each systematic uncertainty, i, is described with a nuisance parameter, θ_i, that continuously interpolates between the systematic variations and the nominal values, e.g. $\theta_i = \pm 1$ for the $\pm\sigma$ variations, and $\theta_i = 0$ for the nominal (center) values. This likelihood function takes the form

$$\begin{aligned} L(n, \theta^0 | \mu_{sig}, b, \theta) &= P_{SR} \times P_{CR} \times C_{syst} \\ &= P(n_S | \lambda_S(\mu_{sig}, b, \theta)) \times \prod_{i \in CR} P(n_i | \lambda_i(\mu_{sig}, b, \theta)) \times C_{syst}(\theta^0, \theta). \end{aligned} \tag{7.1}$$

where the first two factors of Equation 7.1 reflect the Poisson measurements of n_S and n_i, the number of observed events in the signal

S and each control region i [84]. The Poisson expectation values, λ_S and λ_i are functions depending on the predictions b, for the various background sources, the nuissance parameters that parametrize the systematic uncertainties, the normalization factors for the background processes, μ_p, and the signal strength parameter μ_{sig}. The Poisson expectation of observing n events is given by,

$$L_P(n|\nu(\mu,b,\theta)) = \frac{\nu^n}{n!}e^{-\nu}, \nu(\mu,b,\theta) = \mu_{sig} + \theta_i b_i, \tag{7.2}$$

and the impact of systematic uncertainties are modelled by a product of Gaussian distributions,

$$C_{syst}(\theta^0,\theta) = \prod_{j\in S} G(\theta_j^0 - \theta_j), \tag{7.3}$$

where S is the full set of systematics considered. The number of expected events in the Poisson part of the likelihood, $\nu(\mu,b,\theta)$, depends on the backgrounds, b, nuissance parameters, θ, and the signal strength, μ. $\mu = 0$ corresponds to our background only hypothesis while a signal strength $\mu = 1$ corresponds to the signal plus background hypothesis.

The likelihood function is implemented using the ATLAS developed software package, HistFitter [84]. A fitting procedure is carried out using RooStats/RootFit (with Minuit as the backend) [85], to minimize the negative log likelihood by varying the nuissance parame-

ters, θ_j, the backgrounds, b, and signal strengths, μ, while keeping the number of events and central values (θ_j^0) constant. The minimum negative log likelihood corresponds to the model that best fits the data.

Inverted Hypothesis Testing

When the background hypothesis is unable to be rejected, exclusion limits should be set. This is typically done using inverted hypothesis testing for each signal model. There exists some value, α, for which the null hypothesis of any given model is not rejected,

$$P_{model} = \int_{N_{obs}}^{\inf} f(N_{obs}|H_0)dN \leq \alpha. \tag{7.4}$$

Once α is discovered, we can determine the confidence level (CL) $CL = 1 - \alpha$. Exclusion limits are set when the p-value goes below some threshold, typically $p < 0.05$, corresponding to a 95% confidence level (CL).

7.2 Setting Limits for the Recursive Jigsaw Analysis

No significant excess was found and limits on the masses under study were set. As discussed, hypothesis tests are performed in order to determine whether a given point in the ($m_{\tilde{t}_1}$,$m_{\tilde{\chi}_1^0}$) plane can be excluded at 95% CL. These hypothesis tests are run over the $\tilde{t}_1 \to bW\tilde{\chi}_1^0$ signal grid, using all four signal regions and three

control regions in the profile likelihood along with the observed data in each of the regions. The results of these hypothesis tests are summarized in Figure 7.2, where the sensitivity on the $\tilde{t}_1 \to t\tilde{\chi}_1^0$ 2-body signal grid with $\Delta m > 173$ GeV is also evaluated.

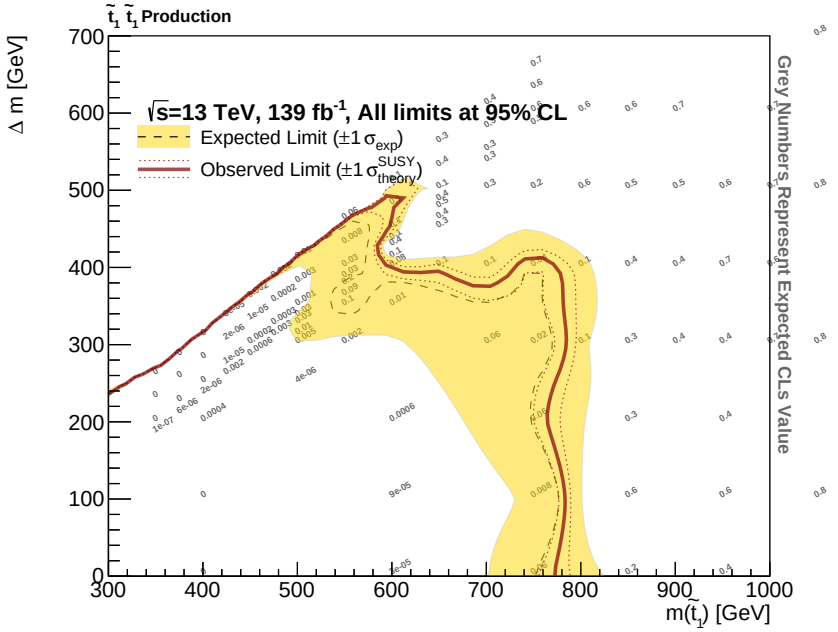

Figure 7.2: 95% CL exclusion contours for the entire Run-2 dataset using the Recursive Jigsaw selection. Our results are evaluated not only on the 3-body signal grid, but also on the 2-body signal grid. The $\pm 1\ \sigma_{theory}$ lines correspond to varying the predicted signal cross-section values up and down within their theoretical uncertainty and re-running the hypothesis tests.

In Figure 7.3, our exclusion results are also presented with the mass splitting, $\Delta m(\tilde{t}_1, \tilde{\chi}_1^0)$, on the y-axis.

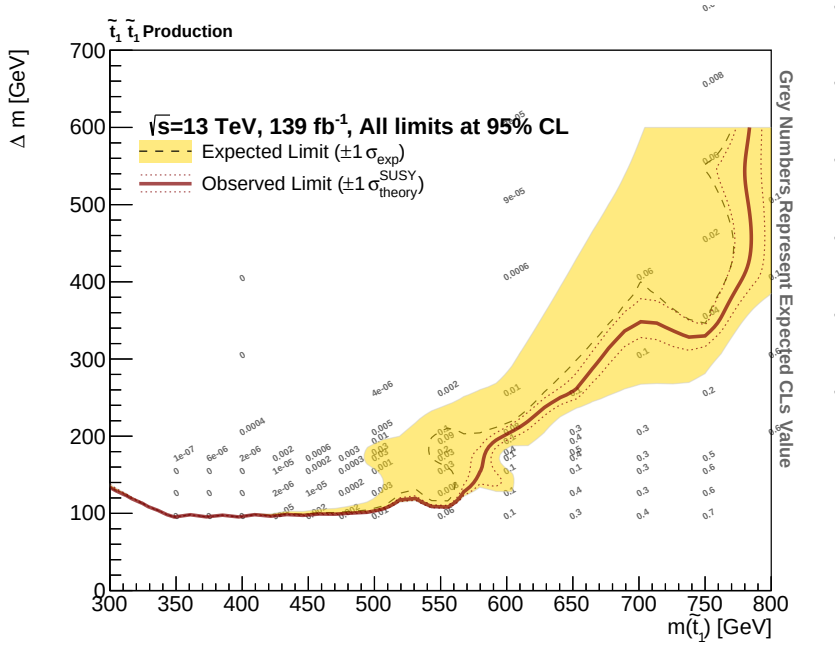

Figure 7.3: CL exclusion contours with the stop mass again on the x-axis but the mass difference, $\Delta m(\tilde{t}_1, \tilde{\chi}^0_1)$, on the y-axis.

7.3 Prospects of the Multivariate Analysis

In order to understand the potential of our multivariate analysis, similar hypothesis tests are performed using the signal regions defined using the boosted decision trees of Section 6.5. In order to get an honest comparison at the current stage of the TMVA analysis, hypothesis test results using the signal regions defined for the Recursive Jigsaw analysis without systematics or the data-driven method for estimating the background are also performed and presented. In this way, the potential of the multivariate analysis is compared with the jigsaw analysis at the same stage. The results

of the hypothesis tests are summarized for a comparison of SR_t^{DF} in Figure 7.4, on the left (right) for the jigsaw (multivariate) analysis.

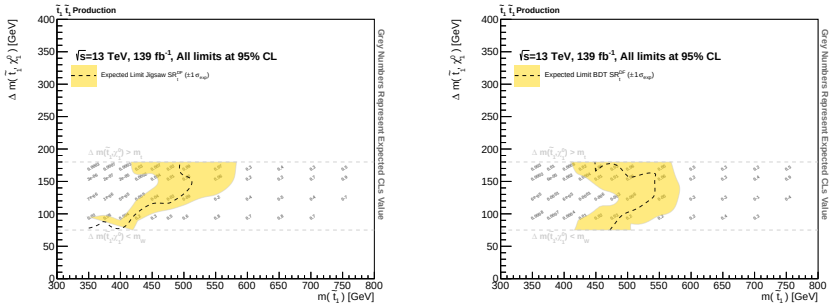

Figure 7.4: 95% CL exclusion contours for the entire Run-2 dataset comparing the Recursive Jigsaw selection with that of the Boosted Decision Trees. The ±1 σ_{theory} lines correspond to varying the predicted signal cross-section values up and down within their theoretical uncertainty and re-running the hypothesis tests.

In Figure 7.5, the combined contours are compared for SR_t^{DF}. The expected limit for the jigsaw analysis is shown in blue, where it can be seen that, for this signal region, the multivariate analysis significantly outperforms the jigsaw analysis.

7.4 Conclusion

Although no significant excess was observed for the Recursive Jigsaw analysis, significant improvements were made on the limits in the two-dimensional mass plane, $(m_{\tilde{t}_1}, m_{\tilde{\chi}_1^0})$. In the 3-body region, stop masses near 600 GeV are now excluded, compared with around 400 GeV in the previous round of analyses. These results were also interpreted in the 2-body region, potentially allowing for the clo-

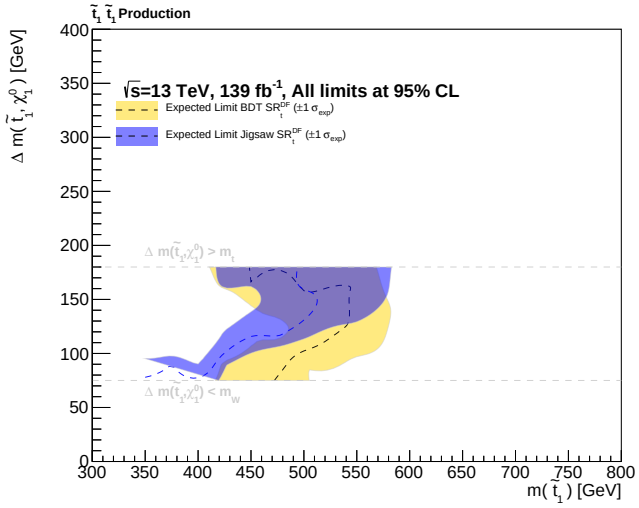

Figure 7.5: 95% CL exclusion contours for the entire Run-2 dataset comparing the Recursive Jigsaw selection with that of the Boosted Decision Trees. The blue contour is the contour for the Recursive Jigsaw selection.

sure of the contour across the top kinematic boundary where there was previously a large gap. Studies for another method, a machine learning method, also look promising. This Multivariate Analysis shows potential for probing signal models with an even higher stop mass. There is still significant work to be done, but I believe it would be worth searching for the stop in the 3-body decay region since it could be sitting just outside of the exclusion regions. More could be done to optimize the multivariate signal regions, but even this limited study shows great discriminating potential.

Chapter 8

Concluding Remarks

A search for stop pair-production decaying via a W-boson, b-quark, and a neutralino in final states containing two leptons was performed. This study analyzes 139 fb^{-1}of $\sqrt{s} = 13$ TeV pp collision data delivered by the LHC and recorded by the ATLAS detector from 2015-2018. Observations are consistent with Standard Model expectations. Exclusion limits were set, using a confidence level of 95%, of up to 600 GeV in the $m(\tilde{t}_1, \tilde{\chi}_1^0)$ plane. Results were also interpreted in the 2-body region, helping to set exclusion limits across the $\Delta m(\tilde{t}_1, \tilde{\chi}_1^0)$ m_t kinematic limit.

The LHC has enjoyed remarkable success, with run-2 culminating in almost 140 fb^{-1}of data recorded by the ATLAS detector. The discovery of the Higgs boson in 2012 was a massive milestone in particle physics, it had remained elusive for 50 years since it was first

introduced as a mechanism for generating mass. Unfortunately, if new physics exists at the TeV-scale it has yet to show itself. However, the LHC is just getting started and over 4000 $fb^{-1}$is expected for the entire High Luminosity LHC (HL-LHC) run, which will allow for searches for rare SUSY processes. We have also demonstrated that further studies of the run-2 data using a multivariate technique would be worth pursuing.

Bibliography

[1] P. A. Dirac, *The quantum theory of the electron*, Proc. Roy. Soc. Lond. A **A117** (1928) 610 (cit. on p. 1).

[2] R. P. Feynman, *Space-Time Approach to Quantum Electrodynamics*, Phys. Rev. **76** (6 1949) 769, URL: https://link.aps.org/doi/10.1103/PhysRev.76.769 (cit. on p. 1).

[3] M. Tanabashi et al., *Review of Particle Physics*, Phys. Rev. D **98** (3 2018) 030001, URL: https://link.aps.org/doi/10.1103/PhysRevD.98.030001 (cit. on p. 3).

[4] S. L. Glashow, *Partial Symmetries of Weak Interactions*, Nucl. Phys. **22** (1961) 579 (cit. on p. 3).

[5] S. Weinberg, *A Model of Leptons*, Phys. Rev. Lett. **19** (21 1967) 1264, URL: https://link.aps.org/doi/10.1103/PhysRevLett.19.1264 (cit. on p. 3).

[6] *The Nobel Prize in Physics 1979*, URL: https://www.nobelprize.org/prizes/physics/1979/summary/ (cit. on p. 4).

[7] P. W. Anderson, *Plasmons, Gauge Invariance, and Mass*, Phys. Rev. **130** (1 1963) 439, URL: https://link.aps.org/doi/10.1103/PhysRev.130.439 (cit. on p. 4).

[8] F. Englert and R. Brout, *Broken Symmetry and the Mass of Gauge Vector Mesons*, Phys. Rev. Lett. **13** (9 1964) 321, URL: https://link.aps.org/doi/10.1103/PhysRevLett.13.321 (cit. on p. 4).

[9] P. W. Higgs, *Broken Symmetries and the Masses of Gauge Bosons*, Phys. Rev. Lett. **13** (16 1964) 508, URL: https://link.aps.org/doi/10.1103/PhysRevLett.13.508 (cit. on p. 4).

[10] G. S. Guralnik, C. R. Hagen, and T. W. B. Kibble, *Global Conservation Laws and Massless Particles*, Phys. Rev. Lett. **13** (20 1964) 585, URL: https://link.aps.org/doi/10.1103/PhysRevLett.13.585 (cit. on p. 4).

[11] A. Collaboration, *Combined measurements of Higgs boson production and decay using up to* 80 fb^{-1} *of proton-proton collision data at* $\sqrt{s} = 13$ TeV *collected with the ATLAS experiment*, Phys. Rev. D **101** (1 2020) 012002, URL: https://link.aps.org/doi/10.1103/PhysRevD.101.012002 (cit. on p. 5).

[12] ATLAS Collaboration, *Observation of a new particle in the search for the Standard Model Higgs boson with the ATLAS detector at the LHC*, Phys. Lett. B **716** (2012) 1, arXiv: 1207.7214 [hep-ex] (cit. on pp. 4, 16, 18, 21).

[13] CMS Collaboration, *Observation of a new boson at a mass of 125 GeV with the CMS experiment at the LHC*, Phys. Lett. B **716** (2012) 30, arXiv: 1207.7235 [hep-ex] (cit. on pp. 4, 16, 18).

[14] ATLAS and CMS Collaborations, *Combined Measurement of the Higgs Boson Mass in pp Collisions at* $\sqrt{s} = 7$ *and* 8 *TeV with the ATLAS and CMS Experiments*, Phys. Rev. Lett. **114** (2015) 191803, arXiv: 1503.07589 [hep-ex] (cit. on pp. 4, 16, 18).

[15] F. Halzen and A. D. Martin, *QUARKS AND LEPTONS: AN INTRODUCTORY COURSE IN MODERN PARTICLE PHYSICS*, 1984, ISBN: 978-0-471-88741-6 (cit. on pp. 6, 7).

[16] M. E. Peskin and D. V. Schroeder, *An Introduction to quantum field theory*, Addison-Wesley, 1995, ISBN: 9780201503975, 0201503972, URL: http://www.slac.stanford.edu/~mpeskin/QFT.html (cit. on p. 8).

[17] P. Ramond, *Journeys beyond the standard model*, Front. Phys. **101** (1999) 1 (cit. on p. 10).

[18] T. Tantau, "Graph Drawing in TikZ," *Graph Drawing*, ed. by W. Didimo and M. Patrignani, Springer Berlin Heidelberg, 2013 517, ISBN: 978-3-642-36763-2 (cit. on p. 17).

[19] *Izaak Neutelings. 'University of Zurich, CMS Wiki Pages'.* URL: https://wiki.physik.uzh.ch/cms/latex:tikz:timescales (cit. on p. 17).

[20] S. P. Martin, *A Supersymmetry Primer*, Adv. Ser. Direct. High Energy Phys. **18** (1998) 1, arXiv: hep-ph/9709356 (cit. on pp. 18, 21, 22, 25, 28).

[21] K. Inoue, A. Kakuto, H. Komatsu, and S. Takeshita, *Aspects of Grand Unified Models with Softly Broken Supersymmetry*, Prog. Theor. Phys. **68** (1982) 927 (cit. on p. 20), Erratum: Prog. Theor. Phys. **70** (1983) 330.

[22] L. Evans and P. Bryant, *LHC Machine*, JINST **3** (2008) S08001 (cit. on pp. 29, 31, 33).

[23] ATLAS Collaboration, *The ATLAS Experiment at the CERN Large Hadron Collider*, JINST **3** (2008) S08003 (cit. on pp. 29, 37–39, 42, 43, 45, 47, 49).

[24] CMS Collaboration, *The CMS experiment at the CERN LHC*, JINST **3** (2008) S08004 (cit. on p. 29).

[25] C. Service graphique, *Overall view of the LHC. Vue d'ensemble du LHC*, (2014), General Photo, URL: https://cds.cern.ch/record/1708849 (cit. on p. 30).

[26] *ATLAS Collaboration. ATLAS Luminosity Public Results Run 2*, URL: https://twiki.cern.ch/twiki/bin/view/AtlasPublic/LuminosityPublicResultsRun2 (cit. on p. 32).

[27] ATLAS Collaboration, *Luminosity determination in pp collisions at* $\sqrt{s} =$ 8 *TeV using the ATLAS detector at the LHC*, Eur. Phys. J. C **76** (2016) 653, arXiv: 1608.03953 [hep-ex] (cit. on p. 32).

[28] T. Sjöstrand et al., *An Introduction to PYTHIA 8.2*, Comput. Phys. Commun. **191** (2015) 159, arXiv: 1410.3012 [hep-ph] (cit. on pp. 35, 55).

[29] ATLAS Collaboration, *The ATLAS Simulation Infrastructure*, Eur. Phys. J. C **70** (2010) 823, arXiv: 1005.4568 [physics.ins-det] (cit. on pp. 35, 94).

[30] *ATLAS inner detector: Technical Design Report, 1*, Technical Design Report ATLAS, CERN, 1997, URL: http://cds.cern.ch/record/331063 (cit. on p. 37).

[31] *ATLAS liquid-argon calorimeter: Technical Design Report*, Technical Design Report ATLAS, CERN, 1996, URL: https://cds.cern.ch/record/331061 (cit. on p. 42).

[32] *ATLAS tile calorimeter: Technical Design Report*, Technical Design Report ATLAS, CERN, 1996, URL: https://cds.cern.ch/record/331062 (cit. on pp. 44, 62).

[33] T. Vazquez Schroeder, *The ATLAS Trigger in Run-2: Design, Menu, and Performance*, tech. rep. ATL-DAQ-PROC-2017-027, CERN, 2017, URL: https://cds.cern.ch/record/2287548 (cit. on p. 52).

[34] S. Weinzierl, *Introduction to Monte Carlo methods*, 2000, arXiv: hep-ph/0006269 [hep-ph] (cit. on p. 54).

[35] M. A. Dobbs et al., *Les Houches Guidebook to Monte Carlo Generators for Hadron Collider Physics*, 2004, arXiv: hep-ph/0403045 [hep-ph] (cit. on p. 54).

[36] G. Aad et al., *The ATLAS Simulation Infrastructure*, The European Physical Journal C **70** (2010) 823, ISSN: 1434-6052, URL: http://dx.doi.org/10.1140/epjc/s10052-010-1429-9 (cit. on p. 55).

[37] S. Agostinelli et al., *GEANT4: A Simulation toolkit*, Nucl. Instrum. Meth. A **506** (2003) 250 (cit. on pp. 55, 65, 94).

[38] G. Aad et al., *Electron and photon performance measurements with the ATLAS detector using the 2015–2017 LHC proton-proton collision data*, Journal of Instrumentation **14** (2019) P12006, ISSN: 1748-0221, URL: http://dx.doi.org/10.1088/1748-0221/14/12/P12006 (cit. on pp. 56, 57).

[39] ATLAS Collaboration, *Electron reconstruction and identification in the ATLAS experiment using the 2015 and 2016 LHC proton–proton collision data at* $\sqrt{s}$ *= 13 TeV*, Eur. Phys. J. (2019), arXiv: 1902.04655 [hep-ex] (cit. on p. 57).

[40] G. Aad et al., *Muon reconstruction performance of the ATLAS detector in proton–proton collision data at* $\sqrt{s}$*=13 TeV*, The European Physical Journal C **76** (2016), ISSN: 1434-6052, URL: http://dx.doi.org/10.1140/epjc/s10052-016-4120-y (cit. on p. 57).

[41] G. P. Salam, *Towards jetography*, The European Physical Journal C **67** (2010) 637, ISSN: 1434-6052, URL: http://dx.doi.org/10.1140/epjc/s10052-010-1314-6 (cit. on p. 59).

[42] M. Cacciari, G. P. Salam, and G. Soyez, *The anti-ktjet clustering algorithm*, Journal of High Energy Physics **2008** (2008) 063, ISSN: 1029-8479, URL: http://dx.doi.org/10.1088/1126-6708/2008/04/063 (cit. on p. 59).

[43] G. Aad et al., *Topological cell clustering in the ATLAS calorimeters and its performance in LHC Run 1*, The European Physical Journal C **77** (2017), ISSN: 1434-6052, URL: http://dx.doi.org/10.1140/epjc/s10052-017-5004-5 (cit. on p. 59).

[44] *Performance ofb-jet identification in the ATLAS experiment*, Journal of Instrumentation **11** (2016) P04008, ISSN: 1748-0221, URL: http://dx.doi.org/10.1088/1748-0221/11/04/P04008 (cit. on p. 61).

[45] *Technical Design Report for the Phase-II Upgrade of the ATLAS Tile Calorimeter*, Technical Design Report ATLAS, CERN, 2017, URL: https://cds.cern.ch/record/2285583 (cit. on pp. 63, 64, 66–69).

[46] J. L. on behalf of the ATLAS collaboration, *The ATLAS Tile Calorimeter Phase-II Upgrade Demonstrator Data Acquisition and Software*, URL: https://pos.sissa.it/321/026/ (cit. on p. 63).

[47] P. Moreno et al., *A new portable test bench for the ATLAS Tile Calorimeter front-end electronics*, Journal of Instrumentation **8** (2013) C02046, URL: https://doi.org/10.1088%2F1748-0221%2F8%2F02%2Fc02046 (cit. on p. 69).

[48] SVN Repository, *Prometeo Web Interface SVN*, tech. rep., CERN, 2015, URL: https://svnweb.cern.ch/trac/atlasgroups/browser/Detectors/%20TileCal/Prometeo/PrometeoWebInterface/trunk (cit. on p. 72).

[49] C. Solans, *An IPbus protocol for the ATLAS Tile calorimeter*, tech. rep. ATU-SYS-EN-0016, CERN, 2015, URL: https://edms.cern.ch/document/1554815/1 (cit. on p. 72).

[50] A. Ruiz-Martinez, F. Monticelli, and S. D. Jones, *Electron and photon trigger efficiency plots with early 2017 data*, tech. rep. ATL-COM-DAQ-2017-066, CERN, 2017, URL: https://cds.cern.ch/record/2272031 (cit. on p. 82).

[51] L. Dell'Asta and S. M. Shaw, *Muon trigger public plots with full 2016 dataset*, tech. rep. ATL-COM-DAQ-2017-005, CERN, 2017, URL: https://cds.cern.ch/record/2242824 (cit. on p. 82).

[52] P. Fayet, *Supersymmetry and Weak, Electromagnetic and Strong Interactions*, Phys. Lett. B **64** (1976) 159 (cit. on p. 85).

[53] P. Fayet, *Spontaneously Broken Supersymmetric Theories of Weak, Electromagnetic and Strong Interactions*, Phys. Lett. B **69** (1977) 489 (cit. on p. 85).

[54] G. R. Farrar and P. Fayet, *Phenomenology of the Production, Decay, and Detection of New Hadronic States Associated with Supersymmetry*, Phys. Lett. B **76** (1978) 575 (cit. on p. 85).

[55] R. Barbieri and G. F. Giudice, *Upper Bounds on Supersymmetric Particle Masses*, Nucl. Phys. B **306** (1988) 63 (cit. on p. 86).

[56] M. Aaboud et al., *Search for direct top squark pair production in final states with two leptons in* $\sqrt{s} = 13\,TeV$ *pp collisions with the ATLAS detector*, The European Physical Journal C **77** (2017), ISSN: 1434-6052, URL: http://dx.doi.org/10.1140/epjc/s10052-017-5445-x (cit. on p. 86).

[57] *https://twiki.cern.ch/twiki/bin/view/AtlasPublic/SupersymmetryPublicResults* (cit. on p. 90).

[58] ATLAS Collaboration, *Simulation of top-quark production for the ATLAS experiment at* $\sqrt{s} = 13$ *TeV*, ATL-PHYS-PUB-2016-004, 2016, URL: https://cds.cern.ch/record/2120417 (cit. on p. 92).

[59] M. Czakon and A. Mitov, *Top++: A Program for the Calculation of the Top-Pair Cross-Section at Hadron Colliders*, Comput.Phys.Commun. **185** (2014) 2930, arXiv: 1112.5675 [hep-ph] (cit. on p. 92).

[60] T. Gleisberg et al., *Event generation with SHERPA 1.1*, JHEP **0902** (2009) 007, arXiv: 0811.4622 [hep-ph] (cit. on pp. 92, 93).

[61] J. Alwall et al., *MadGraph5: going beyond*, JHEP **06** (2011) 128, arXiv: 1106.0522 (cit. on p. 93).

[62] T. Sjöstrand et al., *An Introduction to PYTHIA 8.2*, Comput. Phys. Commun. **191** (2015) 159, arXiv: 1410.3012 (cit. on p. 93).

[63] P. Artoisenet, R. Frederix, O. Mattelaer, R. Rietkerk, *Automatic spin-entangled decays of heavy resonances in Monte Carlo simulations*, Journal of High Energy Physics **03** (2013) 015, arXiv: 1212.3460v2 (cit. on p. 93).

[64] ATLAS Collaboration, *The simulation principle and performance of the ATLAS fast calorimeter simulation FastCaloSim*, ATL-PHYS-PUB-2010-013, 2010, URL: https://cds.cern.ch/record/1300517 (cit. on p. 94).

[65] ATLAS Collaboration, *Selection of jets produced in* 13 *TeV proton–proton collisions with the ATLAS detector*, ATLAS-CONF-2015-029, 2015, URL: https://cds.cern.ch/record/2037702 (cit. on pp. 96, 100).

[66] ATLAS Collaboration, *Muon reconstruction performance in early* $\sqrt{s} =$ 13 *TeV data*, ATL-PHYS-PUB-2015-037, 2015, URL: https://cds.cern.ch/record/2047831 (cit. on p. 98).

[67] ATLAS Collaboration, *Tagging and suppression of pileup jets with the ATLAS detector*, ATLAS-CONF-2014-018, 2014, URL: https://cds.cern.ch/record/1700870 (cit. on p. 99).

[68] J. Gonski, *Jet Cleaning in 2016 and the Event Level Cleaning Tool*, ATL-COM-PHYS-2017-982, 2017, URL: https://cds.cern.ch/record/2272136?ln=it (cit. on p. 100).

[69] ATLAS Collaboration, *Optimisation of the ATLAS b-tagging performance for the 2016 LHC Run*, ATL-PHYS-PUB-2016-012, 2016, URL: https://cds.cern.ch/record/2160731 (cit. on p. 100).

[70] ATLAS Collaboration, *Performance of b-jet identification in the ATLAS experiment*, JINST **11** (2016) P04008, arXiv: 1512.01094 [hep-ex] (cit. on p. 100).

[71] *https://twiki.cern.ch/twiki/bin/viewauth/AtlasProtected/MetSignificance* (cit. on p. 101).

[72] ATLAS Collaboration, *Search for bottom-squark pair production with the ATLAS detector in final states containing Higgs bosons, b-jets and missing transverse momentum in pp collisions at* $\sqrt{s} = 13$ *TeV*, ATLAS-CONF-2018-040, 2018, URL: https://cds.cern.ch/record/2632345 (cit. on p. 101).

[73] ATLAS Internal, *PhysicsAnalysis/AnalysisCommon/AssociationUtils - Overlap removal tools*, 2019, URL: https://gitlab.cern.ch/atlas/athena/tree/21.2/PhysicsAnalysis/AnalysisCommon/AssociationUtils#configuration-helpers (cit. on p. 101).

[74] *PMG Systematic Uncertainty Recommendations*, URL: https://twiki.cern.ch/twiki/bin/view/AtlasProtected/PmgSystematicUncertaintyRecipes (cit. on p. 107).

[75] *SUSY Systematic Uncertainty Recommendations*, URL: https://twiki.cern.ch/twiki/bin/viewauth/AtlasProtected/SUSYTheoreticalUncertainties (cit. on p. 107).

[76] *SUSY Third Generation Systematic Uncertainty Recommendations*, URL: https://twiki.cern.ch/twiki/bin/view/AtlasProtected/ThirdGenTheoreticalUncertaint (cit. on p. 107).

[77] P. Jackson and C. Rogan, *Recursive jigsaw reconstruction: HEP event analysis in the presence of kinematic and combinatoric ambiguities*, Phys. Rev. D **96** (11 2017) 112007, URL: https://link.aps.org/doi/10.1103/PhysRevD.96.112007 (cit. on p. 110).

[78] M. R. Buckley, J. D. Lykken, C. Rogan, and M. Spiropulu, *Super-razor and searches for sleptons and charginos at the LHC*, Physical Review D **89** (2014), ISSN: 1550-2368, URL: http://dx.doi.org/10.1103/PhysRevD.89.055020 (cit. on p. 110).

[79] ATLAS Collaboration, *Search for direct top squark pair production in final states with two leptons in $\sqrt{s} = 13$ TeV pp collisions using 3.2 fb^{-1} of ATLAS data*, ATLAS-CONF-2016-009, 2016, URL: https://cds.cern.ch/record/2139643 (cit. on p. 141).

[80] A. Hocker et al., *TMVA - Toolkit for Multivariate Data Analysis*, (2007), arXiv: physics/0703039 (cit. on pp. 160, 161).

[81] G. Marsaglia, W. W. Tsang, and J. Wang, *Evaluating Kolmogorov's Distribution*, Journal of Statistical Software, Articles **8** (2003) 1, ISSN: 1548-7660, URL: https://www.jstatsoft.org/v008/i18 (cit. on p. 169).

[82] L. Breiman, J. Friedman, R. Olshen, and C. Stone, *Classification and Regression Trees*, new edition [**cart93**]? Wadsworth and Brooks, 1984 (cit. on p. 171).

[83] G. Cowan, K. Cranmer, E. Gross, and O. Vitells, *Asymptotic formulae for likelihood-based tests of new physics*, The European Physical Journal C **71** (2011), ISSN: 1434-6052, URL: http://dx.doi.org/10.1140/epjc/s10052-011-1554-0 (cit. on p. 182).

[84] M. Baak et al., *HistFitter software framework for statistical data analysis*, The European Physical Journal C **75** (2015), ISSN: 1434-6052, URL: http://dx.doi.org/10.1140/epjc/s10052-015-3327-7 (cit. on p. 185).

[85] K. Cranmer, G. Lewis, L. Moneta, A. Shibata, and W. Verkerke, *HistFactory: A tool for creating statistical models for use with RooFit and RooStats*, tech. rep. CERN-OPEN-2012-016, New York U., 2012, URL: https://cds.cern.ch/record/1456844 (cit. on p. 185).

Appendices

Appendix A

Background Samples

In this appendix we gather all of the detailed information about the background samples used.

In order to avoid duplicating the same dataset for all MC campaigns in the following tables, the r-tag is replaced by rX, which stands for *r9364* for mc16a, rX for mc16d, and *r10724* for mc16e, unless explicitly stated.

Category	Name	σ [pb]	MC16 tag
$t\bar{t}$	PhPy8EG_A14_ttbar_hdamp258p75_dil	87.674	DAOD_SUSY2.e6348_s3126_rX_p3703
	PhPy8EG_A14_ttbarMET200_300_hdamp258p75_nonallhad	6.71031	DAOD_SUSY2.e6414_s3126_rX_p3875
	PhPy8EG_A14_ttbarMET300_400_hdamp258p75_nonallhad	0.93082	DAOD_SUSY2.e6414_s3126_rX_p3875
	PhPy8EG_A14_ttbarMET400_hdamp258p75_nonallhad	0.26125	DAOD_SUSY2.e6414_s3126_rX_p3875
Wt	PowhegPythia8EvtGen_A14_Wt_DR_dilepton_top	3.7776	DAOD_SUSY2.e6615_s3126_rX_p3703
	PowhegPythia8EvtGen_A14_Wt_DR_dilepton_antitop	3.7774	DAOD_SUSY2.e6615_s3126_rX_p3703
	PowhegPythia8EvtGen_A14_Wt_DR_inclusive_top_MET200	0.3202	DAOD_SUSY2.e7219_s3126_rX_p3703
	PowhegPythia8EvtGen_A14_Wt_DR_inclusive_top_MET300	0.0628	DAOD_SUSY2.e7219_s3126_rX_p3703
	PowhegPythia8EvtGen_A14_Wt_DR_inclusive_top_MET400	0.0289	DAOD_SUSY2.e7219_s3126_rX_p3703
	PowhegPythia8EvtGen_A14_Wt_DR_inclusive_antitop_MET200	0.3171	DAOD_SUSY2.e7219_s3126_rX_p3703
	PowhegPythia8EvtGen_A14_Wt_DR_inclusive_antitop_MET300	0.0620	DAOD_SUSY2.e7219_s3126_rX_p3703
	PowhegPythia8EvtGen_A14_Wt_DR_inclusive_antitop_MET400	0.0284	DAOD_SUSY2.e7219_s3126_rX_p3703
$t\bar{t}+Z$	aMcAtNloPythia8EvtGen_MEN30NLO_A14N23LO_ttZnunu	0.17212	DAOD_SUSY2.e5070_s3126_rX_p3875
	aMcAtNloPythia8EvtGen_MEN30NLO_A14N23LO_ttZqq	0.58631	DAOD_SUSY2.e5070_s3126_rX_p3875
	aMcAtNloPythia8EvtGen_MEN30NLO_A14N23LO_ttee	0.04129	DAOD_SUSY2.e5070_s3126_rX_p3875
	aMcAtNloPythia8EvtGen_MEN30NLO_A14N23LO_ttmumu	0.04129	DAOD_SUSY2.e5070_s3126_rX_p3875
	aMcAtNloPythia8EvtGen_MEN30NLO_A14N23LO_tttautau	0.04094	DAOD_SUSY2.e5070_s3126_rX_p3875
VV	Sherpa_222_NNPDF30NNLO_gglll_0M4l130	0.0100	DAOD_SUSY2.e6213_s3126_rX_p3875
	Sherpa_222_NNPDF30NNLO_gglll_130M4l	0.0102	DAOD_SUSY2.e6213_s3126_rX_p3875
	Sherpa_222_NNPDF30NNLO_ggllvvInt	0.2685	DAOD_SUSY2.e6525_s3126_r9364_p3875
			DAOD_SUSY2.e6525_s3126_rX_p3703
			DAOD_SUSY2.e6525_s3126_r10724_p3703
	Sherpa_222_NNPDF30NNLO_ggllvvWW	0.4823	DAOD_SUSY2.e6525_s3126_rX_p3703
	Sherpa_222_NNPDF30NNLO_ggllvvZZ	0.0071	DAOD_SUSY2.e6213_s3126_rX_p3736
	Sherpa_221_NNPDF30NNLO_ZqqZvv	4.3079	DAOD_SUSY2.e5525_s3126_rX_p3875
	Sherpa_221_NNPDF30NNLO_ZqqZll	2.2036	DAOD_SUSY2.e5525_s3126_rX_p3875
	Sherpa_221_NNPDF30NNLO_WqqZvv	6.7951	DAOD_SUSY2.e5525_s3126_rX_p3895
	Sherpa_221_NNPDF30NNLO_WqqZll	3.4328	DAOD_SUSY2.e5525_s3126_rX_p3875
	Sherpa_221_NNPDF30NNLO_WpqqWmlv	24.708	DAOD_SUSY2.e5583_s3126_rX_p3875
	Sherpa_221_NNPDF30NNLO_WplvWmqq	24.724	DAOD_SUSY2.e5983_s3126_rX_p3875
	Sherpa_221_NNPDF30NNLO_WlvZqq	11.42	DAOD_SUSY2.e5525_s3126_rX_p3875
	Sherpa_221_NNPDF30NNLO_vvvv	0.6029	DAOD_SUSY2.e5332_s3126_rX_p3875
	Sherpa_222_NNPDF30NNLO_llll	0.9397	DAOD_SUSY2.e5894_s3126_rX_p3875
	Sherpa_222_NNPDF30NNLO_lllv	4.5765	DAOD_SUSY2.e5916_s3126_rX_p3875
	Sherpa_222_NNPDF30NNLO_llvv	12.501	DAOD_SUSY2.e5916_s3126_rX_p3875
	Sherpa_222_NNPDF30NNLO_lvvv	3.2344	DAOD_SUSY2.e5916_s3126_rX_p3875
	Sherpa_222_NNPDF30NNLO_llljj_EW6	0.0105	DAOD_SUSY2.e6055_s3126_rX_p3875
	Sherpa_222_NNPDF30NNLO_lllvjj_EW6	0.0471	DAOD_SUSY2.e6055_s3126_rX_p3875
	Sherpa_222_NNPDF30NNLO_llvvjj_EW6	0.1163	DAOD_SUSY2.e6055_s3126_rX_p3875
	Sherpa_222_NNPDF30NNLO_llvvjj_ss_EW4	0.0252	DAOD_SUSY2.e6055_s3126_r9364_p3875
			DAOD_SUSY2.e6055_s3126_rX_p3875
			DAOD_SUSY2.e6055_s3126_r10724_p3736
	Sherpa_222_NNPDF30NNLO_llvvjj_ss_EW6	0.0408	DAOD_SUSY2.e6055_s3126_rX_p3875
	Sherpa_222_NNPDF30NNLO_llll_lowMllPtComplement	1.4496	DAOD_SUSY2.e6096_s3126_rX_p3875
	Sherpa_222_NNPDF30NNLO_lllv_lowMllPtComplement	2.9599	DAOD_SUSY2.e6133_s3126_rX_p3875
	Sherpa_222_NNPDF30NNLO_llvv_lowMllPtComplement	0.1715	DAOD_SUSY2.e6096_s3126_rX_p3875
	Sherpa_222_NNPDF30NNLO_ggZllZqq	0.1307	DAOD_SUSY2.e6273_s3126_r9364_p3736
	Sherpa_222_NNPDF30NNLO_ggWmlvWpqq	0.6219	DAOD_SUSY2.e6273_s3126_rX_p3703
	Sherpa_222_NNPDF30NNLO_ggWplvWmqq	0.6219	DAOD_SUSY2.e6273_s3126_rX_p3703

Table A.1: Summary table of the MC16 samples used for top processes.

Category / SubCategory	Name	σ [pb]	MC16 tag
Z/γ^*+jets / $Z/\gamma^*(\rightarrow e^+e^-)$+jets	Sherpa_221_NNPDF30NNLO_Zee2jets_Min_N_TChannel	0.6320	DAOD_SUSY2.e5767_s3126_rX_p3875
	Sherpa_221_NNPDF30NNLO_Zee_MAXHTPTV0_70_CVetoBVeto	1587.02	DAOD_SUSY2.e5299_s3126_rX_p3875
	Sherpa_221_NNPDF30NNLO_Zee_MAXHTPTV0_70_CFilterBVeto	219.996	DAOD_SUSY2.e5299_s3126_rX_p3875
	Sherpa_221_NNPDF30NNLO_Zee_MAXHTPTV0_70_BFilter	127.085	DAOD_SUSY2.e5299_s3126_rX_p3875
	Sherpa_221_NNPDF30NNLO_Zee_MAXHTPTV70_140_CVetoBVeto	74.9003	DAOD_SUSY2.e5299_s3126_rX_p3875
	Sherpa_221_NNPDF30NNLO_Zee_MAXHTPTV70_140_CFilterBVeto	20.316	DAOD_SUSY2.e5299_s3126_rX_p3875
	Sherpa_221_NNPDF30NNLO_Zee_MAXHTPTV70_140_BFilter	12.7388	DAOD_SUSY2.e5299_s3126_rX_p3875
	Sherpa_221_NNPDF30NNLO_Zee_MAXHTPTV140_280_CVetoBVeto	24.4198	DAOD_SUSY2.e5299_s3126_rX_p3875
	Sherpa_221_NNPDF30NNLO_Zee_MAXHTPTV140_280_CFilterBVeto	9.2368	DAOD_SUSY2.e5299_s3126_rX_p3875
	Sherpa_221_NNPDF30NNLO_Zee_MAXHTPTV140_280_BFilter	6.0812	DAOD_SUSY2.e5299_s3126_rX_p3875
	Sherpa_221_NNPDF30NNLO_Zee_MAXHTPTV280_500_CVetoBVeto	4.7969	DAOD_SUSY2.e5299_s3126_rX_p3875
	Sherpa_221_NNPDF30NNLO_Zee_MAXHTPTV280_500_CFilterBVeto	2.2497	DAOD_SUSY2.e5299_s3126_rX_p3875
	Sherpa_221_NNPDF30NNLO_Zee_MAXHTPTV280_500_BFilter	1.4943	DAOD_SUSY2.e5299_s3126_rX_p3875
	Sherpa_221_NNPDF30NNLO_Zee_MAXHTPTV500_1000	1.7641	DAOD_SUSY2.e5299_s3126_rX_p3875
	Sherpa_221_NNPDF30NNLO_Zee_MAXHTPTV1000_E_CMS	0.1450	DAOD_SUSY2.e5299_s3126_rX_p3875
	Sherpa_221_NN30NNLO_Zee_Mll10_40_MAXHTPTV0_70_BVeto	2273.2	DAOD_SUSY2.e5421_s3126_rX_p3875
	Sherpa_221_NN30NNLO_Zee_Mll10_40_MAXHTPTV0_70_BFilter	81.721	DAOD_SUSY2.e5421_s3126_rX_p3875
	Sherpa_221_NN30NNLO_Zee_Mll10_40_MAXHTPTV70_280_BVeto	43.8563	DAOD_SUSY2.e5421_s3126_rX_p3875
	Sherpa_221_NN30NNLO_Zee_Mll10_40_MAXHTPTV70_280_BFilter	5.2714	DAOD_SUSY2.e5421_s3126_rX_p3875
	Sherpa_221_NN30NNLO_Zee_Mll10_40_MAXHTPTV280_E_CMS_BVeto	2.7123	DAOD_SUSY2.e5421_s3126_rX_p3875
	Sherpa_221_NN30NNLO_Zee_Mll10_40_MAXHTPTV280_E_CMS_BFilter	0.4869	DAOD_SUSY2.e5421_s3126_rX_p3875
	Sherpa_221_NNPDF30NNLO_Zee_Mll2Ml_MAXHTPTV280_E_CMS	44.8848	DAOD_SUSY2.e6037_s3126_rX_p3895
	Sherpa_221_NNPDF30NNLO_Zee_Mll2Ml_MAXHTPTV70_140	568.54	DAOD_SUSY2.e6544_a875_rX_p3895
	Sherpa_221_NNPDF30NNLO_Zee_Mll2Ml_MAXHTPTV140_280	206.81	DAOD_SUSY2.e6544_a875_rX_p3895
Z/γ^*+jets / $Z/\gamma^*(\rightarrow \mu^+\mu^-)$+jets	Sherpa_221_NNPDF30NNLO_Zmm2jets_Min_N_TChannel	0.6343	DAOD_SUSY2.e5767_s3126_rX_p3875
	Sherpa_221_NNPDF30NNLO_Zmumu_MAXHTPTV0_70_CVetoBVeto	1588.5	DAOD_SUSY2.e5271_s3126_rX_p3875
	Sherpa_221_NNPDF30NNLO_Zmumu_MAXHTPTV0_70_CFilterBVeto	219.474	DAOD_SUSY2.e5271_s3126_rX_p3875
	Sherpa_221_NNPDF30NNLO_Zmumu_MAXHTPTV0_70_BFilter	126.937	DAOD_SUSY2.e5271_s3126_rX_p3875
	Sherpa_221_NNPDF30NNLO_Zmumu_MAXHTPTV70_140_CVetoBVeto	73.423	DAOD_SUSY2.e5271_s3126_rX_p3875
	Sherpa_221_NNPDF30NNLO_Zmumu_MAXHTPTV70_140_CFilterBVeto	20.8973	DAOD_SUSY2.e5271_s3126_rX_p3875
	Sherpa_221_NNPDF30NNLO_Zmumu_MAXHTPTV70_140_BFilter	10.9903	DAOD_SUSY2.e5271_s3126_rX_p3875
	Sherpa_221_NNPDF30NNLO_Zmumu_MAXHTPTV140_280_CVetoBVeto	23.3038	DAOD_SUSY2.e5271_s3126_rX_p3875
	Sherpa_221_NNPDF30NNLO_Zmumu_MAXHTPTV140_280_CFilterBVeto	9.1437	DAOD_SUSY2.e5271_s3126_rX_p3875
	Sherpa_221_NNPDF30NNLO_Zmumu_MAXHTPTV140_280_BFilter	5.5826	DAOD_SUSY2.e5271_s3126_rX_p3875
	Sherpa_221_NNPDF30NNLO_Zmumu_MAXHTPTV280_500_CVetoBVeto	4.6574	DAOD_SUSY2.e5271_s3126_rX_p3875
	Sherpa_221_NNPDF30NNLO_Zmumu_MAXHTPTV280_500_CFilterBVeto	2.2148	DAOD_SUSY2.e5271_s3126_rX_p3875
	Sherpa_221_NNPDF30NNLO_Zmumu_MAXHTPTV280_500_BFilter	1.4686	DAOD_SUSY2.e5271_s3126_rX_p3875
	Sherpa_221_NNPDF30NNLO_Zmumu_MAXHTPTV500_1000	1.7425	DAOD_SUSY2.e5271_s3126_rX_p3875
	Sherpa_221_NNPDF30NNLO_Zmumu_MAXHTPTV1000_E_CMS	0.1439	DAOD_SUSY2.e5271_s3126_rX_p3875
	Sherpa_221_NN30NNLO_Zmm_Mll10_40_MAXHTPTV0_70_BVeto	2272.63	DAOD_SUSY2.e5421_s3126_rX_p3875
	Sherpa_221_NN30NNLO_Zmm_Mll10_40_MAXHTPTV0_70_BFilter	81.0865	DAOD_SUSY2.e5421_s3126_rX_p3875
	Sherpa_221_NN30NNLO_Zmm_Mll10_40_MAXHTPTV70_280_BVeto	43.8285	DAOD_SUSY2.e5421_s3126_rX_p3875
	Sherpa_221_NN30NNLO_Zmm_Mll10_40_MAXHTPTV70_280_BFilter	5.4981	DAOD_SUSY2.e5421_s3126_rX_p3875
	Sherpa_221_NN30NNLO_Zmm_Mll10_40_MAXHTPTV280_E_CMS_BVeto	2.6970	DAOD_SUSY2.e5421_s3126_rX_p3875
	Sherpa_221_NN30NNLO_Zmm_Mll10_40_MAXHTPTV280_E_CMS_BFilter	0.5128	DAOD_SUSY2.e5421_s3126_rX_p3875
	Sherpa_221_NNPDF30NNLO_Zmumu_Mll2Ml_MAXHTPTV280_E_CMS	35.4712	DAOD_SUSY2.e6037_s3126_rX_p3895
	Sherpa_221_NNPDF30NNLO_Zmumu_Mll2Ml_MAXHTPTV70_140	458.51	DAOD_SUSY2.e6544_a875_rX_p3895
	Sherpa_221_NNPDF30NNLO_Zmumu_Mll2Ml_MAXHTPTV140_280	163.96	DAOD_SUSY2.e6544_a875_rX_p3895
Z/γ^*+jets / $Z/\gamma^*(\rightarrow \tau^+\tau^-)$+jets	Sherpa_221_NNPDF30NNLO_Ztautau2jets_Min_N_TChannel	0.6335	DAOD_SUSY2.e5767_s3126_rX_p3875
	Sherpa_221_NNPDF30NNLO_Ztautau_MAXHTPTV0_70_CVetoBVeto	1612.68	DAOD_SUSY2.e5307_s3126_rX_p3875
	Sherpa_221_NNPDF30NNLO_Ztautau_MAXHTPTV0_70_CFilterBVeto	219.634	DAOD_SUSY2.e5307_s3126_rX_p3875
	Sherpa_221_NNPDF30NNLO_Ztautau_MAXHTPTV0_70_BFilter	126.854	DAOD_SUSY2.e5307_s3126_rX_p3875
	Sherpa_221_NNPDF30NNLO_Ztautau_MAXHTPTV70_140_CVetoBVeto	74.739	DAOD_SUSY2.e5307_s3126_rX_p3875
	Sherpa_221_NNPDF30NNLO_Ztautau_MAXHTPTV70_140_CFilterBVeto	20.5294	DAOD_SUSY2.e5307_s3126_rX_p3875
	Sherpa_221_NNPDF30NNLO_Ztautau_MAXHTPTV70_140_BFilter	9.9918	DAOD_SUSY2.e5307_s3126_rX_p3875
	Sherpa_221_NNPDF30NNLO_Ztautau_MAXHTPTV140_280_CVetoBVeto	24.5918	DAOD_SUSY2.e5307_s3126_rX_p3875
	Sherpa_221_NNPDF30NNLO_Ztautau_MAXHTPTV140_280_CFilterBVeto	9.3030	DAOD_SUSY2.e5307_s3126_rX_p3875
	Sherpa_221_NNPDF30NNLO_Ztautau_MAXHTPTV140_280_BFilter	5.6678	DAOD_SUSY2.e5307_s3126_rX_p3875
	Sherpa_221_NNPDF30NNLO_Ztautau_MAXHTPTV280_500_CVetoBVeto	4.7649	DAOD_SUSY2.e5307_s3126_rX_p3875
	Sherpa_221_NNPDF30NNLO_Ztautau_MAXHTPTV280_500_CFilterBVeto	2.2361	DAOD_SUSY2.e5313_s3126_rX_p3875
	Sherpa_221_NNPDF30NNLO_Ztautau_MAXHTPTV280_500_BFilter	1.4895	DAOD_SUSY2.e5313_s3126_rX_p3875
	Sherpa_221_NNPDF30NNLO_Ztautau_MAXHTPTV500_1000	1.7628	DAOD_SUSY2.e5307_s3126_rX_p3875
	Sherpa_221_NNPDF30NNLO_Ztautau_MAXHTPTV1000_E_CMS	0.1446	DAOD_SUSY2.e5307_s3126_rX_p3875
	Sherpa_221_NN30NNLO_Ztt_Mll10_40_MAXHTPTV0_70_BVeto	2274.19	DAOD_SUSY2.e5421_s3126_rX_p3875
	Sherpa_221_NN30NNLO_Ztt_Mll10_40_MAXHTPTV0_70_BFilter	81.6371	DAOD_SUSY2.e5421_s3126_rX_p3875
	Sherpa_221_NN30NNLO_Ztt_Mll10_40_MAXHTPTV70_280_BVeto	43.8705	DAOD_SUSY2.e5421_s3126_rX_p3875
	Sherpa_221_NN30NNLO_Ztt_Mll10_40_MAXHTPTV70_280_BFilter	5.3246	DAOD_SUSY2.e5421_s3126_rX_p3875
	Sherpa_221_NN30NNLO_Ztt_Mll10_40_MAXHTPTV280_E_CMS_BVeto	2.7406	DAOD_SUSY2.e5421_s3126_rX_p3875
	Sherpa_221_NN30NNLO_Ztt_Mll10_40_MAXHTPTV280_E_CMS_BFilter	0.4985	DAOD_SUSY2.e5421_s3126_rX_p3875
	Sherpa_221_NNPDF30NNLO_Ztautau_Mll2Ml_MAXHTPTV280_E_CMS	9.1472	DAOD_SUSY2.e6037_s3126_rX_p3895
	Sherpa_221_NNPDF30NNLO_Ztautau_Mll2Ml_MAXHTPTV70_140	140.71	DAOD_SUSY2.e6544_a875_rX_p3895
	Sherpa_221_NNPDF30NNLO_Ztautau_Mll2Ml_MAXHTPTV140_280	43.265	DAOD_SUSY2.e6544_a875_rX_p3895

Table A.2: Summary table of the MC16 samples used for top processes.

Category / SubCategory	Name	σ [pb]	MC16 tag
Others / $t\bar{t}H$	PhPy8EG_A14NNPDF23_NNPDF30ME_ttH125_dilep	0.056	DAOD_SUSY2.e7148_s3126_rX_p3793
Others / tZ	aMcAtNloPythia8EvtGen_tllq_NNPDF30_nf4_A14	0.0289	DAOD_SUSY2.e7054_s3126_rX_p3749
	aMcAtNloPythia8EvtGen_tWZ_Ztoll_minDR1	0.016071	DAOD_SUSY2.e6423_s3126_rX_p3895
Others / $t\bar{t}WW$	MadGraphPythia8EvtGen_A14NNPDF23_ttbarWW	0.00990	DAOD_SUSY2.e4111_s3126_rX_p3875
Others / $t\bar{t}W$	aMcAtNloPythia8EvtGen_MEN30NLO_A14N23LO_ttW	0.60085	DAOD_SUSY2.e5070_s3126_rX_p3875
Others / $t\bar{t}t$	MadGraphPythia8EvtGen_A14NNPDF23_3top_SM	0.00164	DAOD_SUSY2.e4324_s3126_rX_p3875
Others / $t\bar{t}t\bar{t}$	MadGraphPythia8EvtGen_A14NNPDF23_4topSM	0.00920	DAOD_SUSY2.e4111_s3126_rX_p3875
Others / VVV	Sherpa_222_NNPDF30NNLO_WWW_3l3v_EW6	7.20e-03	DAOD_SUSY2.e5887_s3126_rX_p3875
	Sherpa_222_NNPDF30NNLO_WWZ_4l2v_EW6	1.80e-03	DAOD_SUSY2.e5887_s3126_rX_p3875
	Sherpa_222_NNPDF30NNLO_WWZ_2l4v_EW6	3.55e-03	DAOD_SUSY2.e5887_s3126_rX_p3875
	Sherpa_222_NNPDF30NNLO_WZZ_5l1v_EW6	0.19e-03	DAOD_SUSY2.e5887_s3126_rX_p3875
	Sherpa_222_NNPDF30NNLO_WZZ_3l3v_EW6	0.74e-03	DAOD_SUSY2.e5887_s3126_rX_p3875
	Sherpa_222_NNPDF30NNLO_ZZZ_6l0v_EW6	1.45e-05	DAOD_SUSY2.e5887_s3126_rX_p3875
	Sherpa_222_NNPDF30NNLO_ZZZ_4l2v_EW6	8.65e-05	DAOD_SUSY2.e5887_s3126_rX_p3875
	Sherpa_222_NNPDF30NNLO_ZZZ_2l4v_EW6	0.17e-03	DAOD_SUSY2.e5887_s3126_rX_p3875

Table A.3: Summary table of the MC16 samples used for top processes.

Category / SubCategory	Name	σ [pb]	MC16 tag
Others / $W(\to e\nu)$+jets	Sherpa_221_NNPDF30NNLO_Wenu2jets_Min_N_TChannel	6.8063	DAOD_SUSY2.e5789_s3126_rX_p3875
	Sherpa_221_NNPDF30NNLO_Wenu_MAXHTPTV0_70_CVetoBVeto	15324.2	DAOD_SUSY2.e5340_s3126_rX_p3875
	Sherpa_221_NNPDF30NNLO_Wenu_MAXHTPTV0_70_CFilterBVeto	2430.66	DAOD_SUSY2.e5340_s3126_rX_p3875
	Sherpa_221_NNPDF30NNLO_Wenu_MAXHTPTV0_70_BFilter	832.204	DAOD_SUSY2.e5340_s3126_rX_p3875
	Sherpa_221_NNPDF30NNLO_Wenu_MAXHTPTV70_140_CVetoBVeto	618.697	DAOD_SUSY2.e5340_s3126_rX_p3875
	Sherpa_221_NNPDF30NNLO_Wenu_MAXHTPTV70_140_CFilterBVeto	224.003	DAOD_SUSY2.e5340_s3126_rX_p3875
	Sherpa_221_NNPDF30NNLO_Wenu_MAXHTPTV70_140_BFilter	94.8876	DAOD_SUSY2.e5340_s3126_rX_p3875
	Sherpa_221_NNPDF30NNLO_Wenu_MAXHTPTV140_280_CVetoBVeto	197.307	DAOD_SUSY2.e5340_s3126_rX_p3875
	Sherpa_221_NNPDF30NNLO_Wenu_MAXHTPTV140_280_CFilterBVeto	94.9626	DAOD_SUSY2.e5340_s3126_rX_p3875
	Sherpa_221_NNPDF30NNLO_Wenu_MAXHTPTV140_280_BFilter	35.911	DAOD_SUSY2.e5340_s3126_rX_p3875
	Sherpa_221_NNPDF30NNLO_Wenu_MAXHTPTV280_500_CVetoBVeto	38.3405	DAOD_SUSY2.e5340_s3126_rX_p3875
	Sherpa_221_NNPDF30NNLO_Wenu_MAXHTPTV280_500_CFilterBVeto	22.3643	DAOD_SUSY2.e5340_s3126_rX_p3875
	Sherpa_221_NNPDF30NNLO_Wenu_MAXHTPTV280_500_BFilter	9.5863	DAOD_SUSY2.e5340_s3126_rX_p3875
	Sherpa_221_NNPDF30NNLO_Wenu_MAXHTPTV500_1000	14.5986	DAOD_SUSY2.e5340_s3126_rX_p3875
	Sherpa_221_NNPDF30NNLO_Wenu_MAXHTPTV1000_E_CMS	1.1976	DAOD_SUSY2.e5340_s3126_rX_p3875
Others / $W(\to \mu\nu)$+jets	Sherpa_221_NNPDF30NNLO_Wmunu2jets_Min_N_TChannel	6.7968	DAOD_SUSY2.e5767_s3126_rX_p3875
	Sherpa_221_NNPDF30NNLO_Wmunu_MAXHTPTV0_70_CVetoBVeto	15317.9	DAOD_SUSY2.e5340_s3126_rX_p3875
	Sherpa_221_NNPDF30NNLO_Wmunu_MAXHTPTV0_70_CFilterBVeto	2431.2	DAOD_SUSY2.e5340_s3126_rX_p3875
	Sherpa_221_NNPDF30NNLO_Wmunu_MAXHTPTV0_70_BFilter	828.88	DAOD_SUSY2.e5340_s3126_rX_p3875
	Sherpa_221_NNPDF30NNLO_Wmunu_MAXHTPTV70_140_CVetoBVeto	618.565	DAOD_SUSY2.e5340_s3126_rX_p3875
	Sherpa_221_NNPDF30NNLO_Wmunu_MAXHTPTV70_140_CFilterBVeto	223.358	DAOD_SUSY2.e5340_s3126_rX_p3875
	Sherpa_221_NNPDF30NNLO_Wmunu_MAXHTPTV70_140_BFilter	76.728	DAOD_SUSY2.e5340_s3126_rX_p3875
	Sherpa_221_NNPDF30NNLO_Wmunu_MAXHTPTV140_280_CVetoBVeto	197.793	DAOD_SUSY2.e5340_s3126_rX_p3875
	Sherpa_221_NNPDF30NNLO_Wmunu_MAXHTPTV140_280_CFilterBVeto	96.4494	DAOD_SUSY2.e5340_s3126_rX_p3875
	Sherpa_221_NNPDF30NNLO_Wmunu_MAXHTPTV140_280_BFilter	36.3453	DAOD_SUSY2.e5340_s3126_rX_p3875
	Sherpa_221_NNPDF30NNLO_Wmunu_MAXHTPTV280_500_CVetoBVeto	38.2998	DAOD_SUSY2.e5340_s3126_rX_p3875
	Sherpa_221_NNPDF30NNLO_Wmunu_MAXHTPTV280_500_CFilterBVeto	22.3956	DAOD_SUSY2.e5340_s3126_rX_p3875
	Sherpa_221_NNPDF30NNLO_Wmunu_MAXHTPTV280_500_BFilter	8.7682	DAOD_SUSY2.e5340_s3126_rX_p3875
	Sherpa_221_NNPDF30NNLO_Wmunu_MAXHTPTV500_1000	14.5588	DAOD_SUSY2.e5340_s3126_rX_p3875
	Sherpa_221_NNPDF30NNLO_Wmunu_MAXHTPTV1000_E_CMS	1.198	DAOD_SUSY2.e5340_s3126_rX_p3875
Others / $W(\to \tau\nu)$+jets	Sherpa_221_NNPDF30NNLO_Wtaunu2jets_Min_N_TChannel	6.7976	DAOD_SUSY2.e5767_s3126_rX_p3875
	Sherpa_221_NNPDF30NNLO_Wtaunu_MAXHTPTV0_70_CVetoBVeto	15324.9	DAOD_SUSY2.e5340_s3126_rX_p3875
	Sherpa_221_NNPDF30NNLO_Wtaunu_MAXHTPTV0_70_CFilterBVeto	2443.43	DAOD_SUSY2.e5340_s3126_rX_p3875
	Sherpa_221_NNPDF30NNLO_Wtaunu_MAXHTPTV0_70_BFilter	837.628	DAOD_SUSY2.e5340_s3126_rX_p3875
	Sherpa_221_NNPDF30NNLO_Wtaunu_MAXHTPTV70_140_CVetoBVeto	619.448	DAOD_SUSY2.e5340_s3126_rX_p3875
	Sherpa_221_NNPDF30NNLO_Wtaunu_MAXHTPTV70_140_CFilterBVeto	222.595	DAOD_SUSY2.e5340_s3126_rX_p3875
	Sherpa_221_NNPDF30NNLO_Wtaunu_MAXHTPTV70_140_BFilter	95.3403	DAOD_SUSY2.e5340_s3126_rX_p3875
	Sherpa_221_NNPDF30NNLO_Wtaunu_MAXHTPTV140_280_CVetoBVeto	197.358	DAOD_SUSY2.e5340_s3126_rX_p3875
	Sherpa_221_NNPDF30NNLO_Wtaunu_MAXHTPTV140_280_CFilterBVeto	93.8956	DAOD_SUSY2.e5340_s3126_rX_p3875
	Sherpa_221_NNPDF30NNLO_Wtaunu_MAXHTPTV140_280_BFilter	34.8226	DAOD_SUSY2.e5340_s3126_rX_p3875
	Sherpa_221_NNPDF30NNLO_Wtaunu_MAXHTPTV280_500_CVetoBVeto	39.2811	DAOD_SUSY2.e5340_s3126_rX_p3875
	Sherpa_221_NNPDF30NNLO_Wtaunu_MAXHTPTV280_500_CFilterBVeto	22.2546	DAOD_SUSY2.e5340_s3126_rX_p3875
	Sherpa_221_NNPDF30NNLO_Wtaunu_MAXHTPTV280_500_BFilter	9.4908	DAOD_SUSY2.e5340_s3126_rX_p3875
	Sherpa_221_NNPDF30NNLO_Wtaunu_MAXHTPTV500_1000	14.6035	DAOD_SUSY2.e5340_s3126_rX_p3875
	Sherpa_221_NNPDF30NNLO_Wtaunu_MAXHTPTV1000_E_CMS	1.1973	DAOD_SUSY2.e5340_s3126_rX_p3875

Table A.4: Summary table of the MC16 samples used for top processes.

Appendix B

Signal Samples

In this appendix we gather all of the detailed information about the signal samples used.

$(m_{\tilde{t}}, m_{\tilde{\chi}_1^0})$ [GeV]	Δm [GeV]	σ [pb]	ϵ_{filter}	k factor	N_{events}	Effective Luminosity [fb^{-1}]
(350, 260)	90	4.43	0.048774	1	20000	90.29
(350, 230)	120	4.43	0.065749	1	30000	96.74
(350, 200)	150	4.43	0.089107	1	40000	90.29
(350, 185)	165	4.43	0.10154	1	70000	158.01
(375, 285)	90	3.06	0.048494	1	20000	130.72
(375, 255)	120	3.06	0.066000	1	20000	93.37
(375, 225)	150	3.06	0.088884	1	30000	98.04
(375, 210)	165	3.06	0.10201	1	50000	163.40
(400, 310)	90	2.15	0.048043	1	10000	93.02
(400, 280)	120	2.15	0.065706	1	20000	132.89
(400, 250)	150	2.15	0.089162	1	40000	186.05
(400, 235)	165	2.15	0.10206	1	40000	186.05
(425, 335)	90	1.54	0.048737	1	20000	259.74
(425, 305)	120	1.54	0.066084	1	20000	185.53
(425, 275)	150	1.54	0.089955	1	30000	194.81
(425, 260)	165	1.54	0.10231	1	30000	194.81
(450, 360)	90	1.11	0.049199	1	10000	180.18
(450, 330)	120	1.11	0.066134	1	20000	257.40
(450, 300)	150	1.11	0.089836	1	20000	180.18
(450, 285)	165	1.11	0.10248	1	20000	180.18
(475, 385)	90	0.819	0.049161	1	10000	244.20
(475, 355)	120	0.819	0.066297	1	10000	174.43
(475, 325)	150	0.819	0.089778	1	20000	244.20
(475, 310)	165	0.819	0.10205	1	20000	244.20
(500, 410)	90	0.609	0.049348	1	10000	328.41
(500, 380)	120	0.609	0.065816	1	10000	234.58
(500, 350)	150	0.609	0.089822	1	10000	164.20
(500, 335)	165	0.609	0.10361	1	10000	164.20
(550, 460)	90	0.347	0.049477	1	10000	576.37
(550, 430)	120	0.347	0.066167	1	10000	411.69
(550, 400)	150	0.347	0.089540	1	10000	288.18
(550, 385)	165	0.347	0.10282	1	10000	288.18
(600, 510)	90	0.205	0.049424	1	10000	975.61
(600, 480)	120	0.205	0.066325	1	10000	696.86
(600, 450)	150	0.205	0.089752	1	10000	487.80
(600, 435)	165	0.205	0.10199	1	10000	487.80

Table B.1: The detailed information about the mc16a signal samples used in this analysis.

$(m_{\tilde{t}}, m_{\tilde{\chi}_1^0})$ [GeV]	Δm [GeV]	σ [pb]	ϵ_{filter}	k factor	N_{events}	Effective Luminosity [fb^{-1}]
(350, 260)	90	4.43	0.048774	1	20000	90.29
(350, 230)	120	4.43	0.065749	1	30000	96.74
(350, 200)	150	4.43	0.089107	1	40000	90.29
(350, 185)	165	4.43	0.10154	1	90000	203.16
(375, 285)	90	3.06	0.048494	1	20000	130.72
(375, 255)	120	3.06	0.066000	1	20000	93.37
(375, 225)	150	3.06	0.088884	1	30000	98.04
(375, 210)	165	3.06	0.10201	1	60000	196.08
(400, 310)	90	2.15	0.048043	1	10000	93.02
(400, 280)	120	2.15	0.065706	1	20000	132.89
(400, 250)	150	2.15	0.089162	1	50000	232.56
(400, 235)	165	2.15	0.10206	1	50000	232.56
(425, 335)	90	1.54	0.048737	1	20000	259.74
(425, 305)	120	1.54	0.066084	1	30000	278.29
(425, 275)	150	1.54	0.089955	1	30000	194.81
(425, 260)	165	1.54	0.10231	1	30000	194.81
(450, 360)	90	1.11	0.049199	1	20000	360.36
(450, 330)	120	1.11	0.066134	1	20000	257.40
(450, 300)	150	1.11	0.089836	1	30000	270.27
(450, 285)	165	1.11	0.10248	1	30000	270.27
(475, 385)	90	0.819	0.049161	1	500000	12,210.01
(475, 355)	120	0.819	0.066297	1	500000	8,721.44
(475, 325)	150	0.819	0.089778	1	500000	6,105.01
(475, 310)	165	0.819	0.10205	1	20000	244.20
(500, 410)	90	0.609	0.049348	1	10000	328.41
(500, 380)	120	0.609	0.065816	1	10000	234.58
(500, 350)	150	0.609	0.089822	1	20000	328.41
(500, 335)	165	0.609	0.10361	1	20000	328.41
(550, 460)	90	0.347	0.049477	1	10000	576.37
(550, 430)	120	0.347	0.066167	1	10000	411.69
(550, 400)	150	0.347	0.089540	1	10000	288.18
(550, 385)	165	0.347	0.10282	1	10000	288.18
(600, 510)	90	0.205	0.049424	1	10000	975.61
(600, 480)	120	0.205	0.066325	1	10000	696.86
(600, 450)	150	0.205	0.089752	1	10000	487.80
(600, 435)	165	0.205	0.10199	1	10000	487.80

Table B.2: The detailed information about the mc16d signal samples used in this analysis.

$(m_{\tilde{t}}, m_{\tilde{\chi}_1^0})$ [GeV]	Δm [GeV]	σ [pb]	ϵ_{filter}	k factor	N_{events}	Effective Luminosity [fb^{-1}]
(350, 260)	90	4.43	0.048774	1	50000	231.40
(350, 230)	120	4.43	0.065749	1	50000	171.66
(350, 200)	150	4.43	0.089107	1	70000	171.33
(350, 185)	165	4.43	0.10154	1	120000	270.88
(375, 285)	90	3.06	0.048494	1	40000	269.56
(375, 255)	120	3.06	0.066000	1	40000	198.06
(375, 225)	150	3.06	0.088884	1	60000	220.60
(375, 210)	165	3.06	0.10201	1	80000	261.44
(400, 310)	90	2.15	0.048043	1	30000	290.44
(400, 280)	120	2.15	0.065706	1	40000	283.15
(400, 250)	150	2.15	0.089162	1	60000	279.07
(400, 235)	165	2.15	0.10206	1	60000	279.07
(425, 335)	90	1.54	0.048737	1	20000	259.74
(425, 305)	120	1.54	0.066084	1	30000	278.29
(425, 275)	150	1.54	0.089955	1	40000	259.74
(425, 260)	165	1.54	0.10231	1	40000	259.74
(450, 360)	90	1.11	0.049199	1	20000	360.36
(450, 330)	120	1.11	0.066134	1	20000	257.40
(450, 300)	150	1.11	0.089836	1	30000	270.27
(450, 285)	165	1.11	0.10248	1	30000	270.27
(475, 385)	90	0.819	0.049161	1	20000	488.40
(475, 355)	120	0.819	0.066297	1	20000	348.86
(475, 325)	150	0.819	0.089778	1	30000	366.30
(475, 310)	165	0.819	0.10205	1	30000	366.30
(500, 410)	90	0.609	0.049348	1	10000	328.41
(500, 380)	120	0.609	0.065816	1	20000	469.15
(500, 350)	150	0.609	0.089822	1	20000	328.41
(500, 335)	165	0.609	0.10361	1	20000	328.41
(550, 460)	90	0.347	0.049477	1	10000	576.37
(550, 430)	120	0.347	0.066167	1	10000	411.69
(550, 400)	150	0.347	0.089540	1	10000	288.18
(550, 385)	165	0.347	0.10282	1	10000	288.18
(600, 510)	90	0.205	0.049424	1	10000	975.61
(600, 480)	120	0.205	0.066325	1	10000	696.86
(600, 450)	150	0.205	0.089752	1	10000	487.80
(600, 435)	165	0.205	0.10199	1	10000	487.80

Table B.3: The detailed information about the mc16e signal samples used in this analysis.

Appendix C

Systematic Uncertainties

Collected in this appendix are the breakdowns of the different systematics in the different regions for the Jigsaw analysis.

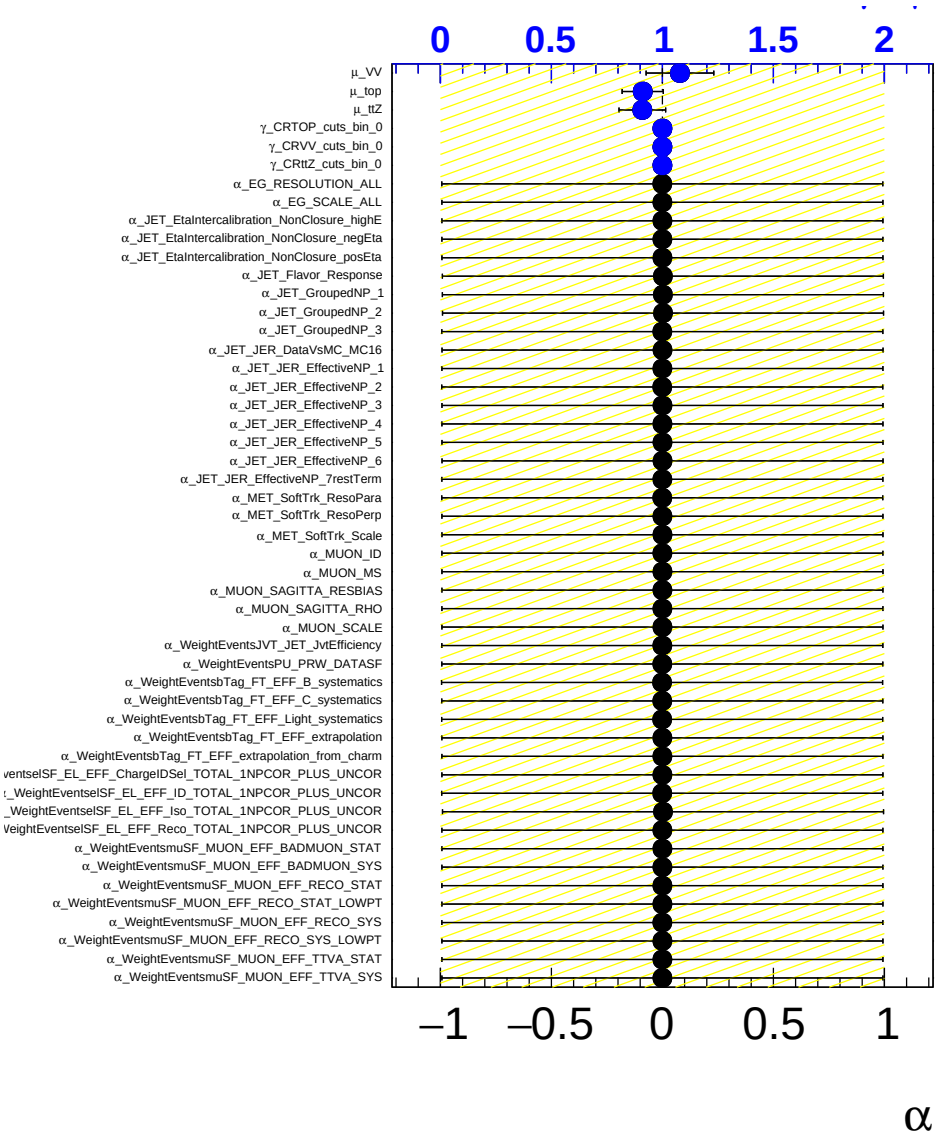

Figure C.1: Fit results parameters: μ represents the scale factors for the considered background processes, γ represents the MC uncertainties and α represent the systematic uncertainties.

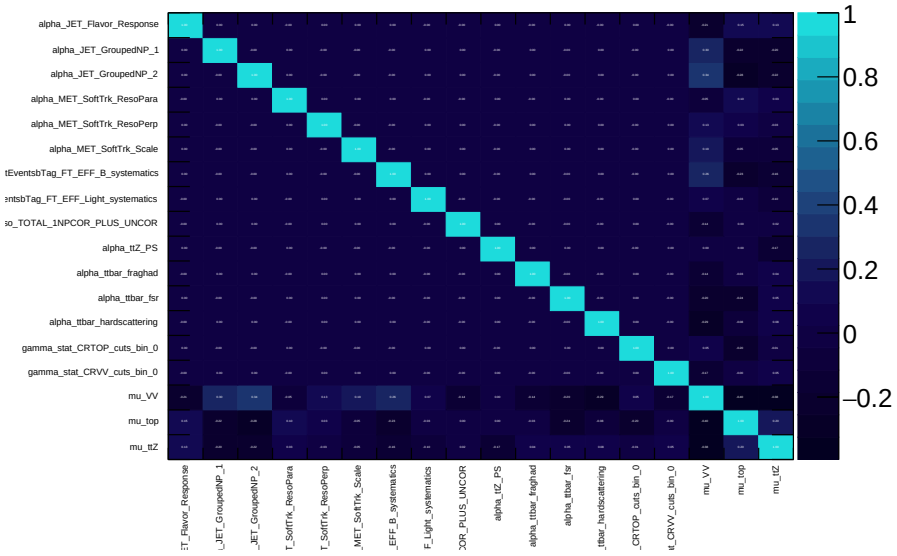

Figure C.2: Reduced correlation matrix for the background fit parameters.

The following tables show the dominant systematic uncertainties on the background estimates.

Uncertainty of channel	SR_W^{DF}	SR_W^{SF}	SR_t^{DF}	SR_t^{SF}
Total background expectation	5.07	3.74	7.30	4.90
Total statistical ($\sqrt{N_{\text{exp}}}$)	±2.25	±1.93	±2.70	±2.21
Total background systematic	±0.94 [18.60%]	±0.99 [26.57%]	±1.39 [19.02%]	±1.07 [21.91%]
mu_VV	±0.76 [14.9%]	±0.75 [20.0%]	±0.05 [0.69%]	±0.10 [2.1%]
gamma_stat_SRWDF_cuts_bin_0	±0.30 [5.8%]	±0.00 [0.00%]	±0.00 [0.00%]	±0.00 [0.00%]
α ttbar_hardscattering	±0.26 [5.1%]	±0.16 [4.2%]	±0.78 [10.6%]	±0.35 [7.2%]
α VV_CKKW	±0.26 [5.1%]	±0.26 [6.8%]	±0.03 [0.41%]	±0.06 [1.2%]
α VV_QSF	±0.26 [5.1%]	±0.26 [6.8%]	±0.02 [0.25%]	±0.04 [0.74%]
α ttbar_fsr	±0.24 [4.8%]	±0.14 [3.8%]	±0.44 [6.0%]	±0.17 [3.4%]
α JET_GroupedNP_1	±0.20 [4.0%]	±0.08 [2.0%]	±0.16 [2.2%]	±0.16 [3.3%]
α ttbar_isr	±0.17 [3.4%]	±0.11 [2.9%]	±0.48 [6.5%]	±0.17 [3.4%]
α VV_scale	±0.14 [2.9%]	±0.08 [2.2%]	±0.02 [0.29%]	±0.02 [0.38%]
α WeightEventsbTag_FT_EFF_B_systematics	±0.14 [2.8%]	±0.09 [2.4%]	±0.11 [1.5%]	±0.04 [0.77%]
α JET_GroupedNP_3	±0.14 [2.7%]	±0.06 [1.5%]	±0.17 [2.4%]	±0.04 [0.79%]
α JET_GroupedNP_2	±0.13 [2.5%]	±0.06 [1.6%]	±0.12 [1.7%]	±0.12 [2.4%]
α ttbar_fraghad	±0.12 [2.5%]	±0.08 [2.0%]	±0.11 [1.5%]	±0.05 [1.0%]
mu_top	±0.12 [2.3%]	±0.07 [1.9%]	±0.36 [5.0%]	±0.17 [3.4%]
α VV_frag	±0.11 [2.1%]	±0.10 [2.8%]	±0.02 [0.27%]	±0.01 [0.28%]
α VRfakes	±0.11 [2.1%]	±0.00 [0.00%]	±0.00 [0.00%]	±0.03 [0.51%]
α JET_JER_EffectiveNP_1	±0.10 [1.9%]	±0.08 [2.0%]	±0.34 [4.7%]	±0.34 [6.8%]
α WeightEventsbTag_FT_EFF_Light_systematics	±0.06 [1.2%]	±0.05 [1.4%]	±0.02 [0.28%]	±0.03 [0.55%]
α JET_JER_EffectiveNP_5	±0.05 [1.0%]	±0.19 [5.1%]	±0.23 [3.1%]	±0.41 [8.3%]
α JET_Flavor_Response	±0.05 [1.0%]	±0.08 [2.2%]	±0.09 [1.3%]	±0.03 [0.64%]
α MET_SoftTrk_ResoPerp	±0.05 [0.91%]	±0.08 [2.1%]	±0.18 [2.4%]	±0.01 [0.26%]
α WeightEventsPU_PRW_DATASF	±0.04 [0.85%]	±0.02 [0.53%]	±0.03 [0.38%]	±0.01 [0.30%]
α MUON_MS	±0.04 [0.80%]	±0.06 [1.5%]	±0.02 [0.28%]	±0.04 [0.76%]
α MUON_ID	±0.04 [0.71%]	±0.01 [0.25%]	±0.05 [0.71%]	±0.02 [0.36%]
α MET_SoftTrk_Scale	±0.03 [0.62%]	±0.01 [0.36%]	±0.12 [1.7%]	±0.04 [0.80%]
α JET_JER_EffectiveNP_2	±0.03 [0.55%]	±0.16 [4.3%]	±0.32 [4.3%]	±0.42 [8.6%]
α WeightEventsbTag_FT_EFF_C_systematics	±0.03 [0.55%]	±0.02 [0.66%]	±0.05 [0.65%]	±0.00 [0.04%]
α WeightEventselSF_EL_EFF_ID_ TOTAL_1NPCOR_PLUS_UNCOR	±0.02 [0.47%]	±0.01 [0.26%]	±0.02 [0.23%]	±0.00 [0.02%]
α JET_JER_EffectiveNP_3	±0.02 [0.47%]	±0.16 [4.2%]	±0.21 [2.9%]	±0.41 [8.4%]
α WeightEventsbTag_FT_EFF_extrapolation	±0.02 [0.46%]	±0.02 [0.42%]	±0.01 [0.12%]	±0.00 [0.03%]
α EG_RESOLUTION_ALL	±0.02 [0.37%]	±0.01 [0.27%]	±0.02 [0.33%]	±0.06 [1.2%]
α WtDS_WtDS	±0.02 [0.36%]	±0.02 [0.51%]	±0.01 [0.19%]	±0.05 [1.1%]
α WeightEventselSF_EL_EFF_Iso_ TOTAL_1NPCOR_PLUS_UNCOR	±0.02 [0.34%]	±0.02 [0.49%]	±0.01 [0.15%]	±0.01 [0.24%]
α JET_JER_DataVsMC_MC16	±0.02 [0.32%]	±0.11 [3.0%]	±0.06 [0.78%]	±0.05 [0.97%]
α MUON_SCALE	±0.02 [0.31%]	±0.02 [0.44%]	±0.02 [0.25%]	±0.04 [0.72%]
α JET_JER_EffectiveNP_7restTerm	±0.02 [0.30%]	±0.18 [4.9%]	±0.32 [4.4%]	±0.23 [4.7%]
mu_ttZ	±0.01 [0.18%]	±0.01 [0.23%]	±0.25 [3.4%]	±0.18 [3.7%]
α WeightEventsSF_global_MUON_EFF_TrigSystUncertainty	±0.01 [0.14%]	±0.01 [0.22%]	±0.01 [0.15%]	±0.01 [0.24%]
α EG_SCALE_ALL	±0.01 [0.12%]	±0.03 [0.89%]	±0.02 [0.28%]	±0.09 [1.9%]
α ttZ_scale	±0.01 [0.11%]	±0.01 [0.17%]	±0.03 [0.46%]	±0.08 [1.6%]
α JET_JER_EffectiveNP_4	±0.00 [0.07%]	±0.14 [3.8%]	±0.12 [1.6%]	±0.27 [5.4%]
α WeightEventselSF_EL_EFF_Reco_ TOTAL_1NPCOR_PLUS_UNCOR	±0.00 [0.07%]	±0.00 [0.02%]	±0.00 [0.02%]	±0.00 [0.01%]
α MUON_SAGITTA_RESBIAS	±0.00 [0.06%]	±0.01 [0.14%]	±0.01 [0.20%]	±0.02 [0.31%]
α JET_JER_EffectiveNP_6	±0.00 [0.05%]	±0.12 [3.3%]	±0.20 [2.7%]	±0.21 [4.2%]
α WeightEventsmuSF_MUON_EFF_RECO_SYS	±0.00 [0.05%]	±0.00 [0.01%]	±0.01 [0.09%]	±0.00 [0.02%]
α JET_EtaIntercalibration_NonClosure_negEta	±0.00 [0.04%]	±0.00 [0.03%]	±0.00 [0.00%]	±0.00 [0.00%]
α JET_EtaIntercalibration_NonClosure_posEta	±0.00 [0.04%]	±0.00 [0.05%]	±0.00 [0.06%]	±0.00 [0.01%]
α WeightEventsSF_global_EL_EFF_Trigger_ TOTAL_1NPCOR_PLUS_UNCOR	±0.00 [0.03%]	±0.00 [0.00%]	±0.00 [0.04%]	±0.00 [0.01%]
α ttZ_PS	±0.00 [0.03%]	±0.00 [0.03%]	±0.04 [0.49%]	±0.03 [0.54%]
α WeightEventsSF_global_MUON_EFF_TrigStatUncertainty	±0.00 [0.02%]	±0.00 [0.03%]	±0.00 [0.01%]	±0.00 [0.03%]
α WeightEventsmuSF_MUON_EFF_ISO_SYS	±0.00 [0.01%]	±0.00 [0.05%]	±0.00 [0.00%]	±0.00 [0.05%]
α MET_SoftTrk_ResoPara	±0.00 [0.01%]	±0.02 [0.41%]	±0.07 [0.95%]	±0.08 [1.6%]
α WeightEventsJVT_JET_JvtEfficiency	±0.00 [0.01%]	±0.00 [0.12%]	±0.00 [0.04%]	±0.01 [0.12%]
α WeightEventsbTag_FT_EFF_extrapolation_from_charm	±0.00 [0.01%]	±0.00 [0.04%]	±0.00 [0.02%]	±0.01 [0.17%]
α WeightEventsSF_global_EL_EFF_TriggerEff_ TOTAL_1NPCOR_PLUS_UNCOR	±0.00 [0.01%]	±0.00 [0.00%]	±0.00 [0.01%]	±0.00 [0.00%]
α WeightEventsmuSF_MUON_EFF_RECO_STAT	±0.00 [0.01%]	±0.00 [0.01%]	±0.00 [0.01%]	±0.00 [0.01%]
α WeightEventsmuSF_MUON_EFF_ISO_STAT	±0.00 [0.00%]	±0.00 [0.01%]	±0.00 [0.01%]	±0.00 [0.01%]
gamma_stat_SRTDF_cuts_bin_0	±0.00 [0.00%]	±0.00 [0.00%]	±0.41 [5.7%]	±0.00 [0.00%]
α DDFakes_upperlimit_SRWDF	±0.00 [0.00%]	±0.00 [0.00%]	±0.23 [3.1%]	±0.00 [0.00%]
α ttZ_rad	±0.00 [0.00%]	±0.00 [0.00%]	±0.08 [1.0%]	±0.06 [1.1%]
gamma_stat_SRWSF_cuts_bin_0	±0.00 [0.00%]	±0.28 [7.5%]	±0.00 [0.00%]	±0.00 [0.00%]
gamma_stat_SRTSF_cuts_bin_0	±0.00 [0.00%]	±0.00 [0.00%]	±0.00 [0.00%]	±0.33 [6.8%]
α DDFakes_upperlimit_SRWSF	±0.00 [0.00%]	±0.25 [6.7%]	±0.00 [0.00%]	±0.00 [0.00%]

Table C.1: Breakdown of the dominant systematic uncertainties on background estimates in the various signal regions. Note that the individual uncertainties can be correlated and do not necessarily add up quadratically to the total background uncertainty. The percentages show the size of the uncertainty relative to the total expected background.

	CRTOP
Total background expectation	191.84
Total statistical ($\sqrt{N_{exp}}$)	±13.85
Total background systematic	±13.84 [7.22%]
mu_top	±16.95 [8.8%]
alpha_JET_GroupedNP_2	±4.75 [2.5%]
alpha_ttbar_fsr	±4.04 [2.1%]
alpha_WeightEventsbTag_FT_EFF_B_systematics	±3.96 [2.1%]
alpha_JET_GroupedNP_1	±3.77 [2.0%]
gamma_stat_CRTOP_cuts_bin_0	±3.35 [1.7%]
alpha_JET_Flavor_Response	±2.63 [1.4%]
alpha_MET_SoftTrk_ResoPara	±1.70 [0.89%]
alpha_ttbar_hardscattering	±1.26 [0.65%]
alpha_MET_SoftTrk_Scale	±0.84 [0.44%]
alpha_WeightEventsPU_PRW_DATASF	±0.75 [0.39%]
alpha_JET_JER_EffectiveNP_6	±0.70 [0.36%]
alpha_ttbar_fraghad	±0.56 [0.29%]
alpha_JET_JER_EffectiveNP_3	±0.53 [0.28%]
alpha_EG_SCALE_ALL	±0.49 [0.26%]
alpha_JET_JER_DataVsMC_MC16	±0.46 [0.24%]
alpha_WeightEventsbTag_FT_EFF_Light_systematics	±0.45 [0.23%]
alpha_JET_JER_EffectiveNP_2	±0.44 [0.23%]
alpha_MET_SoftTrk_ResoPerp	±0.44 [0.23%]
alpha_WeightEventsJVT_JET_JvtEfficiency	±0.44 [0.23%]
alpha_JET_JER_EffectiveNP_5	±0.36 [0.19%]
alpha_EG_RESOLUTION_ALL	±0.35 [0.18%]
alpha_MUON_MS	±0.30 [0.16%]
alpha_JET_JER_EffectiveNP_7restTerm	±0.27 [0.14%]
alpha_ttbar_isr	±0.26 [0.13%]
alpha_WeightEventselSF_EL_EFF_ID_TOTAL_1NPCOR_PLUS_UNCOR	±0.24 [0.13%]
alpha_JET_JER_EffectiveNP_1	±0.24 [0.12%]
alpha_JET_GroupedNP_3	±0.23 [0.12%]
alpha_MUON_SAGITTA_RESBIAS	±0.20 [0.10%]
alpha_ttZ_rad	±0.17 [0.09%]
mu_ttZ	±0.16 [0.09%]
alpha_MUON_SCALE	±0.15 [0.08%]
alpha_WeightEventsbTag_FT_EFF_C_systematics	±0.14 [0.07%]
alpha_WeightEventsmuSF_MUON_EFF_TrigSystUncertainty	±0.09 [0.05%]
alpha_JET_EtaIntercalibration_NonClosure_posEta	±0.05 [0.03%]
alpha_ttZ_scale	±0.03 [0.02%]
alpha_WtDS_WtDS	±0.03 [0.01%]
alpha_ttZ_PS	±0.02 [0.01%]
mu_VV	±0.02 [0.01%]
alpha_WeightEventselSF_EL_EFF_Trigger_TOTAL_1NPCOR_PLUS_UNCOR	±0.02 [0.01%]
alpha_WeightEventsmuSF_MUON_EFF_RECO_SYS_LOWPT	±0.02 [0.01%]
alpha_JET_JER_EffectiveNP_4	±0.02 [0.01%]
alpha_MUON_ID	±0.02 [0.01%]
alpha_WeightEventsmuSF_MUON_EFF_RECO_SYS	±0.01 [0.01%]
alpha_WeightEventselSF_EL_EFF_Iso_TOTAL_1NPCOR_PLUS_UNCOR	±0.01 [0.01%]
alpha_WeightEventselSF_EL_EFF_Reco_TOTAL_1NPCOR_PLUS_UNCOR	±0.01 [0.01%]
alpha_VV_CKKW	±0.01 [0.01%]
alpha_VV_scale	±0.01 [0.01%]
alpha_WeightEventsmuSF_MUON_EFF_ISO_SYS	±0.01 [0.00%]
alpha_WeightEventsmuSF_MUON_EFF_ISO_STAT	±0.01 [0.00%]
alpha_WeightEventsbTag_FT_EFF_extrapolation	±0.00 [0.00%]
alpha_WeightEventsmuSF_MUON_EFF_RECO_STAT_LOWPT	±0.00 [0.00%]
alpha_WeightEventsmuSF_MUON_EFF_TrigStatUncertainty	±0.00 [0.00%]
alpha_WeightEventsmuSF_MUON_EFF_TTVA_STAT	±0.00 [0.00%]
alpha_WeightEventsbTag_FT_EFF_extrapolation_from_charm	±0.00 [0.00%]
alpha_WeightEventsmuSF_MUON_EFF_RECO_STAT	±0.00 [0.00%]
alpha_WeightEventselSF_EL_EFF_TriggerEff_TOTAL_1NPCOR_PLUS_UNCOR	±0.00 [0.00%]
alpha_WeightEventsmuSF_MUON_EFF_TTVA_SYS	±0.00 [0.00%]
alpha_JET_EtaIntercalibration_NonClosure_negEta	±0.00 [0.00%]
gamma_stat_SRWDF_cuts_bin_0	±0.00 [0.00%]
alpha_MUON_SAGITTA_RHO	±0.00 [0.00%]
gamma_stat_VRVV_cuts_bin_0	±0.00 [0.00%]
gamma_stat_SRTDF_cuts_bin_0	±0.00 [0.00%]
gamma_stat_SRTSF_cuts_bin_0	±0.00 [0.00%]
gamma_stat_CRVV_cuts_bin_0	±0.00 [0.00%]
alpha_WeightEventsmuSF_MUON_EFF_BADMUON_SYS	±0.00 [0.00%]
gamma_stat_VRTOP1_cuts_bin_0	±0.00 [0.00%]
gamma_stat_SRWSF_cuts_bin_0	±0.00 [0.00%]
gamma_stat_VRTOP2_cuts_bin_0	±0.00 [0.00%]
gamma_stat_CRttZ_cuts_bin_0	±0.00 [0.00%]
alpha_VV_QSF	±0.00 [0.00%]
alpha_WeightEventsmuSF_MUON_EFF_BADMUON_STAT	±0.00 [0.00%]
alpha_WeightEventselSF_EL_EFF_ChargeIDSel_TOTAL_1NPCOR_PLUS_UNCOR	±0.00 [0.00%]
alpha_JET_EtaIntercalibration_NonClosure_highE	±0.00 [0.00%]

Table C.2: Breakdown of the dominant systematic uncertainties on background estimates in the various signal regions. Note that the individual uncertainties can be correlated, and do not necessarily add up quadratically to the total background uncertainty. The percentages show the size of the uncertainty relative to the total expected background.

	VRTOP1
Total background expectation	38.31
Total statistical ($\sqrt{N_{exp}}$)	±6.19
Total background systematic	±5.93 [15.48%]
mu_VV	±3.41 [8.9%]
mu_top	±2.33 [6.1%]
alpha_JET_GroupedNP_2	±1.97 [5.1%]
alpha_WeightEventsbTag_FT_EFF_B_systematics	±1.88 [4.9%]
alpha_ttbar_fraghad	±1.82 [4.8%]
alpha_ttbar_fsr	±1.76 [4.6%]
alpha_JET_GroupedNP_1	±1.68 [4.4%]
alpha_JET_JER_EffectiveNP_2	±1.39 [3.6%]
gamma_stat_VRTOP1_cuts_bin_0	±1.25 [3.3%]
alpha_JET_JER_EffectiveNP_3	±1.25 [3.3%]
alpha_JET_JER_EffectiveNP_1	±1.03 [2.7%]
alpha_JET_Flavor_Response	±1.02 [2.7%]
alpha_VV_CKKW	±1.00 [2.6%]
alpha_JET_JER_EffectiveNP_7restTerm	±0.97 [2.5%]
alpha_JET_JER_EffectiveNP_4	±0.80 [2.1%]
alpha_VV_QSF	±0.80 [2.1%]
alpha_ttbar_isr	±0.70 [1.8%]
alpha_ttbar_hardscattering	±0.66 [1.7%]
alpha_MET_SoftTrk_Scale	±0.62 [1.6%]
alpha_MET_SoftTrk_ResoPara	±0.61 [1.6%]
alpha_JET_JER_EffectiveNP_6	±0.40 [1.0%]
alpha_MET_SoftTrk_ResoPerp	±0.39 [1.0%]
alpha_WeightEventsbTag_FT_EFF_Light_systematics	±0.35 [0.92%]
alpha_WeightEventselSF_EL_EFF_ID_TOTAL_1NPCOR_PLUS_UNCOR	±0.35 [0.92%]
alpha_MUON_MS	±0.35 [0.90%]
alpha_VV_scale	±0.35 [0.90%]
alpha_JET_GroupedNP_3	±0.34 [0.89%]
alpha_JET_JER_EffectiveNP_5	±0.27 [0.72%]
alpha_JET_JER_DataVsMC_MC16	±0.24 [0.63%]
alpha_WeightEventsPU_PRW_DATASF	±0.19 [0.50%]
alpha_WeightEventsbTag_FT_EFF_C_systematics	±0.15 [0.39%]
alpha_MUON_ID	±0.13 [0.34%]
alpha_WeightEventsmuSF_MUON_EFF_TrigSystUncertainty	±0.11 [0.28%]
alpha_EG_SCALE_ALL	±0.09 [0.24%]
alpha_WeightEventselSF_EL_EFF_Iso_TOTAL_1NPCOR_PLUS_UNCOR	±0.06 [0.17%]
alpha_EG_RESOLUTION_ALL	±0.05 [0.13%]
alpha_WeightEventselSF_EL_EFF_Reco_TOTAL_1NPCOR_PLUS_UNCOR	±0.03 [0.09%]
alpha_JET_EtaIntercalibration_NonClosure_negEta	±0.03 [0.07%]
alpha_WeightEventsbTag_FT_EFF_extrapolation	±0.03 [0.07%]
alpha_MUON_SCALE	±0.03 [0.07%]
alpha_WeightEventsJVT_JET_JvtEfficiency	±0.02 [0.06%]
alpha_ttZ_scale	±0.02 [0.05%]
alpha_ttZ_rad	±0.02 [0.04%]
alpha_MUON_SAGITTA_RESBIAS	±0.02 [0.04%]
alpha_WeightEventselSF_EL_EFF_Trigger_TOTAL_1NPCOR_PLUS_UNCOR	±0.01 [0.04%]
alpha_WeightEventsmuSF_MUON_EFF_TrigStatUncertainty	±0.01 [0.03%]
alpha_WeightEventsmuSF_MUON_EFF_RECO_SYS	±0.01 [0.03%]
mu_ttZ	±0.01 [0.02%]
alpha_WeightEventsmuSF_MUON_EFF_ISO_SYS	±0.01 [0.01%]
alpha_WeightEventsbTag_FT_EFF_extrapolation_from_charm	±0.00 [0.01%]
alpha_WtDS_WtDS	±0.00 [0.01%]
alpha_WeightEventsmuSF_MUON_EFF_RECO_SYS_LOWPT	±0.00 [0.01%]
alpha_WeightEventsmuSF_MUON_EFF_ISO_STAT	±0.00 [0.00%]
alpha_WeightEventsmuSF_MUON_EFF_TTVA_STAT	±0.00 [0.00%]
alpha_WeightEventsmuSF_MUON_EFF_RECO_STAT_LOWPT	±0.00 [0.00%]
alpha_JET_EtaIntercalibration_NonClosure_posEta	±0.00 [0.00%]
alpha_ttZ_PS	±0.00 [0.00%]
alpha_WeightEventselSF_EL_EFF_TriggerEff_TOTAL_1NPCOR_PLUS_UNCOR	±0.00 [0.00%]
alpha_WeightEventsmuSF_MUON_EFF_RECO_STAT	±0.00 [0.00%]
alpha_WeightEventsmuSF_MUON_EFF_TTVA_SYS	±0.00 [0.00%]
gamma_stat_SRWDF_cuts_bin_0	±0.00 [0.00%]
alpha_MUON_SAGITTA_RHO	±0.00 [0.00%]
gamma_stat_VRVV_cuts_bin_0	±0.00 [0.00%]
gamma_stat_SRTDF_cuts_bin_0	±0.00 [0.00%]
gamma_stat_SRTSF_cuts_bin_0	±0.00 [0.00%]
gamma_stat_CRVV_cuts_bin_0	±0.00 [0.00%]
alpha_WeightEventsmuSF_MUON_EFF_BADMUON_SYS	±0.00 [0.00%]
gamma_stat_SRWSF_cuts_bin_0	±0.00 [0.00%]
gamma_stat_VRTOP2_cuts_bin_0	±0.00 [0.00%]
gamma_stat_CRttZ_cuts_bin_0	±0.00 [0.00%]
gamma_stat_CRTOP_cuts_bin_0	±0.00 [0.00%]
alpha_WeightEventsmuSF_MUON_EFF_BADMUON_STAT	±0.00 [0.00%]
alpha_WeightEventselSF_EL_EFF_ChargeIDSel_TOTAL_1NPCOR_PLUS_UNCOR	±0.00 [0.00%]
alpha_JET_EtaIntercalibration_NonClosure_highE	±0.00 [0.00%]

Table C.3: Breakdown of the dominant systematic uncertainties on background estimates in the various signal regions. Note that the individual uncertainties can be correlated, and do not necessarily add up quadratically to the total background uncertainty. The percentages show the size of the uncertainty relative to the total expected background.

	VRTOP2
Total background expectation	141.89
Total statistical ($\sqrt{N_{exp}}$)	±11.91
Total background systematic	±24.99 [17.61%]
alpha_ttbar_hardscattering	±19.55 [13.8%]
mu_top	±12.26 [8.6%]
alpha_JET_GroupedNP_2	±8.67 [6.1%]
alpha_JET_GroupedNP_1	±7.26 [5.1%]
alpha_JET_Flavor_Response	±4.87 [3.4%]
alpha_JET_JER_EffectiveNP_1	±4.68 [3.3%]
alpha_ttbar_isr	±4.32 [3.0%]
alpha_JET_JER_EffectiveNP_2	±3.46 [2.4%]
alpha_MET_SoftTrk_Scale	±3.24 [2.3%]
alpha_JET_JER_EffectiveNP_7restTerm	±2.96 [2.1%]
alpha_ttbar_fsr	±2.82 [2.0%]
gamma_stat_VRTOP2_cuts_bin_0	±2.49 [1.8%]
alpha_JET_JER_EffectiveNP_3	±2.30 [1.6%]
alpha_MET_SoftTrk_ResoPerp	±1.99 [1.4%]
alpha_JET_JER_EffectiveNP_5	±1.41 [0.99%]
alpha_WeightEventsbTag_FT_EFF_B_systematics	±1.36 [0.96%]
alpha_WeightEventselSF_EL_EFF_ID_TOTAL_1NPCOR_PLUS_UNCOR	±1.11 [0.78%]
alpha_JET_JER_EffectiveNP_4	±0.95 [0.67%]
alpha_WeightEventsPU_PRW_DATASF	±0.88 [0.62%]
alpha_JET_GroupedNP_3	±0.82 [0.58%]
alpha_ttbar_fraghad	±0.74 [0.52%]
alpha_JET_JER_EffectiveNP_6	±0.64 [0.45%]
alpha_EG_SCALE_ALL	±0.57 [0.40%]
alpha_JET_JER_DataVsMC_MC16	±0.51 [0.36%]
alpha_MUON_SCALE	±0.43 [0.31%]
alpha_MUON_MS	±0.42 [0.30%]
alpha_ttZ_rad	±0.35 [0.25%]
alpha_WeightEventsmuSF_MUON_EFF_TrigSystUncertainty	±0.33 [0.24%]
mu_VV	±0.28 [0.20%]
alpha_MET_SoftTrk_ResoPara	±0.25 [0.17%]
mu_ttZ	±0.17 [0.12%]
alpha_VV_CKKW	±0.15 [0.11%]
alpha_WeightEventsJVT_JET_JvtEfficiency	±0.13 [0.09%]
alpha_VV_QSF	±0.13 [0.09%]
alpha_EG_RESOLUTION_ALL	±0.13 [0.09%]
alpha_JET_EtaIntercalibration_NonClosure_posEta	±0.11 [0.08%]
alpha_WeightEventselSF_EL_EFF_Reco_TOTAL_1NPCOR_PLUS_UNCOR	±0.10 [0.07%]
alpha_WeightEventsbTag_FT_EFF_C_systematics	±0.10 [0.07%]
alpha_MUON_ID	±0.09 [0.06%]
alpha_ttZ_scale	±0.07 [0.05%]
alpha_VV_scale	±0.06 [0.04%]
alpha_WeightEventsbTag_FT_EFF_Light_systematics	±0.06 [0.04%]
alpha_MUON_SAGITTA_RESBIAS	±0.05 [0.03%]
alpha_WeightEventsmuSF_MUON_EFF_TrigStatUncertainty	±0.04 [0.03%]
alpha_WtDS_WtDS	±0.04 [0.03%]
alpha_WeightEventselSF_EL_EFF_Trigger_TOTAL_1NPCOR_PLUS_UNCOR	±0.04 [0.03%]
alpha_JET_EtaIntercalibration_NonClosure_negEta	±0.04 [0.03%]
alpha_WeightEventsmuSF_MUON_EFF_RECO_SYS	±0.03 [0.02%]
alpha_WeightEventselSF_EL_EFF_Iso_TOTAL_1NPCOR_PLUS_UNCOR	±0.03 [0.02%]
alpha_ttZ_PS	±0.03 [0.02%]
alpha_WeightEventsmuSF_MUON_EFF_ISO_SYS	±0.02 [0.01%]
alpha_WeightEventsbTag_FT_EFF_extrapolation	±0.02 [0.01%]
alpha_WeightEventselSF_EL_EFF_TriggerEff_TOTAL_1NPCOR_PLUS_UNCOR	±0.00 [0.00%]
alpha_WeightEventsmuSF_MUON_EFF_ISO_STAT	±0.00 [0.00%]
alpha_WeightEventsmuSF_MUON_EFF_TTVA_STAT	±0.00 [0.00%]
alpha_WeightEventsmuSF_MUON_EFF_RECO_STAT	±0.00 [0.00%]
alpha_WeightEventsmuSF_MUON_EFF_RECO_STAT_LOWPT	±0.00 [0.00%]
alpha_WeightEventsmuSF_MUON_EFF_TTVA_SYS	±0.00 [0.00%]
alpha_WeightEventsbTag_FT_EFF_extrapolation_from_charm	±0.00 [0.00%]
alpha_WeightEventsmuSF_MUON_EFF_RECO_SYS_LOWPT	±0.00 [0.00%]
gamma_stat_SRWDF_cuts_bin_0	±0.00 [0.00%]
alpha_MUON_SAGITTA_RHO	±0.00 [0.00%]
gamma_stat_VRVV_cuts_bin_0	±0.00 [0.00%]
gamma_stat_SRTDF_cuts_bin_0	±0.00 [0.00%]
gamma_stat_SRTSF_cuts_bin_0	±0.00 [0.00%]
gamma_stat_CRVV_cuts_bin_0	±0.00 [0.00%]
alpha_WeightEventsmuSF_MUON_EFF_BADMUON_SYS	±0.00 [0.00%]
gamma_stat_VRTOP1_cuts_bin_0	±0.00 [0.00%]
gamma_stat_SRWSF_cuts_bin_0	±0.00 [0.00%]
gamma_stat_CRttZ_cuts_bin_0	±0.00 [0.00%]
gamma_stat_CRTOP_cuts_bin_0	±0.00 [0.00%]
alpha_WeightEventsmuSF_MUON_EFF_BADMUON_STAT	±0.00 [0.00%]
alpha_WeightEventselSF_EL_EFF_ChargeIDSel_TOTAL_1NPCOR_PLUS_UNCOR	±0.00 [0.00%]
alpha_JET_EtaIntercalibration_NonClosure_highE	±0.00 [0.00%]

Table C.4: Breakdown of the dominant systematic uncertainties on background estimates in the various signal regions. Note that the individual uncertainties can be correlated, and do not necessarily add up quadratically to the total background uncertainty. The percentages show the size of the uncertainty relative to the total expected background.

	CRVV
Total background expectation	169.07
Total statistical ($\sqrt{N_{exp}}$)	±13.00
Total background systematic	±12.96 [7.66%]
mu_VV	±22.27 [13.2%]
alpha_ttbar_hardscattering	±6.95 [4.1%]
mu_top	±6.09 [3.6%]
alpha_ttbar_fsr	±5.89 [3.5%]
alpha_JET_GroupedNP_2	±5.83 [3.4%]
alpha_JET_GroupedNP_1	±5.33 [3.2%]
alpha_WeightEventsbTag_FT_EFF_B_systematics	±4.36 [2.6%]
alpha_MET_SoftTrk_Scale	±3.98 [2.4%]
gamma_stat_CRVV_cuts_bin_0	±3.88 [2.3%]
alpha_JET_Flavor_Response	±3.74 [2.2%]
alpha_ttbar_fraghad	±3.26 [1.9%]
alpha_MET_SoftTrk_ResoPerp	±3.08 [1.8%]
alpha_WeightEventselSF_EL_EFF_Iso_TOTAL_1NPCOR_PLUS_UNCOR	±3.08 [1.8%]
alpha_VV_scale	±1.98 [1.2%]
alpha_JET_JER_EffectiveNP_3	±1.95 [1.2%]
alpha_JET_JER_EffectiveNP_2	±1.41 [0.83%]
alpha_WeightEventsbTag_FT_EFF_Light_systematics	±1.34 [0.79%]
alpha_JET_JER_EffectiveNP_1	±1.09 [0.64%]
alpha_EG_SCALE_ALL	±1.00 [0.59%]
alpha_JET_JER_EffectiveNP_4	±0.75 [0.44%]
alpha_MET_SoftTrk_ResoPara	±0.58 [0.34%]
alpha_WeightEventsbTag_FT_EFF_C_systematics	±0.56 [0.33%]
alpha_MUON_SCALE	±0.56 [0.33%]
alpha_WeightEventsJVT_JET_JvtEfficiency	±0.50 [0.29%]
alpha_JET_GroupedNP_3	±0.43 [0.25%]
alpha_EG_RESOLUTION_ALL	±0.40 [0.23%]
alpha_VV_CKKW	±0.37 [0.22%]
alpha_JET_JER_EffectiveNP_6	±0.37 [0.22%]
alpha_JET_JER_EffectiveNP_7restTerm	±0.36 [0.21%]
alpha_JET_JER_DataVsMC_MC16	±0.35 [0.20%]
alpha_MUON_ID	±0.26 [0.15%]
alpha_WeightEventsPU_PRW_DATASF	±0.22 [0.13%]
alpha_WeightEventselSF_EL_EFF_ID_TOTAL_1NPCOR_PLUS_UNCOR	±0.20 [0.12%]
alpha_ttbar_isr	±0.18 [0.11%]
alpha_MUON_SAGITTA_RESBIAS	±0.18 [0.11%]
mu_ttZ	±0.14 [0.08%]
alpha_VV_QSF	±0.14 [0.08%]
alpha_ttZ_rad	±0.09 [0.05%]
alpha_WeightEventsmuSF_MUON_EFF_RECO_SYS	±0.08 [0.05%]
alpha_MUON_MS	±0.07 [0.04%]
alpha_WeightEventselSF_EL_EFF_Reco_TOTAL_1NPCOR_PLUS_UNCOR	±0.06 [0.04%]
alpha_JET_EtaIntercalibration_NonClosure_posEta	±0.06 [0.03%]
alpha_WtDS_WtDS	±0.05 [0.03%]
alpha_WeightEventsbTag_FT_EFF_extrapolation	±0.05 [0.03%]
alpha_JET_JER_EffectiveNP_5	±0.04 [0.02%]
alpha_WeightEventsmuSF_MUON_EFF_ISO_SYS	±0.04 [0.02%]
alpha_WeightEventsmuSF_MUON_EFF_RECO_SYS_LOWPT	±0.03 [0.02%]
alpha_WeightEventsbTag_FT_EFF_extrapolation_from_charm	±0.03 [0.02%]
alpha_ttZ_scale	±0.03 [0.02%]
alpha_ttZ_PS	±0.02 [0.01%]
alpha_WeightEventsmuSF_MUON_EFF_TTVA_STAT	±0.01 [0.01%]
alpha_WeightEventsmuSF_MUON_EFF_RECO_STAT	±0.01 [0.01%]
alpha_WeightEventsmuSF_MUON_EFF_TrigStatUncertainty	±0.01 [0.01%]
alpha_WeightEventsmuSF_MUON_EFF_TrigSystUncertainty	±0.01 [0.01%]
alpha_WeightEventsmuSF_MUON_EFF_ISO_STAT	±0.01 [0.00%]
alpha_WeightEventsmuSF_MUON_EFF_RECO_STAT_LOWPT	±0.01 [0.00%]
alpha_WeightEventsmuSF_MUON_EFF_TTVA_SYS	±0.00 [0.00%]
alpha_JET_EtaIntercalibration_NonClosure_negEta	±0.00 [0.00%]
alpha_WeightEventselSF_EL_EFF_TriggerEff_TOTAL_1NPCOR_PLUS_UNCOR	±0.00 [0.00%]
alpha_WeightEventselSF_EL_EFF_Trigger_TOTAL_1NPCOR_PLUS_UNCOR	±0.00 [0.00%]
gamma_stat_SRWDF_cuts_bin_0	±0.00 [0.00%]
alpha_MUON_SAGITTA_RHO	±0.00 [0.00%]
gamma_stat_VRVV_cuts_bin_0	±0.00 [0.00%]
gamma_stat_SRTDF_cuts_bin_0	±0.00 [0.00%]
gamma_stat_SRTSF_cuts_bin_0	±0.00 [0.00%]
alpha_WeightEventsmuSF_MUON_EFF_BADMUON_SYS	±0.00 [0.00%]
gamma_stat_VRTOP1_cuts_bin_0	±0.00 [0.00%]
gamma_stat_SRWSF_cuts_bin_0	±0.00 [0.00%]
gamma_stat_VRTOP2_cuts_bin_0	±0.00 [0.00%]
gamma_stat_CRttZ_cuts_bin_0	±0.00 [0.00%]
gamma_stat_CRTOP_cuts_bin_0	±0.00 [0.00%]
alpha_WeightEventsmuSF_MUON_EFF_BADMUON_STAT	±0.00 [0.00%]
alpha_WeightEventselSF_EL_EFF_ChargeIDSel_TOTAL_1NPCOR_PLUS_UNCOR	±0.00 [0.00%]
alpha_JET_EtaIntercalibration_NonClosure_highE	±0.00 [0.00%]

Table C.5: Breakdown of the dominant systematic uncertainties on background estimates in the various signal regions. Note that the individual uncertainties can be correlated, and do not necessarily add up quadratically to the total background uncertainty. The percentages show the size of the uncertainty relative to the total expected background.

	VRVV
Total background expectation	96.89
Total statistical ($\sqrt{N_{exp}}$)	±9.84
Total background systematic	±14.93 [15.41%]
mu_VV	±12.17 [12.6%]
alpha_ttbar_hardscattering	±8.95 [9.2%]
mu_top	±4.16 [4.3%]
alpha_WeightEventsbTag_FT_EFF_B_systematics	±4.01 [4.1%]
alpha_ttbar_isr	±3.45 [3.6%]
alpha_JET_GroupedNP_1	±3.01 [3.1%]
alpha_VV_QSF	±2.69 [2.8%]
alpha_VV_CKKW	±2.44 [2.5%]
alpha_MET_SoftTrk_Scale	±2.38 [2.5%]
alpha_JET_GroupedNP_2	±2.27 [2.3%]
alpha_VV_scale	±1.97 [2.0%]
alpha_ttbar_fsr	±1.69 [1.7%]
gamma_stat_VRVV_cuts_bin_0	±1.47 [1.5%]
alpha_MET_SoftTrk_ResoPara	±1.29 [1.3%]
alpha_WeightEventsbTag_FT_EFF_Light_systematics	±1.13 [1.2%]
alpha_MET_SoftTrk_ResoPerp	±1.08 [1.1%]
alpha_JET_JER_EffectiveNP_3	±1.05 [1.1%]
alpha_JET_Flavor_Response	±1.01 [1.0%]
alpha_JET_GroupedNP_3	±1.01 [1.0%]
alpha_JET_JER_EffectiveNP_6	±0.98 [1.0%]
alpha_JET_JER_EffectiveNP_2	±0.88 [0.91%]
alpha_JET_JER_EffectiveNP_5	±0.79 [0.82%]
alpha_JET_JER_DataVsMC_MC16	±0.74 [0.76%]
alpha_EG_SCALE_ALL	±0.71 [0.74%]
alpha_ttbar_fraghad	±0.69 [0.71%]
alpha_JET_JER_EffectiveNP_1	±0.67 [0.69%]
alpha_JET_JER_EffectiveNP_7restTerm	±0.55 [0.57%]
alpha_WeightEventsbTag_FT_EFF_C_systematics	±0.44 [0.46%]
alpha_MUON_SCALE	±0.39 [0.40%]
alpha_WtDS_WtDS	±0.28 [0.29%]
alpha_MUON_SAGITTA_RESBIAS	±0.26 [0.26%]
alpha_WeightEventselSF_EL_EFF_Iso_TOTAL_1NPCOR_PLUS_UNCOR	±0.25 [0.26%]
alpha_WeightEventsbTag_FT_EFF_extrapolation	±0.25 [0.26%]
alpha_ttZ_rad	±0.25 [0.25%]
alpha_EG_RESOLUTION_ALL	±0.24 [0.24%]
alpha_MUON_ID	±0.23 [0.24%]
alpha_JET_JER_EffectiveNP_4	±0.17 [0.17%]
mu_ttZ	±0.10 [0.10%]
alpha_WeightEventsPU_PRW_DATASF	±0.07 [0.08%]
alpha_JET_EtaIntercalibration_NonClosure_posEta	±0.07 [0.07%]
alpha_MUON_MS	±0.05 [0.05%]
alpha_WeightEventselSF_EL_EFF_ID_TOTAL_1NPCOR_PLUS_UNCOR	±0.04 [0.04%]
alpha_ttZ_scale	±0.03 [0.03%]
alpha_WeightEventsmuSF_MUON_EFF_TrigSystUncertainty	±0.03 [0.03%]
alpha_WeightEventsmuSF_MUON_EFF_RECO_SYS	±0.03 [0.03%]
alpha_WeightEventsmuSF_MUON_EFF_ISO_SYS	±0.03 [0.03%]
alpha_WeightEventselSF_EL_EFF_Reco_TOTAL_1NPCOR_PLUS_UNCOR	±0.02 [0.02%]
alpha_WeightEventsJVT_JET_JvtEfficiency	±0.02 [0.02%]
alpha_JET_EtaIntercalibration_NonClosure_negEta	±0.02 [0.02%]
alpha_ttZ_PS	±0.02 [0.02%]
alpha_WeightEventsbTag_FT_EFF_extrapolation_from_charm	±0.01 [0.01%]
alpha_WeightEventselSF_EL_EFF_Trigger_TOTAL_1NPCOR_PLUS_UNCOR	±0.01 [0.01%]
alpha_WeightEventsmuSF_MUON_EFF_RECO_SYS_LOWPT	±0.00 [0.01%]
alpha_WeightEventsmuSF_MUON_EFF_TrigStatUncertainty	±0.00 [0.00%]
alpha_WeightEventsmuSF_MUON_EFF_TTVA_STAT	±0.00 [0.00%]
alpha_WeightEventsmuSF_MUON_EFF_ISO_STAT	±0.00 [0.00%]
alpha_WeightEventsmuSF_MUON_EFF_RECO_STAT	±0.00 [0.00%]
alpha_WeightEventsmuSF_MUON_EFF_RECO_STAT_LOWPT	±0.00 [0.00%]
alpha_WeightEventselSF_EL_EFF_TriggerEff_TOTAL_1NPCOR_PLUS_UNCOR	±0.00 [0.00%]
alpha_WeightEventsmuSF_MUON_EFF_TTVA_SYS	±0.00 [0.00%]
gamma_stat_SRWDF_cuts_bin_0	±0.00 [0.00%]
alpha_MUON_SAGITTA_RHO	±0.00 [0.00%]
gamma_stat_SRTDF_cuts_bin_0	±0.00 [0.00%]
gamma_stat_SRTSF_cuts_bin_0	±0.00 [0.00%]
gamma_stat_CRVV_cuts_bin_0	±0.00 [0.00%]
alpha_WeightEventsmuSF_MUON_EFF_BADMUON_SYS	±0.00 [0.00%]
gamma_stat_VRTOP1_cuts_bin_0	±0.00 [0.00%]
gamma_stat_SRWSF_cuts_bin_0	±0.00 [0.00%]
gamma_stat_VRTOP2_cuts_bin_0	±0.00 [0.00%]
gamma_stat_CRttZ_cuts_bin_0	±0.00 [0.00%]
gamma_stat_CRTOP_cuts_bin_0	±0.00 [0.00%]
alpha_WeightEventsmuSF_MUON_EFF_BADMUON_STAT	±0.00 [0.00%]
alpha_WeightEventselSF_EL_EFF_ChargeIDSel_TOTAL_1NPCOR_PLUS_UNCOR	±0.00 [0.00%]
alpha_JET_EtaIntercalibration_NonClosure_highE	±0.00 [0.00%]

Table C.6: Breakdown of the dominant systematic uncertainties on background estimates in the various signal regions. Note that the individual uncertainties can be correlated, and do not necessarily add up quadratically to the total background uncertainty. The percentages show the size of the uncertainty relative to the total expected background.